# FABRICATION AND CHARACTERISATION OF GRAPHENE-BASED MULTI-FUNCTIONAL COATINGS

by

**SHAOJUN QI**

A thesis submitted to

**The University of Birmingham**

for the degree of

**DOCTOR OF PHILOSOPHY**

School of Metallurgy and Materials
College of Engineering and Physical Sciences
The University of Birmingham
August 2017

# Synopsis

The unusual tribological and corrosion inhibiting properties of graphene have been revealed by nano-scale experimental and theoretical studies. The ever-increasing demand in utilising these extraordinary properties calls for production of graphene-based coatings with high uniformity and in large area. This research was aimed at exploring different surface engineering techniques towards cost-effective and scalable fabrication of such coatings on metallic surfaces.

Graphene oxide (GO) was employed as the coating precursor, and various coating routes were investigated in the project to produce coatings mostly on 316L stainless steel. Self-assembly and electrophoretic deposition (EPD) were employed to produce single- and multi-layer GO coatings with thickness values ranging from 1 nm to hundreds of nm, whilst electroplating and electro-brush plating were used to deposit nickel-GO composite coatings on the steel substrates. The chemical compositions and microstructures of the resultant coatings were characterised. The tribological behaviours of the coatings in reciprocating sliding contacts were studied and their corrosion performance evaluated. Particularly, the mechanical properties and thermal stability of the Ni-GO composite coatings were investigated using nanoindentation.

The results have showed that both EPD and self-assembly are capable of depositing thin and uniform GO coatings onto steel. The EPD technique exhibited advantages such as good control of coating thickness and *in-situ* reduction of GO. The tribological and corrosion tests have showed promising properties of the GO coatings in terms of a much lower friction coefficient, 30-times smaller corrosion current density and a 9-time higher corrosion impedance compared to the bare steel. However, the

EPD coatings were prone to damage due to interlayer shear and the weak coating adhesion to the steel substrate. It was found that specific surface topography helped retain the GO coatings. Alternatively, pre-modification of the steel surface with a self-assembled monolayer of silane can also enhance the bonding of the GO sheets to the steel surface, thus improving the wear performance of the ultra-thin GO coating in terms of a 10-fold reduction in wear and increased coating durability by 20 times.

Ni-GO composite coatings were produced successfully by conventional electroplating. A grain refinement effect due to GO incorporation has been confirmed by XRD. The hardness and elastic modulus of the nickel matrixes were improved up to 42% and 7.5%, respectively. Unfortunately, the corrosion resistance was worsened, mainly due to the adverse GO agglomerations within the deposit.

In contrast, the electro-brush plated Ni-GO nano-composite coatings exhibited significantly improved compactness and homogeneity. A similar grain refinement and improvement in the elastic properties yet an 8% reduction in plasticity were observed. More importantly, the GO-containing nano-composite coatings exhibited enhanced thermal stability, in terms of a better retention of the hardness and elastic properties after annealing up to 600 ℃. Meanwhile, the Ni-GO composite coatings showed 37% lower friction and 88% lower wear compared to neat nickel coating. The corrosion performance was also upgraded in terms of a 70% reduction in corrosion current and a 5-time increase in total corrosion impedance. The findings indicate that electro-brush plating is a very promising technique to produce novel nano-composite coatings.

Based on the experimental results, the potential mechanisms involved in grain refinement, greatly increased mechanical properties, effectively enhanced tribological and corrosion performance and significantly improved thermal stability are discussed.

# Acknowledgements

First of all, I would like to express my immense gratitude to my academic supervisors, Prof. Hanshan Dong and Dr. Xiaoying Li, for their invaluable supervision and support throughout my 4-year study. Both of them have contributed plenty of inspiring advice, guidance as well as great patience without which I could not have got through every difficult moment, developed all of my research experience and interest and felt my PhD life an enjoyable one.

I must express my deep appreciation to the University of Birmingham and the China Scholarship Council for providing the PhD studentship and all the financial support which made my oversea PhD study possible.

It has been such a pleasure of mine to be part of the Surface Engineering Research Group. Special thanks go to Dr. Kaijie Lin, who picked me up from the airport the very first day I arrived, and gave me continuous life and research tips thereafter. I would like to thank our group members/alumni Dr. Linhai Tian, Dr. Santiago Corujeira Gallo, Dr. Yangchun Dong, Dr. Zhenxue Zhang, Mr. Xiaochao Ji, Dr. Dennis Formosa, Mr. Behnam Dashtbozorg, Ms. Yana Liang, Ms. Tatiana Mukinay, Mr. Elliot Walters, and our fresh graduates Ms. Yuan Liang, Dr. Shiling Zhang and Dr. Qiongxi Liu. I really enjoyed the moments together at our lunch corner, and appreciate all the assistance from and the brain storms with every of them.

I would also like to acknowledge Prof. Jian Chen and Prof. Stefan Dimov for offering the academic collaboration opportunities, Mrs Theresa Morris at the Centre for Electron Microscopy who kindly provided the trainings, and Prof. Tim Button for his help with the fume cupboard in my first year.

Finally, I would like to express my love and gratitude to my parents and sister who always care and are proud of me, and to my dear fiancée who gives her constant support and encouragement to me. Thanks also to all my friends who have shared memories with me and helped me in any manners.

# List of Publications

## Journals

- ***S. Qi***, X. Li, H. Dong (2017). Improving the macro-scale tribology of monolayer graphene oxide coating on stainless steel by a silane bonding layer. Materials Letters, 209, 15-18.

- ***S. Qi***, X. Li, Z. Zhang, H. Dong (2017). Fabrication and characterisation of electro-brush plated nickel-graphene oxide nano-composite coatings. Thin Solid Films, in press.

- H. Dong, ***S. Qi*** (2015). Realising the potential of graphene-based materials for biosurfaces – A future perspective. Biosurface and Biotribology, 1, 229-248.

- J. Chen, X. Shi, ***S. Qi***, M. Mohai, I. Bertóti, Y. Gao, H. Dong (2015). Reducing and multiple-element doping of graphene oxide using active screen plasma treatments. Carbon, 95, 338-346.

- E.C. Romani, S. Nardecchia, C. Vilani, L. Nachez, ***S. Qi***, H. Dong, F.L. Freire Jr (2017). Synthesis and characterization of polyurethane/graphene oxide composite deposited on steel. Surface coatings and technology, submitted.

## Conferences

- Preparation and tribological performance of nickel-graphene oxide composite coatings. Poster presentation. **European Graphene Forum**, June 2016, Paris, France

- Graphene oxide coatings on 316L steel for tribological & anti-corrosion applications. Poster presentation. **Graphene Week**, June 2015, Manchester, UK

# Table of Contents

# List of Figures

# List of Tables

# Nomenclature

## Symbols

| | |
|---|---|
| $A$ | electrode surface area |
| $C$ | particle concentration |
| $CPE_c$ | capacitance of coating |
| $CPE_{dl}$ | capacitance of electric double layer |
| $E$ | electrical field strength (EPD) |
| $e$ | elementary charge |
| $E$ | Young's modulus (Mechanics) |
| $E_{corr}$ | corrosion potential |
| $E_r$ | reduced elastic (Young's) modulus |
| $f$ | efficiency factor of an EPD process (Henry constant) |
| $F$ | tangential frictional force |
| $H$ | hardness |
| $h$ | Planck's constant |
| $H_v$ | Vickers hardness |
| $I_{corr}$ | corrosion current density |
| $I_D/I_G$ | intensity ratio of the D to G Raman bands |
| $k$ | dimensionless wear coefficient |
| $K$ | Scherrer constant |
| $L$ | crystallite size |
| $n$ | phase shift index (EIS) |
| $R_a$ | surface roughness |

| | |
|---|---|
| $R_c$ | coating resistance |
| $R_{ct}$ | interfacial charge transfer resistance |
| $R_s$ | resistance of the electrolyte solution |
| $s$ | the total sliding distance |
| $t$ | deposition time |
| $V$ | volume of material loss |
| $W$ | applied normal load (tribology) |
| $W$ | weight gain during EPD |
| $Z$ | electrochemical impedance |
| $\beta$ | FWHM of the diffraction peak |
| $\varepsilon$ | average microstrain |
| $\zeta$ | zeta potential |
| $\theta$ | diffraction angle |
| $\lambda$ | wavelength of radiation |
| $\mu$ | coefficient of friction (tribology) |
| $\mu$ | electrophoretic mobility of the particles |
| $\mu_{adh}$ | *friction coefficient due to adhesion* |
| $\sigma$ | compression yield strength (tribology) |
| $\sigma_{int}$ | intrinsic strength |
| $\tau$ | shear strength |
| $\tau_i$ | shear strength of the interfacial film |
| $\Phi$ | diameter |
| $\psi$ | electric potential |
| $\Psi$ | plasticity index (mechanics) |

## Acronyms

| | |
|---|---|
| 316L | type 316L stainless steel |
| AFM | atomic force microscope |
| APTES | (3-Aminopropyl)triethoxysilane |
| ARPES | angle-resolved-photoemission spectroscopy |
| CNT | carbon nanotube |
| COF | coefficient of friction |
| CPE | constant phase element |
| CV | cyclic voltammetry |
| CVD | chemical vapour deposition |
| DC | direct current |
| DFT | density functional theory |
| EBP | electro brush plating |
| EDX/EDS | energy dispersive x-ray spectroscopy |
| EEC | electrical equivalent circuit |
| EIS | electrochemical impedance spectroscopy |
| ENG | electroplated nickel-GO composite |
| EPD | electrophoretic deposition |
| FEM | finite element modelling |
| FFM | friction force microscope |
| FIB | focused ion beam |
| FWHM | full width half maximum |
| G3500 | type G3500 cast iron |
| GIC | graphite intercalation compound |

| | |
|---|---|
| GN | graphene nano-sheet |
| GO | graphene oxide |
| HA | hydroxyapatite |
| HOPG | highly oriented pyrolytic graphite |
| ICR | interfacial contact resistance |
| MD | molecular dynamics |
| MEMG | mechanically exfoliated multilayer graphene |
| MEMS | micro-electromechanical systems |
| MGO | multilayer graphene oxide |
| MRGO | multilayer reduced graphene oxide |
| MWCNT | multiwall carbon nanotube |
| NEMS | nanoelectromechanical systems |
| NG | electro brush plated nickel-GO composite |
| NGr | electro brush plated nickel-graphite composite |
| OCP | open circuit potential |
| PI | plasticity index |
| PMMA | polymethyl methacrylate |
| PTFE | polytetrafluoroethylene |
| QHE | quantum Hall effect |
| rGO | reduced graphene oxide |
| SAED | selected area electron diffraction |
| SAM | self-assembled monolayer |
| SBF | simulated body fluid |
| SCE | saturated calomel electrode |

| | |
|---|---|
| SEM | scanning electron microscopy |
| SPG | solution-processed graphene |
| TEM | transmission electron microscope |
| UHMWPE | ultrahigh molecular weight polyethylene |
| WCA | water contact angle |
| XPS | X-ray photoelectron spectroscopy |
| XRD | x-ray diffraction |

# CHAPTER 1 INTRODUCTION

Graphene is a young yet very attractive carbon material owing to its extraordinary properties. Its unusual electronic properties have made it the centre of post-silicon era research [1, 2]. The high aspect ratio and strong $sp^2$ C-C bonds of graphene make it not only the thinnest and ultralight material, but also the strongest material ever discovered to date [3]. The light transmittance of monolayer graphene can be as high as 97.7% [1], making graphene a promising candidate material for various electronic and optoelectronic applications such as field emission transistors [4], transparent and flexible electrodes/films [5, 6], window materials for solar cells [7] and gas/chemical sensors [8].

Recently, there has been an increasing research interest in the tribology of graphene [9, 10]. Nano- and microscopic studies have demonstrated that graphene can show extraordinary lubricity, even superior to bulk graphite [11]. Importantly, graphene has a thickness of merely 0.34 nm, rendering it probably the thinnest solid lubricant ever. However, in the literature there is just a limited number of reports on graphene-based surface coatings for combating friction and wear at macro scale [12, 13]. This is mainly due to the difficulties in obtaining such coatings continuously on a large area. Nonetheless, graphene films of 100 metres long and premium quality have been produced by chemical vapour deposition (CVD) [14]. However, due to the strict selection criteria and thus very limited choices for the substrate material [15], the growth of such graphene films on arbitrary substrates has yet to be effectively realised. Meanwhile, the cost of CVD-graphene is still too high for scalable applications. In addition, the graphene surface coatings made via transfer of CVD-graphene [11] or other solvent evaporation methods [6, 16, 17] usually show inadequate bonding to common engineering materials surfaces [18].

Furthermore, it has also been demonstrated that graphene is theoretically impermeable to all molecules and ions, suggesting it an ideal corrosion barrier [19]. This unusual feature has been stimulating a vast number of studies exploring the use of graphene-related materials as protective coatings. Notwithstanding the fact that CVD-graphene has shown great potential as an effective inhibitor against both ambient oxidation [20] and wet corrosion [21], the same challenges as mentioned in the preceding paragraph remain. The combination of established protective coatings and graphene-related materials has resulted in a series of anti-corrosion composite coatings, especially those of polymeric matrixes that are suitable for cheap and mass production [22-24] and readily applicable on common metallic surfaces [25, 26]. However, graphene-metal composite coatings have yet to be widely studied, due to the lack of techniques for generating well-bonded, compact and homogeneous coatings.

Therefore, the overall aim of this PhD project was to explore different methods towards cost-effective and scalable fabrication of graphene-based coatings on metallic surfaces, and to optimise the coating process for enhanced performance at macro scale. The specific research objectives were:

- To fabricate surface coatings based on chemically derived graphene (graphene oxide) via wet-chemistry routes on steel.
- To develop advanced methods for deposition of graphene-based coatings of high homogeneity, good coverage and in large area.

- To fully characterise the chemical composition and microstructure of the coatings using various techniques, thus understanding the advantages and disadvantages of the different fabrication techniques employed.
- To investigate the mechanical properties of the coatings and the tribological behaviour in a macro-scale context for better understandings towards the different strengthening and wear mechanisms.
- To evaluate the anti-corrosion performance of the coatings electrochemically and contribute to the interpretation of the protection mechanisms.

As a quick overview, the following chapters of the thesis are outlined below:

- **Chapter 2** provides a survey of the literature starting from the discovery, structure and basic properties of graphene, to an introduction of the established methods for graphene and graphene-based coatings, followed by a review of the studies concerning graphene in the field of surface engineering, in particular tribology and corrosion.
- **Chapter 3** describes all the experimental procedures for sample preparation and coating fabrication. Details of the microstructure and property characterisation techniques are also given.
- **Chapter 4** is the first half of the whole results and discussion, covering four chronological topics which are GO synthesis, electrophoretic deposition and self-assembly of GO coatings, and electroplating of Ni-GO composite coatings.
- **Chapter 5** is the second half of the results and discussion which focuses on the novel fabrication of Ni-GO composite coatings by electro-brush plating. It covers the general characterisation and the promising mechanical, tribological,

corrosion properties and enhanced thermal stability of the obtained coatings.

- **Chapter 6** concludes the key findings and implications throughout the project.
- **Chapter 7** gives recommendations for scientific future work.

# CHAPTER 2 LITERATURE REVIEW

## 2.1 History and development of graphene research

Graphene is a one-atom-thick, honeycomb-like sheet of $sp^2$-hybridised carbon atoms. 2D graphene is the building block for many other carbon structures such as 0D fullerene, 1D carbon nanotube (CNT) and 3D graphite, as illustrated in Figure 2.1. This new member of the carbon materials family was first prepared in laboratory by Geim, Novoselov and co-workers in 2004 by developing a “Scotch-tape” method [27].

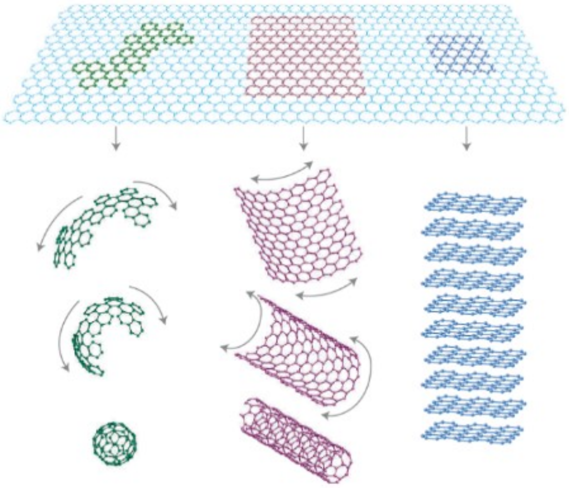

Figure 2.1 Schematic of 2D graphene, 0D fullerene, 1D CNT and graphite [28].

Actually, before their “ground-breaking experiments” [29] the theoretical research on graphene had taken place for decades [30-32]. However, for a long period graphene was thought to be a not real but “academic” material [33]. It was believed that 2D crystals could not exist independently due to thermal fluctuations which should deteriorate the long-range order and make the 2D structure highly unstable [28, 34-36]. Nevertheless, in the hope of obtaining 2D graphene, various attempts were made by researchers over the years, via either top-down or bottom-up methods [37-43]. The term “graphene” was originally coined by Boehm et al. in 1986 when referring to a single carbon layer of graphite intercalation compounds (GICs) [44]. Although the efforts never stopped, it was not until 2004 that pristine, monolayer graphene of high quality was prepared in a laboratory. Since then the unique structure and properties of graphene have been intensively investigated, with a huge number of breakthroughs published.

## 2.2 Structure and properties of graphene

### 2.2.1 Atomic structure of graphene

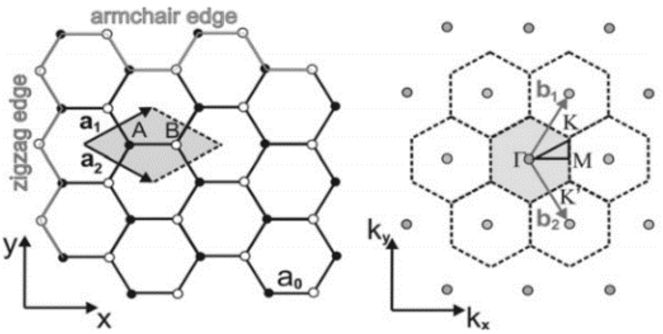

Figure 2.2 (a) Honeycomb lattice of graphene in real space. A and B represent the two types of nonequivalent carbon atoms. The basic vectors of the unit cell are set as $a_1$ and $a_2$. (b) the corresponding reciprocal lattice with basic vectors $b_1$ and $b_2$ and its first Brillouin zone (grey marked) [45].

Figure 2.2a is an atomic model of the graphene crystal. The honeycomb-like lattice consists of two sets of non-equivalent carbon atoms A and B. The corresponding reciprocal lattice of graphene is shown in Figure 2.2b. In graphene carbon atoms are $sp^2$-hybridised, which means for each carbon atom, three of the four exterior electrons couple with those of the nearest carbon atoms, forming three in-plane σ-bonds with included angles of 120°, thus resulting in the planar hexagonal lattice of graphene. The carbon atoms are separated by a lattice constant of 1.42 Å (0.142 nm). Within the lattice the C-C bonding energy of 615 kJ/mol is even stronger than that of $sp^3$-hybridised diamond (345 kJ/mol) [45], which gives rise to graphene's extraordinary mechanical properties. The remaining fourth exterior electron occupies an orbital perpendicular to the basal plane, and interacts with neighbouring counterparts, forming so-called delocalised π-bonds. Unlike strong σ-bonds, these π electrons are bonded much weakly and of high freedom, resulting in most of the electronic properties of graphene.

The conflict between the theoretical prediction and the successful laboratory discovery of 2D graphene is mediated by the fact that most of the reported graphenes are not standing alone, but either supported by [27] or grown epitaxially on [43] proper 3D substrates. With the benefit of supporting substrates, the thermal fluctuations within the graphene structure are suppressed and thus crystal defects are limited substantially. In the case of free standing graphene, both experimental observation [46] and theoretical simulation [47] have proved that suspended graphene membranes are actually not perfectly flat but with lots of intrinsic ripples of 5-20 nm laterally and 1 nm in the third dimension, as illustrated in Figure 2.3. These localised out-of-plane deformations, although much smaller than the sample size, help to resist thermal fluctuations and maintain long-range order.

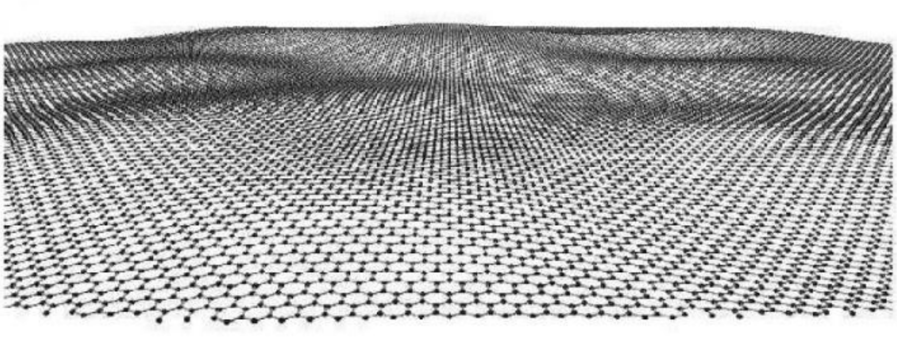

Figure 2.3 Schematic of intrinsic ripples in graphene [46].

### 2.2.2 Electronic properties

As depicted in the reciprocal lattice (Figure 2.2b [45]), the Brillouin zone of graphene is hexagonal with several high symmetry points Γ, M, K and K´. The two boundary points K and K´ are known as Dirac points. By using a tight-bonding approach, the band structure of single-layer graphene can be described as in Figure 2.4 [48]. The neighbouring π electron orbitals overlap, and the valence (π electron occupied) and conductance bands (vacancies) meet exactly at Dirac points.

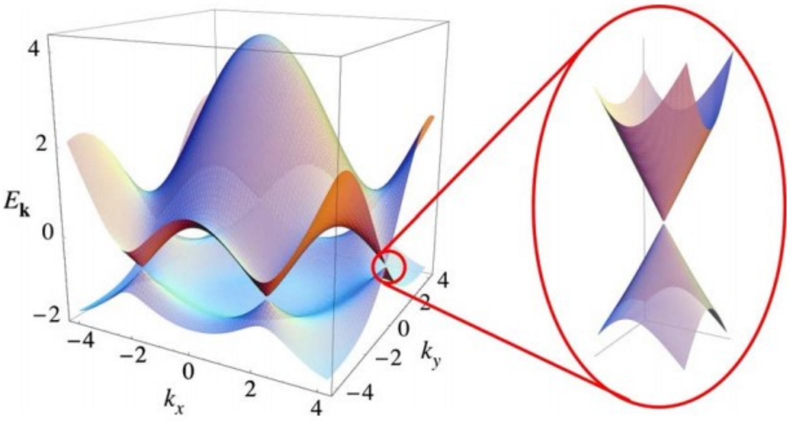

Figure 2.4 Band structure of graphene. Inset: enlarged view of the energy dispersion near one of the Dirac points where the valence and conductance bands meet [48].

This unique band structure configuration determines that graphene is a zero-gap semiconductor (i.e. charge carriers can be modulated between electrons and holes continuously) [28]. Graphene exhibits a super high charge carrier mobility up to 100,000 cm$^2$V$^{-1}$s$^{-1}$ at room temperature and should not be affected much by high charge carrier densities or chemical doping [28, 45]. For comparison, some semiconductors such as InSb can achieve a room temperature carrier mobility of 77,000 cm$^2$V$^{-1}$s$^{-1}$, but that is obtained from bulk materials without chemical doping, which is commonly employed to modulate the band gap (for logical applications in semiconductor industry) or electrical activity (for electrochemical applications such as supercapacitors and batteries). Moreover, half-integer quantum Hall effect (QHE) can be observed in single layer graphene at room temperature, and the conductivity of graphene will in no circumstance fall below a minimum threshold of $e^2/h$ [49, 50].

Based on these unusual properties, graphene is believed to have a huge potential in the post silicon era. Indeed, the majority of graphene research interest has been intensively focused on electronic applications such as high frequency (THz) transistors (For reference, the best high frequency Si transistor available now can perform at 330 GHz [1]) and logic transistors.

### 2.2.3 Mechanical properties

Click on link to view image in public domain

Figure 2.5 An artist impression of an elephant standing on a pencil, supported merely by a graphene sheet [51].

Graphene is often cited as the strongest material ever, outperforming structural steel by some 200 times [52]. Another vivid statement is that graphene is mechanically so strong that “It would take an elephant, balanced on a pencil, to break through a sheet of graphene the thickness of Saran wrap (cling film)” [52], as depicted in Figure 2.5 an artist impression of the magical scene [51]. These statements on media were actually based on experimental studies including one by a group of researchers at Columbia University [3]. They produced circular wells on a silicon wafer before the single-layer graphene was mechanically deposited on the substrate surface. The mechanical properties of the suspended graphene monolayer were then tested by atomic force microscopy (AFM) nanoindentation, as illustrated in Figure 2.6. Their experimental results suggest that graphene should have a Young's modulus $E$ as high as 1.0 terapascals (TPa), assuming the effective thickness of graphene as 0.335 nm. From the same samples, they obtained an intrinsic strength $\sigma_{int}$ of 130 gigapascals (GPa), with a corresponding fracture strain of 25%, which suggests graphene is not only extremely strong but also highly stretchable. In comparison to graphene, carbon steel usually exhibits a Young's modulus of some 200 GPa and an intrinsic strength of 400 MPa.

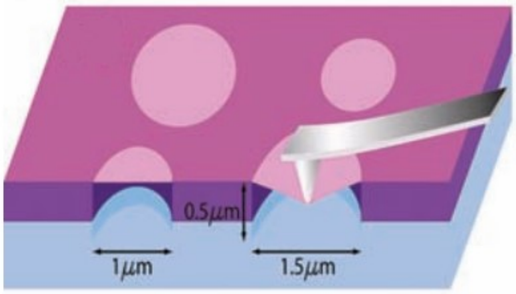

Figure 2.6 Schematic of nanoindentation on suspended graphene membrane using an AFM tip [3].

Nonetheless, it has been reported [53] that the mechanical properties of graphene depends much on the type and degree of defects. Among all the defect forms, for instance, whilst sp$^3$-type defects do not degrade graphene's strength even at high defect densities, vacancy-type defects result in a significant drop in mechanical properties. Therefore, quality control of graphene, especially when employing large-area graphene, is of particular importance in order to maintain graphene's extraordinary mechanical properties. For graphene-based composites, for the same reason, it is also highly desired to enhance the bonding and interactions between graphene fillers and the matrix [2].

### 2.2.4 Chemical properties

As mentioned earlier, graphene is a lattice of carbon atoms and has a compact yet very concise crystal structure. Therefore, despite its surprising electronic properties, pristine graphene is chemically inert, like graphite which is actually stacked graphene layers. Graphene, as well as graphite, is commonly seen as a hydrophobic material, although recently some authors have pointed out that the wettability of graphene should be affected by the ambient environment (i.e. contaminations and hydrocarbon species that could be adsorbed onto graphene surface) [54, 55], or the liquid-graphene and liquid-substrate interactions [56]. On the other hand, graphene has been reported to be impermeable to almost any molecules and ions [19, 57, 58], which suggests that graphene can act as a superior barrier against corrosive species and oxygen diffusion (the related applications will be reviewed later in Section 2.5.2).

Functionalisation of graphene provides a box of tools for promoting the chemical reactivity and exploring graphene's potential in chemistry such as electronic bandgap modulation [59-61], electrochemical catalysts [62-64], bio-sensors [8, 65] and biomedicine [66, 67]. Graphene can be functionalised via either non-covalent or covalent routes [68]. The former is achieved by simply van der Waals forces or π- π stacking between the graphene plane and external aromatic molecules (see Figure 2.7a, where pyrene butanoic acid succidymidyl ester (PBASE) molecules are absorbed on graphene [61]), whilst the latter is based on the breaking of $sp^2$-bonds in graphene and the grafting of external functional groups, as illustrated in Figure 2.7b [45]. As their interaction mechanisms differ, the non-covalent functionalisation has little impact on the $\pi$ conjugated structure of graphene, and thus the intrinsic electronic and mechanical properties can be retained furthest; in contrast, covalent functionalisation always means a $sp^2$ to $sp^3$ transition, thus usually resulting in the formation of graphene derivatives, as to be reviewed in the following section.

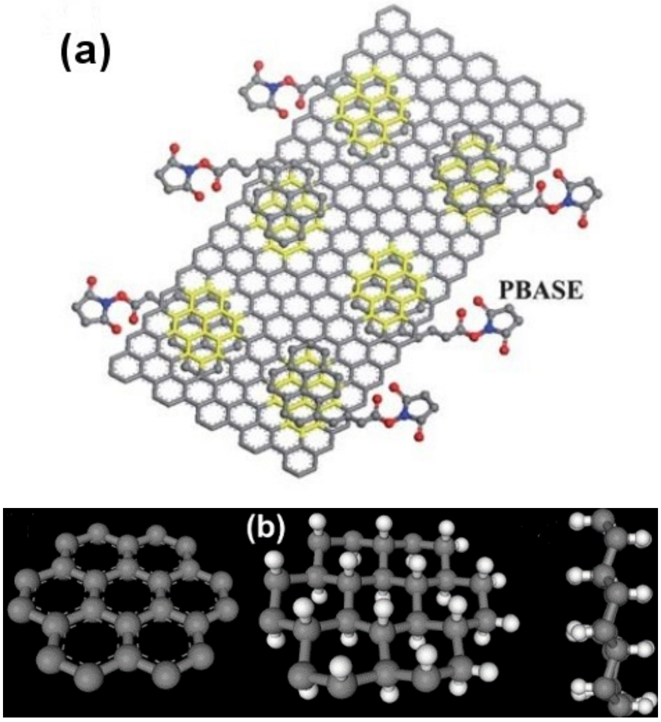

Figure 2.7 Schematic of (a) non-covalent functionalization and $\pi$-$\pi$ stacking interactions [61] and (b) covalent functionalization. In (b) Grey atoms are carbon and white atoms are hydrogen [45].

### 2.2.5 Graphene derivatives and their properties

#### 2.2.5.1 Graphene oxide and reduced graphene oxide

Among various derivatives of graphene, graphene oxide (GO) and its reduced form rGO are the most intensively studied, due to their cost-effective and scalable processing.

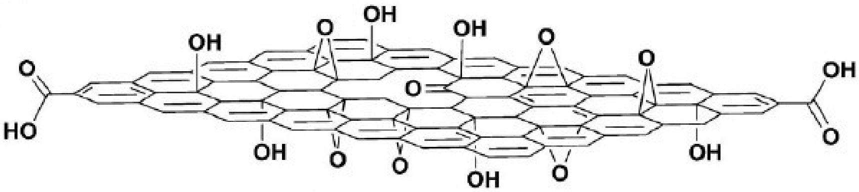

Figure 2.8 Structural model of GO, indicating the presence of oxygen functional groups either on plane or at the edges [69].

A few structural models of GO were proposed by various authors over the past decades [70], and the most recent model is the one suggested by Lerf, Klinowski and co-workers [71]. In this model, graphene is decorated with oxygen-containing functional groups such as hydroxyl (-OH) and epoxide (-O-) groups which are located mainly on the basal plane, and carboxylic (-COOH) and carbonyl groups which are located at the edges, as illustrated in Figure 2.8 [69]. GO has a typical carbon to oxygen atomic ratio (C/O ratio) of 4:1 to 2:1 [72, 73], and an expanded layer thickness around 1 nm [74] due to the presence of oxygen groups and other $sp^3$ defects. Accordingly, the original properties of graphene, such as electrical conductivity and mechanical strength usually degrade considerably. To restore the pristine structure and properties (electronic properties in particular), graphene oxide can be either reduced via various routes to form rGO (Section 2.3.6), or functionalised further to enable numerous applications other than electronics [75, 76].

### 2.2.5.2 Other derivatives from doping

Graphene can also be modified by other elements including but not limited to hydrogen, fluorine and nitrogen. Similar to the formation of GO, these doping processes also break the C-C $sp^2$-bonds in order to graft the doping atoms to the lattice or replace carbon atoms by the doping atoms [59]. Hydrogen doped and fluorine doped graphenes are so called graphane and fluorographene, respectively. Among all these derivatives, nitrogen-doped graphene is of most interest, for its great potential in graphene electronics, sensors and electrochemical reaction catalysts [60, 62-64, 77].

#### 2.2.5.1 Summary of material definitions

To clarify the differences between graphite, graphene and related derivatives that are covered in this thesis, the recommended definition for each material [78] is listed below:

- ***Graphite*** is one of the many allotropes of carbon. It consists of individual carbon layers stacking in sequences of so-called Bernal (ABAB…, hexagonal) or rhombohedral (ABC…). The layers are bonded via weak van der Waals forces, with an interlayer spacing of ~3.35 Å (0.335 nm).
- ***Graphene*** is a single-atom-thick sheet of hexagonally arranged, $sp^2$-bonded carbon atoms that is not an integral part of a carbon material, but is freely suspended or adhered on a foreign substrate.
- ***Few-layer graphene*** is a 2D sheet-like material consisting of a small number (2-5) of well-defined, countable, stacked graphene layers.
- ***Graphene oxide (GO)*** is chemically modified graphene prepared by oxidation and exfoliation that is accompanied by extensive oxidative modification of the basal plane.
- ***Reduced graphene oxide (rGO)*** is graphene oxide that has been reductively processed by chemical, thermal or other possible methods to reduce its oxygen content.
- ***Graphite oxide*** is a bulk solid made by oxidation of graphite through processes that functionalise the basal planes and increase the interlayer spacing. Graphite oxide can be exfoliated in solution to form graphene oxide.

## 2.3 Methods for obtaining graphene

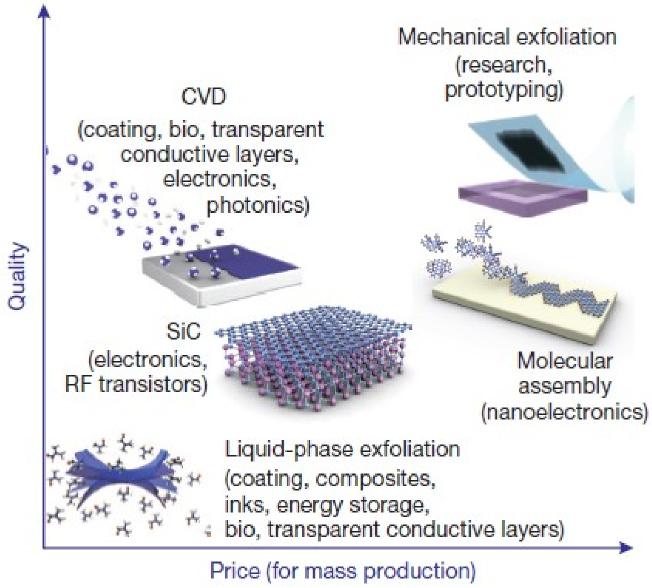

Figure 2.9 The main methods available for graphene. The diagram compares their quality and price, respectively [1].

### 2.3.1 Mechanical exfoliation

It is by mechanical exfoliation (or so-called “Scotch-tape” method) that graphene was first realized in laboratory in 2004 [27]. The idea is to repeatedly peel highly oriented pyrolytic graphite (HOPG) using scotch tape to thin down the graphite layer gradually. By repeating the operation carefully, some single-layer graphene can be found in the debris. This is a simple and effective way to produce graphene of high quality and few defects. The first astonishing discoveries [3, 27, 49, 50, 79] were all based on graphenes made by this method. Today there are still groups of researchers using mechanically exfoliated graphene for nano-fabrication of electronic devices [80, 81]. However, the yield by this route is very low and it is difficult to separate single or few layers from the resulting debris. Therefore, it is a premium choice for laboratory research but not for mass production. Figure 2.9 is a comparison of different methods for graphene synthesis, taking their quality and price for mass production into consideration [1].

### 2.3.2 Liquid exfoliation

A cost-effective and potentially scalable way to isolate graphene from graphite is via exfoliation in solvents. To cleave bulk graphite, the van der Waals forces that hold graphene layers together in the graphite structure must be overcome. A minimum input energy of 2 eV/nm$^2$ [82] is required, and this can be fulfilled by ways such as ultrasonication. After exfoliation, it is also essential that the solvent can prevent the graphene sheets from restacking.

The research group led by Jonathan Coleman at Trinity College Dublin stands out in this field due to their significant and continuous contribution to this technique [83-89]. In 2008, they reported that a suspension of graphene (<5 layers) with a concentration up to 0.01 mg ml$^{-1}$ could be obtained in "good solvents" such as N-methylpyrrolidone (NMP) [85]. Based on quantitative analysis they also predicted that any solvent with a surface tension of 40-50 mJ/m$^2$ is desirable, as the surface energies of such solvents match that of graphene [85]. The group then further improved the resulting concentration in the same organic solvent NMP [87], investigated the exfoliation in water and the effect of various surfactants [86], and expanded their research to other 2D materials successfully [84].

Liquid exfoliation gives graphene with few defects and highly compatible with many liquid-phase processing, like polymer composites. While it is worth noting that due to the high boiling points of some organic solvents, it is a challenge to purify and transfer the graphene for some applications. Moreover, toxicity could be another issue.

### 2.3.3 Chemical vapour deposition (CVD)

Apart from mechanical exfoliation and liquid exfoliation which isolate graphene in a top-down fashion, there are a few bottom-up graphene synthesis choices, including chemical vapour deposition (CVD) [11, 90, 91].

In a typical process, carbon sources, such as methane the most commonly used [92], are fed into the reaction chamber at elevated temperature (usually 1000 °C) where a catalyst substrate (e.g. a Cu foil) is located. The carbon feedstock is then catalytically decomposed and carbon atoms adsorbed on the substrate surface to form graphene.

While many transition metals other than Cu, such as Ni, Co, Ru, Ir, Pt and Pd can also catalyse the graphene synthesis [11, 15], copper is superior due to the much lower carbon solubility of copper and thus a better control of the graphene layer number (one to few-layer for Ni *vs.* nearly 100% monolayer for Cu) [15, 92]. Other factors that affect the synthesis process considerably include feedstock compositions, flow rate, exposure time, cooling rate, etc. [15], indicating the complexity of this synthesis route.

Notwithstanding, CVD has been the most popular route for preparing large-area, high-quality graphene (for instance, 30-inch [93] and 100-m-long [14] graphene film by roll-to-roll production, as illustrated in Figure 2.10, have been reported), and thus is regarded as the most promising route for graphene's commercialisation [1].

The main challenges remaining for CVD graphene include how to improve the transfer process onto arbitrary surfaces [94], how to get a better control to the graphene grain size and orientation (most CVD grown graphenes are polycrystalline) and eventually realize single graphene synthesis [1], as well as lowering down its energy consumption and cost [95].

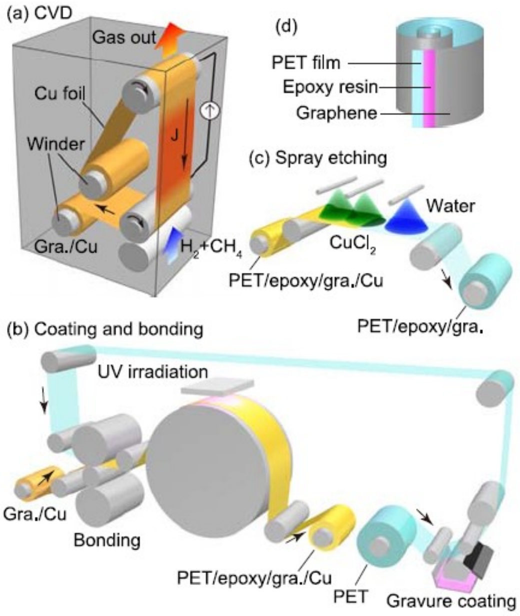

Figure 2.10 Schematic of continuous roll-to-roll production of graphene. (a) CVD synthesis of graphene on Cu foil roll. (b) Gravure coating of epoxy resin onto PET film and sandwich bonding with graphene/Cu foil. (c) Spray etching of the Cu foil. (d) The resulting PET/epoxy/graphene film roll ready for use [14].

### 2.3.4 Epitaxial growth on SiC

Another bottom-up method for graphene synthesis is epitaxial growth on silicon carbide (SiC) [43, 96]. As SiC is a carbon source as it literally should be, instead of relying on external carbon feedstock, this technique is based on controlled sublimation of Si from the compound surface, thus eventually leaving a graphitic layer, namely graphene. The SiC here serves as both the carbon source and targeting substrate, which means there is no need for metallic catalysts. On the other hand, SiC is a widely used material in high-power electronics [1], and can be tailored with patterns by means of lithography, making this route a versatile, transfer-free alternative to CVD graphene synthesis.

Graphene can grow on both the (0001) (i.e. Si-terminated) and $(000\bar{1})$ (C-terminated) faces of SiC. Those grown on the C-terminated face are usually multi-layer with inhomogeneous layer numbers due to the relatively high activity of that face.

Besides the layers tend to have a high density of rotational disorder [96]. In contrast, the Si-terminated face exhibits advantages as it allows homogenous graphene growth and easier control of the layer number. The main drawback for (0001) face growth, however, is that the Si-terminated surface usually features terraces where the graphene nucleation occurs. Thus, the graphene film, although uniform, just follows the topography of the substrate. Figure 2.11 is a comparison of the SiC substrate before and after graphene growth, in which some steps can be clearly seen [97].

Like the CVD route, epitaxial growth of graphene could receive more attention if the synthesis temperature (also around 1000 °C) can be reduced and the reaction conditions further optimised.

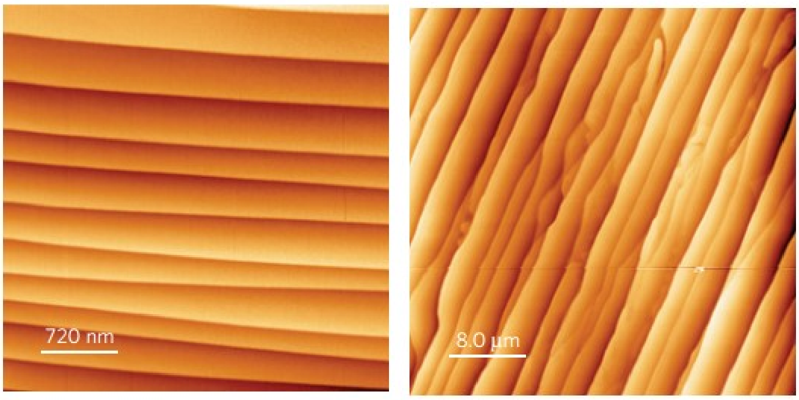

Figure 2.11 AFM images of (a) initial surface of 6H-SiC(0001) substrate and (b) graphene grown on the SiC substrate formed by annealing in Ar environment (900 mbar, 1650 °C) [97].

### 2.3.5 Bottom-up molecular assembly

Various chemical routes can be used to obtain graphene products out of molecules. The molecules, normally in forms of polycyclic aromatic hydrocarbon, serve as the building bricks for graphene and usually the synthesis is implemented via solution-based approaches. The small monomer precursors are brought together to form linear polyphenylenes, then to larger aromatic hydrocarbon structures via coupling reactions under selected conditions. However, due to the reduced solubility of large polycyclic products, this method is not suitable for large-area synthesis of graphene, but feasible for the quick and controllable production of high quality graphene nano-ribbons, T-shape or Y-shape graphene nano quantum dots. For instance, Yang *et al.* reported the use of 1,4-diiodo-2,3,5,6-tetraphenylbenzene for the synthesis of graphene nanoribbons. After reacting with 4-bromophenylboronic acid to form a hexaphenylbenzene intermediate product, and twofold lithiation with n-butyllithium and 2-isopropoxy-4,4,5,5-tetramethyl-1,3,2dixaborolane, the obtained monomers were subject to polymerisation and cyclo-dehydrogenation reactions to form graphene-like nanoribbons. The schematic of this process is shown in Figure 2.12.

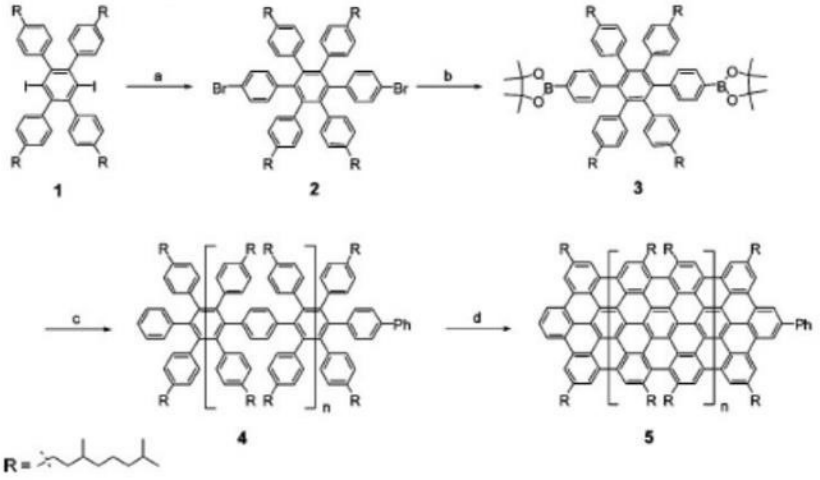

Figure 2.12 Schematic of graphene nanoribbon synthesis [98].

The main drawback of this synthesis route for its development is the high cost (even higher than CVD methods) and the low yield of this method. As mentioned above, the synthesis of large-area graphene via this route is not practical. The chemical process is usually complex and thus cannot be easily adapted for large-scale applications.

### 2.3.6 Reduction of graphene oxide

Probably the cheapest way for mass production of graphene, reduction of graphene oxide (GO) is now widely adapted by researchers in different fields.

Basically, this method consists of three steps, which are the oxidation of graphite, the exfoliation of graphite oxide and the reduction of graphene oxide, successively. During the first stage the graphite layered structure is intercalated and expanded by oxidative ions and molecules, resulting in the formation of so-called graphite oxide. After exfoliation, graphene oxide, which has been introduced in Section 2.2.5.1, is obtained. The graphene oxide can then be used readily, or reduced by various ways before final use (see Sections 2.3.6.2 - 2.3.6.4).

#### 2.3.6.1 Methods for graphene oxide

The story of graphene oxide can date back to more than a century ago (far earlier than the boom of graphene!), when graphite structure and graphite intercalation compounds (GICs) were attracting the interest of chemists [37, 99]. The first well-known graphite intercalation method was reported by Brodie in 1895 [100], which was slightly improved by Staudenmaier 40 years later [101]. These two methods are still being used today for GO or rGO synthesis, while the main stream method, is the one invented later by Hummers and Offeman in 1958 [102] as well as its modified versions [103-106].

As per the Hummers method, a mixture of concentrated sulphuric acid and potassium permanganate is used to intercalate and oxidise graphite. The reaction could last for 30 min [102] up to 12 hours [103], varying from method to method. The functioning oxidant during this period is believed to be dimanganese heptoxide ($Mn_2O_7$), formed as described below [70]:

$$KMnO_4 + 3\, H_2SO_4 \rightarrow K^+ + MnO_3^+ + H_3O^+ + 3\, HSO_4^- \qquad (2.3\text{-}1)$$

$$MnO_3^+ + MnO_4^- \rightarrow Mn_2O_7 \tag{2.3-2}$$

At the end of oxidation, the resulting product (i.e. graphite oxide) is subject to an exfoliation process powered by ultrasonication, during which graphite oxide is split into individual layers, i.e. graphene oxide.

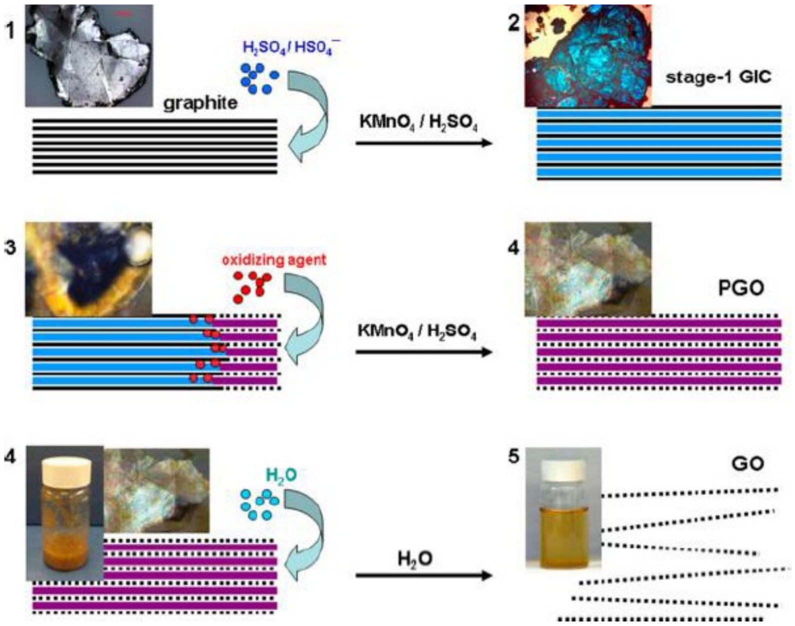

Figure 2.13 Schematic of the intercalation and oxidation process of graphite in the presence of concentrated sulfuric acid and potassium permanganate [107].

A detailed study [107] has suggested that the formation of graphene oxide contains three stages, namely the conversion of graphite into graphite intercalation compound (GIC), the conversion of GIC into pristine graphite oxide (oxidised graphite) and finally the conversion of pristine graphite oxide into graphene oxide upon exposure to a proper solvent under ultrasonication. The process is shown in Figure 2.13.

Owing to the presence of the polar functional groups (Figure 2.8), GO sheets can disperse well in water and some organic solvents, as demonstrated in Figure 2.14 [108]. However, the functional groups disrupt the conjugated structure of graphene, having a huge impact on the properties of graphene, especially electronic properties. Hence, reduction of graphene oxide is often necessary.

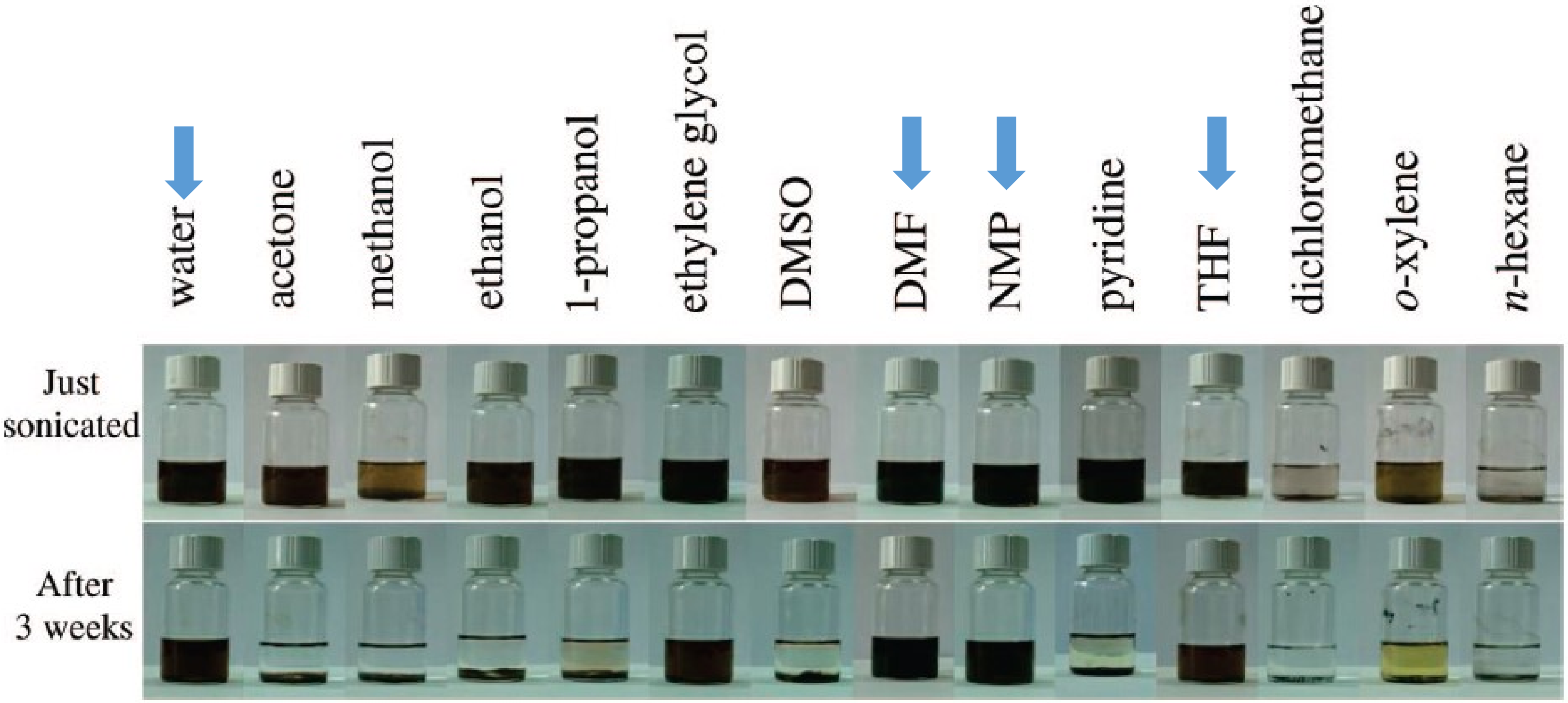

Figure 2.14 Graphene oxide dispersed in water and 13 organic solvents [108].

#### 2.3.6.2 Chemical reduction

Hydrazine ($N_2H_4$) [72] was one of the earliest reported agents for GO reduction. The reduction was fulfilled by adding hydrazine hydrate into a graphene oxide suspension and maintaining at 100 °C for 24 h. The C/O ratio of the reduced material increased remarkably to 10.3 from 2.7, indicating a considerable removal of the oxygen groups in GO. As a side effect, however, the rGO sheets agglomerated and precipitated out [72]. As the rGO sheets became less hydrophilic and restacked together, it is difficult to re-disperse them anyway [74]. Although measures can be taken to stabilize rGO sheets, such as adding a stabilising polymer before reduction [72], adding ammonia [109] or KOH [104] to the reduction formula or using anhydrous hydrazine (chemically pure without water) [110], the highly toxic hydrazine should not be the first choice for the sake of health and environment. Alternatively, there are a number of other chemicals that have been accepted as effective reducing agents, such as sodium borohydride ($NaBH_4$) [111], hydroiodic acid (HI) [112], L-ascorbic acid (Vitamin C) [113], etc. The last mentioned is of particular interest because it is very gentle to humans and totally green (and Vitamin C was invented here at UoB, winning a Nobel Prize for the author and the University [114]). A comprehensive summary and comparison of the reductants is available in ref. [115].

#### 2.3.6.3 Thermal reduction

GO can be reduced via thermal-shock at elevated temperature in vacuum, inert (Ar) or reducing (e.g. $H_2$) atmospheres. It has been demonstrated that upon heating GO undergoes a significant mass loss at 200-250 °C, due to the decomposition of oxygen functional groups [74]. Below 100 °C or above 250 °C only slight mass loss occurs due to the evaporation of adsorbed water [74]. However, to build up the pressure between graphene oxide layers rapidly and finally exfoliate them, a heating rate of 2000 °C/min and a holding temperature above 1000 °C are usually required [116]. As a protection, the annealing is conducted in vacuum [16], inert gases such as argon [116] or reducing atmosphere [7]. Although thermal reduction has been reported to yield graphene with high electrical conductivity [116], the main drawback is the high energy consumption, and thermal reduction is not suitable for substrates with low melting points such as polymers [73].

#### 2.3.6.4 Electrochemical reduction

The electrochemical reduction of GO is non-destructive, quick, clean and energy-saving. The reduction mechanism is simply by electron exchange between the GO and the counter electrode [73], which means there is no need for strong chemical, high temperature or bulky vacuum instruments – usually a normal electrochemical cell will do, at room temperature. This method is particularly favourable for the reduction of GO coatings, because once a GO coating is fabricated onto the targeting substrate (Si wafer, ITO glass, PET film, metallic surfaces, etc.), it can be reduced in-situ [117-119]. By this way, the re-dispersion issue for rGO is avoided.

The electrochemical process could be programmed to be either a cyclic voltammetry or at a fixed voltage (DC). In the case of cyclic voltammetry, taking the work by Wang et al. [119] for instance, the GO coated electrode and the counter electrodes were immersed in 0.5 M NaCl solution and subject to a scanning range from 0.7 to -1.1 V with a scan rate of 50 mV $s^{-1}$. On the other hand, Peng et al. [118] reported the reduction of their solid GO film at a fixed voltage of -1.1 V in 0.5 M $NaNO_3$ solution. In both cases, the electrochemically reduced GO exhibited comparable [118] or even outperforming [119] electrochemical activity as chemically reduced GO.

## 2.4 Methods to obtain graphene-based coatings

### 2.4.1 Transfer of CVD-grown graphene thin films

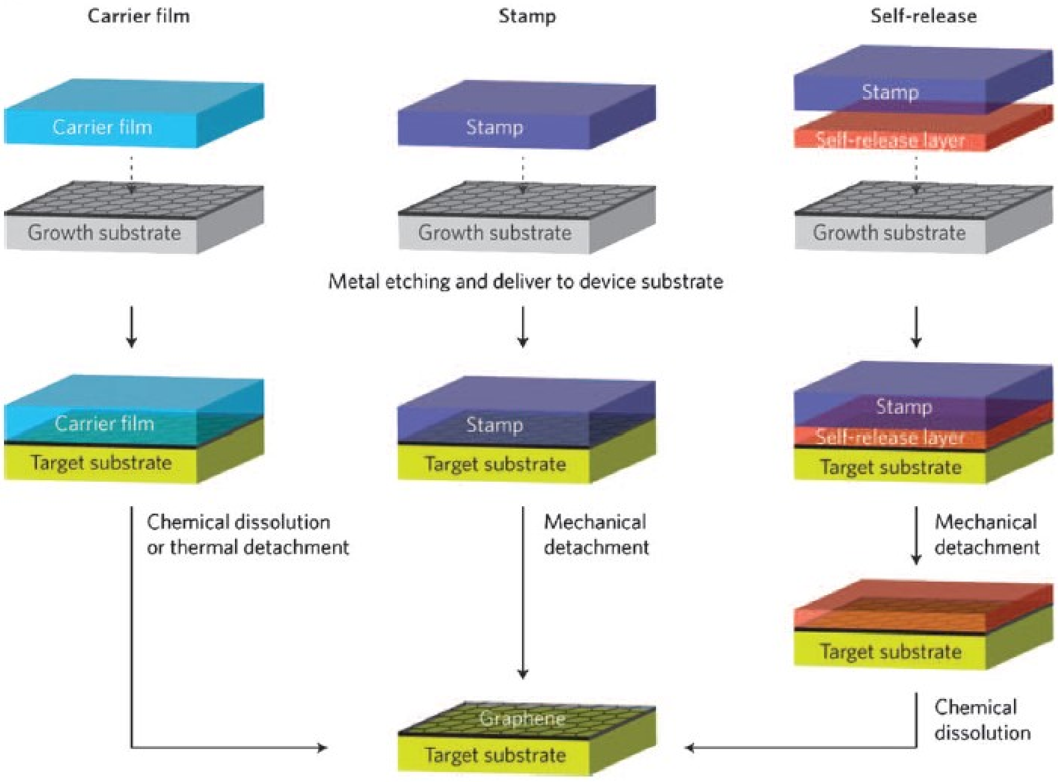

Figure 2.15 A summary of several versions of the wet transfer of CVD-grown graphene [120].

As CVD-grown graphene keeps building up its market share [15, 90], it is critical to develop and optimise techniques for the transfer of CVD graphene onto arbitrary substrates for downstream applications [1, 94]. The most important transfer approach to date is via wet chemical transfer, employing an intermediate carrier material, usually polymethyl methacrylate (PMMA) [92]. Figure 2.15 is an illustration of the transfer process [120]. The typical procedures are: (i) coating a layer of PMMA on top of the graphene grown on Cu substrate; (ii) etching away the Cu substrate using chemical solutions such as $FeCl_3$; (iii) rinsing the PMMA coated graphene with deionised (DI) water and transferring to the targeting substrate; (iv) removal of the PMMA top layer in organic solvents such as acetone; (v) drying and annealing the graphene coating to remove the chemical residues; (vi) transfer completed. Based on this protocol, a number of modifications have been practised, including direct transfer using isopropanol (IPA) droplets [121]; substitution of fragile PMMA with firm polymers like PET film, based on which the roll-to-roll transfer of 100-m-long graphene has been reported [14]; electrochemically bubbling delamination and transfer [122], etc.

Unfortunately, defects are inevitably introduced into the graphene thin film during the transfer operation and thus the coating integrity suffers. This problem can lead to the loss of a lot of properties, such as anti-friction [11] and anti-corrosion [123].

### 2.4.2 Self-assembly monolayer & multilayer

GO or rGO coatings can be fabricated from a GO suspension conveniently by techniques such as spin coating [16], spray coating [17], dip coating [105], Langmuir-Blodgett assembly [6, 124] and vacuum filtration [5]. However, the adhesion of these coatings is usually weak as the GO or rGO sheets are just physically covering the substrate surface. This is acceptable for electronic applications, while for the applications that require a good bonding to the substrate (for example, anti-friction or anti-corrosion applications), the interaction between the coating and the substrate must be enhanced.

To this end, the graphene-based coating, appearing as either a single form or part of a multi-layer system, can be fabricated through self-assembly techniques. Self-assembly is a process in which molecules array themselves regularly, without external guidance, onto the surface of solids (or liquids), and bind to the surface via the interlinking of the chemical head-groups of both [125]. Since the head-groups of the molecules usually have a high affinity for the surface, the assembly process keeps going until the surface is fully occupied. Due to its nano-scale nature (typically 1-3 nm, depending on the molecule size), self-assembly is widely used for studies in nanoscience and nanotechnology [125].

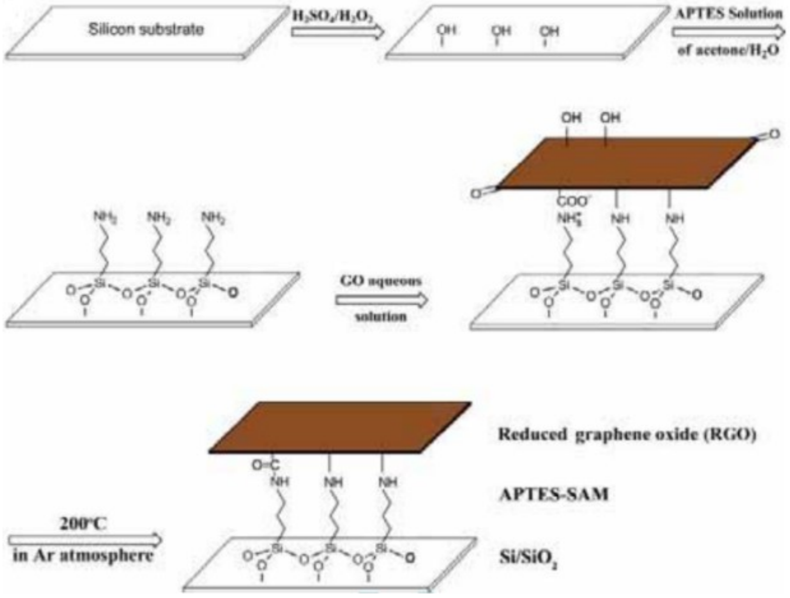

Figure 2.16 Schematic of the self-assembly of APTES-GO thin film on silicon wafer [126].

Ou and co-workers used an intermediate layer (also self-assembled) of (3-Aminopropyl)triethoxysilane (APTES) as the bonding layer beneath the GO topcoat, and investigated the tribological performance of the coatings [126]. Figure 2.16 depicts the self-assembly of APTES-GO thin film on a silicon wafer. The resulting sample exhibited a prolonged anti-wear life in contrast to the silicon substrate coated only with GO or rGO, which was attributed to the enhanced bonding by the APTES layer. The group then expanded the use of APTES to various sandwich coating structures [127-129], on other substrates such as titanium alloys [130, 131] and further found that other agents such as polydopamine (PDA) [132] and polyethyleneimine (PEI) [133] could also promote the adhesion of the graphene-based coating. However, to our knowledge there is no report yet about such use on such common metallic materials as steel. The changes in the chemistry status of the assembled coating was not addressed, too. Moreover, the normal loads used in the documented studies were mainly in the order of mN, which is not compatible with macro-scale applications.

### 2.4.3 Electrophoretic deposition (EPD)

There has been a call for techniques towards large-scale production of graphene-based functional coatings and graphene-based composites. A facile, applicable technique should be able to fabricate graphene-related materials homogeneously and cost-effectively. Electrophoretic deposition (EPD) could be such a candidate.

#### 2.4.3.1 Fundamentals of EPD

EPD is a colloidal process in which charged particles move towards and deposit onto the oppositely charged electrode in the presence of an electric field [134]. The wet deposit is then subject to drying or sintering to obtain a dense coating. Through this method it is possible to deposit particles of various sizes (nano- or micro-range) and of almost all types of materials, including but not limited to metals, ceramics, polymers, glasses [135] and carbon nanotubes (CNTs) [136], as long as a stable suspension of the working particles is available.

Though literally similar, the main differences between electroplating and electrophoretic deposition are:

a. In electroplating, the charge carriers and moving species are the ions in the electrolyte, for example, the $Ni^{2+}$ ions in nickel plating; while in EPD, it is mostly the solid particles not the free ions that dominate the deposition.

b. In EPD a liquid medium of low conductivity is favourable, as the suspending particles and ions are competing species. In contrast, an electrolyte of high ion concentration and conductivity is likely to lead to a successful electrodeposition;

c. Although an aqueous suspension can be used for EPD, usually organic liquid media are preferred. This is because during a water-based EPD process water electrolysis and Joule heating (heat accumulation near the electrodes) could occur [135] as a side effect of the low conductivity of the electrolyte. On the contrary, for electrodeposition water-based electrolytes are commonly used.

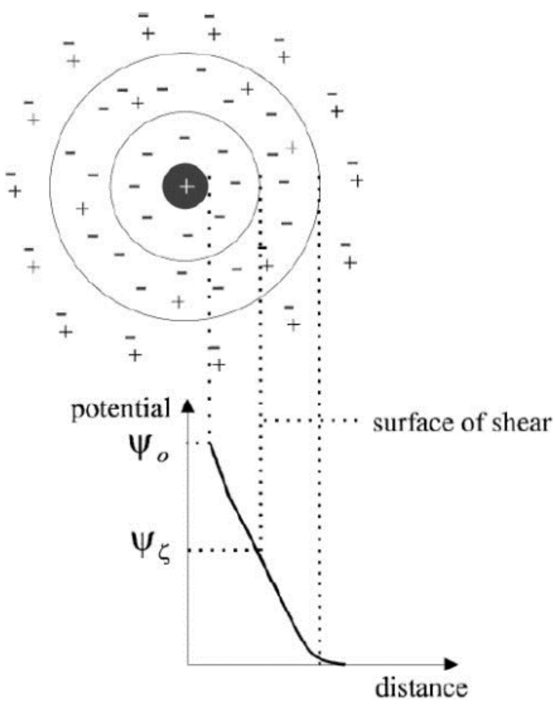

Figure 2.17 The electric double-layer developed surrounding a charged particle in a suspension. The zeta-potential describes the potential at the shear plane [135].

Some important factors that influence a EPD process are: the electrophoretic mobility of the particles, the conductivities of the suspension and substrate, the applied voltage, etc. The mobility in turn depends linearly on the zeta-potential of the particle ($\zeta$) in a given colloidal system (in terms of the permittivity and viscosity of the solvent

[134]). Zeta-potential is closely related to the electric double-layer established around a charged particle as illustrated in Figure 2.17 [135]. It describes the potential difference from the shear plane (the boundary between the liquid moving with the particle and the liquid that does not) far to the bulk fluid [135]. It determines the repulsion strength between particles and the moving direction (if the particles are positively charged, they migrate to and deposit on the cathode). In general, a higher zeta potential means a greater suspension stability and particle mobility. It has been reported that the absolute value of the zeta potential should be no less than 30 mV to prevent the particles from coagulation or flocculation [137].

Upon charged particles reach the electrode, several mechanisms for the deposition have been suggested [134], such as particle flocculation near the electrode, particle charge neutralisation, electrochemical particle coagulation and electric double-layer distortion and thinning. A common view is that the deposition depends much on the loss of short-range order, i.e. the drop of the suspension stability and electrophoretic mobility near of the electrode. The charged particles get reduced zeta-potential near the electrode, suppressed by either local ions or surrounding counterpart particles or contact with the oppositely charged electrode, and thus the particles tend to accumulate and coagulate, and finally deposit on the electrode.

Based on the understandings above, some advantages and disadvantages of EPD can be drawn. The advantages include:

- Cost-effective and easy equipment;
- Less safety concerns. Room-temperature deposition possible and few chemicals are required;
- Controllable deposition (kinetics, coating thickness, etc. [138]);

- Possibility to coat substrates with complex shapes (e.g. metal foams [139]);
- Co-deposition of wide range of materials such as particles [140] and metals [141].

The disadvantages are:

- A conductive substrate is required, although deposition on non-conductive surface has been reported [142];
- Side effects such as water electrolysis for aqueous EPD and the melting of metallic anodes.
- For some applications (such as EPD of ceramics) sintering is necessary.

#### 2.4.3.2 EPD of graphene-based materials

Recently, EPD of graphene-based materials for various applications has attracted an increasing amount of interest [4, 137, 142-149]. In most of these reports, GO rather than defect-free graphene was involved in the EPD. This is because in the presence of polar liquid such as water, the deprotonation of the carboxylic groups on GO sheets (see Equation 2.4-1 below) makes GO sheets readily negatively charged, resulting in a highly stable suspension even without any additives, which is ideal for EPD use.

$$RCOOH \rightarrow RCOO^{-} + H^{+} \qquad (2.4\text{-}1)$$

Several studies have used aqueous suspensions of GO for EPD, taking advantage of GO’s good dispersity in water. The applied voltages in these cases were in the range of a few [138, 149, 150] to tens of volts [148]. While some others reported the EPD of graphene-based coatings from organic suspensions, such as isopropanol [4], ethanol [140, 151] and N,N´-dimethylformamide (DMF) [152]. The applied voltage for organic EPD could be as high as 160 V [4], since the gas evolution and Joule heating in aqueous systems can be eliminated owing to the much higher decomposition potential and low electrical conductivity of the organic solvent.

### 2.4.4 Electro brush plating

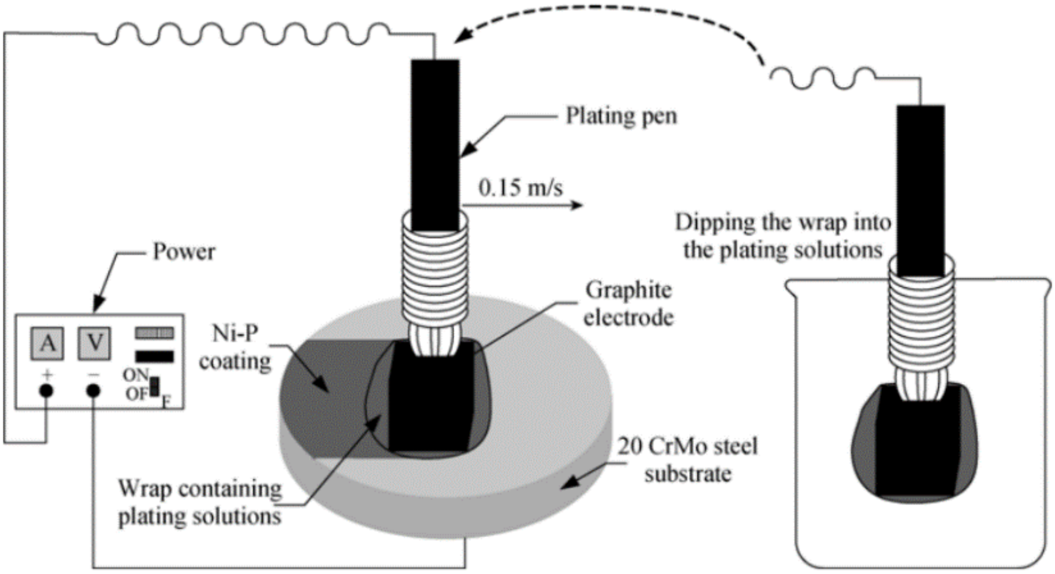

Figure 2.18 A typical electro brush plating set-up. In this example a Ni-P coating is deposited on a  CrMo steel substrate using a plating pen [153].

Electro brush plating (EBP) has been an important way for the processing of composite coatings and received interest from both industry and nano-tech researchers due to its easy operation, high deposition rate and compatibility [154, 155]. It is an extensively practised technique for component repairing and strengthening [154, 155].

Electro brush plating is conceptually a derivative of conventional electroplating, in which an electric field is applied between two electrodes in an electrolyte (for example, a solution of nickel salts for nickel plating) and the coating is usually obtained at the cathode (the target article). The main difference is that in electroplating the two electrodes remain static [156-158]; while in electro brush plating the pen-like anode is wrapped with an absorbent material that can hold the plating solution. During the plating process the operator brushes the anode pen against the workpiece surface evenly at a proper speed. While the power supply is constantly on, the current flow is triggered and the deposition obtained only when the anode pen is in contact with the workpiece [154]. Figure 2.18 is a schematic of a brush plating set-up for a Ni-P coating [153]. It is clearly an advantage of EBP that the deposition is highly target-oriented and thus saving electric power as well as the plating solution.

A promising application for EBP is its use for nano-composite coatings. A wide range of particles, such as alumina ($Al_2O_3$) [155], silicon carbide (SiC) [159], zirconia ($ZrO_2$) [160], molybdenum disulphide ($MoS_2$) [161], nano Cu and carbon particles [162] can be added into the plating solution and incorporated into the deposit. Composites containing carbon nanotubes (CNTs) can also be deposited by EBP [163]. Compared to conventional electro co-deposition, composite coatings by EBP benefit from its compactness and good adhesion [164]. Besides, the fact that the anode pen moves against the target surface means that the particles can be “pushed” into the deposit physically in addition to the electrolytic driving force, thus boosting the particle loading. While there have been a few reports on the electrodeposition of graphene-based composites [165-170], no report has yet been published on the use of EBP for the fabrication of such composites.

## 2.5 Surface engineering with graphene-based materials

### 2.5.1 Tribological applications

#### 2.5.1.1 Nano/micro-scale tribology of graphene

(a) Frictional behaviour of pristine graphene

One of the earliest studies in this field was reported by Lee et al. in 2009 [171], in which the frictional behaviour of mechanically exfoliated graphene with varying layer numbers was investigated using AFM and FFM (friction force microscope) techniques. It was found that the frictional force decreased monotonically as the number of graphene layers increased and eventually reached that of bulk graphite [171]. Similar results were reported by Filleter et al. [172], who found that for graphene grown epitaxially on SiC, the friction of monolayer was twice that of bilayer.

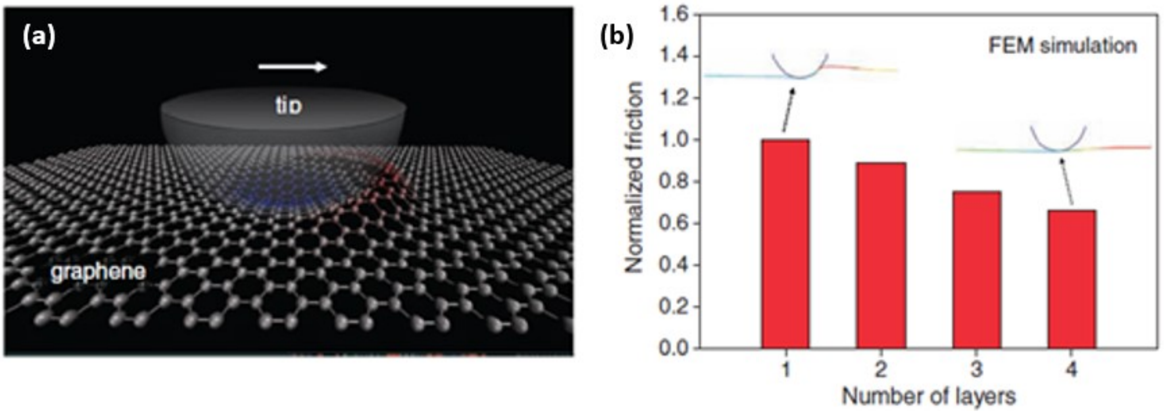

Figure 2.19 (a) Schematic of puckering effect of a graphene sheet under an AFM tip and (b) the layer dependence of friction based on FEM simulation [173].

Earlier TEM observation has revealed that to achieve thermal stability graphene monolayer is not perfectly flat but has intrinsic ripples [46]. Thus a “rippling-rug” mechanism was proposed [171, 173]: the out-of-plane ripples and puckering increase the contact area between the tip and the graphene sheet (Figure 2.19), thus increasing the friction. Further experiments [174] and finite element modelling (FEM) [173] also demonstrated that this rippling-rug or puckering effect is more evident for monolayer graphene which is weakly bonded to the substrate or freely suspended; the effect will be suppressed if graphene is strongly bonded to the substrate or the graphene sheet is thick and stiff. This out-of-plane deformation mechanism has been supported by molecular dynamics (MD) simulations [175, 176]. In addition, Filleter et al. [172, 177] concluded from angle-resolved-photoemission spectroscopy (ARPES) results that the friction difference between mono- and bi-layer graphene could arise from their different energy dissipation behaviour.

It was reported by Li et al. [174] that the trend of decreasing friction force with respect to graphene thickness was absent in the case of mica substrate, where the graphene is strongly adhered to the mica sheet. This is mainly because the surface of freshly cleaved mica is atomically flat and graphene always follows the contour of the underlying substrate [178]. The suppression of out-of-plane deformation reduces the friction. This is echoed by Cho et al. [179] who investigated the friction of graphene on various substrates. They found that on atomically flat substrates, such as h-BN and bulk-like graphene, the friction was not only as low as that of bulk graphite but also independent of the number of graphene layers. Marchetto et al. [180] investigated the friction and wear of single layer graphene epitaxially grown on SiC at microscale using multi-asperity FFM fitted with Ruby sphere tips. A super low initial friction coefficient of 0.02 was found, and the value evolved to be 0.08 after a hundred cycles of reciprocating sliding. The remarkable lubricating behaviour was attributed to the hard SiC substrate and strong interface bonding that prevented the out-of-plane deformation, thus reducing the contact area, which in turn reduced the friction.

Transferring a graphene film from the mother substrate to another leads to deformation and defects in the graphene layer, which will usually increase the friction. For example, the friction coefficient of graphene films grown on Ni foil by CVD was 0.03 [11]; however, after being transferred on to a silicon dioxide substrate the friction coefficient raised up to 0.12, close to that of bulk graphite (Figure 2.20). The reason for this increase was mainly contributed to the inadequate adhesion between the transferred graphene film and the foreign substrate, and partially due to the contaminations and wrinkles caused during the transfer.

It follows from the above review that graphene can show very low friction if it is firmly bonded on the substrate. Therefore, for potentially tribological applications it is essential to secure the bonding of a graphene coating to the substrate.

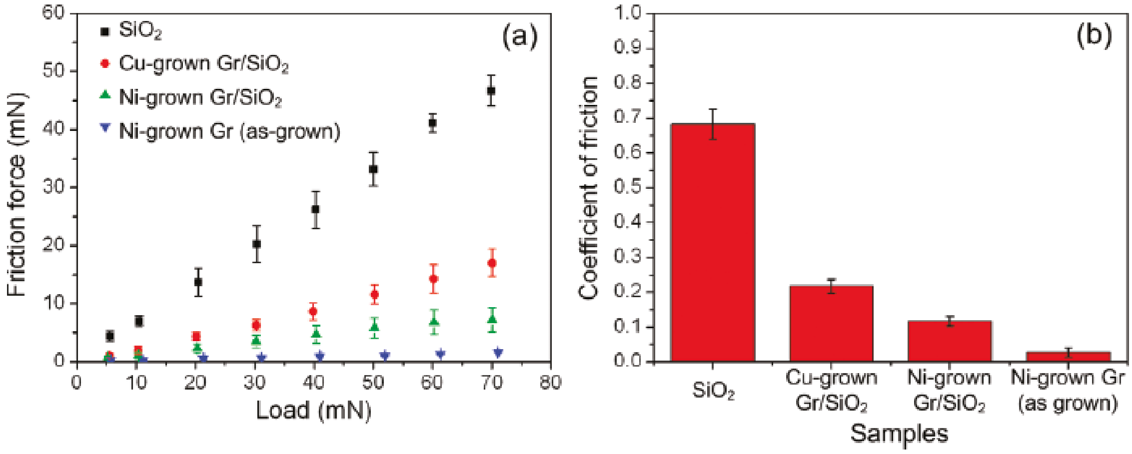

Figure 2.20 (a) Friction force as a function of load and (b) coefficient of friction for graphene samples. Gr: graphene [11].

(b) Frictional behaviour of functionalised graphene

As graphene products always contain defects, deformations and functional groups in the graphene lattice, the reported tribological characteristics of graphene are usually far from the theoretically expected values. For instance, it has been reported by Shin et al. [181] that the friction of both mechanically exfoliated and epitaxially-grown graphene increased after oxygen plasma treatment. The defects induced by ion bombardment increased the polarity of graphene surface and the attractive van der Waals forces between the AFM tip and graphene layer, thus resulting in an increase of friction. In the tribological simulations by Bonelli et al. [182], graphene with a larger flake size exhibited lower friction, even superlubricity, compared with smaller flakes. This is because the edges of the graphene flakes can be treated as structural defects, so larger graphene flakes tend to have less such defects due to their higher area-to-edge ratios. Similar influence of defects on the friction of graphene has also been reported by Won et al. [183].

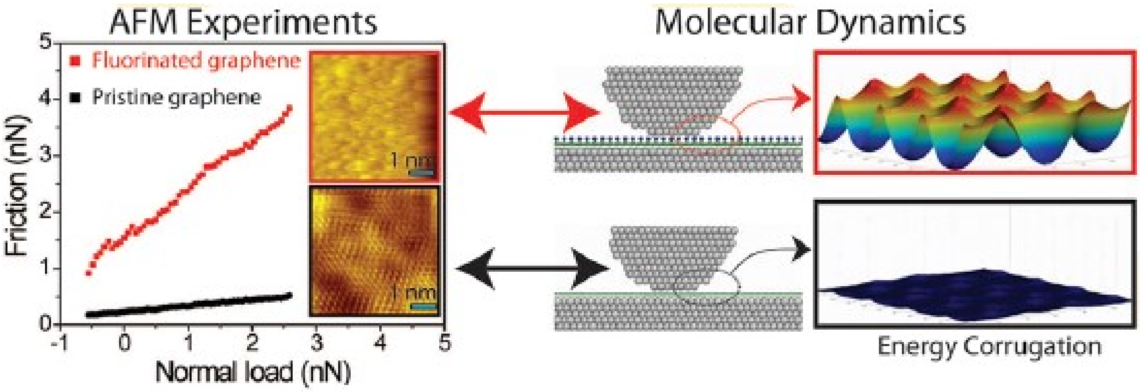

Figure 2.21 Friction as a function of normal load for pristine (black) and fluorinated (red) graphenes and their AFM friction images. A clear stick-slip motion is demonstrated on pristine graphene. Contour maps of the tip-sample potential energy for the two samples are provided [184].

Ko, Kwon and co-workers [185, 186] investigated the nano-tribological behaviour of fluorinated, hydrogenated and oxidised graphenes by FFM measurements and density functional theory (DFT) calculations. They found that the nanoscale friction increased by 2, 6 and 7 times for hydrogenated, fluorinated and oxidised graphenes, respectively, compared to pristine graphene. Several friction and wear mechanisms for functionalised graphene have also been reported [184, 187-189]. Li et al. [184] concluded from their experiments and simulations on fluorinated graphene that the dramatic friction increase is due to increased energy corrugation, as demonstrated in Figure 2.21, which is probably caused by  the strong local charge concentrated at fluorine sites. Fessler and co-workers [187] observed a similar increase of friction for hydrogenated graphene on $SiO_2$ substrate using FFM. Berman et al. [188] conducted nano-tribological tests on multilayer graphene and graphene oxide using AFM. It was shown that the quality of multilayer graphene plays an important role in the friction reduction. High-purity graphene grown by CVD showed significantly lower friction than highly oriented pyrolytic graphite (HOPG) and oxidised graphene.

In a report by Peng and co-workers [189], mechanically exfoliated multilayer graphene (MEMG), multilayer graphene oxide (MGO) and multilayer reduced graphene oxide (MRGO) were deposited on $SiO_2$ substrates and their nanotribological properties were investigated by AFM in ambient conditions. All three types of graphene layers exhibited reduced friction with respect to bare $SiO_2$ substrates. The friction value is reduced in the order of MEMG, MRGO and MGO. The MEMG holds the lowest friction coefficient due to its perfect planar lattice and hydrophobic nature. In contrast, the oxygen functional groups lead to a hydrophilic surface, especially for MGO, thus increasing the friction. More recent work by Chen and Filleter [190] has further confirmed that when applied as solid lubricants between a sliding contact, few layer graphene and GO can reduce friction by about 6 and 2 times, respectively, compared to the unlubricated contact. In addition, the wear of GO decreased with increasing C/O ratio and it is possible to achieve graphene-like tribological properties by tailoring the structure of GO.

It is worth noting that in some published studies the friction of bulk graphite was shown to be lower than that of graphene (< 5 layers) [171, 173, 174, 179, 191], whilst in contrary some other authors reported a higher friction for bulk graphite [11, 172, 177, 180, 181, 188]. This difference can be attributed to the effect of various graphite sources and testing environments, the quality and purity of graphene [188] and the bonding between the graphene and the substrate [11].

#### 2.5.1.2 Macro-scale tribology of graphene-based materials

While the nano/micro scale studies (those normally done using AFM and/or tribometers with a small load of less than 1000 nN) have provided many insights towards the tribology of graphene, it is essential to investigate the tribology of graphene and graphene-based materials at macro scale using conventional reciprocating or unidirectional sliding tribometers to provide more relevant information for real applications. Generally, the macro-scale friction and wear properties of graphene have been studied in forms of graphene-based coatings, graphene-reinforced composites and graphene-based lubricant additives (which is not reviewed due to the irrelevance to this project).

(a) Graphene-based surface coatings

Berman et al. from Argonne National Laboratory in the USA pioneered the attempts at using graphene as a solid lubricating coating on metallic substrates [12, 13, 192-194]. In their work [12, 13], solution-processed graphene (SPG) prepared by chemical exfoliation of graphene was dispersed in ethanol and then spread on highly polished surfaces of 440C stainless steel. After evaporating the ethanol in dry nitrogen, a graphene coating of 2-3 layers was formed on the steel surface. The graphene coating was non-continuous with merely 25% coverage, while exhibiting excellent lubricity (coefficient of friction 0.15-0.20) regardless of humid or dry nitrogen environments. The wear rates were reduced by 4 and 2 orders of magnitude in humid air and dry nitrogen, respectively. This is in contrast to graphite, which lubricates well in humid environment but is much less effective in dry environment [192].

The reports by Berman and co-workers seem to be the only publications that employed graphene as a solid lubricant at a macro scale. This is partially due to the difficulty in obtaining such coatings continuously on a large area, but more likely due to the weak adhesion of graphene-based coatings to most engineering materials surfaces [18].

Liang et al. [148] fabricated a graphene oxide film directly on silicon wafer using

EPD. The results of tribological tests showed that the friction coefficient and wear rate of the GO coated silicon wafer were reduced by 6 and 24 times, respectively, indicating the potential of GO as a solid lubricant for micro/nanoelectromechanical systems (MEMS/NEMS). However, the normal load used in this work was only 400 mN and further studies under higher loads should be conducted to evaluate the durability, adhesion and load bearing capacity of the EPD deposited GO coating.

As reviewed in Section 2.5.1.1, the adhesion of the graphene-based coating to the substrate can have a major influence on its tribological performance. Engineering material surfaces cannot be as flat and smooth as mica and h-BN. Therefore, either the graphene source or the target substrate needs to be engineered to enhance the adhesion between them, and more efforts are still needed to improve the reliability and durability of graphene-based coatings.

(b) Graphene-based composites

To address the technological challenge of relatively weak bonding of graphene coatings on large areas of materials surfaces (such as biomaterials), graphene-based composite coatings have been developed and their tribological properties explored [195-201].

Thangavel et al. [198] reported the structural and tribological properties of GO reinforced poly(vinylidene fluoride) (PVDF) nanocomposite thin films. The tribological properties of the composite coatings were evaluated using a reciprocating tribometer with a stainless steel counter ball under a load of 10 mN. The addition of GO in the polymer coating reduced the friction and wear of PVDF. As expected, an optimal GO content was observed, above which point both the friction coefficient and wear rate increased with GO content (Figure 2.22 [198]). Likewise, Min et al. [199] found that the incorporation of GO into polyimide (PI) not only improved the mechanical and tribological properties but also enhanced the thermal stability of the composite. The effect of GO was believed to stem from the oxygen functional groups in GO which can help form a strong interface with the PI matrix. The composites are toughened by GO sheets due to their intrinsic strength and high aspect ratio. Similarly, Song et al. [200] reported that as a nano-filler for poly(ether ether ketone) (PEEK), GO was superior to multiwall carbon nanotube (MWCNT) in terms of the ability of reducing friction, extending wear life and improving the Young's modulus and tensile strength.

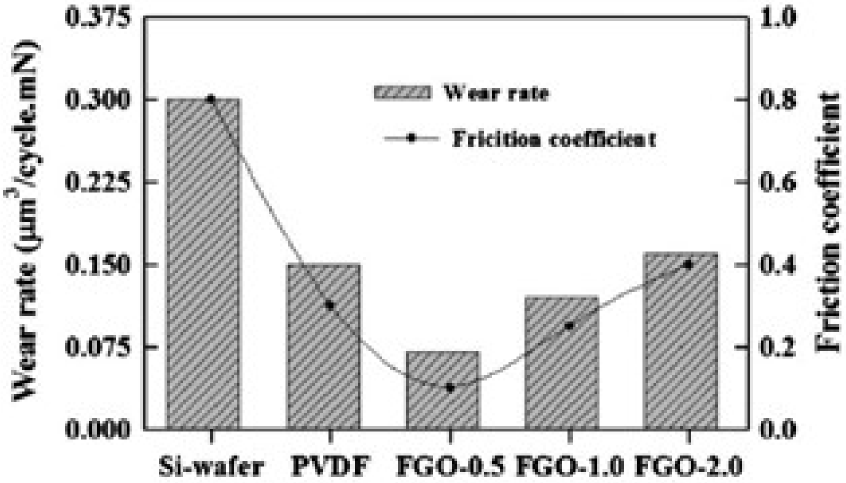

Figure 2.22 Friction coefficients and wear rates of the PVDF-FGO thin films with different GO content [198].

Apart from graphene/polymer composite coatings, Li et al. [201] were able to fabricate graphene nano-sheets (GNs) reinforced zirconia ceramic coatings on Ti-6Al-4V substrates by plasma spraying. To enhance the adhesion a Ni-Cr bonding layer was applied. It was found that an addition of 1 wt% GNs reduced the wear rate by ~50%, and the friction coefficient was reduced from 0.27 to 0.19 when the normal load increased from 10 to 100 N. The improvement by GNs, especially under high load can be attributed to the formation of a continuous GN-reinforced transfer layer which effectively prevents the substrate from further damage, as demonstrated in Figure 2.23. However, compared with GNs, graphite was less effective since the transfer layer was discontinuous.

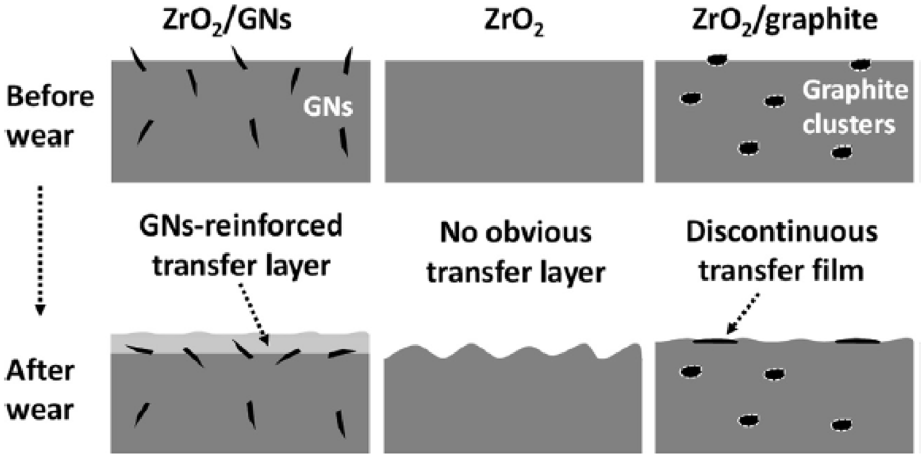

Figure 2.23 Schematic of the formation of the transfer layer during wear test [201].

It seems that GO instead of pristine graphene can be the first choice as reinforcements for bulk composites, due to the oxygen groups in GO that can enhance the interactions with the composite matrix and due to the relatively low cost and wide availability. However, most of these studies [140, 202-209] have focused on the mechanical characteristics of the composites, and their tribological properties were rarely addressed.

Tai et al. [210] prepared GO/ultrahigh molecular weight polyethylene (UHMWPE) composites by hot pressing. It was found that both the hardness and wear resistance of the GO reinforced composites increased with the GO content up to 1.0 wt%. A transfer layer mechanism was proposed to explain the wear reduction, which agrees with other reports [201, 211-213]. However, the friction increased slightly with increasing GO loading, consistent with reported phenomenon with CNT/UHMWPE composites [210]. Similar friction increase was also reported by Shen et al. [214, 215] in their studies on GO/epoxy composites. The infusion of GO was found to increase the friction yet to reduce the wear significantly. Kandanur et al. [216] reported the suppression of wear in GO reinforced polytetrafluoroethylene (PTFE) composites under a high normal load of 50 N. The wear rate was reduced by 10-fold with only 0.32 wt% GO fillers, and dramatically by 4000-fold with 10 wt% of GO platelets. Graphite reinforced PTFE, on the other hand, showed 10-30 times higher wear rate than in the GO case, indicating the huge advantage of graphene as a lubricating nano-filler. These documented studies were all targeted at polymeric graphene-containing composites. Unfortunately, however, few reports on metal-graphene composites were found. Therefore, it is worth exploring the fabrication and the corresponding mechanical and tribological properties of metallic composites reinforced by graphene-related materials.

### 2.5.2 Corrosion applications

#### 2.5.2.1 Impermeability of graphene

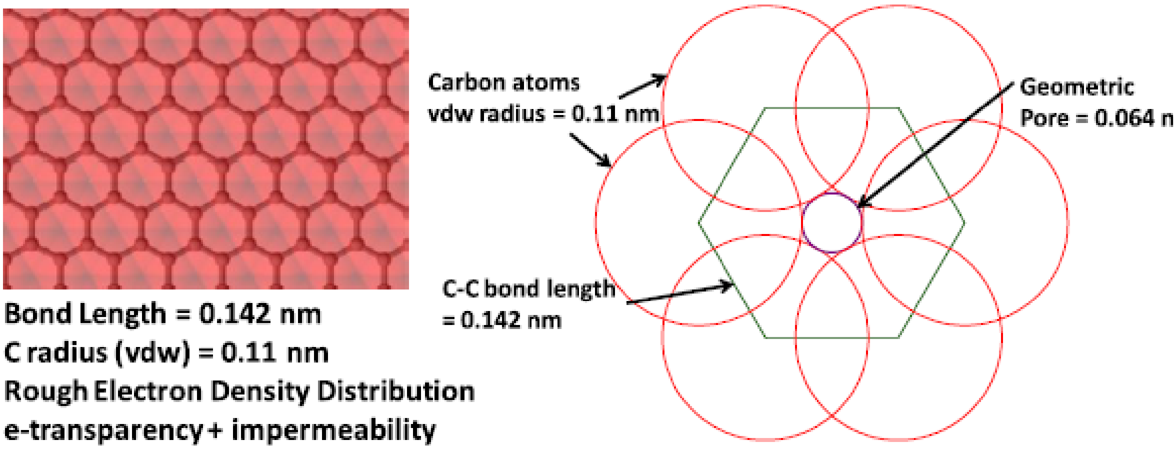

Figure 2.24 (a) Molecule structure and (b) the geometric schematic of graphene [19].

Graphene's unique 2D structure gives rise to some unique properties, including its impermeability. Graphene, although only one-atom-thick, can block all molecules including helium the smallest from passing through, given that it is free of defect [57]. This is mainly due to graphene's compact carbon lattice. Figure 2.24 is a schematic of graphene's molecular structure [19]. As the C-C bond length in graphene is 0.142 nm, taking only the nuclei into calculation, the geometric pores in the honeycomb lattice would have a diameter of 0.246 nm. Further considering the van der Waals (vdw) radius of carbon atoms (0.11 nm), the pore size would reduce further to 0.064 nm, as indicated in Figure 2.24b. This pore size is even smaller than those of the smallest gas molecules such as helium (0.28 nm = 2 × 0.14 nm (vdw atomic radius)) and hydrogen (0.314 nm = 0.074 nm (H-H bond length) + 2 × 0.12 nm (vdw atomic radius)). For comparison, the van der Waals diameters of chloride ion ($Cl^-$) and fluoride ion ($F^-$), two common corrosive species are 0.35 nm and 0.29 nm, respectively. In addition, the overlapping π-electron cloud in the vicinity of graphene's basal plane renders a repelling field to foreign atoms and molecules, while remaining transparent to electrons [19]. These characteristics imply that graphene can be the world's thinnest separation membrane [57] and corrosion barrier [217].

Despite the excellent barrier properties of pristine graphene, proved both experimentally [57, 218] and theoretically [219-221], the processing of graphene may influence the impermeability to some extent. Graphene grown by CVD often contains defects that allow helium to pass through [221]; Nair et al. observed that a membrane of GO (sub-micrometre thick) is completely impermeable to all tested molecules including helium, but allows quick penetration of water, which can be attributed to the capillary effect between 2D GO laminates [222]. As the GO laminates usually contain a high level of defects and oxygen groups (thus high surface energy and hydrophilic), water molecules can squeeze through the defective sites and overlapping edges. The results of molecular dynamics simulation by some other authors agree with this observation, suggesting that water molecules in the bulk of GO laminates tend to aggregate into the oxidised sections, leading to a further opening of the compact GO laminates [219]. This drawback can be compensated by reducing the GO membrane thermally or using chemicals such as hydroiodic (HI) acid and vitamin C (VC) [58]. After reduction, no permeation of water, $Cl^-$ ions and even hydrofluoric (HF) acid can be detected. This is also applicable for GO thin coatings more than 100 nm thick on top of PET films, glass, Cu and Ni substrates [58]. The enhanced barrier effect can be attributed to the reduction of the interlayer spacing and the recovery of the graphene structure, i.e. the graphitisation of the GO laminates. Thus, the trick behind the impermeability variation of graphene-based materials is the structural integrity and surface chemistry.

### 2.5.2.2 Single coatings

#### (a) CVD-grown graphene

The exploration of graphene as a protective coating was initiated just 5 years ago, when the technique of large-area CVD-graphene came to reality [20, 93]. It has been reported that CVD-graphene can protect the underlying substrate from air oxidation [20, 223]. Chen et al. investigated the effect of graphene films on the oxidation behaviour of the growth substrates by exposing in hot air at elevated temperature and in hydrogen peroxide [20]. After annealing at 200 °C for 4 h no visible surface change can be seen on the graphene coated metals. X-ray photoelectron spectroscopy (XPS) results showed pronounced oxidation peaks from bare Cu and Cu/Ni foils, corresponding to CuO and $Cu(OH)_2$ for Cu, and NiO and $Ni(OH)_2$ for Ni, respectively, which were all absent for the graphene-coated foils. In addition, Raman spectra suggested that the graphene retained its Raman features in the oxidising atmosphere. Thus, the great protection effect of graphene can be attributed to not only its impermeability but also its chemical resistance [20].

Furthermore, some samples were immersed into a hydrogen peroxide ($H_2O_2$) aqueous solution (30%) for a short time. Once again, much fewer oxidising attacks were found at the graphene-coated side where the copper penny coin is still shiny; in contrast, the uncoated side appeared black after the etching, indicating severe corrosion. In another report, Nilsson et al. [223] showed that a single layer of graphene grown on a Pt(100) surface by CVD effectively suppress the reconstruction of the Pt(100) under $O_2$ pressures up to $10^{-4}$ mbar, and CO pressures up to $10^{-6}$ mbar. The density functional theory (DFT) calculations also demonstrated that graphene can keep its basal plane intact under extremely harsh conditions such as 2000 K hot atomic hydrogen.

CVD-grown graphene can also protect the metallic substrate from wet corrosion effectively [21, 123, 224-230]. Prasai et al. investigated the corrosion behaviour of copper foils after graphene growth in 0.1 M $Na_2SO_4$ solution via a set of electrochemical techniques including cyclic voltammetry (CV), polarisation and electrochemical impedance spectroscopy (EIS) [21]. The CV measurements of the graphene coated copper did not show strong redox peaks that were present for the bare copper, indicating graphene’s low affinity to oxygen and remarkable barrier effect for ion diffusions. The graphene coated sample showed just minor corrosion at some isolated spots, rather than an entire damage for the bare copper. It was then inferred that corrosion only occurred through the cracks in the graphene film. The following polarisation measurements demonstrated dramatic reduction of the corrosion rates (7 times for graphene-coated copper and 20 times for graphene-coated nickel), indicating an extraordinary protection offered by the as-grown graphene films. EIS analysis and electrical equivalent circuit (EEC) models suggested that corrosion initiated at the defective sites in the graphene and developed from these sites to larger area underneath [21].

Kirkland et al. reported the corrosion performance (in 0.1 M NaCl) of graphene grown on both copper and nickel by CVD and suggested different protection mechanisms for graphene-covered nickel and copper [224]. Graphene appeared as a barrier to the anodic reaction of the underlying Ni substrate, i.e. the oxidation of metal $Ni \rightarrow Ni^{2+} + 2e^{-}$; while the Cu was protected cathodically, i.e. suppressing the cathodic reaction $O_2 + 2H_2O + 4e^{-} \rightarrow 4OH^{-}$. Raman and co-workers [225] reported their work on copper with CVD-graphene under similar testing conditions but ended up with results contrary to Kirkland et al. The corrosion potential of the graphene coated copper turned to be more positive than the bare copper, together with a nearly two orders of magnitude reduction towards the corrosion current density. The authors attributed the variations between the reports to the different processing conditions and graphene qualities. In another study graphene films were grown on the surface of nickel coated SUS304 stainless steel [228]. The thin multi-layer graphene coating was found to protect the stainless steel from pitting or surface passivation after 20 scanning cycles in 3.5wt% NaCl solution. The graphene coated Ni/steel exhibited only negligible increase of interfacial contact resistance (ICR) after the polarisation, implying that graphene could be a promising coating for fuel cell bipolar plates [228]. The use of graphene as protective coatings in other environments such as the Ni anode of microbial fuel cells [229] and biological aqueous environments [230] have also been explored with encouraging results.

Despite the promising property indicated by the results, many authors also pointed out that the grain boundaries [20], defects [226, 231] and wrinkles [123] in CVD-graphene may still allow oxidation and wet corrosion to take place, or even promote the corrosion underneath [232, 233]. Schriver et al. investigated the oxidation behaviour of bare and graphene coated copper in both hot air and ambient environment and found graphene “worse than nothing” [232]. The authors attributed the poor protection to the loss of graphene’s impermeability over a long time and the galvanic corrosion promoted by graphene which is electrochemically nobler than Cu [217, 225]. They also argued that the high conductivity of graphene may help spread the electrochemical reactions across the surface, thus promoting larger-scale oxidation. The oxidation promotion effect of graphene here is consistent with the findings by Zhou et al. [233]. The defects in CVD-graphene can also lead to a reduced barrier effect. The anti-corrosion property of graphene could be enhanced if the defects in graphene are passivated, as demonstrated by Hsieh et al. using atomic layer deposition [226].

(b) GO and rGO

Recently GO and rGO were being studied as protective coating materials due to their cost-effective and scalable synthesis. Importantly, GO can be dispersed in many colloidal systems and readily used for the following coating fabrication process, making them more promising for anti-corrosion applications. GO coatings can be fabricated via methods such as spin coating [234], rod coating [235] and electrophoretic deposition (EPD) [145]. The results suggests that GO and rGO could be as effective as CVD-grown graphene for corrosion inhibition [21, 225], as long as the coating is compact [145], intact and strongly adhered to the substrate [234, 235].

### 2.5.2.3 Composite coatings

The rise of graphene-based composites as protective coatings is because pure graphene coatings, either grown by CVD or made from GO and rGO, are vulnerable and can be easily removed by scratches, heating or simply liquid erosion. On the other hand, it is difficult to rule out the defects in such graphene coatings completely, thus resulting in the loss of impermeability, as already mentioned before. Therefore, the incorporation of graphene-based materials in a composite could be more practical and reliable for real anti-corrosion applications.

Graphene-based materials such as GO in particular, have been incorporated into polymers [22-26, 150, 236-244], inorganic/ceramic materials [140, 245, 246] as well as metallic matrices [167, 170] to form composites for corrosion protection.

(a) Polymer composites

Anti-corrosion graphene-polymer composites emerged only two or three years ago [238, 240, 241]. GO was intensively involved in the relevant studies (nearly 9 out of 10), because the oxygen-containing functional groups in the GO structure renders GO sheets highly stable in many solvents [108], making it compatible with many liquid-phase polymer processing.

A wide range of polymer matrixes have been reported, such as poly(styrene sulfonate) (PSS) [238], polystyrene (PS) [242], poly(hexamethylene diisocyanate) (HDI) [239], polyisocyanate (crosslinked with hydroxyl functional acrylic adhesive) (PIHA) [240, 241], polyester (PE) resin [150], alkyd resin [25], epoxy resin [24, 26, 244], polyurethane (PU) [23], polyvinyl butyral (PVB) [22, 243], to name a few. GO sheets were mixed with the polymer (or corresponding monomers) in water [238-241, 244] or organic solvents such as NMP, tetrahydrofuran (THF) [242], methanol [22, 243], N,Ndimethylformamide (DMF) [23] or resin bases [24-26]. In order to get a homogenous composite, measures such as vigorous stirring [243], ultrasonication [24, 239, 241, 242, 244], ball milling [25, 26] and shear mixing [23] were taken. Upon the completion of the composite mixture, coatings can be fabricated easily by spin coating [238], dip coating [22, 243], bar coating [23, 242], spraying [24], etc. In addition, some electrochemical methods such as electrochemical electrodeposition [239], electrophoretic deposition [240, 241] have been adapted for the fabrication of graphene-polymer composite coatings, which allows one-pot fabrication [241], uniform deposition as well as good control to the coating thickness [150, 241]. The resulting GO-polymer composites are usually well attached to metallic substrates such as steel and copper due to the good compatibility of the polymer to the metal surface [25, 26]. And some polymers can naturally have strong bonding with graphene [238]. Nevertheless, the interactions between GO sheets and the polymer matrix need to be enhanced to secure the barrier effect of graphene as well as a good mechanical strength. This can be done by chemically promoting the crosslinking between GO sheets and the polymer matrix. For example, GO can be functionalised with other molecules such as polyisocyanate (PI) [23], *p*-phenylenediamine (PPDA) [242, 244] and even ceramic particles like alumina ($Al_2O_3$) [24].

(b) Inorganic/ceramic composites

Compared with the large amount of studies on graphene-polymer composites, there are fewer studies so far on graphene-inorganic composite coatings, such as graphene-hydroxyapatite (HA) composites. Li et al. reported their work on the fabrication and characterisation of GO/HA nanocomposite coatings [140, 246]. In their study the coatings were fabricated on titanium substrates from a co-suspension of GO and HA nano-particles by electrophoretic deposition (EPD). TEM observation confirmed a uniform distribution of HA particles on GO sheets, and SEM images show dense morphology and much less cracks for the GO reinforced HA coating. Apart from the strengthened mechanical properties, the GO containing coatings showed improved corrosion resistance in simulated body fluid (SBF), and superior in-vitro biocompatibility (~95% cell viability for 2wt% GO). In a very recent report, Janković et al. prepared similar GO/HA composite coatings and evaluated their bio-activity as well as the corrosion behaviour in simulated body fluid [245]. The hardness, elastic modulus and thermal stability were all found increased, and an apatite layer was freshly formed in SBF, indicating the good biocompatibility of the composite coating. The GO/HA composite coatings demonstrated an improved corrosion resistance as confirmed by EIS measurements, although no antibacterial activity observed.

## 2.6 Summary

In this chapter, the development of graphene and related research is briefly reviewed (Section 2.1), followed by an introduction of the structure and main unusual properties of graphene (Section 2.2) and methods for obtaining graphene (Section 2.3). Graphene oxide (GO) and reduced graphene oxide (rGO) stand a good chance in many engineering applications (where super electronic properties are not essential) due to their low-cost synthesis and potential for mass production.

Moreover, although CVD-graphene usually exhibits better performance in laboratory, GO and related materials facilitate convenient fabrication of graphene-based coatings in large area via various wet-chemistry routes (Section 2.4). Among the reviewed coating fabrication methods, self-assembly has been reported to enhance the bonding of graphene-based coatings to silicon wafer and titanium for nano- and micro-tribological applications. However, no work has been done about the use of such a bonding layer on other common metallic surfaces like steel. Electrophoretic deposition (EPD) is capable for quick and controllable deposition of graphene-based coatings from a simple aqueous suspension. On the other hand, as an advanced electrodeposition technique, electro-brush plating (EBP) has multiple advantages for the fabrication of nano-composite coatings, in particular the easy operation and the coating homogeneity. There is no report yet in the literature exploring the use of EBP for graphene-based coatings, which is worth investigating.

Being the main scope of this project, the tribological applications and anti-corrosion applications of graphene-based materials are reviewed in Section 2.5. The attractive tribological properties of graphene are highlighted by both nano- to microscale and macroscale studies. Nevertheless, the importance of integrity and adequate bonding of the graphene-based coatings is emphasised by many reports. To crack the bonding issue, graphene-based composite coatings rather than pure graphene coatings (formed of solely graphene and/or its derivatives) can be adapted. The documented studies on graphene-polymer composite coatings showed encouraging improvements in both mechanical and tribological performance. However, few reports on metal-graphene composites were found.

The impermeability of graphene is then reviewed prior to the corrosion applications of graphene and related materials, as it is believed to be the root of graphene’s extraordinary anti-corrosion properties. Indeed, according to the earliest studies on CVD-grown graphene and GO/rGO coatings, impressive physical barrier effect against oxidation and wet corrosion was observed. However, similar issues such as defects and coating adhesion remain. Graphene-polymer and graphene-inorganic composite coatings have shown their potential for long-lasting corrosion protection. Unfortunately, those studies on graphene-metal composite coatings are rare.

# CHAPTER 3 EXPERIMENTAL

## 3.1 Substrate materials

In this study, the main material used for substrates is type 316L austenitic stainless steel. 3-mm-thick stainless steel plate was sectioned into 20 × 30 mm$^2$ coupons using a Struers Accutom-5 cutting machine. The coupons were then wet ground from grit 200 up to 2500 using silicon carbide grinding paper. After rinsing and washing with soapy water, the samples were further degreased in acetone for 10 minutes with the assistance of ultrasonication. The cleaned samples were blow dried and used immediately unless otherwise mentioned.

Some of the samples were further polished on an automatic metallographic polisher when a lower surface roughness is required, for example, the mounted samples for cross-section observations under microscope. In these cases, 6 μm and 1 μm diamond pastes were used successively to get a mirror finish. The polished samples were then cleaned the same way as instructed above.

## 3.2 Graphene oxide synthesis

Graphite oxide was prepared based on a modified Hummers' method [103]. Typically, 1 g graphite powder (Alfa Aesar, -325 mesh natural flakes) was mixed with 6 g potassium permanganate ($KMnO_4$), then subject to chemical reactions with a blend of chilled concentrated sulphuric acid ($H_2SO_4$, 120 mL) and phosphoric acid ($H_3PO_4$, 13.5 mL) under rigorous stirring for 12 h at 50 ℃. The mixture was then left cooling down overnight to room temperature. To terminate the reactions, the resultant chocolate-coloured slurry was poured carefully onto ice (made from 150 ml deionised water), followed by the addition of 30 wt% hydrogen peroxide ($H_2O_2$) solution under continuous stirring until the mixture turned bright yellow in colour (for the doses described here 3-5 mL $H_2O_2$ solution is required).

After left to stand for a few hours, the supernatant was discarded and the solids, i.e. graphite oxide, were collected and washed repeatedly with 10 wt% hydrochloric acid (HCl) solution. For each wash, the solid material and the acid were mixed well and subject to centrifugation (6000 rpm for 10 min) with the supernatant being decanted away. This process was repeated (usually 10-15 times) until sulphate radical can no longer be detected from the supernatant using diluted barium chloride ($BaCl_2$) solution. In order to remove acid residues after these washes, the remaining solid was washed with copious absolute ethanol in a similar way as described above, until the pH of the supernatant increased to 6-7. The obtained material was dried thoroughly in hot air.

The graphite oxide after the washing procedures described above is clean enough for most purposes in this study. In just a few cases, dialysis was involved as an enhanced purifying process. Dialysis bags were home-made by dispensing 10 ml collodion solution (4-8 % in ethanol/diethyl ether) in an Erlenmeyer flask, followed by tilting and rotating until a full coverage of collodion on the interior of the flask was obtained. After 1 h the solvent evaporated and the dialysis bag was peeled off with extra care. The dialysis bag was filled with graphite oxide slurry and immersed in distilled water which was replaced regularly, until the pH of the surrounding water increased to approximately 7 and no $SO_4^{2-}$ can be detected by $BaCl_2$.

Graphite oxide can be exfoliated into individual graphene oxide (GO) layers in many polar solvents including water under ultrasonication, and readily used for the following coating process. To obtain a 1 mg/mL GO aqueous suspension, for instance, 100 mg of the dried product was dispersed in 100 ml deionised water under continuous ultrasonication (200 W, Ultrawave U2500H) for 2-3 h. The suspension was centrifuged at 1000 rpm for 30 min with the precipitates (mostly heavy and un-exfoliated graphite oxide) being discarded.

## 3.3 Coating fabrication

### 3.3.1 Self-assembly thin film

Prior to thin film fabrication, target substrates (316L stainless steel) were first cleaned in acetone and then treated in a Piranha solution (7:3 v/v mixture of concentrated $H_2SO_4$ and 30 wt% $H_2O_2$ solution) at 80 °C for 30 min to modify the surface with hydroxyl (-OH) groups. Extra care must be taken here as the Piranha solution is highly corrosive. After rinsing with deionised water and blow drying, the specimens were kept in a 3 vol% (3-Aminopropyl)triethoxysilane (APTES) solution in ethanol-water (5:1 v/v) at room temperature for 30 min. The obtained samples were then rinsed and dried thoroughly.

The self-assembly of GO coating was done by keeping the APTES-treated steel substrates into the GO suspension at 60 °C for 12 h. After that, the samples were rinsed and ultrasonicated to remove excessive GO sheets floating on the surface. This type of samples was named 316L-A-GO. For comparison, the same immersion process was applied to untreated stainless steel (namely 316L-GO).

### 3.3.2 Electrophoretic deposition (EPD)

A purpose-built electrophoretic deposition cell was used, as shown in Figure 3.1. Briefly, two stainless steel plates facing each other with a separation of 20 mm served as the working and counter electrodes, respectively. The electrodes were immersed into a 1 mg/mL GO aqueous suspension. The anode of the DC power supply was connected to the working electrode while the cathode to the counter electrode. Electrophoretic deposition was performed in constant voltage mode with a voltage level ranging from 1-10 V. After a specific deposition time (for example 2 minutes), the two electrodes were withdrawn from the suspension slowly while keeping the power on. The DC power was then cut off and the coated sample was dried in 80℃ hot air for 1 h. For EPD in water without any additives, one should expect GO coatings formed on the anode, i.e. the working electrode.

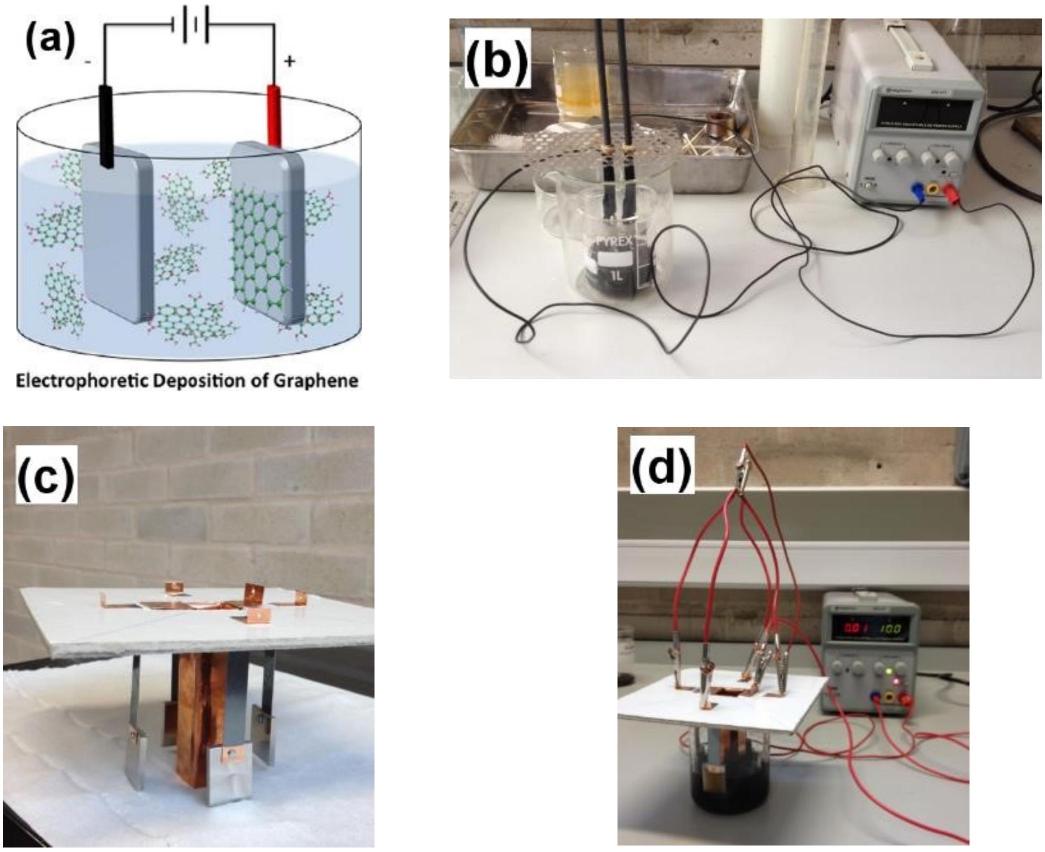

Figure 3.1 (a) Schematic of electrophoretic deposition of graphene [147] and (b-d) home-made deposition fixtures for (b) one- and (c) four-anode deposition.

### 3.3.3 Electro-plating

A three-electrode system similar to the electrophoretic deposition fixture was used in the electroplating of pure Ni and Ni-GO composite coatings. Briefly, a piece of nickel plate was placed in the middle of the deposition cell as the anode. Two 316L stainless steel coupons with dimensions of 20 × 30 $mm^2$ were placed in symmetry in the cell. The deposition area was approximately 20 × 20 $mm^2$ for each sample and the separation between the nickel anode and the stainless steel cathode was fixed at 25 mm. The deposition process was controlled by a DC power supply working in constant-current mode. A PTFE-coated magnetic stirrer on the bottom of the deposition cell was powered during the deposition to provide agitation to the plating solution. The deposition cell was kept in a thermostatic water bath in order to maintain the deposition temperature.

To remove the oxide scale developed on the substrate surface and thus improve the coherence of the nickel coating to the substrate, after being cleaned and degreased, the stainless steel was submerged in a 10 wt% $H_2SO_4$ solution at 50 ℃ for 30 seconds as an activation process. The substrate was then rinsed, dried and used for deposition immediately.

The nickel plating solution was prepared according to the classical Watts bath recipe which consists of $NiSO_4 \cdot 6H_2O$ (250 g/L), $NiCl_2 \cdot 6H_2O$ (40 g/L) and $H_3BO_3$ (30 g/L) with a typical pH value of 3.5-4.5 which was adjusted using diluted $H_2SO_4$ and NaOH solution. All the chemicals used were analytical-grade pure and dissolved in deionised water followed by sieving through analytical filter paper in order to remove insoluble impurities. The temperature of the electrolyte was carefully selected from the range of 40-60 ℃ and kept constant during deposition. A current density of 4 $A/dm^2$

was used.

Nickel-graphene oxide composite plating bath was prepared by adding 4 mg/mL GO suspension dropwise into the original Watts plating solution under continuous ultrasonication (200 W) while shaking the container to minimise agglomeration. For 100 mL nickel solution, 5 mL of the GO suspension would result in a GO concentration of approximately 0.2 g/L in the final plating solution, considering that the 5 mL addition does not increase the total volume much. After GO addition the plating bath was subject to further ultrasonication for at least 1 h prior to use. The GO concentrations in the final nickel plating bath varied from 0.2 up to 1.5 g/mL.

### 3.3.4 Brush-plating

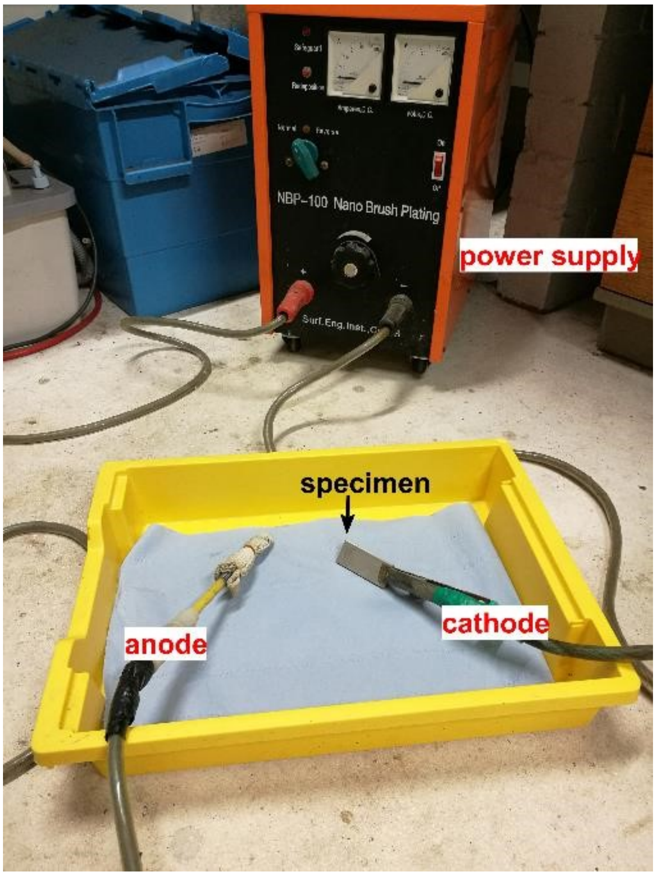

Figure 3.2 Digital photo of the electro-brush plating equipment.

The electro-brush plating of nickel and nickel-GO nano-composite coatings was performed using a nano brush plating unit (NBP-100) developed by the Surface Engineering Research Institute, CMES, China (Figure 3.2). It is basically a DC power pack yet with specially designed controllers which enable precise output of voltage and current, enhanced overload protection and one-click switch of the electrode polarities.

There are two poles (positive and negative) leading out of the power pack, with one of which being connected to the brush and the other attached to the workpiece. The brush is a graphite rod wrapped with absorbent material (cotton cloth). When plating the brush carrying plating electrolyte wipes against the target surface gently and continuously. In this study, the speed of brush motion was kept at 10 cm/s.

Table 3.3-1 Operation procedures for electro-brush plating of Ni and Ni-GO composite coatings

| No. | Operation | Connection | Voltage | Time |
|---|---|---|---|---|
| 1 | Electro-cleaning | Brush (+)<br>Sample (-) | 10 V | 1 min |
| 2 | Electro-activation | Brush (-)<br>Sample (+) | 10 V | 2 min |
| 3 | Pre-plating<br>(acid nickel) | Brush (+)<br>Sample (-) | 18 V<br>12 V | 5 s<br>2 min |
| 4 | Working coating<br>(ductile nickel + GO) | Brush (+)<br>Sample (-) | 18 V<br>14 V | 5 s<br>30 min |

The plating solutions used in this work were commercially available (Sifco ASC), including electro-cleaning solution, electro-activation solution, acid nickel solution and ductile nickel solution. For Ni-GO nano-composite coatings, the composite plating solution was prepared by adding GO suspension into the original ductile nickel solution, a process equivalent to the one described in Section 3.3.3. The GO concentrations in the final nickel plating bath varied from 0.5 up to 4 g/mL.

By following the plating procedures detailed in Table 3.3-1 and brushing these solutions in succession onto the article, nickel coatings of 10 - 15 μm were obtained after a deposition time of 30 minutes. Note that after each step in Table 3.3-1 the sample was rinsed and dried as described before.

## 3.4 General characterisation

### 3.4.1 X-ray diffraction (XRD)

The crystallisation status of the synthesised GO and the phase structures of the coatings were analysed by XRD using a Bruker D8 Advance x-ray diffractometer working with Cu-$K_\alpha$ radiation ($\lambda$ = 0.154 nm). PANalytical X'Pert Highscore Plus software was used for the analysis of the acquired XRD patterns, such as peak indexing, d-spacing calculating, phase determination as well as grain size estimation.

### 3.4.2 Raman spectroscopy

Raman spectra of GO and GO-containing coatings were recorded using a confocal Raman microscope (Renishaw inVia Reflex, laser wavelength 488 nm). The target sample was focused under a 20X objective microscope and the laser power was limited at 10% out of the 35 W in order to minimise the damage to the sample. An exposure time of 10 seconds per scan and six accumulations per sample were taken. A WiRE software (version 4.2) by Renishaw was used for the data processing.

### 3.4.3 X-ray photon spectroscopy (XPS)

XPS was employed to investigate the elemental and chemical states of GO and GO-containing samples within an extremely small depth (less than 10 nm) beneath the surface. XPS spectra were collected on a Thermo Scientific ESCALAB 250Xi facility. Full-range spectra as well as detailed $C_{1s}$ spectra were recorded in order to understand the bonding status and the oxidation/reduction degree of the GO.

XPS samples were cut to sizes of less than 10×10 $mm^2$ in lateral and 3 mm in height to fit in the instrument. Considering that carbon is the most interested information in this study, the sample surfaces were etched with argon ions for 1 minute prior to each measurement in order to remove the surface contaminations, especially external carbon species.

### 3.4.4 Atomic force microscopy (AFM)

AFM is known for its extremely high spatial resolution and thus widely used in nanotechnology. Unlike other common microscopes such as optical and electron microscopes which can only provide 2D images, one can obtain the 3D topography of a surface. The morphology of graphene oxide sheets and self-assembled GO thin coatings were characterised by an AFM (NanoWizard III, JPK Instruments) in tapping mode. A silicon cantilever of 125 μm in length, with a resonant frequency 300 kHz and a spring constant 40 N/m was used in this work. The scan rate was 0.5-1 Hz.

GO samples were prepared by simply putting a droplet of diluted (nearly colourless) GO-ethanol suspension on a silicon wafer and then blow drying. Highly polished silicon wafer (surface roughness ~1 nm) was chosen as the background material due to its atomically high degree of flatness.

### 3.4.5 Zeta-potential

Zeta potential, as briefly introduced in Literature Review, indicates the stability and electrophoretic mobility of the particles in a suspension and thus is one of the fundamental parameters for an EPD process. The zeta potential of GO was measured using a Zetasizer Nano system (Malvern Instruments). GO was dispersed in ultra-pure deionised water by ultrasonication with gradient concentrations of 0.25, 0.33, 0.5 and 1.0 mg/mL. At least six measurements were taken for each GO concentration in order to obtain a good average.

### 3.4.6 Scanning electron microscopy (SEM)

A Philips XL-30 field emission scanning electron microscopy (FESEM) was used throughout this study for the observation of surface morphology, fractography as well as wear tracks. In most cases the accelerating voltage was fixed at 10 kV. Samples to be examined were attached to the holder using sticky carbon or copper tape and a nano gold sputter (coating rate 10 - 12 nm every 3 min) was used to improve the electron conductivity.

cross-section samples were cut from the bulk on a Struers Accutom-5 cutting machine before being mounted in conductive Bakelite stubs using an Opal 400 mounting press. The grinding, polishing and cleaning procedures were the same as described before.

Where a coating fracture was required, the sample was hand-sawed from the back side (uncoated side) until a very thin skin of material (with the coating) was left before complete separation. The sample was then soaked in liquid nitrogen (personal protective measures taken) for about 3 minutes and bent immediately using pliers to fracture the sample from the notch.

### 3.4.7 Energy dispersive x-ray spectroscopy (EDX)

The SEM employed is also fitted with an EDX instrument (INCA Energy, Oxford instruments) which was used to in-situ analyse the elemental information near the sample surface with a spatial resolution of approximately 1-2 μm. The accelerating voltage, electron beam spot size and working distance were adjusted to optimal prior to EDX requisitions. Both pointing and mapping requisition modes were involved as per the sample type and analysis requirements.

### 3.4.8 Transmission electron microscopy (TEM)

TEM observations were performed on a JEOL 2100 TEM equipped with a $LaB_6$ filament working at 200 kV. Electron diffraction (ED) was also conducted on site.

Graphene oxide TEM samples were prepared by putting a small droplet of diluted (close to colourless) GO-ethanol suspension on a TEM support grid (with lacey carbon film) and then drying in ambient environment. Due to the nano-scale thickness of GO sheets, the sample made in this way can be readily used for TEM observation.

### 3.4.9 Roughness

Surface roughness and wear track profiles were measured using an Ambios XP-200 stylus profilometer (Figure 3.3). For a 2D measurement the stylus with a diamond tip scans against the sample surface at a speed of 0.05-0.1 mm/s under a slight load of 1-5 mg. The height profile along the scanning direction was recorded and the surface roughness was given afterwards. 3D topography profiles were obtained by programming multiple parallel 2D scans with a fixed separation between every two. For example, for a 0.5×0.5 $mm^2$ square scanning, a 0.5-mm-long 2D scan and 100 repetitions separated by gaps of 0.005 mm were programmed. The instrument then ran the scans one by one automatically and ended up with a 3D topography image of the selected area with the assistance of the integrated software.

Figure 3.3 Digital photo of the 3D profilometer used for surface roughness measurements and wear track mapping.

## 3.5 Mechanical property assessment

### 3.5.1 Micro-hardness

Micro-hardness measurements were conducted using a Mitutoyo MVK-H1micro-hardness tester fitted with a Vickers indenter (Figure 3.4). A load range of 10-1000 g was available and a standard sample brick (EP9716400, 757.3 $HMV_{0.3}$) was used for calibration prior to every session. The measurement was taken in accordance with the standard *ASTM E92-16*. In this study a load of either 50 g or 100 g was used, while for some thinner coating samples lighter loads were chosen in order to ensure the indentation depth within 1/10 of the coating thickness. At least six repeats were taken on each sample, with a separation of no less than three Vickers diagonal length between every two.

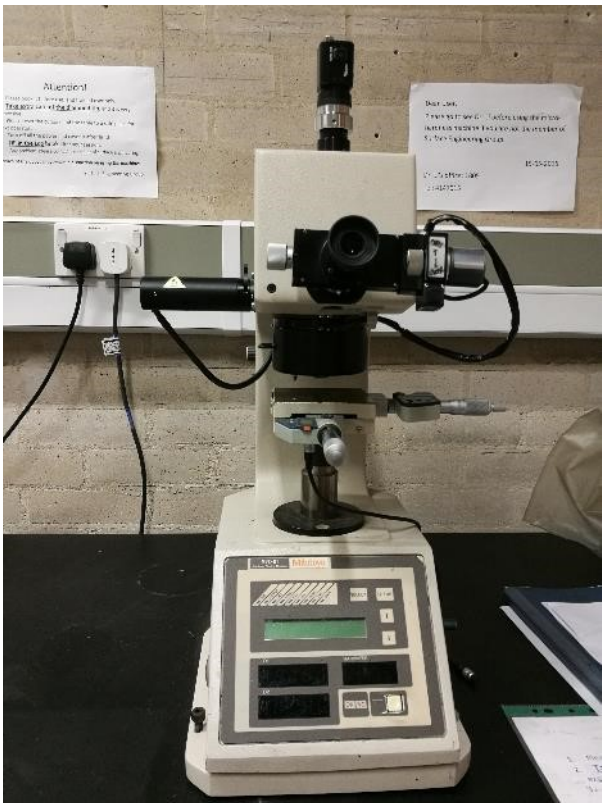

Figure 3.4 Vickers hardness tester in the Surface Engineering lab.

### 3.5.2 Nano-indentation

A NanoTest Vantage instrument (Micro Materials Ltd.) fitted with a Berkovich tip was employed for nanoindentation studies (Figure 3.5). The indenter approached to the sample with an initial contact load of 0.02 mN and a maximum load of 10 mN. Both loading and unloading time were set as 30 seconds, with a dwell time of 5 seconds at the maximum load. An extra dwell time of 60 seconds during the unloading period was taken for the purpose of thermal drift correction. At least 10 indents were performed on each sample, with a separation of at least 10 μm in between. The samples were all polished (down to 1 μm diamond paste) under gentle force before nanoindentation. After testing, the indents were checked using an in-situ optical microscope and SEM.

The raw data was analysed with the built-in software by Micro Materials Ltd. The hardness and Young's moduli were calculated from the loading-unloading curves based on a power law fit developed by Oliver and Pharr [247].

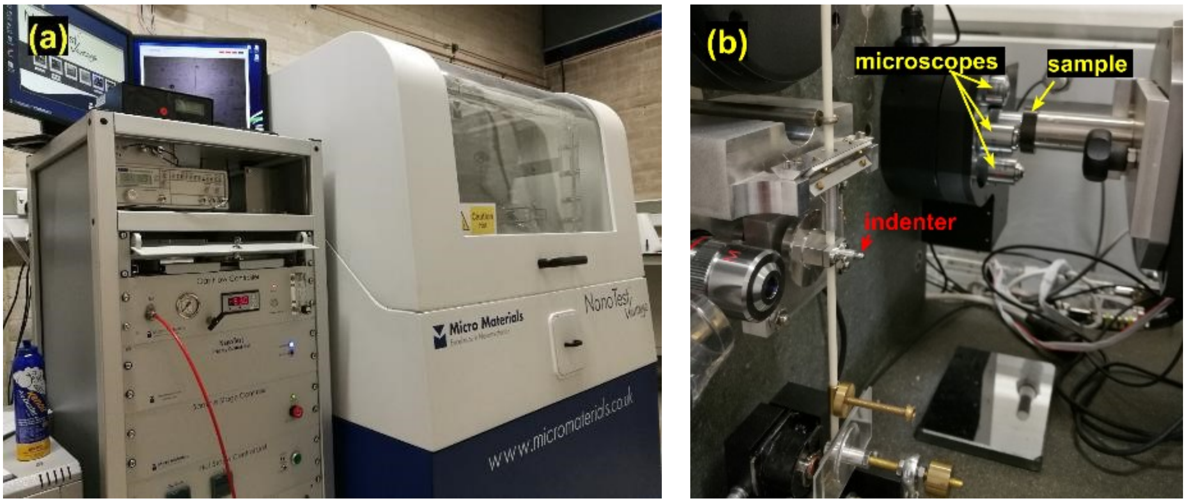

Figure 3.5 (a) Nanoindentation equipment in the Surface Engineering lab and (b) close look of the indentation configuration.

### 3.5.3 Tribological testing

Reciprocating tribological tests were carried out at room temperature on a ball-on-plate tribometer (TE79 multi-axis, Phoenix Tribology Ltd., UK). The samples were glued on a horizontal plane, sliding back and forth against a ϕ8mm ball at a speed of 5 mm/s with a frequency of 1 Hz. Two counter ball materials, including 316 stainless steel and alumina, were used throughout this study. Figure 3.6 shows the digital photos of the tribometer. The normal loads and sliding cycle number varied, depending on the sample material and wear conditions. Friction forces during the sliding were recorded and the coefficient of friction (COF) was obtained by dividing the friction force with the normal force.

After the reciprocating tribological test, the samples were removed from the holder and examined by means of a profilometer. With regards to the profilometer, the wear tracks were measured at no less than 3 different positions (left, middle and right) of each wear track. The wear loss volume was determined by taking the mean value of the three (or more) wear scar areas and then multiplying by the length of the wear track. The morphology of the worn surface was examined by means of SEM and EDX.

**(a)**

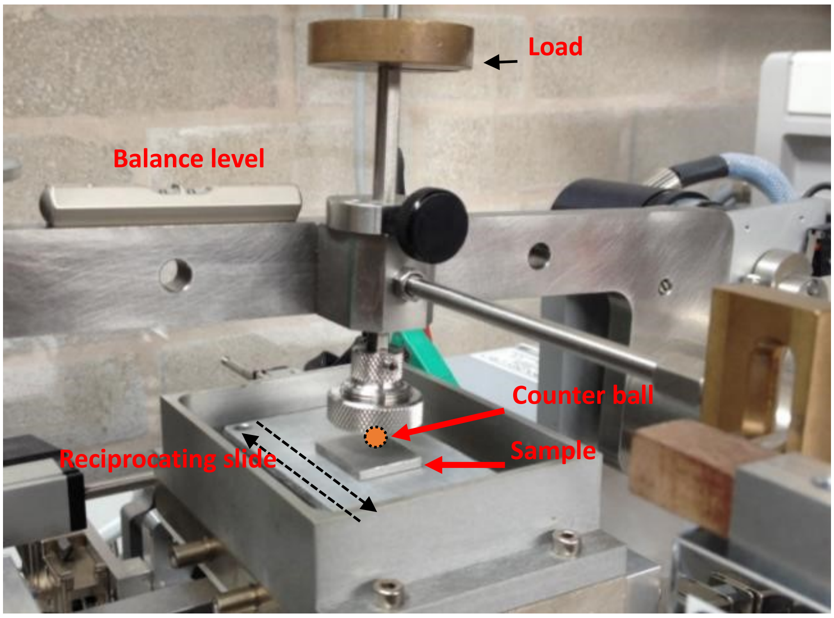

**(b)**

Figure 3.6 (a) TE79 multi-axis tribometer and (b) enlarged view of the working table.

## 3.6 Corrosion property assessment

### 3.6.1 Sample and equipment preparation

Samples coated with GO only or Ni-GO composite were cleaned with extra care under running tap water and deionised water in succession, and then blow dried in air. Any marks or contaminations on the back side of the samples were cleaned in order to secure electric conductivity. All the glassware involved in the corrosion tests, such as the corrosion cell, beakers, triangle funnel, volumetric flask and measuring tubes were washed with soapy water, flushed thoroughly under running water, and then rinsed with deionised water and blow dried.

The corrosion environment in this study was 3.5wt.% sodium chloride (NaCl) aqueous solution at room temperature unless otherwise specified. Typically, to make 1000 g solution, 35 g NaCl was mixed with 965 mL water at room temperature under continuous stirring. The solution was then filtered through analytical filter paper before use.

All corrosion tests were performed on a Gamry Interface 1000 potentiostat. The instrument was subject to signal calibration regularly and warmed-up for 3 minutes before every session. A three-electrode configuration was adapted with a platinum coated rod (ϕ6mm) used as the counter electrode, and a saturated calomel electrode (SCE, Gamry Instruments) as the reference. Before testing, the counter and reference electrodes were cleaned with running water and deionised water, and then dried carefully using soft tissue. They were cleaned and dried the same way for storage after testing. Figure 3.7 displays the configuration of the corrosion experiments.

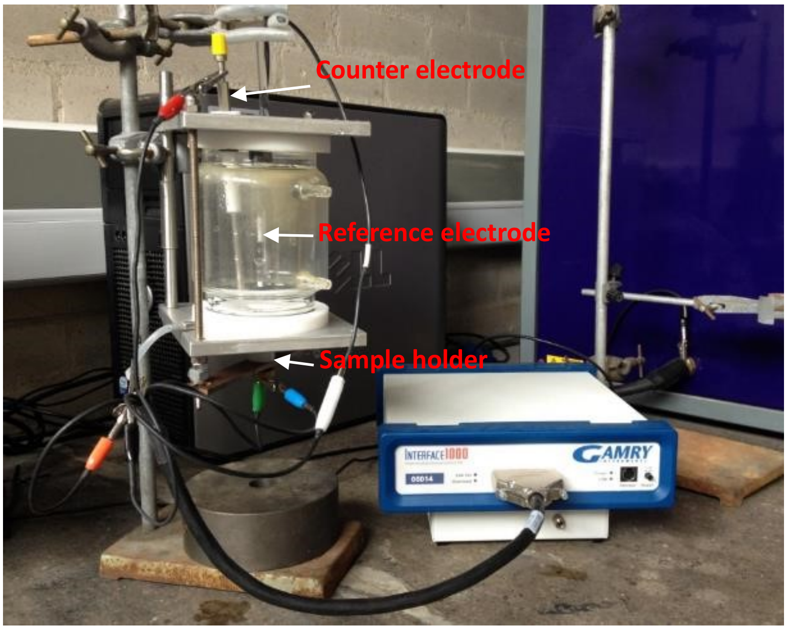

Figure 3.7 Electrochemical measurement equipment.

### 3.6.2 Open circuit potential

Open circuit potential (OCP) refers to the difference between the electrical potentials of the sample and the reference electrode (i.e. SCE in this study) that are detached from a circuit without external load. OCP measurements were always performed first in order to familiarise the sample with the corrosion environment and establish a stable electrochemical interface before any further measurements. For all tests the OCP was recorded continuously over a period of 60 minutes.

### 3.6.3 Potentiodynamic polarisation

The polarisation test started immediately the OCP measurement finished, scanning from -0.2 to +1.0 V (versus the finishing OCP level) at a scan rate of 1 mV/s, during which both cathodic and anodic polarisation measurements were performed. Once the polarisation measurement finished, the sample was removed from the corrosion cell and rinsed using deionised water and dried. At least three measurements were taken for each sample to ensure the reproducibility.

The data obtained was analysed using a built-in software (Echem Analyst, Gamry Instruments). The corrosion potential ($E_{corr}$) and corrosion current density ($I_{corr}$) were determined by applying Tafel fit to the polarisation curve.

### 3.6.4 Electrochemical impedance spectroscopy

Electrochemical impedance spectroscopy (EIS) is an electrochemical technique widely used in coating research in terms of the anti-corrosion properties and the coating degrading process in a specific electrolyte. EIS measurements were performed using the same Gamry Interface 1000 potentiostat and three-electrode connection in 3.5 wt.% NaCl solution at room temperature. A platinum rod and an SCE electrode were used as the counter and reference electrodes, respectively, as described before. The sample area exposed to the solution was 0.503 cm$^2$. OCP was monitored for an hour before EIS measurement, which commenced at the finishing OCP with a sinusoidal voltage amplitude of 10 mV. The impedance was measured over a voltage wave frequency range of 0.01 Hz -100k Hz. At least three measurements were taken for each sample to ensure the reproducibility.

The data obtained were analysed using the built-in software (Echem Analyst, Gamry Instruments). The Bode and Nyquist plots were produced individually and equivalent circuit models were established using a built-in fitting module.

# CHAPTER 4 RESULTS AND DISCUSSION: PART I

## - Pure GO and electroplated Ni-GO composite coatings

As stated in Chapters 1 and 2, one of the major issues for realising the technological and economic potential of graphene in engineering and manufacturing fields is the difficulties in obtaining graphene products in large area. Chemically derived graphene oxide (GO) could be a promising solution as it facilitates low-cost and scalable production of graphene and graphene-based composite coatings via diverse chemical routes.

This chapter presents the first part of the results and discussion portfolio, covering GO synthesis, GO single coatings by electrophoretic deposition and by self-assembly, and Ni-GO composite coatings by electroplating. The morphology and microstructures of the GO synthesised from the research are first reported in Section 4.1; the morphology, microstructures, layer structure, chemical bonding, and tribological and corrosion behaviour of the GO and the GO-based coatings are reported in Sections 4.2-4.4. The experimental results are finally interpreted and discussed in Section 4.5 to advance scientific understanding.

## 4.1 GO synthesis

### 4.1.1 Synthesis process

Figure 4.1-1 is the schematic of the processing route for graphene oxide (GO) synthesis in this project. Briefly, the synthesis of GO was a wet chemical route, which

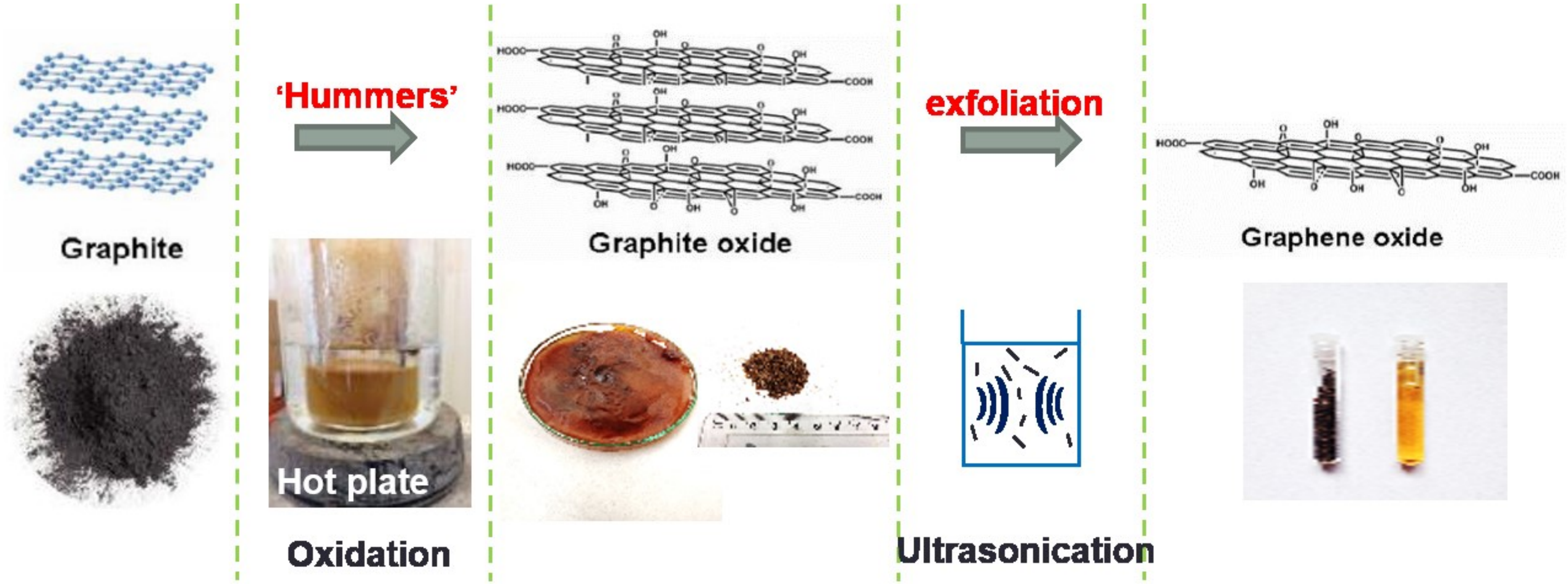

Figure 4.1-1 Schematic of the graphene oxide synthesis process.

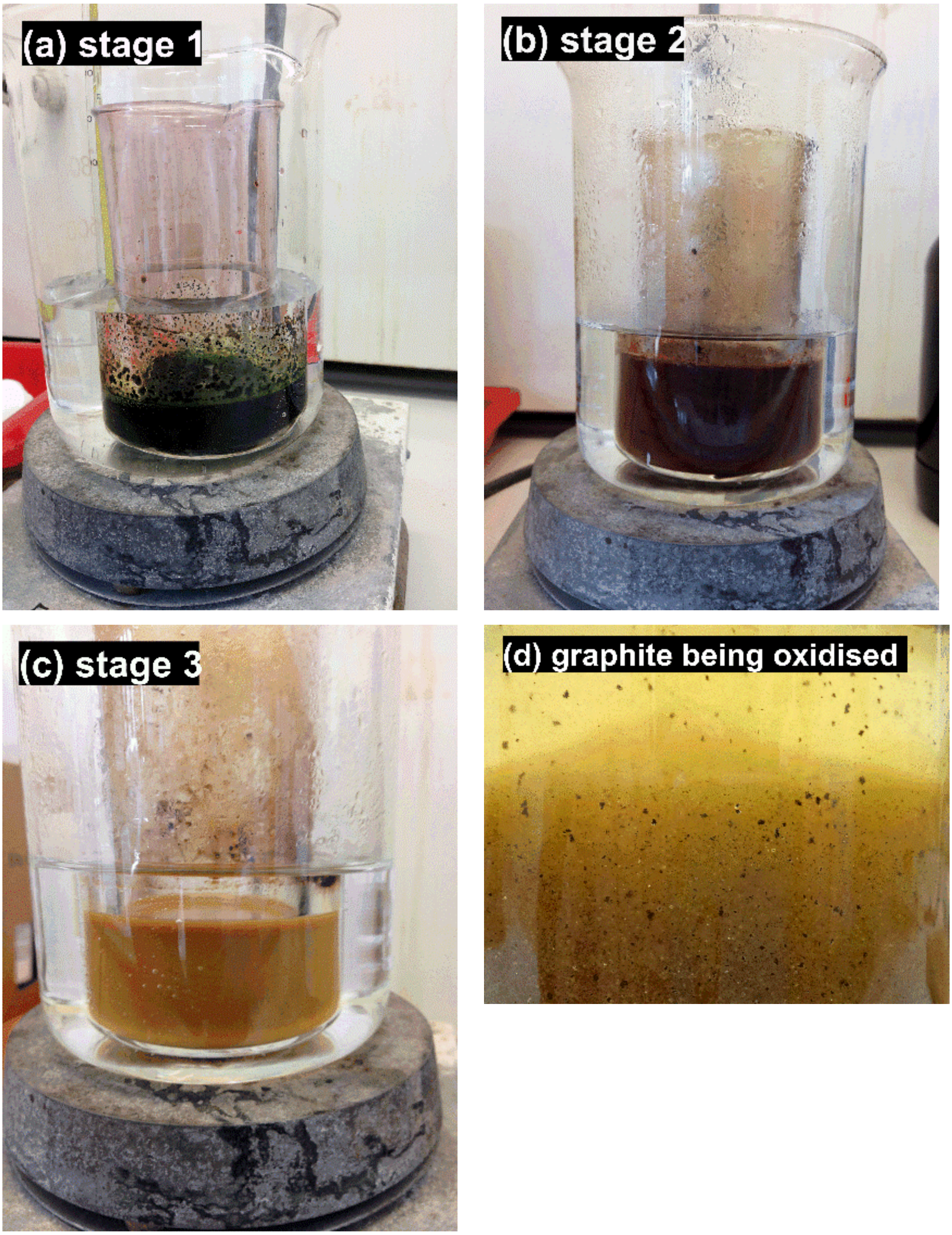

Figure 4.1-2 Snapshots of (a-c) different stages during the Hummers' process (graphite oxidation) and (d) close view of partially oxidised graphite.

was based on the expansion of the layered structure of graphite, followed by ultrasonication-assisted exfoliation into individual carbon sheets. As the oxidation of graphite (the most critical part of the synthesis process) went on, the colour of the reacting mixture changed from dark green (Figure 4.1-2a) to chocolate brown (Figure 4.1-2b). At the end of the reactions hydrogen peroxide ($H_2O_2$) solution was added and the slurry turns bright yellow (Figure 4.1-2c), which is characteristic of a complete oxidation. As the graphite structure is oxidised and with an expanded interlayer spacing, the obtained solids are so-called graphite oxide. In case of an incomplete oxidation process, the slurry showed graphite particles with dark core and light edge, as can be seen in Figure 4.1-2d. Usually a successful synthesis can lead to an output of ~1.3 g dried graphite oxide powder for every 1 g graphite. The extra 0.3 g is mainly due to the oxygen functional groups on the carbon plane, as depicted in Figure 4.1-1.

As the graphite structure has been expanded considerably by intercalation and oxidation, single-layer and few-layer (<5 layers) GO can be obtained easily via a period of ultrasonication. Depending on the power of the ultrasonic bath (150 W in this lab), usually 1-2 hours is sufficient to get a clear aqueous dispersion of GO.

### 4.1.2 Morphology, phase and structure

Figure 4.1-3 shows the morphology of the raw material graphite, as-synthesised graphite oxide and graphene oxide. The nominal lateral size of the natural graphite flakes used in this project was no more than 45 μm, and the actual sizes observed were in the range of 5-20 μm, as shown in Figure 4.1-3a. The corresponding graphite oxide sheets exhibited similar lateral dimensions but reduced thickness. The graphite architecture was expanded so effectively that many graphite oxide sheets of identical shape were obtained. Wrinkles were also found on graphite oxide sheets, which is

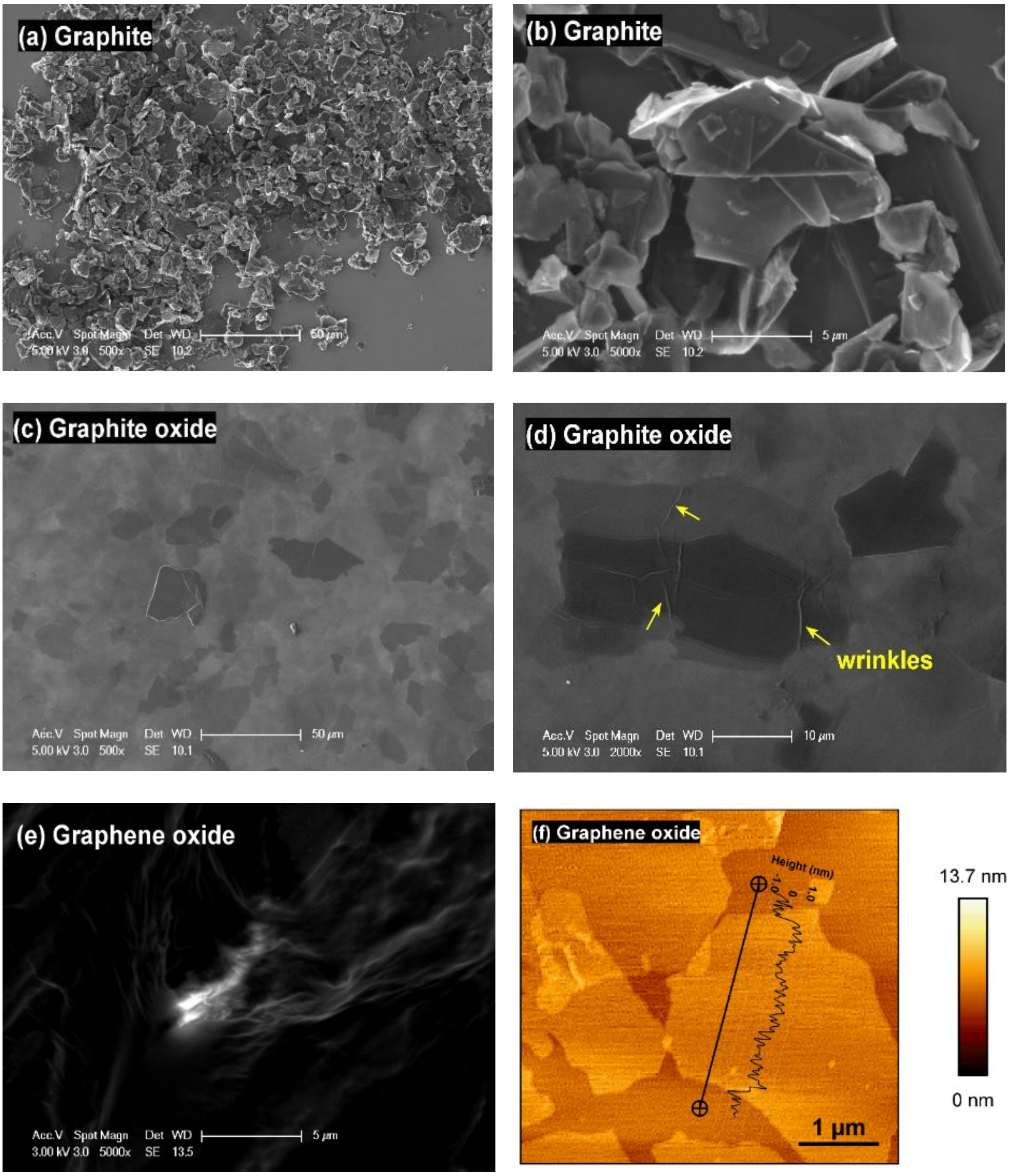

Figure 4.1-3 Micrographs of (a-b) graphite powder, (c-d) graphite oxide and (e-f) graphene oxide (GO) in low (left) and high (right) magnifications.

indicative of weakened interlayer bonding (Figure 4.1-3d). The different nomenclatures for graphite oxide and graphene oxide are mainly due to their different thickness. Usually graphene oxide (<5 layers for few-layer GO, and <10 layers for multi-layer GO) is too thin to resolve using a normal SEM configuration; however, silk-like translucent GO sheets full of wrinkles can be observed under high contrast (Figure 4.1-3e). Figure 4.1-3f is a topography survey of the obtained GO sheets by AFM. The GO sheets exhibited similar contrast against the background (a silicon wafer), indicative of a uniform thickness. The inserted height profile revealed a thickness of approximately 1 nm for a sheet. It is known that each individual layer in graphite is 0.34 nm [45]. The thickness of graphene, however, is usually measured to be larger than 0.34 nm due to out-of-plane deformation. A layer of graphene oxide could be even thicker due to the presence of oxygen function groups. Therefore, the measured 1 nm thickness by AFM corresponds to one single graphene oxide layer, which has been well-accepted [74].

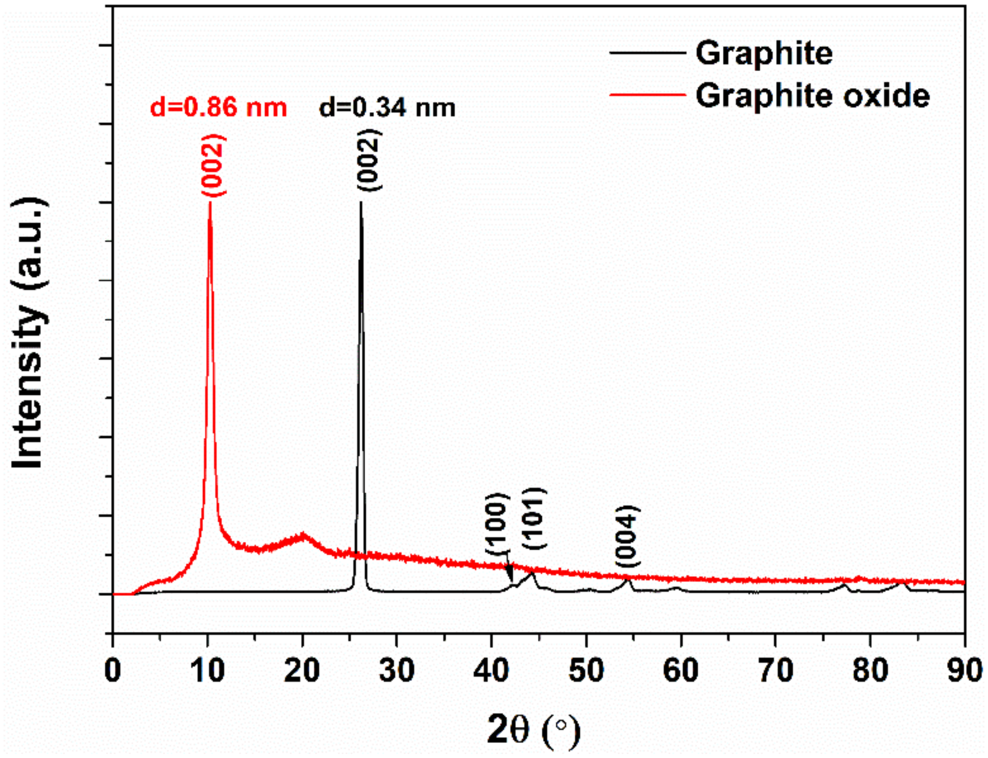

Figure 4.1-4 XRD patterns of graphite and graphite oxide.

Figure 4.1-4 is the XRD patterns obtained from the graphite flakes and the graphite oxide (dried powder). Graphite is characterised by a prominent sharp peak around 26.23° (2θ) arising from the diffraction of (002) plane, which indicates an interlayer spacing of 0.34 nm according to Bragg's law. The peak at 54.39° is the secondary diffraction of the (002) plane, or referred to the diffraction of the imaginary plane (004) of graphite. There are several other weak peaks detected, such as these at 42.2° and 44.33°, which correspond to the (100) and (101) planes, respectively. In comparison, graphite oxide shows a dominant crystalline peak at 10.26°, which suggests an interlayer space of 0.86 nm. The expanded spacing effectively reduces the $\pi$-$\pi$ bonding and van de Waals forces and hence facilities easy detachment of individual layers, which is in agreement with the SEM observation on the graphite oxide (Figure 4.1-3d). The additional small peak around 20° is consistent with the observations by some others [103, 112, 248] and is likely due to those solid products remaining a higher graphitic degree after the oxidation.

It is very difficult to acquire an XRD pattern for graphene oxide since it is an extremely thin 2D crystal. Transmission electron microscopy (TEM) and selected area electron diffraction (SAED) are effective in characterising graphene oxide. Figure 4.1-5 presents the morphology of a GO sheet and the corresponding ED patterns. It is clear that the GO sheet is very flexible, bending, rumpling and twisting freely on the lacey support film. Figure 4.1-5b shows the diffraction patterns from zone A in Figure 4.1-5a. The inner circle of six diffraction spots represent the $(10\bar{1}0)$ planes of graphene with a lattice spacing of 0.213 nm, whilst the outer circle of diffraction spots correspond to the $(11\bar{2}0)$ planes with a smaller lattice spacing of 0.123 nm [45]. The second set of diffraction pattern, as indicated in the plot, was a result of the incommensurate (rotational) stacking of an extra GO monolayer on the existing GO layer. Therefore, the zone A in Figure 4.1-5a was likely formed of two randomly stacked monolayer GO.

However, complicated diffraction patterns could be obtained from a higher number of stacked GO monolayers, as evidenced in Figure 4.1-5c, which was originated from zone B in Figure 4.1-5a.

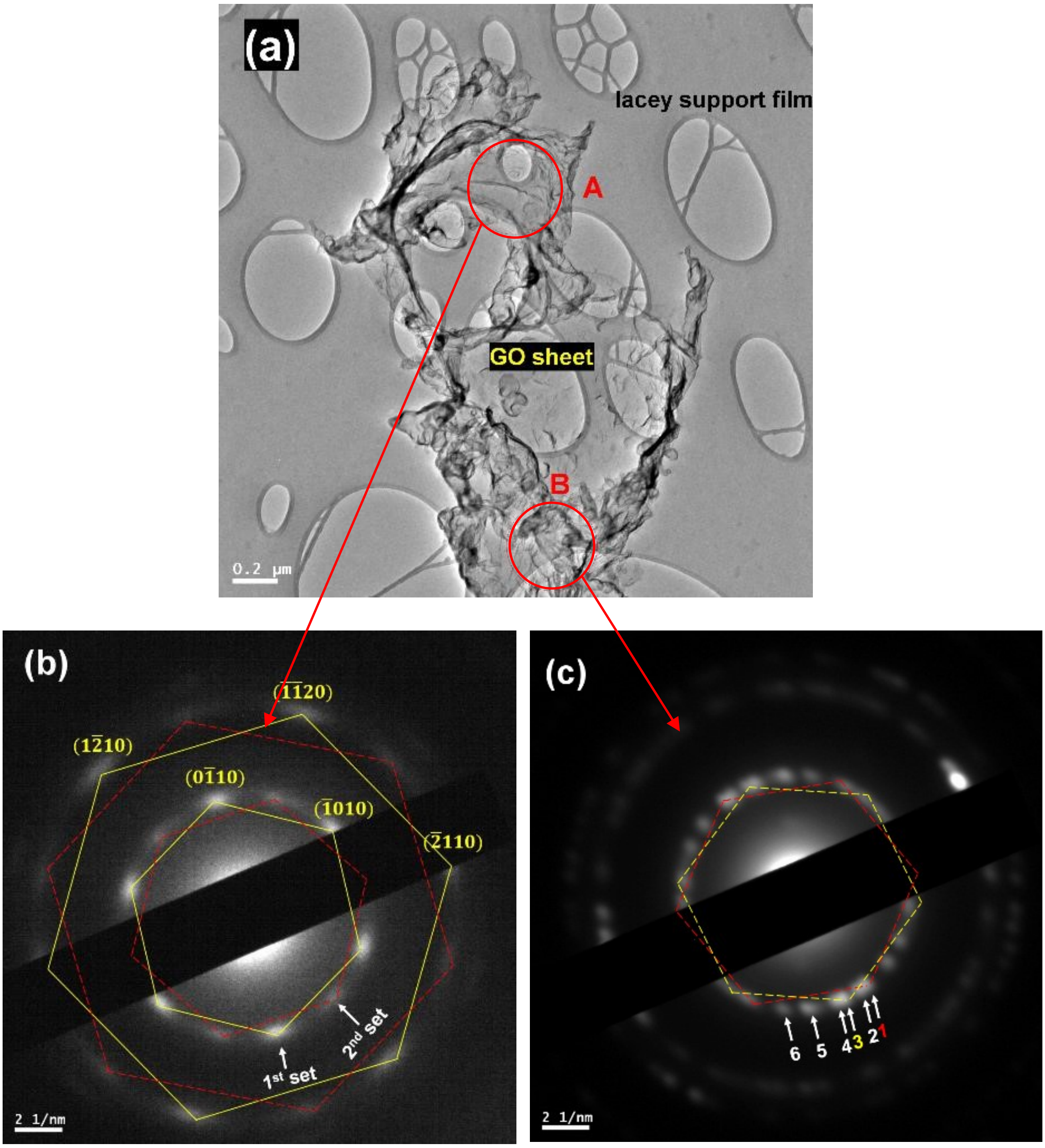

Figure 4.1-5 TEM image (a) and corresponding selected area diffraction patterns from zone A, a bilayer graphene oxide (b) and from Zone B, a 6-layer GO (c).

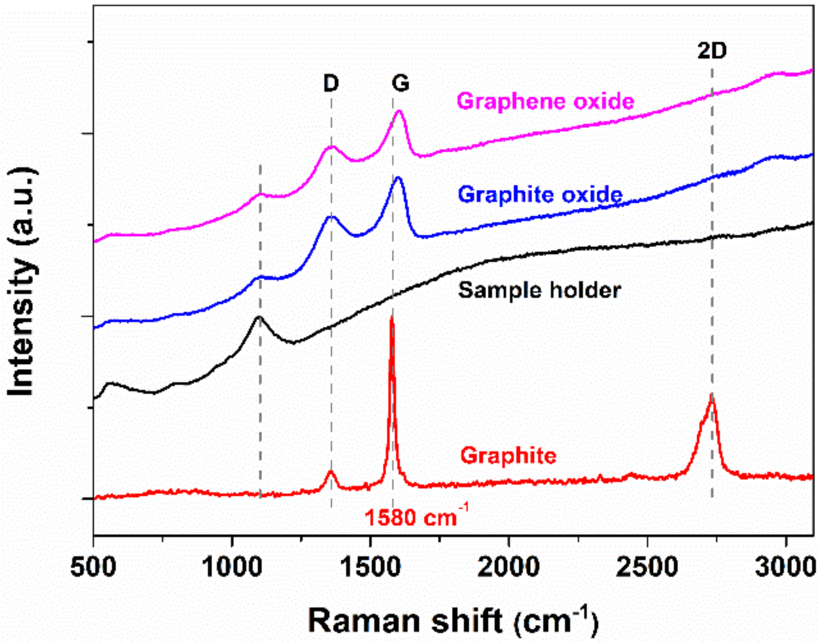

Figure 4.1-6 Raman spectra of graphite, graphite oxide and graphene oxide.

Raman spectra of graphite, graphite oxide and graphene oxide (GO) were collected using 488 nm laser excitation and compared in Figure 4.1-6. A laser wavelength of 488 nm was chosen since carbon materials are more sensitive to shorter wavelengths. Graphite showed a prominent peak around 1580 cm$^{-1}$, namely G band, and a broad 2D band around 2700 cm$^{-1}$ which is the second most prominent Raman feature of graphite. The G band arises from intrinsic bond stretching of sp$^2$-hybridised carbon atoms. Another peak around 1355 cm$^{-1}$, the D band, is also detectable for graphite. Usually the D mode is forbidden, but it is allowed in presence of structural disorders and defects in graphite (or graphene). The intensity ratio of the D to G ($I_D/I_G$) is therefore usually used as an indicator of the disorder degree in graphene. As displayed in Figure 4.1-6, graphite oxide and graphene oxide also showed D and G modes. The D band for both sits around the same position as graphite but is significantly more intense. The position of G band, however, was blue-shifted from 1580 cm$^{-1}$ for graphite to 1590 cm$^{-1}$ for graphite oxide and graphene oxide. The $I_D/I_G$

values for graphite oxide and graphene oxide are 0.71 and 0.73, respectively. The slightly increased $I_D/I_G$ ratio for GO could be due to the increased defect number after ultrasonic exfoliation.

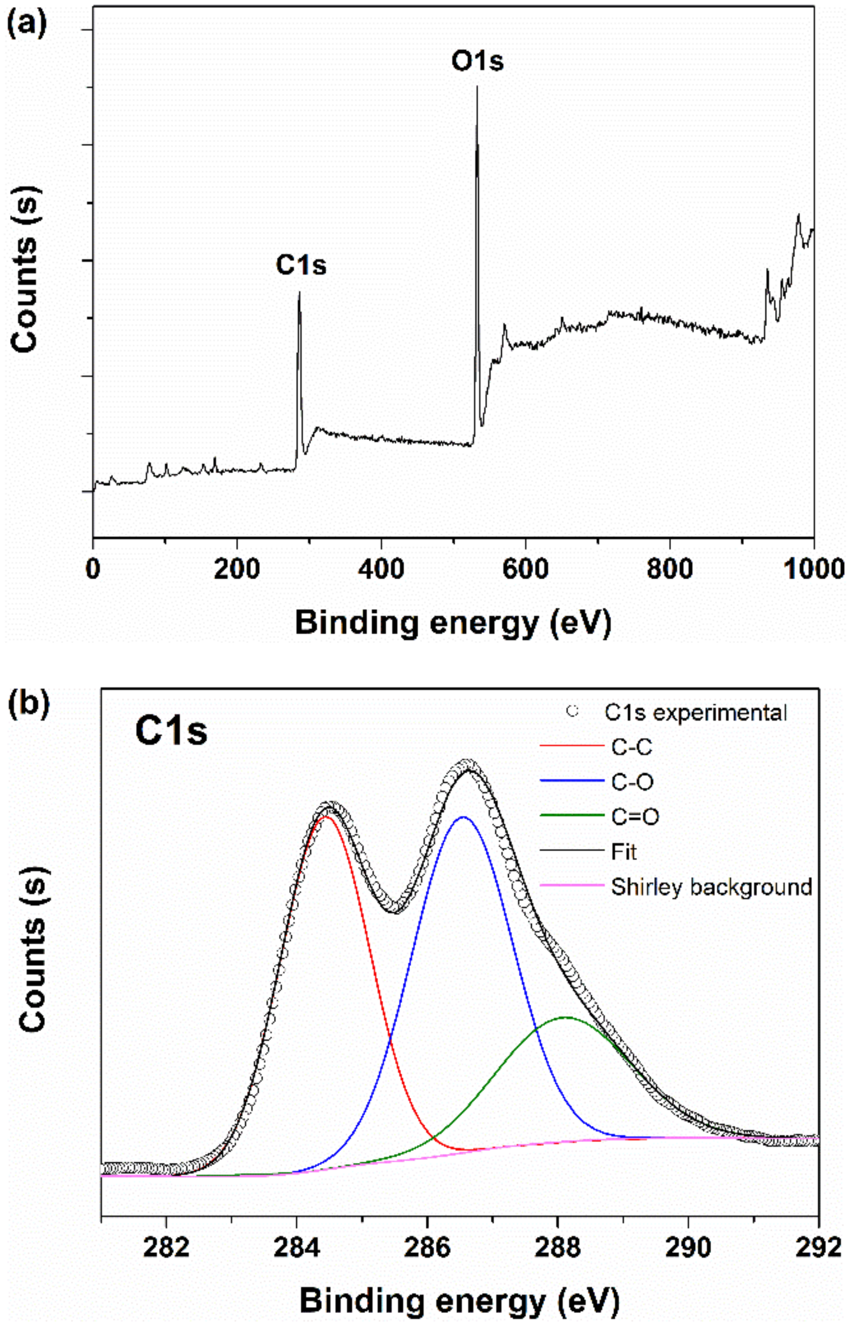

Figure 4.1-7 XPS survey and $C_{1s}$ spectra of graphene oxide.

Figure 4.1-7 shows the XPS survey (a) and the detailed C1s (b) spectra of the synthesised GO. An oxygen peak of high intensity was detected, and the spectrum suggested a carbon to oxygen ratio of 5:3 (at. %), indicating a high oxidation degree of the GO product. The Gauss fitting of the C1s spectra revealed three prominent peaks, as shown in Figure 4.1-7b. The C-C 284.4 eV peak represents the $sp^2$ hybridised carbon, while the C-O 286.5 eV and C=O 288.1 eV peaks indicate the presence of multiple types of oxygen functional groups on the GO. The XPS spectra of graphite and graphite oxide were not recorded due to the limited access to the XPS facilities.

### 4.1.3 Dried powder and dispersions

Figure 4.1-8 Different forms of GO products.

Figure 4.1-8 demonstrates varying forms of GO products resulted from the synthesis process as reported in Chapter 3. The GO slurry shown in Figure 4.1-8a was prepared by repeatedly washing the solids after graphite oxidation and exfoliation using absolute ethanol. After vacuuming the slurry through a 0.22 μm micro-pore filter paper, a flexible GO film can be obtained, as shown in Figure 4.1-8b, which is the so-called GO paper in the literature. Alternatively, the slurry can be dried straight forward and then ground to get GO powder as shown in Figure 4.1-8c. Note that each flake of the powder as seen is actually not associated with one single GO sheet, but many microscopic GO sheets agglomerated together. It is a favoured way for the storage of GO, and a GO aqueous suspension can be easily prepared from a small mass of the GO powder, as shown in Figure 4.1-8d.

Zeta potential is an important parameter of a particle-containing suspension which characterises the stability and electrical mobility of the particles. As GO aqueous suspensions were widely involved in the coating deposition afterwards in this project, the zeta potentials of GO suspensions with different GO content were measured and the results are shown in Figure 4.1-9. Note that usually a GO suspension shows a negative zeta potential as GO sheets are negatively charged in most polar solvents due to the electrolysis of the carboxyl groups (R-COOH to R-COO$^-$) on GO. From the plots, it is clear that the absolute value of the zeta potential decreased slightly as the GO concentration was reduced. The suspension with 1 mg/ml GO exhibited a zeta potential of -61.7 mV, while the 0.33 mg/ml suspension showed -50.87 mV. Nevertheless, the zeta potential values of the four suspensions were all well-above the -30 mV threshold, which is considered to be the critical level for a stable suspension [135]. It was also found that the tested GO suspensions were very stable, with hardly seen precipitates even after 6 months of standing. Thus, the zeta potential over time was not recorded.

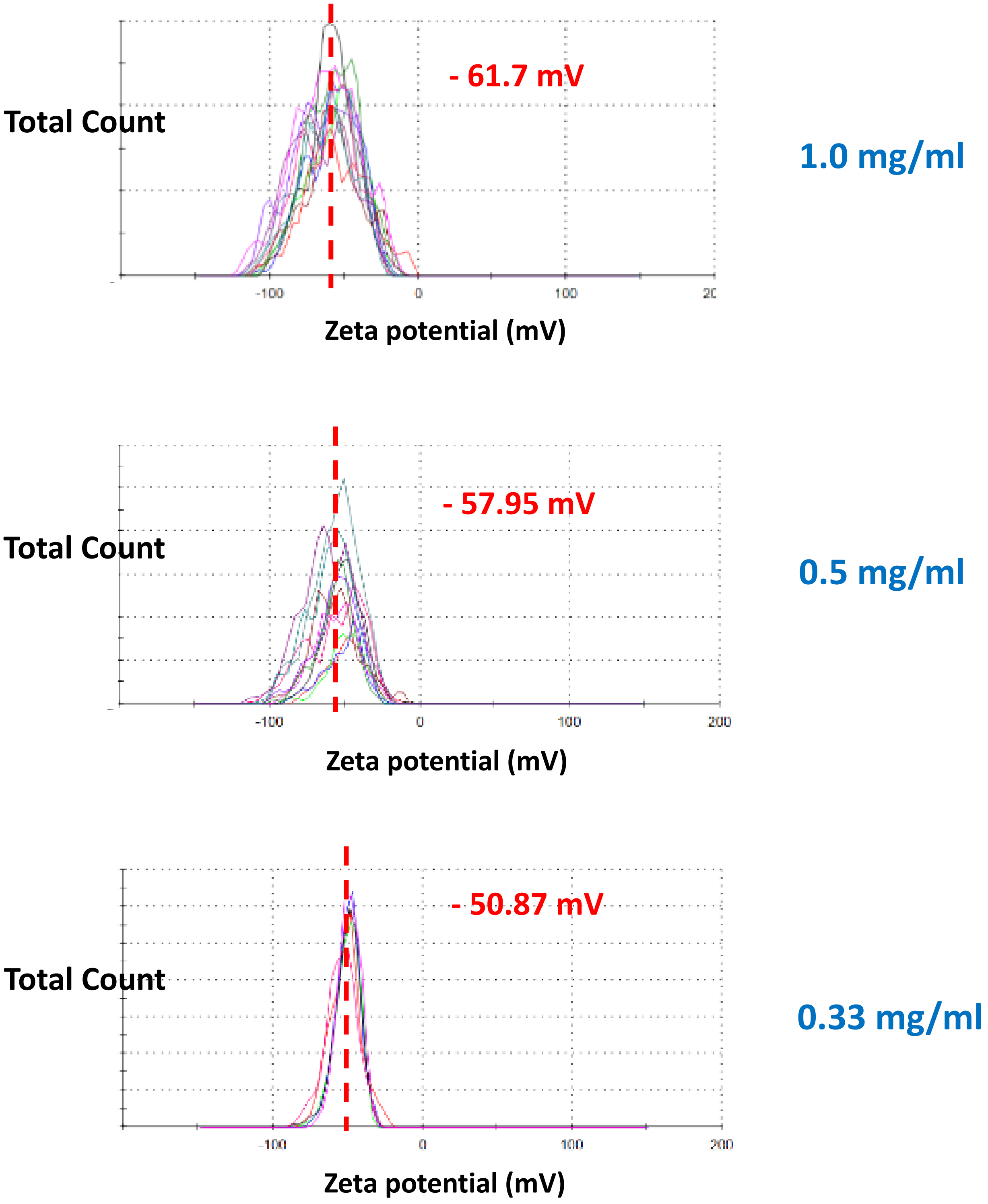

Figure 4.1-9 Zeta potentials of GO aqueous suspensions of varying concentrations.

## 4.2 Electrophoretic deposition of GO coatings

As already introduced in Chapter 2 the literature review, electrophoretic deposition (EPD) is a versatile and promising method for nano-particle coatings in terms of the easy procedure, simple equipment, controllable deposition kinetics and coating thickness, etc. EPD was hence employed in the first place in this research to produce GO coatings on stainless steel surface with a deposition area of about 4 cm$^2$ and a 1 mg/ml GO aqueous suspension.

### 4.2.1 Deposition kinetics and coating morphology

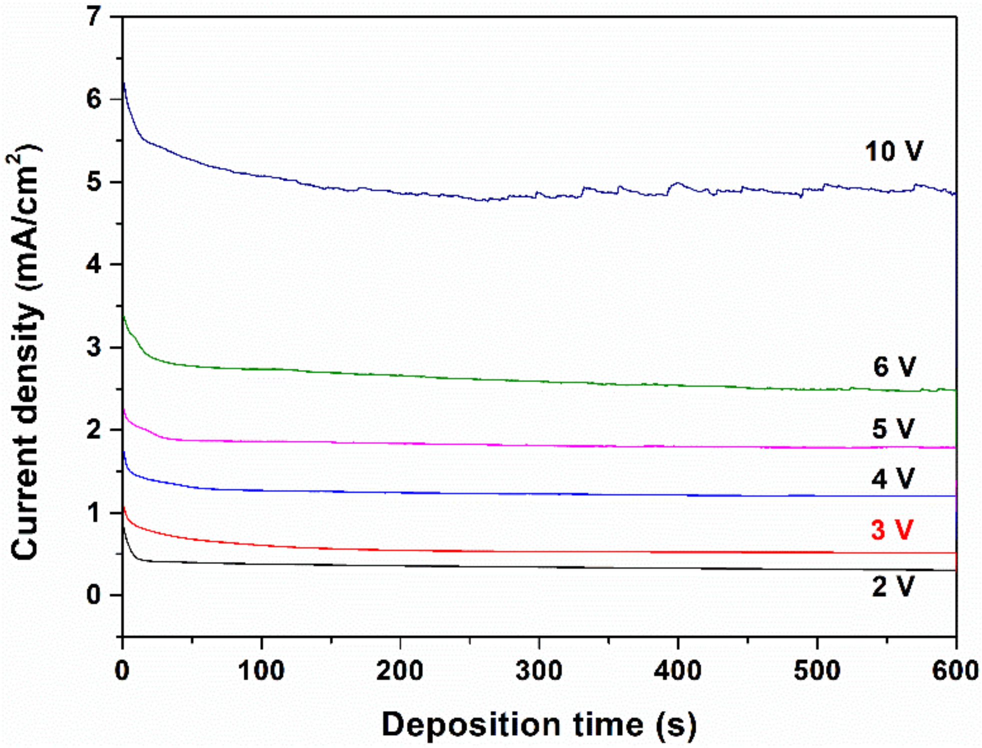

Figure 4.2-1 Electric current density as function of deposition time during EPD using voltages of 2-10 V. GO concentration 1 mg/ml in suspension for all runs.

In order to investigate the kinetics of the deposition process, tests were performed at varying voltages 2-10 V in the same deposition cell and the current density over deposition time was monitored and recorded in Figure 4.2-1. Overall, the deposition current density decreased quickly in the first tens of seconds due to the fact that GO is less conductive than the steel substrate. Afterwards the current levelled off, indicating steady growth of the GO coating on the steel surface. At a deposition voltage of 10 V, the electric current exhibited fierce fluctuations. Simultaneously, many bubbles were observed at both the anode and the cathode due to the electrolysis of water.

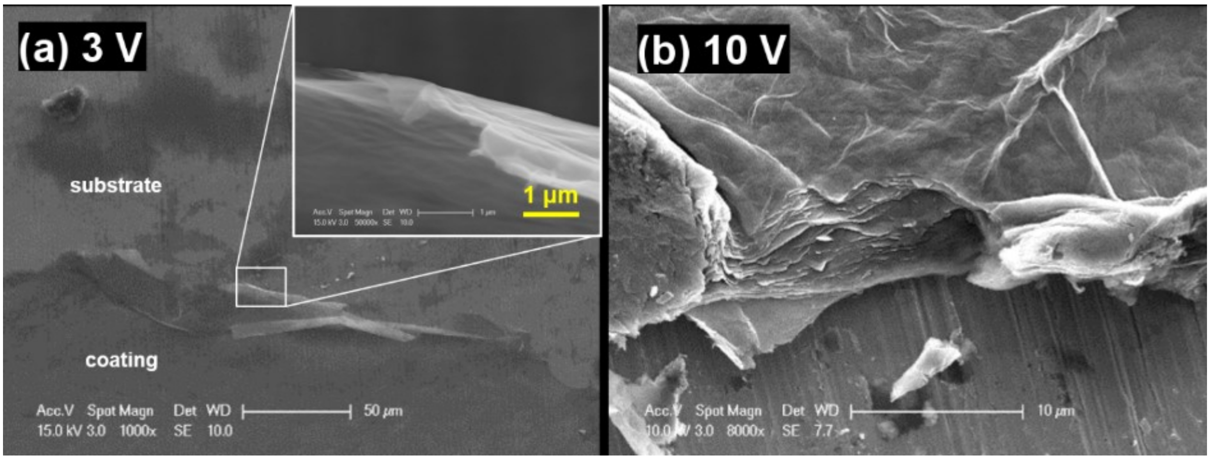

Figure 4.2-2 GO coatings deposited at (a) 3 V for 4 min and (b) 10 V for 4 min.

As the applied voltage was reduced, the current fluctuation was inhibited and the curve became smooth. At deposition voltages above 6 V, gas was formed at the electrodes in a considerable amount. For EPD at 2-4 V, however, bubble evolution was mitigated substantially, which is indicative of a stable deposition. Figure 4.2-2 compares the coatings obtained at 3 V and 10 V for the same deposition time of 4 min. It is clear that 10 V led to a much thicker (~7 μm) but relatively loose deposit, most likely due to the unstable current distribution and bubble evolution. The coating deposited at 3 V was uniform and smooth, conforming to the substrate topography well.

The voltage was then fixed at 3 V and the deposition time was modulated in order to obtain coatings with different thicknesses. Figure 4.2-3 plots of the coating thickness as a function of the deposition time. It can be found that the thickness of the resultant GO coating increased proportionally with the deposition time. For instance, EPD for 15 seconds resulted a coating thickness of around 30 nm, which increased to around 63 nm after 60-second deposition, and nearly 200 nm after deposition for 4 min. The EPD process showed the potential for preparing a GO coating of more than half a micron (430 nm for 10 min in Figure 4.2-3).

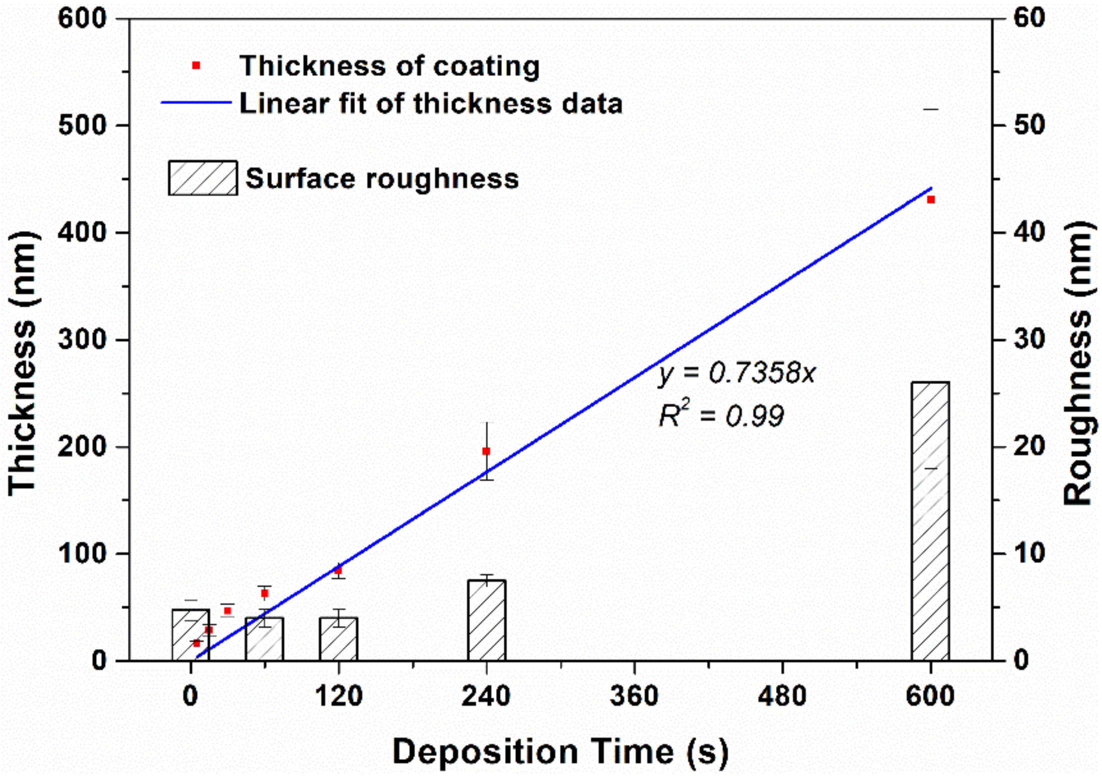

Figure 4.2-3 The thickness and surface roughness of GO coatings by EPD as function of deposition time with a fixed operation voltage of 3 V.

However, surface irregularities were formed and the coating became inhomogeneous for a deposition time longer than 10 min, as also reflected by the large deviation of the coating thickness value at 10 min. Assuming that the coating density is constant across the thickness, the experimental data (red points) showed good agreement with the prediction (blue line) by Hamaker's law [134] through the following equation:

$$W(t) = \int_{t_1}^{t_2} f \cdot \mu \cdot E \cdot A \cdot C dt \tag{4.2-1}$$

where $W$ is the weight gain during deposition, $f$ is the efficiency factor of the EPD process, $\mu$ is the electrophoretic mobility of the particles which is proportional to the zeta-potential of those particles, $E$ is the electrical field strength, $A$ is the electrode surface area, $C$ is the particle concentration in the suspension, and $t$ is the deposition time.

The roughness of the coated steel surface (Figure 4.2-3) was initially comparable to that (~4 nm) of the polished bare steel within a deposition time of 2 min, indicating compact deposition of the 2D GO sheets. After EPD for 4 min the coating roughness doubled. After deposition for 10 min the roughness built up to ~25 nm.

Figure 4.2-4 shows the evolution of the surface morphology of GO coatings fabricated on steel surface by EPD at 3 V with the deposition time. For a short deposition time up to 60 s, the coating was so thin that the polishing tracks left on the substrate were seen through. The coating followed the contour of the substrate well with a small number of wrinkles as marked in Figure 4.2-4a. Figure 4.2-4b shows a scratched GO coating, from which it is clear that the coating was uniform in thickness. For a deposition time longer than 120 s, as mentioned above, the number of such irregularities as wrinkles and agglomerations increased.

Raman and XPS spectra of the GO coating by EPD were shown in Figure 4.2-5. As annotated in Figure 4.2-5a, the EPD-GO coating exhibited an $I_D/I_G$ ratio of 0.84, which is larger than that (0.73) of the as-synthesised GO. XPS survey spectra (Figure 4.2-5b) indicated a dramatically reduced C/O ratio (12:1, atomic percentage) compared to that (C/O=5:3) of as-synthesised GO. The detailed XPS C1s spectra (Figure 4.2-5 c-d) revealed a strong suppression to the –COOH and –C=O peaks, suggesting a significantly reduced oxygen content in the GO coating (thus forming rGO) due to the reduction effect of EPD process.

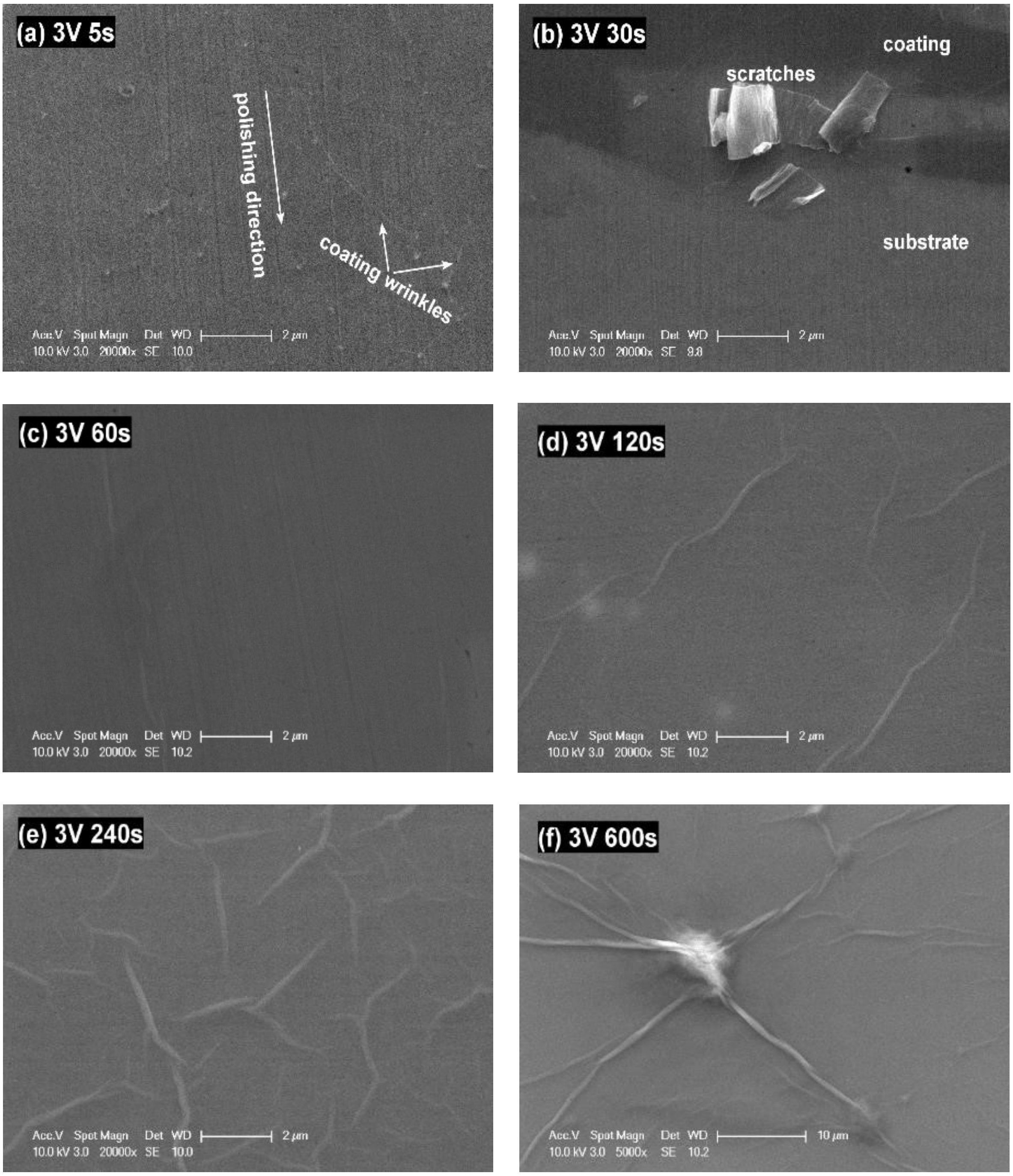

Figure 4.2-4 Morphology of GO coatings by EPD at 3 V after varying deposition time of 5-600 seconds.

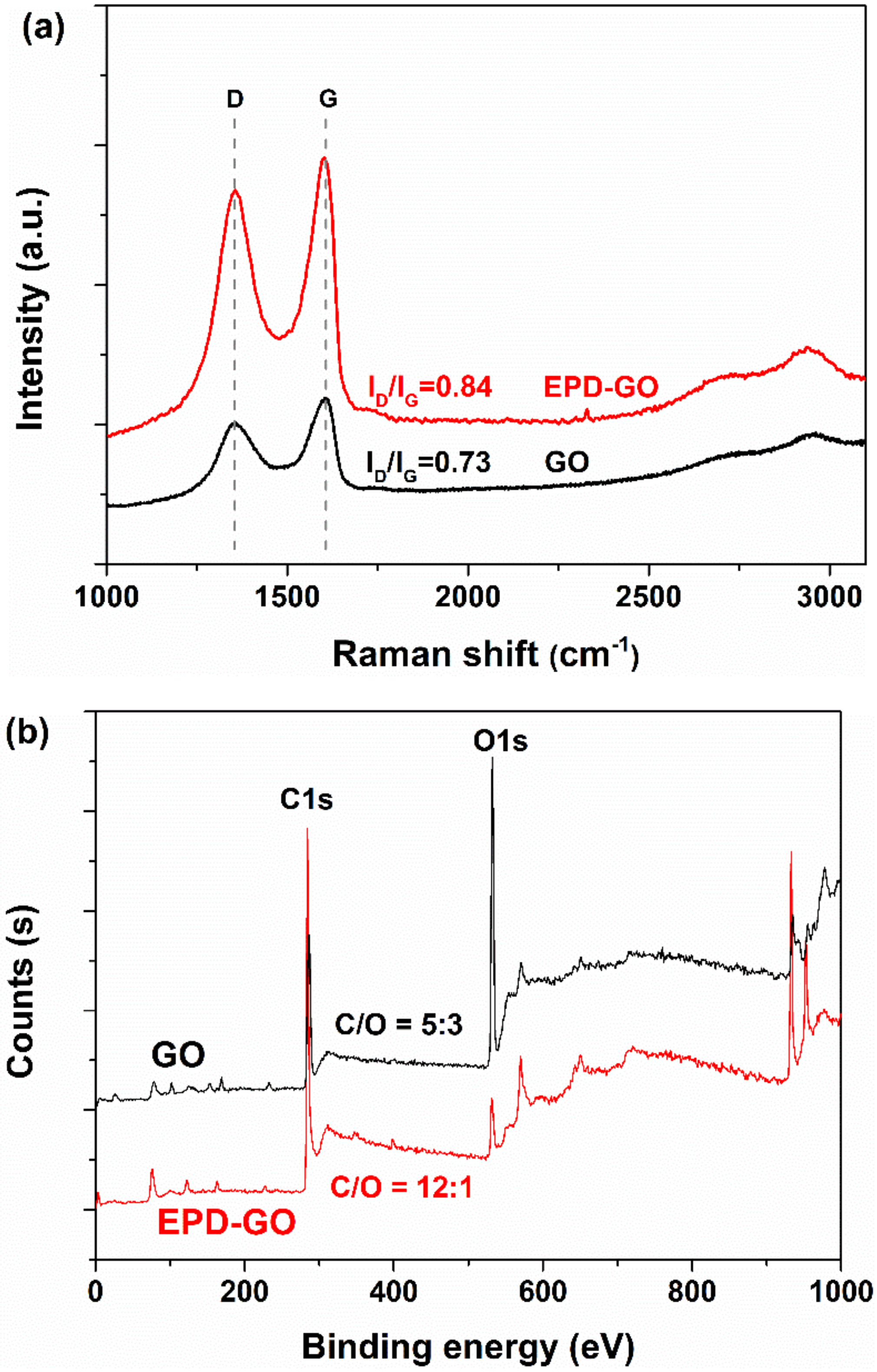

Figure 4.2-5 Raman (a) and XPS survey (b) spectra of as-prepared GO and EPD-GO coating.

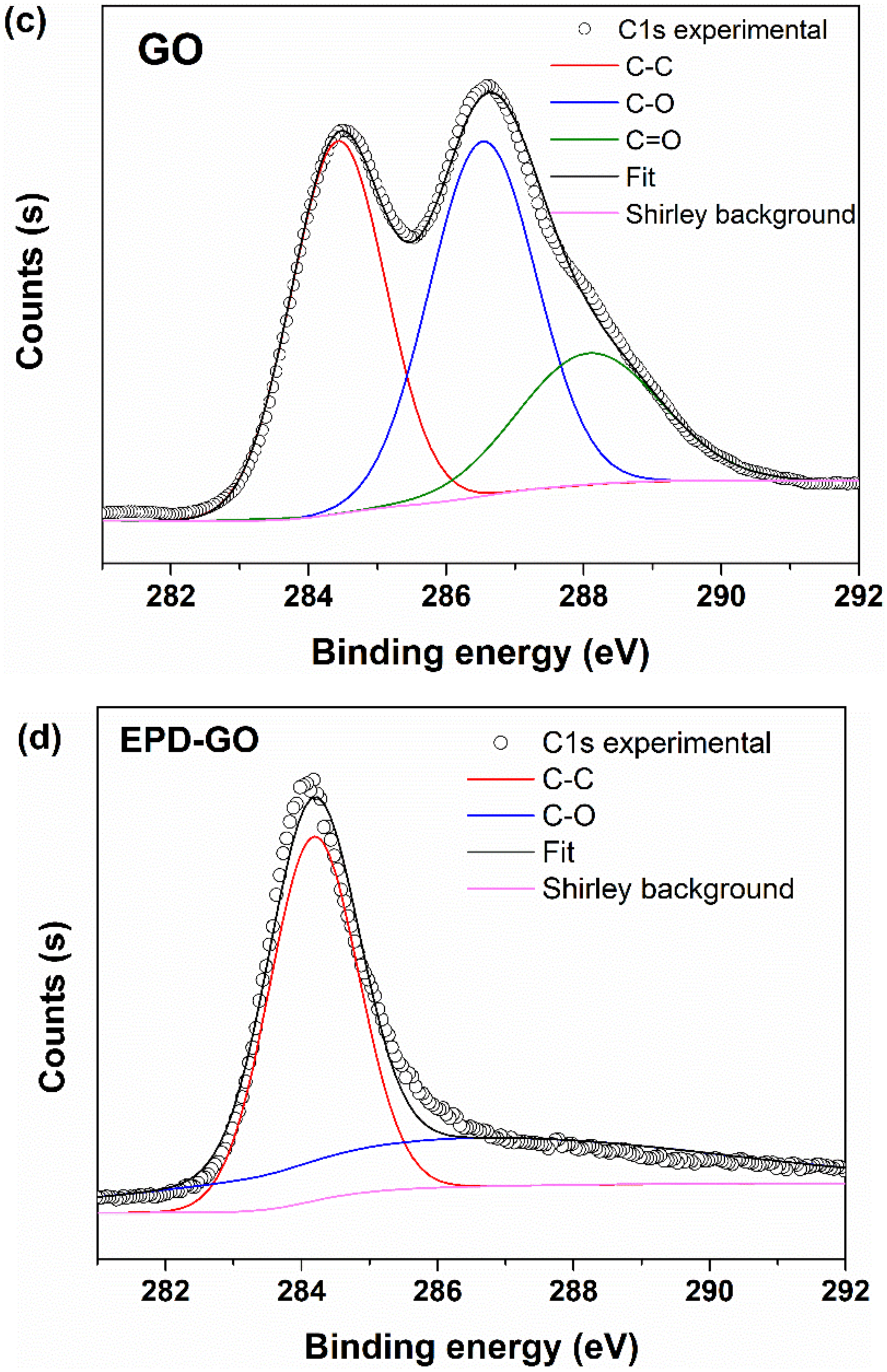

Figure 4.2-5(continued) XPS C1s spectra of as-prepared GO (c) and EPD-GO coating (d).

### 4.2.2 Tribological behaviour

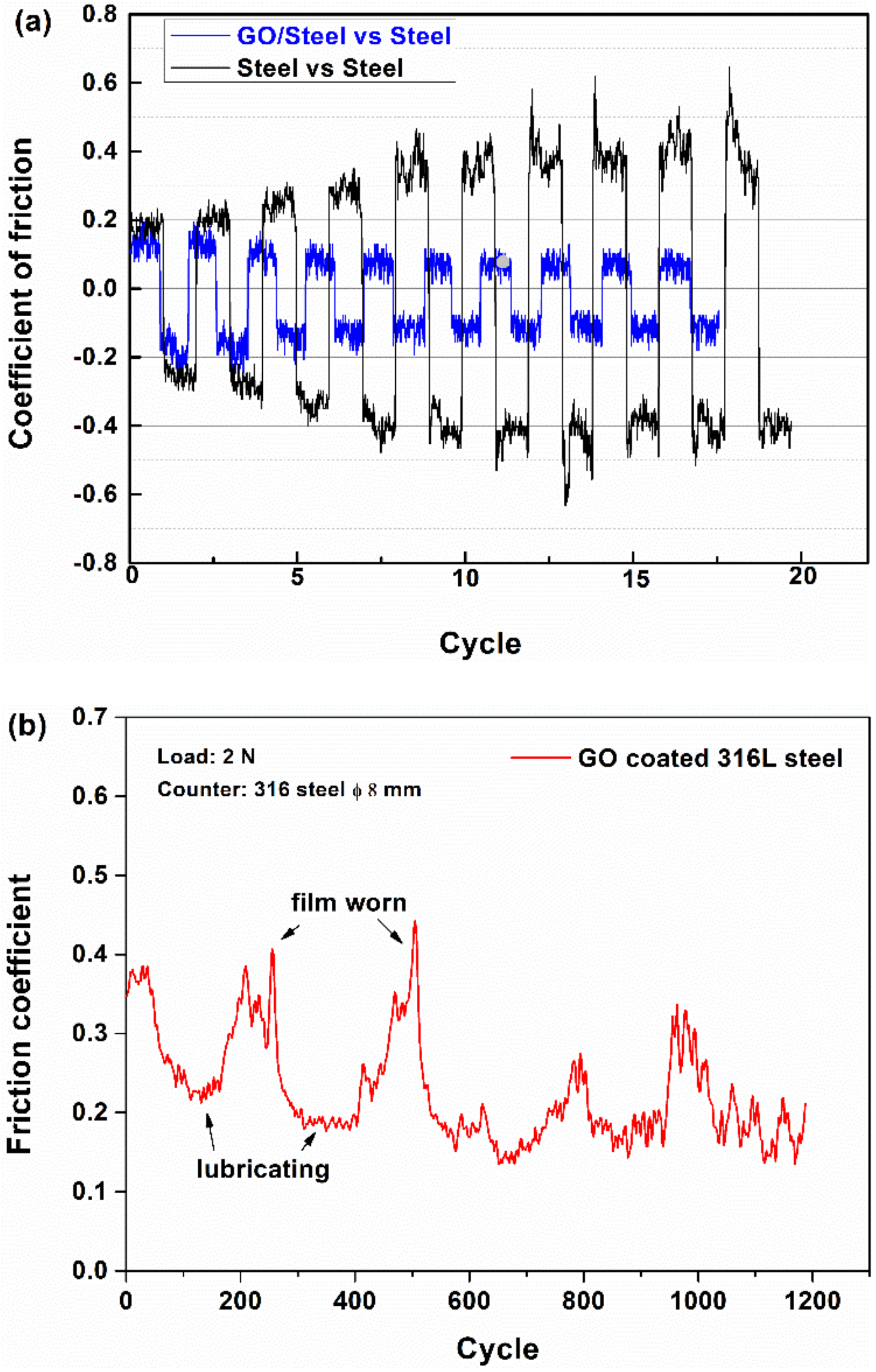

Figure 4.2-6 Coefficient of friction during low cycle (a) and high cycle (b) frictional tests for GO coating on a ground 316L stainless steel surface.

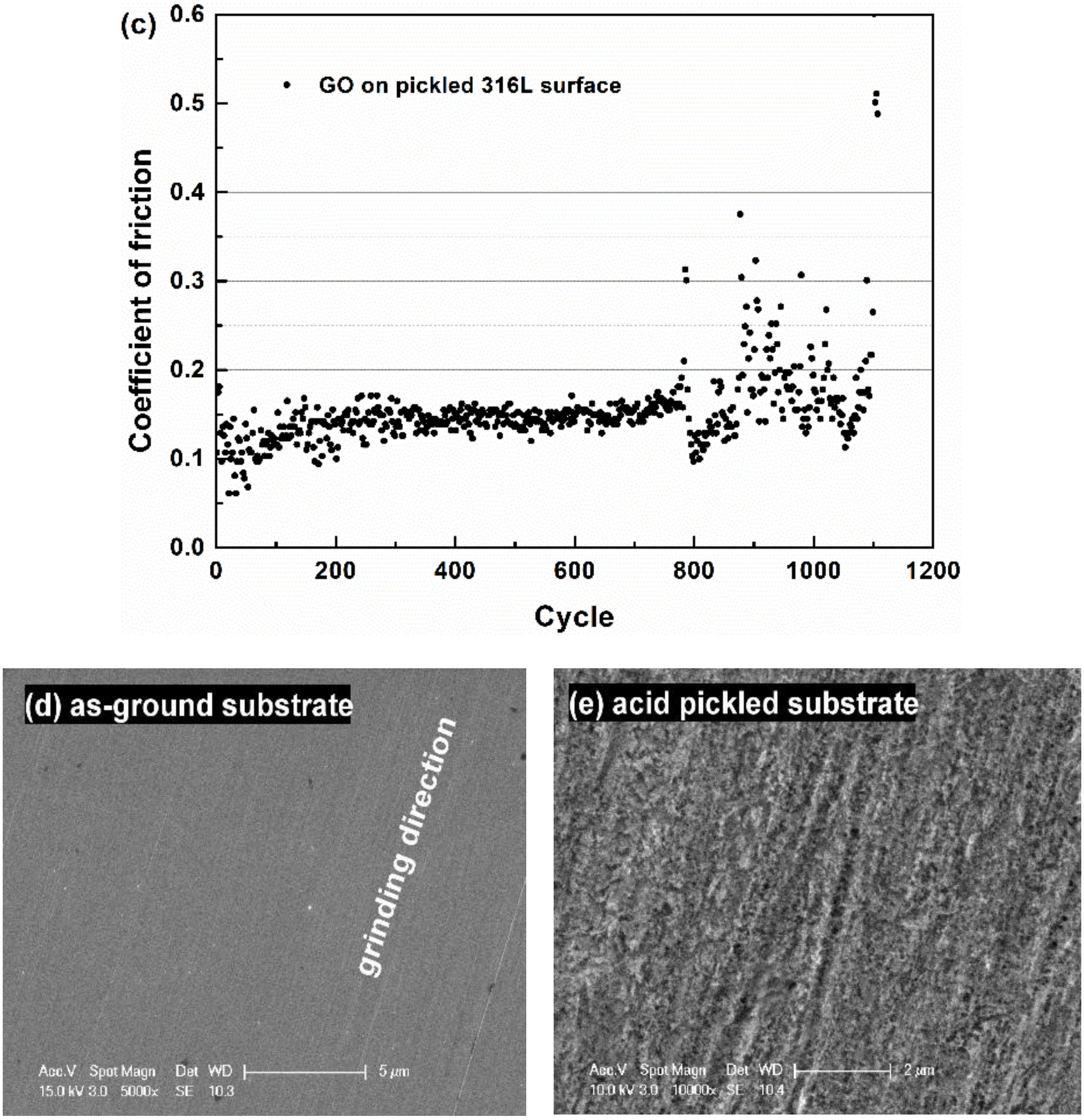

Figure 4.2-6(continued) Coefficient of friction for GO coating on an acid-treated steel substrate (c) and micrographs of as-ground (d) and acid-pickled (e) substrates.

The frictional behaviour of the GO coating fabricated on 316L stainless steel by EPD (3 V, 2 min as described above) was investigated on a reciprocating ball-on-plate tribometer. A 316 stainless steel ball with a diameter of 8 mm (ϕ8) was used as the counter material, sliding against the sample surface with a speed of 5 mm/s and frequency of 1 Hz, under a normal load of 2 N (initial Herts contact stress ~650 MPa).

Figure 4.2-6a shows the coefficient of friction (COF) of the GO-coated steel and bare 316L steel reciprocating against a 316 ball during the first 20 cycles. The bare 316L stainless steel surface exhibited a COF of 0.4 after the running-in period, while the GO-coated stainless steel surface showed a steady-state COF of ~0.1, indicating the great lubricity of the GO coating. However, as the test continued the COF curve showed an ‘unexpected’ sudden increase to ~0.4 (equal to bare steel COF), implying the damage to the GO coating by the slider (Figure 4.2-6b). The COF peak was then smoothed down, probably due to partially recovery of the lubricating coating by the slider when it reciprocated and brought some coating fragments back to the sliding contact. The failure-recovery cycle re-occurred periodically during the reciprocating sliding, indicating an unstable lubricating effect.

It is believed that the weak bonding between the GO coating and the metallic surface was responsible for the early failure of the lubricating coating. To this end, the same stainless steel but slightly etched by a diluted acid solution (10 wt% $H_2SO_4$) was used as the substrate for the GO coating. As a result, the coating showed a prolonged life of about 800 cycles (Figure 4.2-6c). SEM observation showed that the acid-pickled steel surface was characterised by small yet dense cavities (Figure 4.2-6 d-e). The results above came along with an idea that specific surface topography may be able to promote the bonding and retention of the GO coating to the substrate, thus contributing to the improved anti-friction life of the coating.

To this end, stainless steel substrates with artificial dimples, produced by a nano-second laser based in the School of Mechanical Engineering, University of Birmingham, were coated with EPD-GO coatings and tested. Figures 4.2-7 demonstrates the morphology of three patterned 316L surfaces with the dimple diameter of 30 μm, 50 µm and 70 µm, respectively. The dimple/surface ratio was fixed at 15% for all the three patterns. Figure 4.2-7c shows the details of a dimple. The laser parameters were tuned carefully so that the influence on the original surface flatness was minimised.

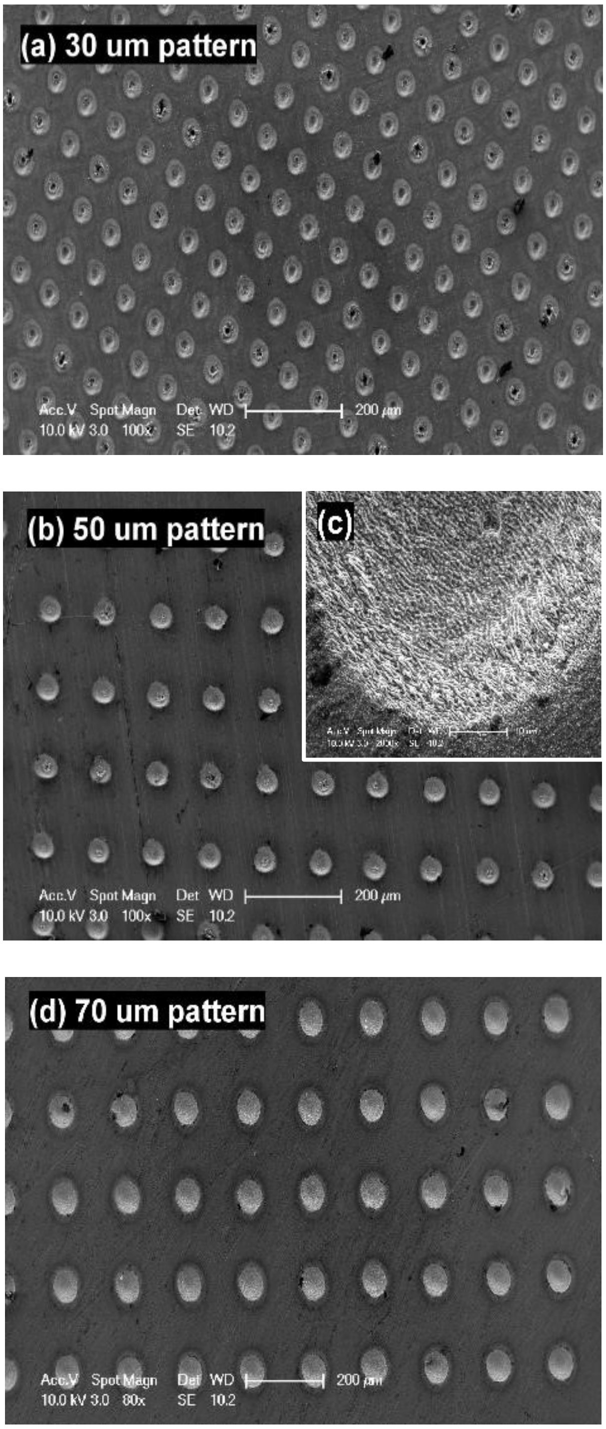

Figure 4.2-7 Surface patterns produced on 316L stainless steel by laser with dimple diameters of (a) 30 µm, (b-c) 50 µm and (d) 70 µm.

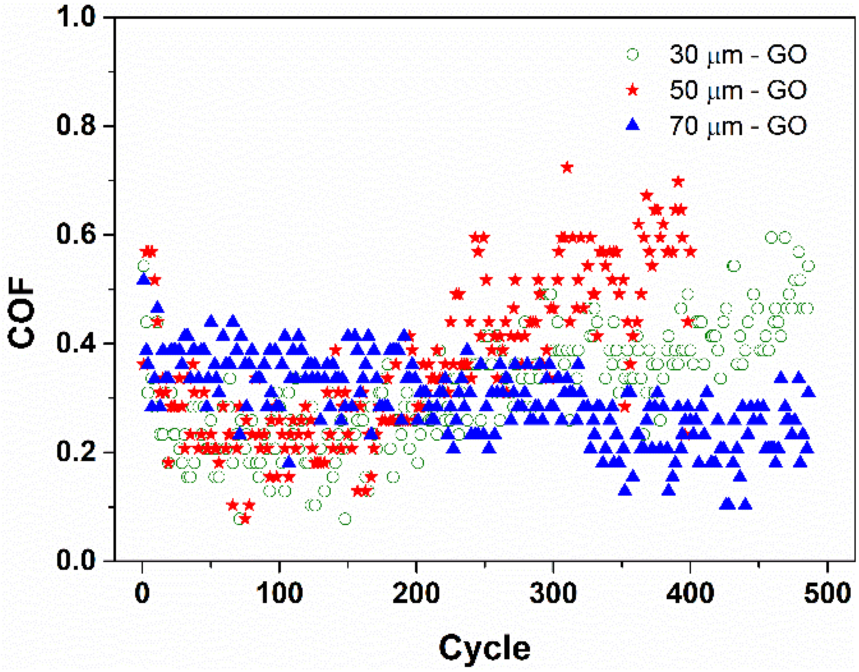

Figure 4.2-8 Coefficient of friction of GO coatings on laser patterned steel surfaces with different dimple sizes.

Figure 4.2-8 shows the COF of the three patterned and GO-coated samples. No sudden increase of the COF occurred. Overall the sample with 70 µm dimples exhibited the best retention of the GO coating, although its starting COF was higher than the other two samples. However, from the results it is clear that when coated with the same EPD-GO the steady-state COF (~0.2) of the patterned samples were higher than that (0.15) of un-patterned samples as shown in Figure 4.2-6. This is probably due to the additional resistance (hence friction) caused by the re-cast material particles along the rim of the dimples induced by laser patterning.

### 4.2.3 Corrosion behaviour

The corrosion performance of GO-coated 316L stainless steel was evaluated by means of potentiodynamic polarisation and electrochemical impedance spectroscopy (EIS) in a 3.5 wt% NaCl solution. Figure 4.2-9a shows the open circuit potential (OCP) curves of the bare steel and GO-coated steel. After left stabilising for 1 h, the bare steel samples exhibited OCPs of around -140 mV (vs. SCE), while the GO-coated steels exhibited significantly uplifted OCPs of around +290 mV. Figure 4.2-9b shows the polarisation curves.

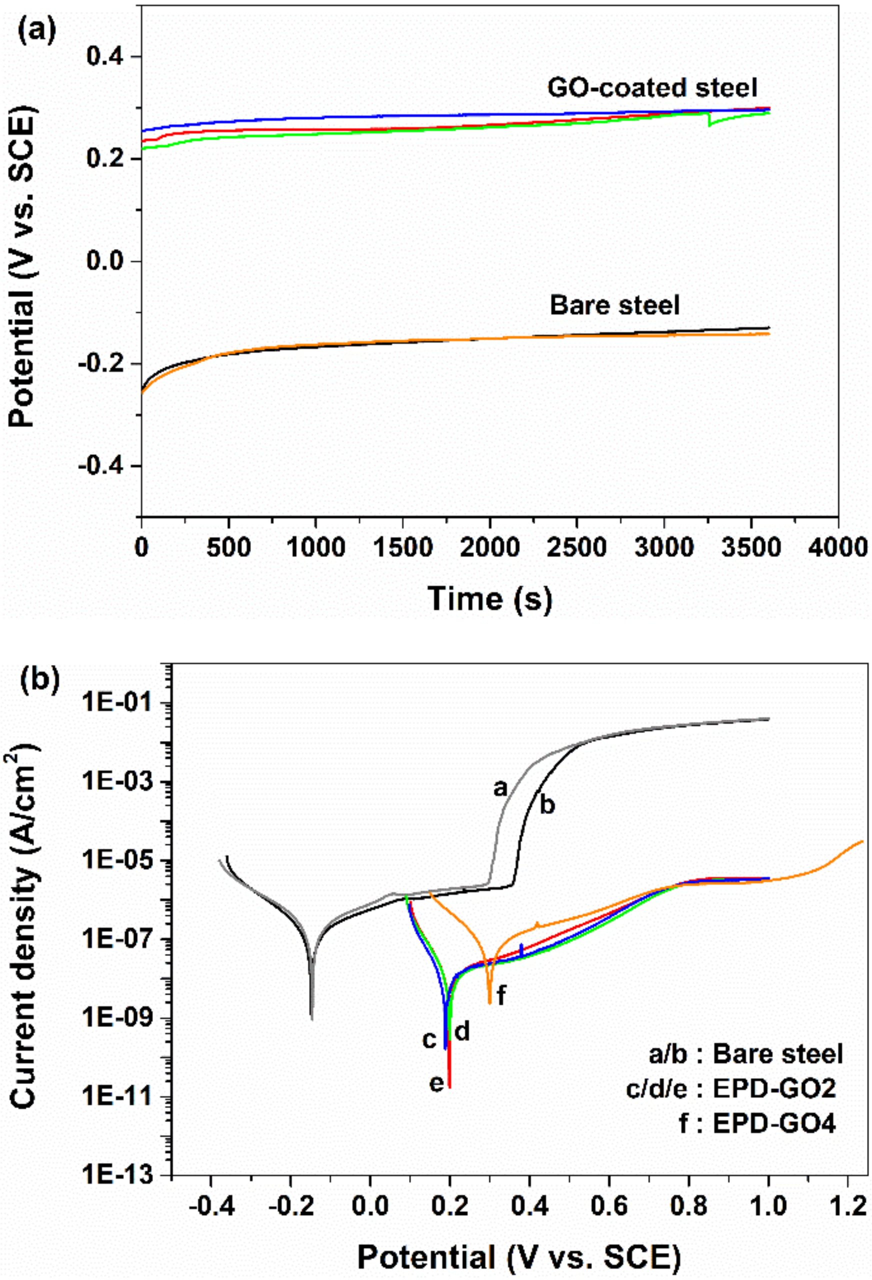

Figure 4.2-9 (a) Open circuit potential (OCP) and (b) polarisation curves of bare steel and GO coated steels. The ‘2’ and ‘4’ in the legend of (b) indicate a deposition time of 2 min and 4 min, respectively.

Table 4.2-1 Tafel fit parameters for polarisation curves of bare steel and EPD-GO steels

| Sample | $E_{corr}$ (mV) | $I_{corr}$ ($\times 10^{-9}$ A/cm$^2$) |
|---|---|---|
| Bare steel (a) | -149 | 251 |
| Bare steel (b) | -146 | 368 |
| EPD-GO2 (c) | +198 | 10.4 |
| EPD-GO2 (d) | +199 | 10.2 |
| EPD-GO2 (e) | +188 | 9.45 |
| EPD-GO4 (f) | +299 | 117 |

Tafel fitting to each curve was performed and the results are summarised in Table 4.2-1. A clear knee point around 400 mV was present on the anodic polarisation curve of the bare steel, due to pitting of the stainless steel. The steel with EPD-GO2 (produced by EPD at 3 V for 2 min) exhibited a positive corrosion potential ($E_{corr}$) of around +200 mV. The $E_{corr}$ was positively shifted remarkably by 350 mV compared to the bare steel (-150 mV vs. SCE), indicating a much less tendency to corrosion in presence of the GO coating. Meanwhile, the corrosion current density ($I_{corr}$) of EPD-GO2 was about $10\times10^{-9}$ A/cm$^2$, which is 30 times smaller than that (~$300\times10^{-9}$ A/cm$^2$) of the bare steel. More importantly, no pitting occurred on the GO-coated stainless steel, implying the excellent corrosion barrier effect of GO. As shown in Figure 4.2-9b, EPD-GO4 (produced by EPD at 3 V for 4 min) exhibited even more positive $E_{corr}$ (+299 mV vs. SCE). This improvement could be attributed to the increased thickness of EPD-GO4 compared to EPD-GO2, thus promoting the physical barrier effect. However, it is worth noting that the corrosion current of EPD-GO4 ($117\times10^{-9}$ A/cm$^2$) is clearly higher than that of EPD-GO2 when tested below 0.8 V (vs. SCE). It may be related to the increased coating surface roughness and inhomogeneity for a longer deposition time

(Figures 4.2-3 & 4.2-4).

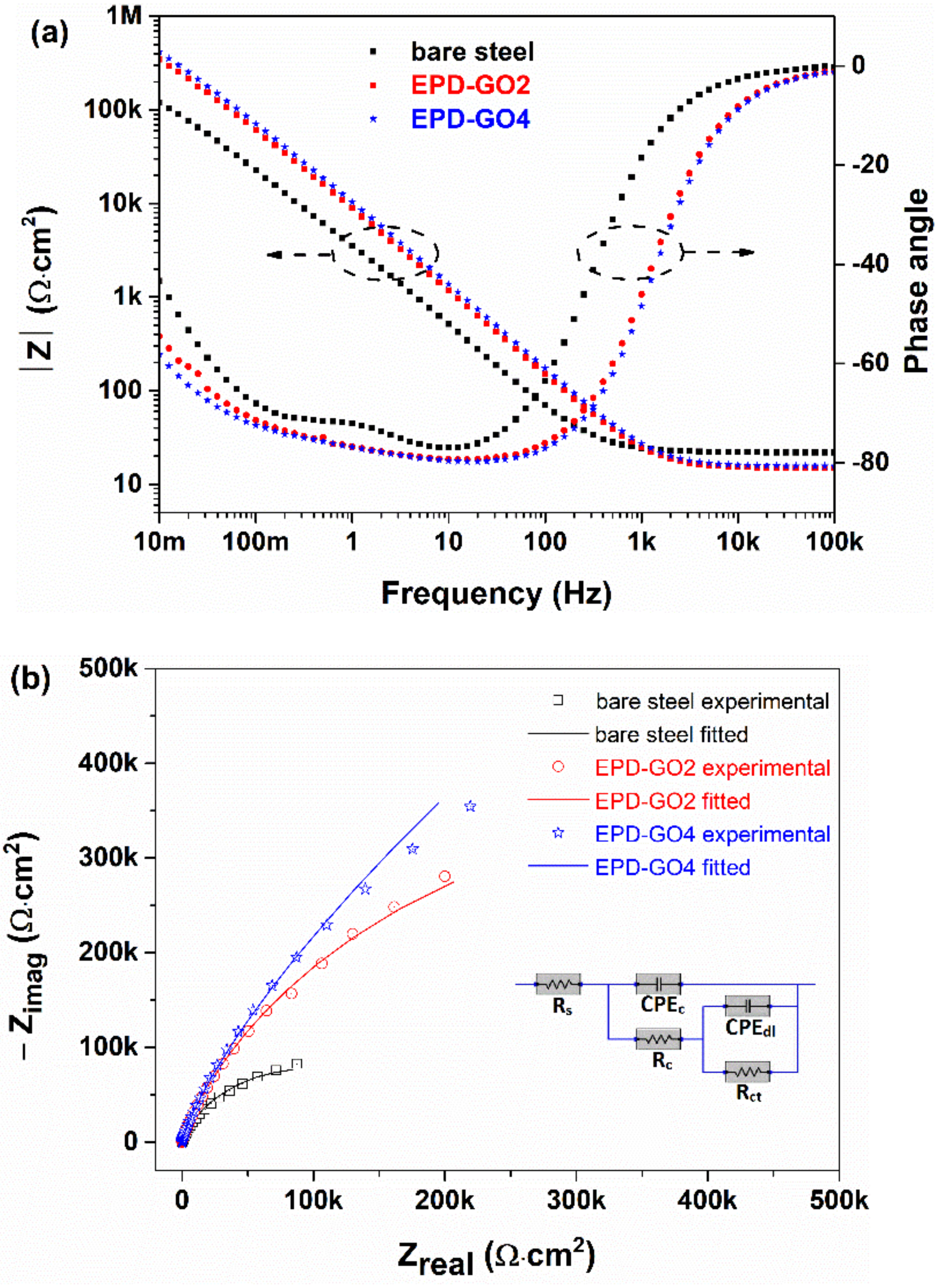

Figure 4.2-10 EIS Bode (a) and Nyquist (b) plots of bare steel and GO coated steels in 3.5wt% NaCl solution. The inserted plot in (b) is the equivalent circuit model for the coating system.

Electrochemical impedance spectroscopy (EIS) measurements were also performed in order to elucidate the corrosion protection mechanism for the GO coating. A small sinusoidal electrical signal (±10 mV, 10m – 100k Hz) about the open circuit potential was applied to the sample whose electrochemical response to the excitation at different frequencies was recorded and analysed. Figure 4.2-10a is the Bode plots where the absolute values of the impedance (|Z|) and phase angles are plotted as a function of excitation frequency. At the lowest frequencies, the impedance moduli |Z| of EPD-GO2 and EPD-GO4 were both half an order of magnitude higher than that of the bare steel, indicating higher corrosion resistance. Figure 4.2-10b shows the corresponding Nyquist plots where the impedance at each frequency is plotted according to its real (resistive) and imaginary (capacitive) components. The data points close the origin were recorded at the highest frequencies, while the points at the far end were recorded at the lowest frequencies. Basically, a larger impedance semi-circle usually means a higher corrosion resistance. In the Nyquist plots, the two GO-coated samples exhibited much larger impedance arcs, indicating significantly improved corrosion resistance. EPD-GO4 was found to possess higher impedance than EPD-GO2, due to its increased thickness. Due to the limited measurement frequency range, the full semicircles were not observed.

Curve fitting to the EIS data points was conducted using an equivalent circuit model as illustrated in Figure 4.2-10b. The model is widely adapted by corrosion scientists in simulating coatings with internal defects and/or under developing corrosion attack. $R_s$ is the resistance of the electrolyte solution, $R_c$ is the coating resistance, and $CPE_c$ is the capacitance of the coating. *CPE* is short for constant phase element, which is a circuit element with a constant phase shift over the frequency, and was employed in this work to model an imperfect capacitor, whose impedance is expressed as:

$$Z_{CPE}(\omega) = \frac{1}{CPE\cdot(j\omega)^n} \tag{4.2-2}$$

where n is the phase shift index (n=1 for an ideal capacitor). An extra pair of double layer capacitance ($CPE_{dl}$) and interfacial charge transfer resistance ($R_{ct}$) were introduced in order to simulate the situation where the electrolyte penetrates into the coating and forms a new electric double layer at the liquid/metal interface. The fitting lines are shown in Figure 4.2-10 and the fitting parameters are summarised in Table 4.2-2. Compared with the bare steel, EPD-GO2 and EPD-GO4 behaved less capacitive but more resistive. The overall polarisation resistance ($R_c$ + $R_{ct}$) for the two GO-coated samples were 977 kΩ·cm$^2$ and 1895 kΩ·cm$^2$, which are 5 and 9 times higher than that (199 kΩ·cm$^2$) of the bare steel, respectively.

Table 4.2-2 Equivalent circuit fit parameters for the EIS samples

| Sample | $R_s$ (Ω·cm$^2$) | $R_c$ (kΩ·cm$^2$) | $CPE_c$ (μS·s$^n$·cm$^{-2}$) | $n_1$ | $R_{ct}$ (kΩ·cm$^2$) | $CPE_{dl}$ (μS·s$^n$·cm$^{-2}$) | $n_2$ |
|---|---|---|---|---|---|---|---|
| Bare steel | 21.87 | 9.96 | 44.8 | 0.910 | 189 | 23.5 | 0.767 |
| EPD-GO2 | 14.78 | 34.9 | 19.4 | 0.909 | 942 | 6.09 | 0.651 |
| EPD-GO4 | 15.55 | 14.5 | 15.6 | 0.920 | 1880 | 5.76 | 0.621 |

Figure 4.2-11 shows the corrosion morphology of the samples after the polarisation tests. Catastrophic corrosion was found on the bare steel, with pitting holes of nearly 500 μm in diameter. In sharp contrast, the GO-coated steel showed no appreciable change after polarisation. Higher magnification image (Figure 4.2-11d) confirmed the presence of the GO coating after corrosion.

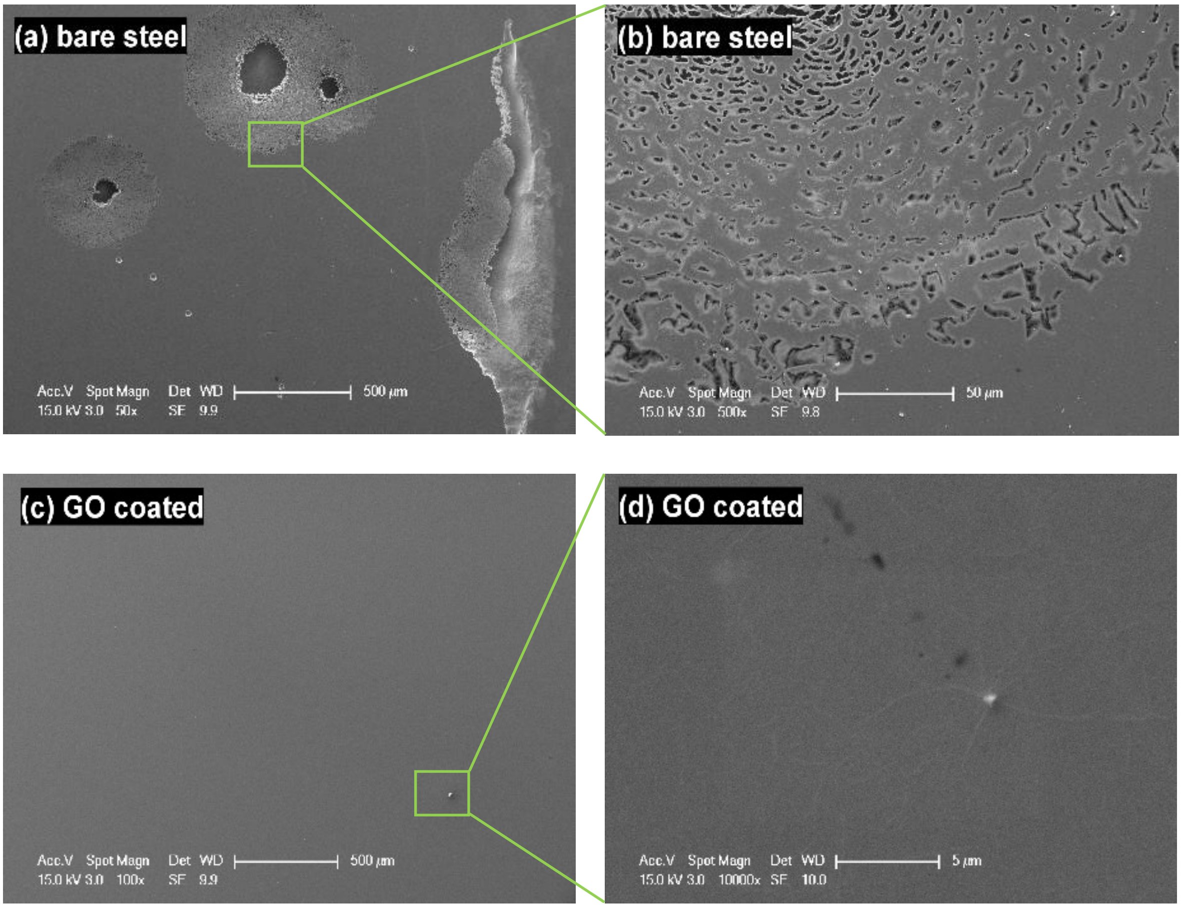

Figure 4.2-11 Morphology of (a-b) uncoated 316L stainless steel and (c-d) GO-coated 316L stainless steel after polarisation corrosion in 3.5wt% NaCl solution.

## 4.3 Self-assembly of GO thin films

Graphene can show extraordinary lubricity even superior to bulk graphite and is probably the thinnest solid lubricant ever. However, in the literature there are just a limited number of reports on graphene-based surface coatings for combating friction and wear at a macro scale. This is partially due to the difficulty in obtaining such coatings continuously on a large area, but as already demonstrated in Section 4.2, it is more likely due to the weak adhesion of graphene-based coatings to most engineering materials surfaces.

(3-Aminopropyl)triethoxysilane (APTES) is a coupling agent widely used in the surface modification of inorganic and polymeric materials. In this section, the tribological behaviour and durability of the graphene oxide (GO) coatings fabricated on APTES modified stainless steel surfaces by self-assembly as instructed in Chapter 3 are reported and the effect of APTES treatment is discussed.

### 4.3.1 Coating morphology and structure

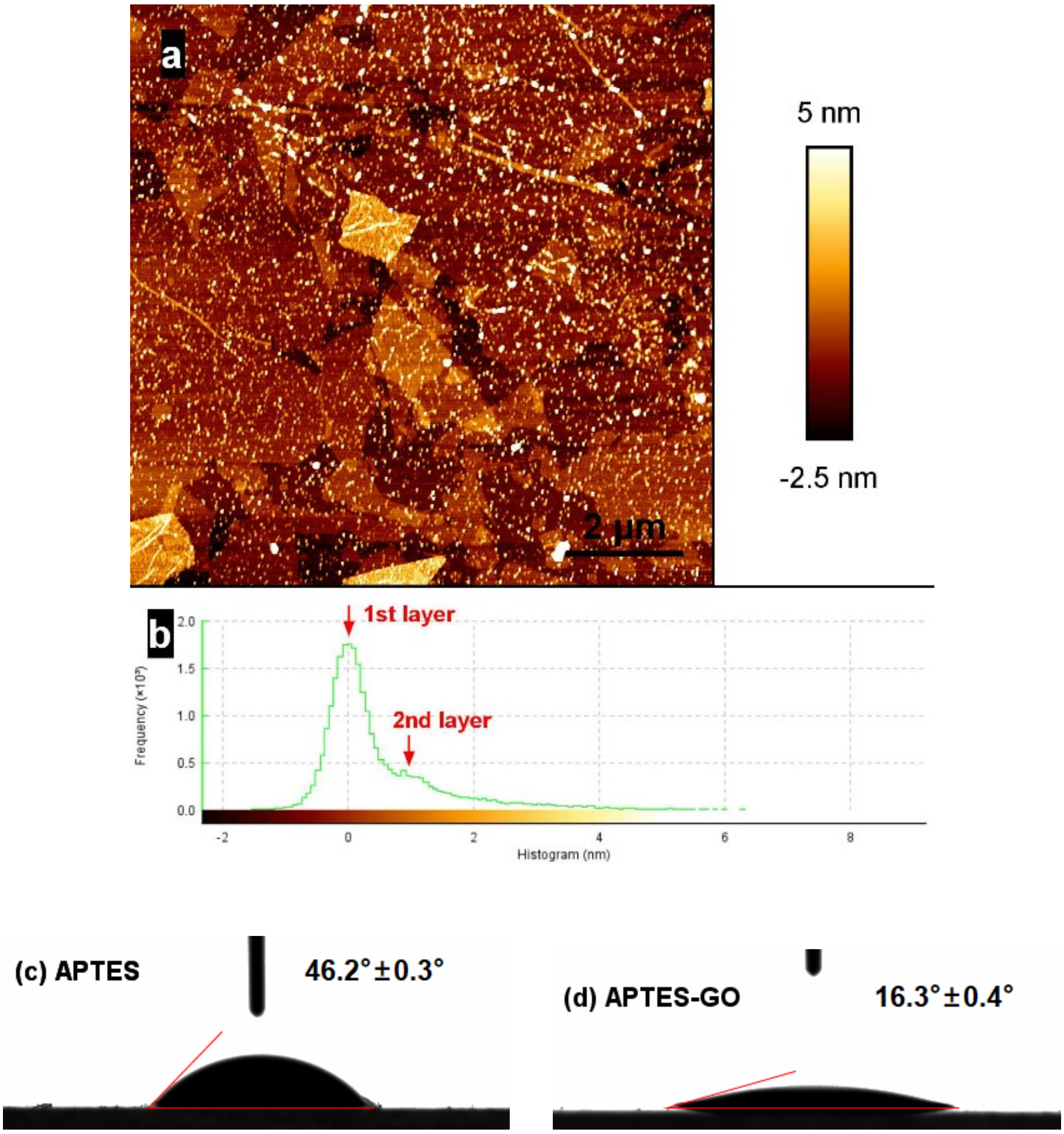

Figure 4.3-1 (a) AFM image of the self-assembled APTES-GO coating and (b) histogram of the thickness across the area. (c-d) snapshots of the water contact angle tests on APTES and APTES-GO, respectively.

The GO coating self-assembled on an APTES-treated steel substrate (316L-A) was named as 316L-A-GO. For comparison, a dummy self-assembly was performed on an untreated stainless steel (i.e. 316L-GO). Figure 4.3-1a is an AFM image of the obtained APTES-GO coating (i.e. 316L-A-GO). It features a GO coverage rate of more than 90% with a small number of gaps between some GO sheets. The similar contrast across the surface is indicative of relatively uniform coating thickness. The widespread white dots are likely short-range agglomerations of APTES molecules, which is consistent with the observations by other researchers on self-assembled monolayer (SAM) [249, 250].

Figure 4.3-1b is the height histogram across the AFM examined area. The substrate level is assigned as -2.5 nm with the majority of the surface heights falling at 0 nm, indicating that the APTES-GO coating has an average thickness of 2-2.5 nm. Considering that the thickness of an APTES layer usually measures 1-1.5 nm [250], the GO top coat here likely has a thickness of ~1 nm, which corresponds to one single layer GO. Likewise, the shoulder peak around 1 nm in the histogram represents the second GO layer stacking on the top, in a small fraction though. Compared to the water contact angle (WCA) of ~46° for the APTES layer (Figure 4.3-1c), the WCA decreased to ~16° with an additional self-assembled GO layer (Figure 4.3-1d), due to the hydrophilic oxygen groups in GO.

### 4.3.2 Tribological behaviour

Reciprocating sliding friction and wear tests were conducted under a load of 1 N (equivalent Hertz contact pressure ~530 MPa, contact area diameter 60 μm). Four types of samples, namely bare 316L, 316L-A (APTES-treated 316L), 316L-A-GO (GO coated 316L-A) and 316L-GO (GO coated 316L), were tested. The coefficient of friction

(COF) for each sample over the sliding cycles is shown in Figure 4.3-2. The COF for 316L-A fluctuated wildly in the running-in period and levelled off at 0.35 after 500 cycles, which is slightly below that (~0.45) of bare 316L. It is clear that the APTES layer alone offered little lubricating effect. 316L-GO initially benefited from graphene's lubricity as evidenced by the very low initial COF of 0.12 for the first 100 cycles. However, the COF then rose suddenly (as demonstrated in the enlarged view inserted in Figure 4.3-2) and eventually increased all the way up to 0.4, which is very close to that of bare 316L stainless steel, implying that the GO coating might have been removed completely away from the sliding contact, and it was actually steel vs. steel afterwards.

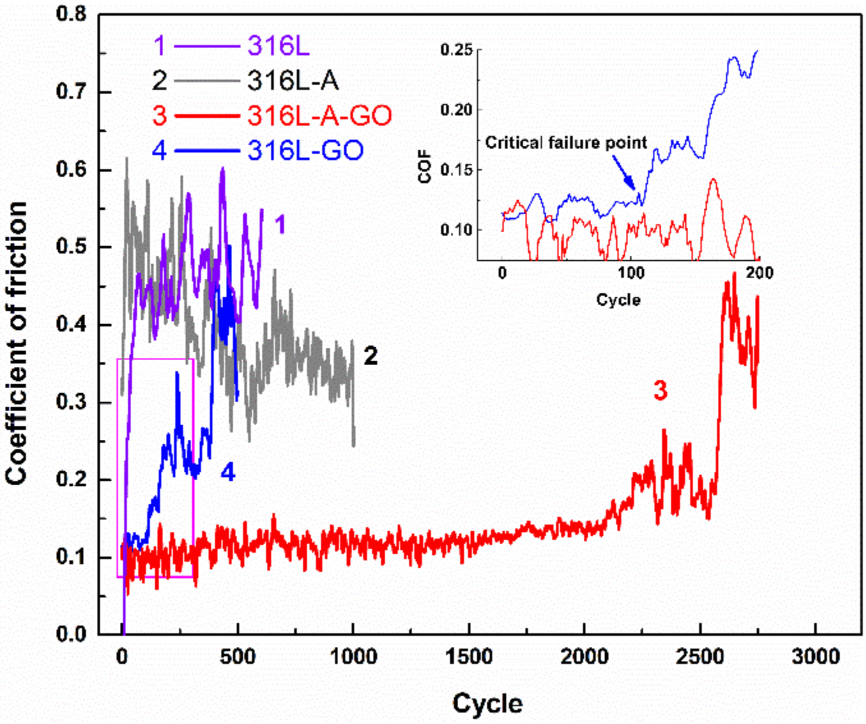

Figure 4.3-2 Coefficient of friction curves of samples against a stainless steel ball in air under a load of 1 N and the enlarged view of the first 200 cycles (inserted plot).

In comparison, with an additional APTES layer beneath the GO coating, 316L-A-GO exhibited substantially reduced friction and improved wear life. The COF was as low as 0.1 during early cycles, similar to 316L-GO. After that, no sudden increase of friction but a slight rise to 0.12-0.13 took place, and the low-friction regime was extended remarkably from 100 to some 2000 cycles under the same testing conditions. The friction then underwent mild turbulence before functionally failure of the coating around the 2500th cycle.

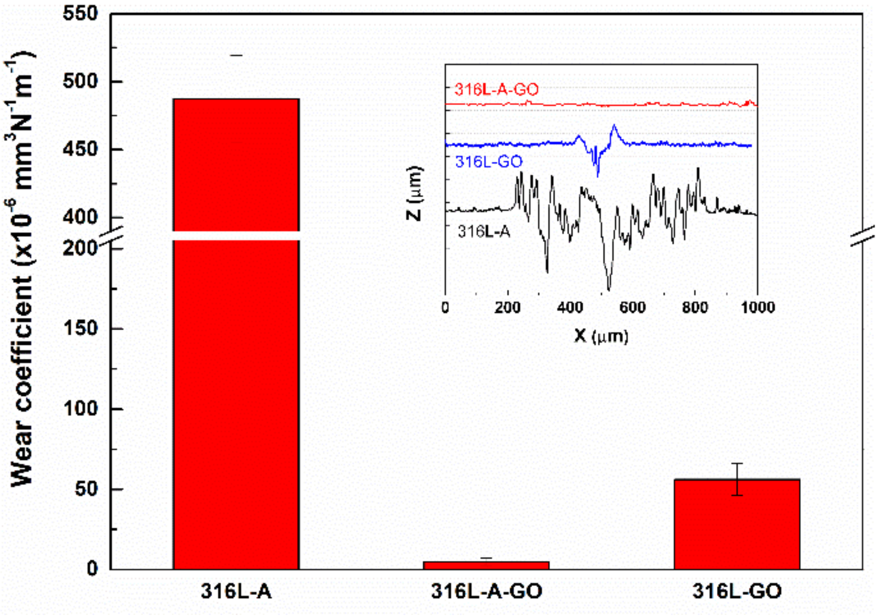

Figure 4.3-3 Wear coefficient of each sample measured after 1000 cycles sliding against the stainless steel counterball and the cross-sectional profiles of the corresponding wear tracks (inserted plot).

Figure 4.3-3 compares the wear coefficient values and the corresponding wear tracks after 1000 cycles (inset plot). As expected, 316L-A exhibited the highest wear coefficient (488 ×10$^{-6}$ mm$^3$N$^{-1}$m$^{-1}$), with a broad track (around 600 μm) comprising of deep furrows and build-ups, suggesting that severe material deformation and adhesive wear occurred. 316L-GO showed moderate wear coefficient (56.2 ×10$^{-6}$ mm$^3$N$^{-1}$m$^{-1}$) and wear track, which is in line with its friction history, suggesting a limited protection provided by a GO coating alone. In contrast, a dramatic wear reduction of one order of magnitude (4.9 ×10$^{-6}$ mm$^3$N$^{-1}$m$^{-1}$) was seen on 316L-A-GO. Accordingly, the wear track of this sample is negligible, indicating the excellent anti-wear performance of the coating system.

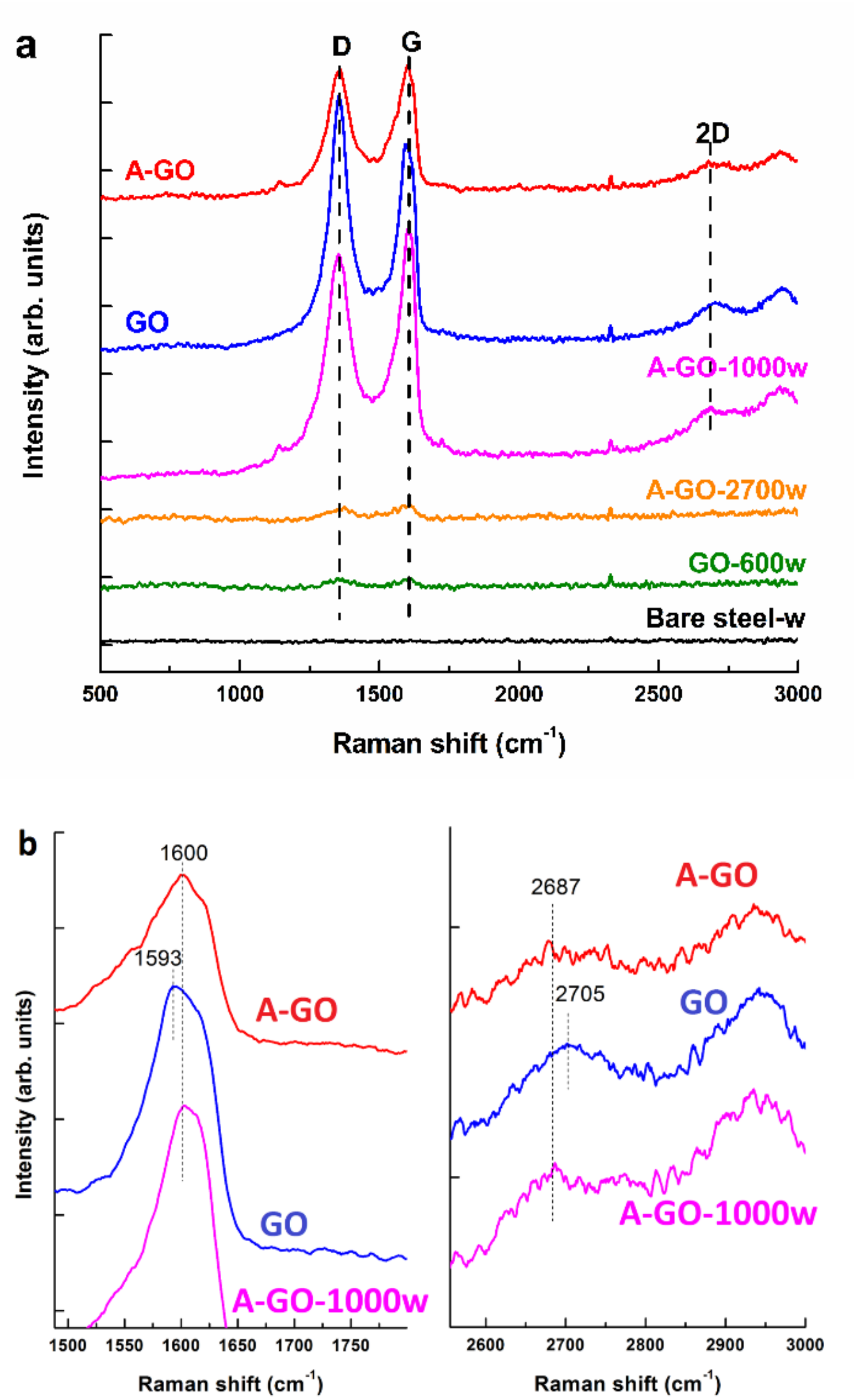

Figure 4.3-4 (a) Raman spectra of as-coated (A-GO and GO) and worn (the rest) surfaces after a given number (*viz.* 1000, 2700, 600) of sliding cycles. (b) enlarged view of the G and 2D modes in the Raman spectra.

Raman spectroscopy is an efficient tool in determining structure changes and/or disorder formations in carbon materials. Raman spectra of 316L-A-GO and 316L-GO, both before and after specific numbers of sliding cycles, were recorded and showed in Figure 4.3-4. The spectra of the as-coated surfaces feature three bands around 1350, 1600 and 2680 cm$^{-1}$. The G band around 1600 cm$^{-1}$ is characteristic of the sp$^2$-hybridised structure of graphene, arising from the intrinsic bond stretching of sp$^2$ carbon atoms. The D band around 1350 cm$^{-1}$ is related to structural disorders, *i.e.* oxygen functional groups or doping species [77] on the graphene basal plane. The intensity ratio of the D to G bands ($I_D/I_G$) is therefore usually used as an indicator of the disorder degree in graphene. The calculated $I_D/I_G$ ratio for the A-GO coating is 0.92, which is significantly smaller than that (1.24) of the GO coating.

Moreover, it is worth noting that the G band of 316L-GO coating downshifted by 7 cm$^{-1}$ and the 2D band upshifted by 18 cm$^{-1}$ compared to 316L-A-GO, as shown in Figure 4.3-4b the zoomed-in views. According to the literature [251], these peak shifts suggest that the graphene layer number of 316L-GO is likely larger than that of 316L-A-GO. However, the bands of 316L-GO shrank to minimum after 600 sliding cycles, indicating severe destruction, if not a complete removal of that coating. In contrast, 316L-A-GO kept substantially the same Raman features even after 1000 cycles sliding. Also importantly, no position change of the G and 2D bands was detected (Figure 4.3-4b), indicating a good structure integrity. Even after 2700 cycles when the friction has risen high to ~0.4, the D and G peaks can still be seen in the Raman spectrum. The results of Raman analysis are in good agreement with the frictional tests and support the idea that APTES is effective in enhancing the bonding of the GO coating.

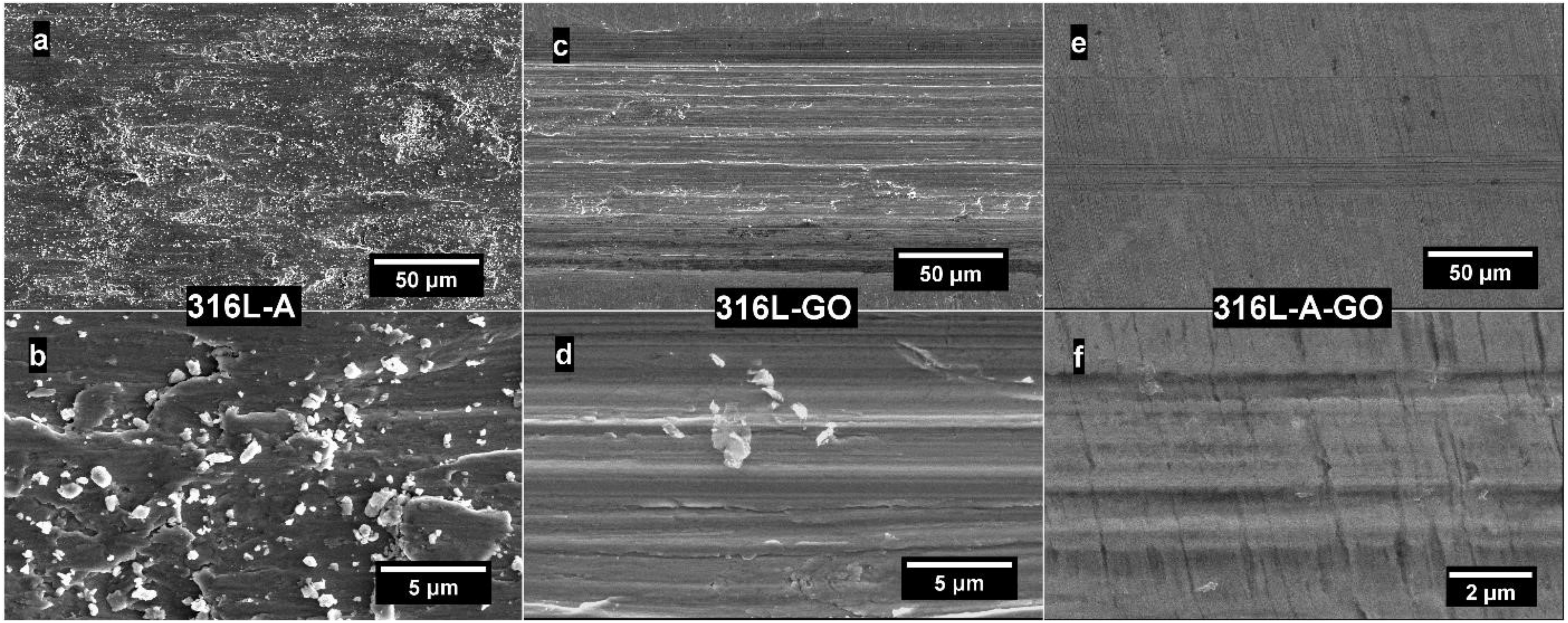

Figure 4.3-5 SEM images of the worn surfaces after 1000 cycle frictional tests.

Figures 4.3-5 displays the SEM morphology of the worn surfaces after 1000 tribological test cycles. The worn 316L-A surface showed rather high roughness and galling (Figures 4.3-5 a-b) due to adhesive wear at the steel-steel interface, which is in line with the measured wear track profile (see Figure 4.3-3). The widespread debris with sizes of around 1 μm in the wear track suggests that three-body abrasive wear may also have occurred. In comparison, 316L-GO showed a smoother wear track, but the shallow yet regularly arrayed grooves along the sliding direction are still indicative of limited protection by the GO coating (Figure 4.3-5c). Some fragments of the GO coating are visible inside the wear track as evidenced in Figure 4.3-5d. In contrast, 316L-A-GO exhibited negligible material loss after the wear test (Figure 4.3-5e). No coating debris or galling was observed, except for a minor degree of material deformation (Figure 4.3-5f). EDX was performed inside the wear tracks to figure out the chemical composition differences. Interestingly, the worn 316L-A-GO showed nearly 20 times less oxygen signal compared to 316L-A (Figure 4.3-6).

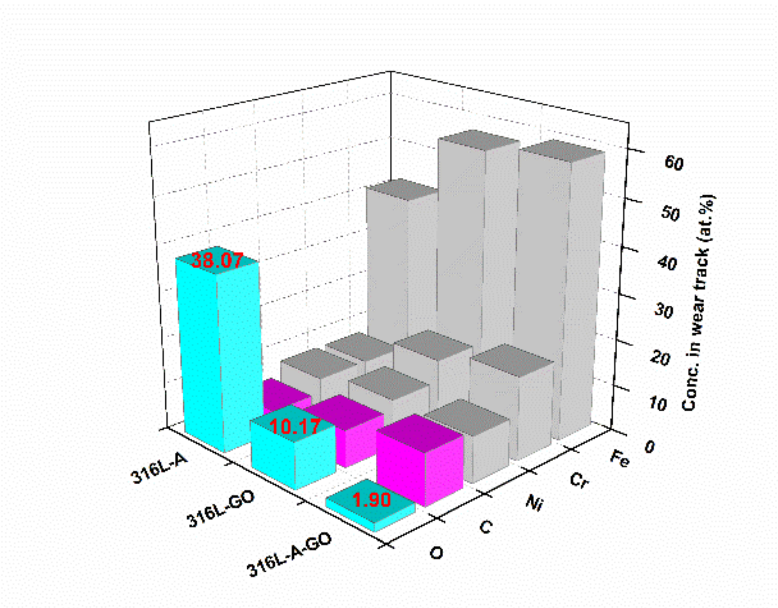

Figure 4.3-6 EDX analysis for the worn surfaces of 316L-A, 316L-GO and 316L-A-GO.

## 4.4 Electro-plated nickel-GO composite coatings

In view of the durability issue of graphene-based coatings directly deposited on metallic surfaces, it is worth trying to incorporate graphene-related materials into well-established metallic surface coatings and benefit from both. In this section, attempts were made to produce nickel-graphene oxide composite coatings using conventional electroplating method. A classical Watts nickel bath was prepared and varying GO contents were added into the plating bath under vigorous stirring and ultrasonication. The coatings were fabricated on planar steel surfaces as per the procedures described in Chapter 3. As summarised in Table 4.4-1, the coatings were coded according to the GO concentration (mg/ml) in the electrolyte used for the electroplating.

Table 4.4-1 Sample specification and deposition conditions

| Sample code | GO concentration (mg/ml) | Deposition conditions |
|---|---|---|
| Ni | 0 | $NiSO_4 \cdot 6H_2O$ 250 g/l<br>$NiCl_2 \cdot 6H_2O$ 40 g/l<br>$H_3BO_3$ 30 g/l<br>pH ~4<br>Temperature ~50 ℃<br>Current 4 A/dm$^2$ |
| ENG02 | 0.2 | |
| ENG05 | 0.5 | |
| ENG15 | 1.5 | |

### 4.4.1 Coating morphology and structure

Figure 4.4-1 shows the SEM morphology of neat Ni (GO-free) coating. The coating was uniform, formed of compactly spaced pyramidal grains. Figure 4.4-2 shows the surface morphology of ENG02 sample, the coating with the smallest amount (0.2

mg/ml) of GO. It did not show significant change in morphology and the surface roughness is comparable to neat Ni although some discontinuous dark zones were observed. After zooming in at the dark zone, silk-like GO sheets embedded between nickel grains were observed, as marked in Figure 4.4-2b. Unfortunately, due to the low GO content and high aspect ratio of GO, it was unsuccessful in acquiring a distinct carbon signal from these points by EDS.

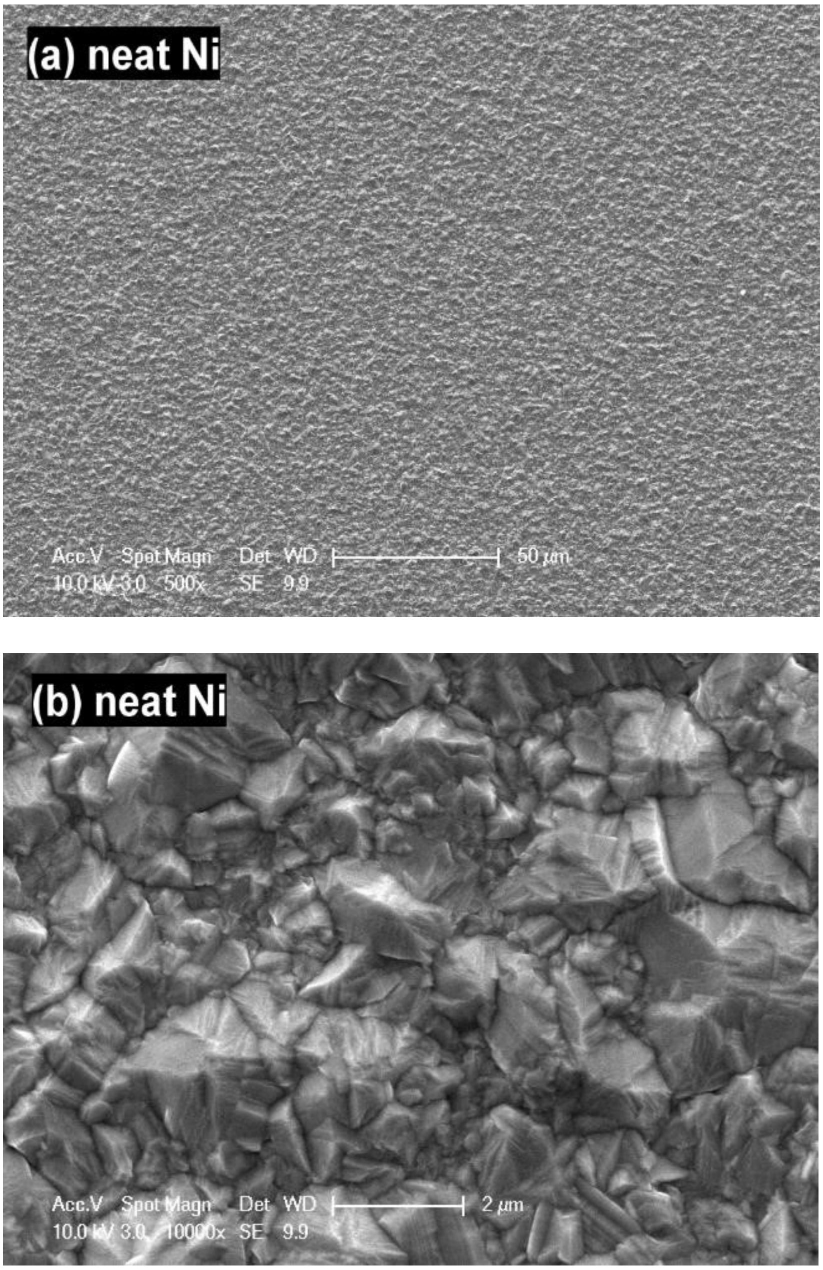

Figure 4.4-1 SEM images of electroplated neat Ni coating.

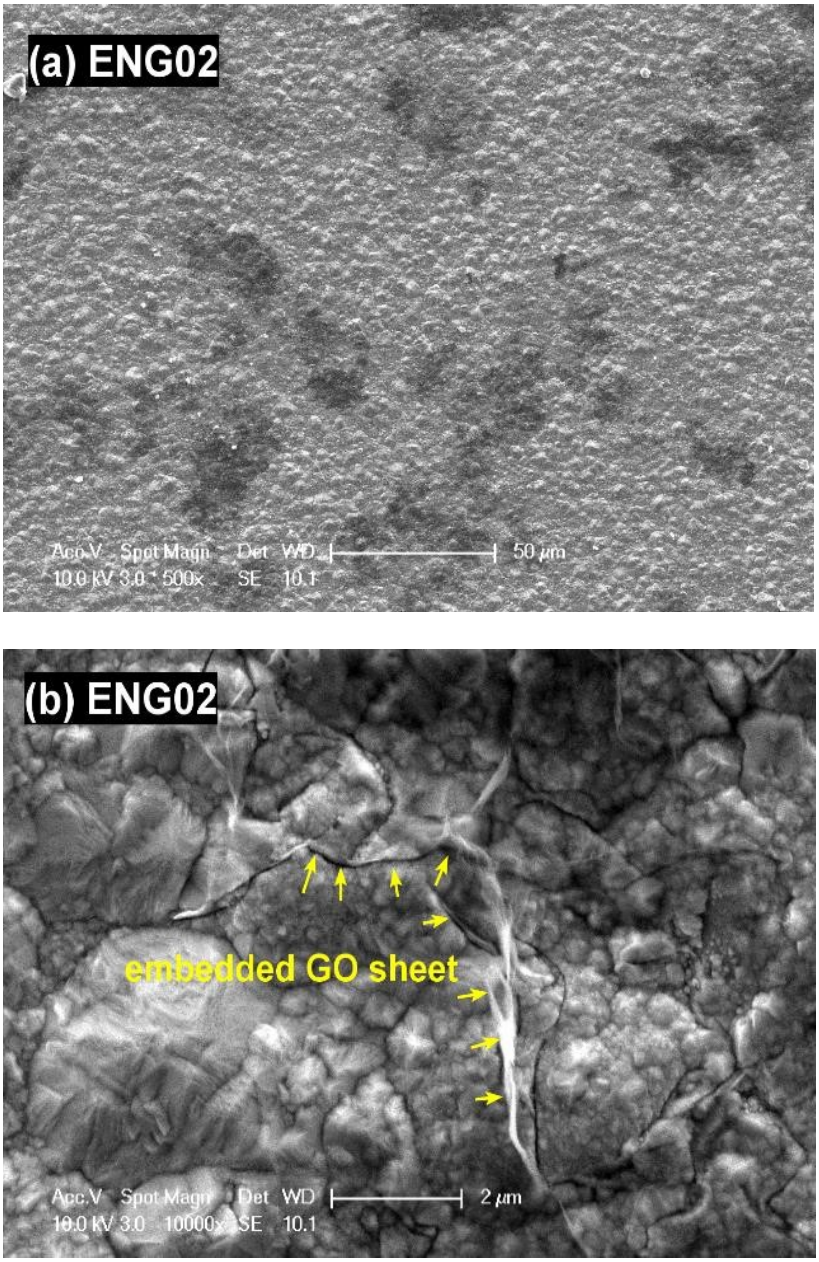

Figure 4.4-2 SEM images of electroplated ENG02 (GO 0.2 mg/ml) coating.

When the GO content in the plating solution increased to 0.5 mg/ml, the resultant coating ENG05 appeared different from neat Ni and ENG02 as evidenced by the widespread surface irregularities shown in Figure 4.4-3. Bulges and nodules were formed and distributed randomly across the coating surface. EDS analysis revealed a composition of 4.4 at% carbon for the normal nickel grains (Spot 1 in Figure 4.4-3b), while 18 at% carbon for the irregularities (Spot 2 in Figure 4.4-3b). It is very likely that

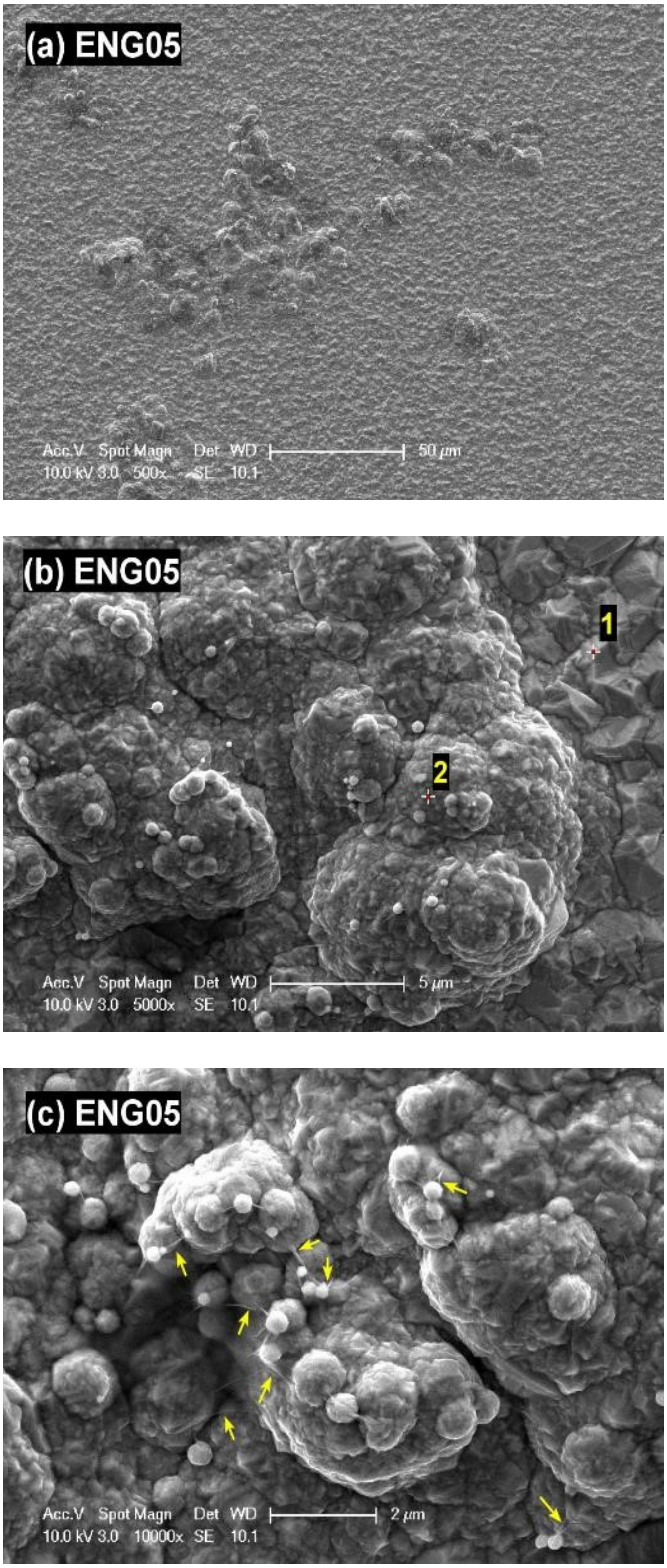

Figure 4.4-3 SEM images of electroplated ENG05 (GO 0.5 mg/ml) coating under different magnifications.

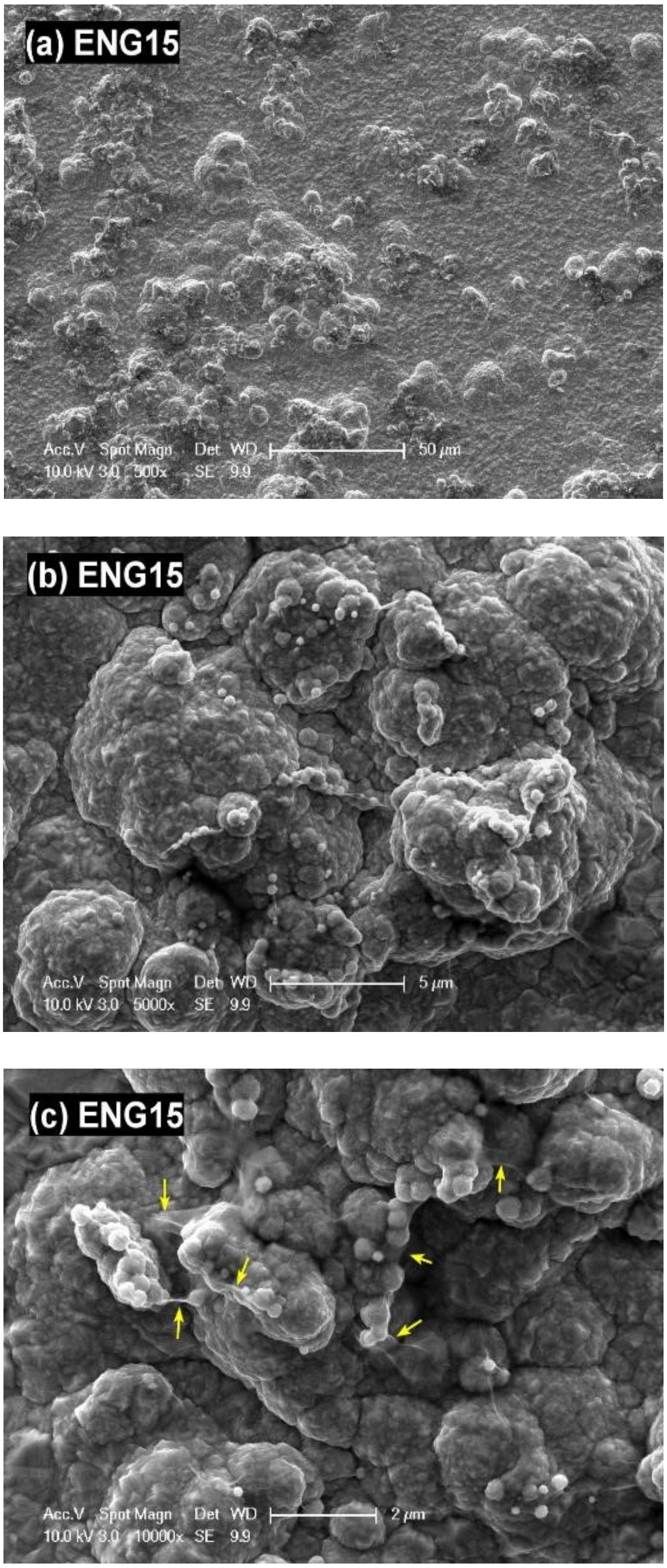

Figure 4.4-4 SEM images of electroplated ENG15 (GO 1.5 mg/ml) coating under different magnifications.

these surface bulges and nodules were induced by the incorporated and probably agglomerated GO sheets as the flat positions are much less affected by GO addition. It is also noted that fine-sized nickel spheres were formed on the surface of these bulges. The higher magnification micrograph (Figure 4.4-3c) showed that these small spheres were netted and linked by GO sheets as pointed by the arrows.

The change in morphology is more pronounced for ENG15, which was made from a solution with 1.5 mg/ml GO. As shown in Figure 4.4-4, a larger number of bulges were formed probably due to a higher degree of GO agglomerations. Indeed, the significantly increased surface roughness can be felt by fingers when compared with the other three samples. Small nickel spheres were present on top of these bulges with increased number (Figure 4.4-4b). It is easy in this case to see the translucent GO sheets (indicated by yellow arrows in Figure 4.4-4d) existing among these small crystals. It appears like the GO sheets stimulated or catalysed the growth of new crystals.

Figure 4.4-5 compares the fractography of neat Ni, ENG05 and ENG15 coatings. The fractures were prepared by chilling the thin samples in liquid nitrogen and then breaking by hammer. As demonstrated in Figures 4.4-5a&b, the neat Ni exhibited a columnar cross-sectional microstructure which is typically seen in electroplated nickel. For ENG05 (Figure 4.4-5c) the columnar feature disappeared and the coating was much denser than the neat Ni. Edges of GO sheets were clearly visible from the cross section, as marked by the yellow arrows. Figure 4.4-5d shows an exposed GO sheet within the cross section of ENG05. It is believed that such flexible nano sheets changed the microstructure of the nickel matrix. ENG15 showed a fracture comparable to ENG05 (Figure 4.4-5e). However, the GO content was so high that the fracture was characterised by a high density of hanging and twisted 2D GO sheets (Figure 4.4-5f).

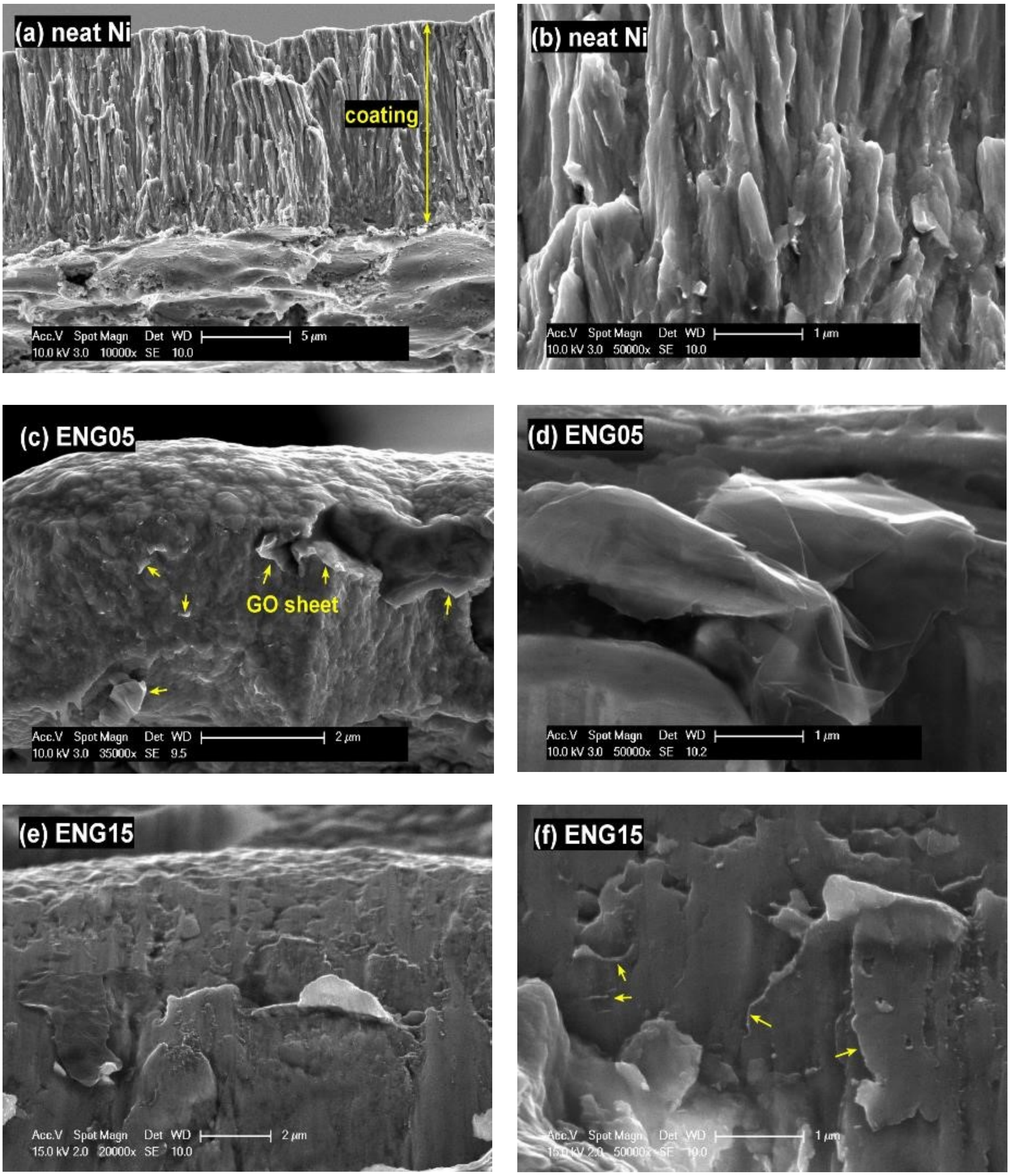

Figure 4.4-5 Fractography of electroplated (a-b) neat Ni, (c-d) ENG05 and (e-f) ENG15 coatings under different magnifications.

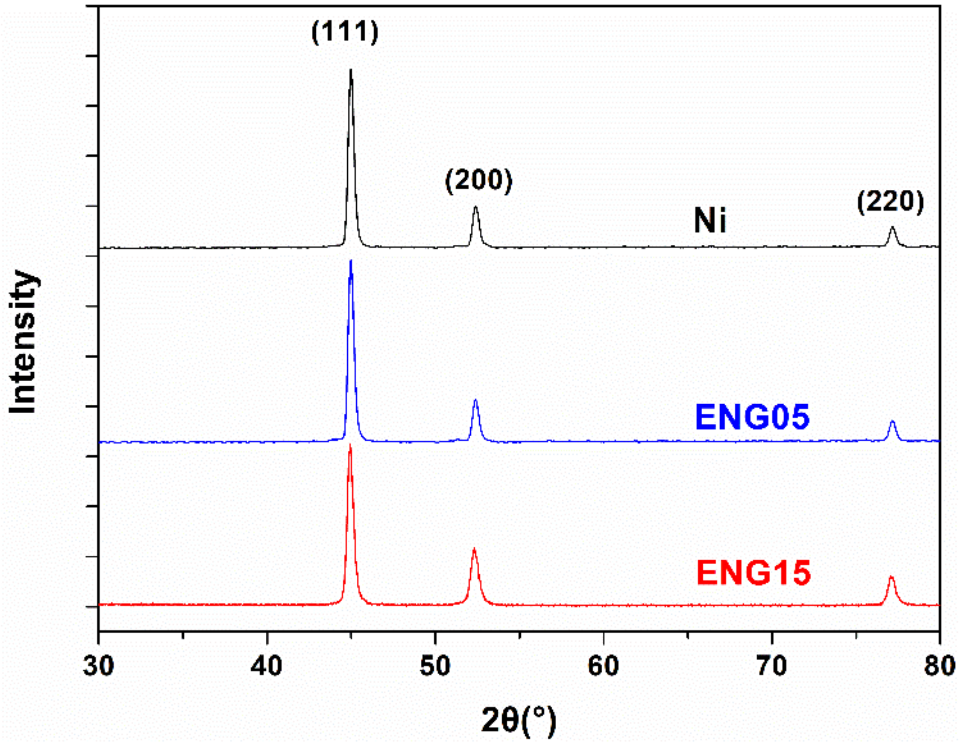

Figure 4.4-6 XRD patterns of electroplated neat Ni, ENG05 and ENG15 coatings.

The XRD patterns of neat Ni, ENG05 and ENG15 are presented in Figure 4.4-6. All the three samples showed a prominent peak around 45°, which corresponds to the (111) crystallographic planes of nickel. Two other peaks, around 53° and 77°, arose for (200) and (220) diffractions, respectively. It was found that the diffraction peaks were broadened after GO was introduced into the matrixes, implying a potential grain size reduction. To quantify the change in crystallisation, the crystallite size for each sample was estimated using Scherrer equation as below:

$$\beta = \frac{K\lambda}{L\cos\theta} \cdot \frac{180^\circ}{\pi} \qquad (4.4\text{-}1)$$

where β is the full width half maximum (FWHM) of the diffraction peak in 2θ degree, *K* is Scherrer constant (0.94 used here), λ is the wavelength of Cu-$K_\alpha$ radiation (0.154 nm), θ is the diffraction angle, and *L* is the crystallite size in nm. The (111) peak was used for the calculation and the results are summarised in Table 4.4-2. The neat Ni coating exhibited a crystallite size of 28 nm. In comparison, ENG05 and ENG15 exhibited a reduced crystallite size of 25 and 20 nm, respectively, indicating a clear grain refinement by GO.

Table 4.4-2 Estimated crystallite size for electroplated neat Ni, ENG05 and ENG15 coatings.

| Sample | (111) peak position (2θ/°) | FWHM (2θ/°) | Grain size (nm) |
|---|---|---|---|
| Ni | 45.30 | 0.32 | 28 |
| ENG05 | 45.20 | 0.36 | 25 |
| ENG15 | 45.18 | 0.45 | 20 |

### 4.4.2 Mechanical properties

Nanoindentation tests were performed on neat Ni, ENG05 and ENG15 coatings using a maximum load of 10 mN. The instrumental details can be found in Chapter 3. In light of the high surface roughness of Ni-GO composite coatings due to the presence of bulges, the indentation measurements were made on polished coating cross-sections (Figure 4.4-7b). The typical loading-displacement curve for each sample is shown in Figure 4.4-7a. The peak and final indentation depth for the neat Ni coating were 350 nm and 285 nm, respectively. These values were reduced by about 85 nm and 60 nm respectively for ENG05. The penetration maximum was reduced a little further for ENG15 due to its higher hardness.

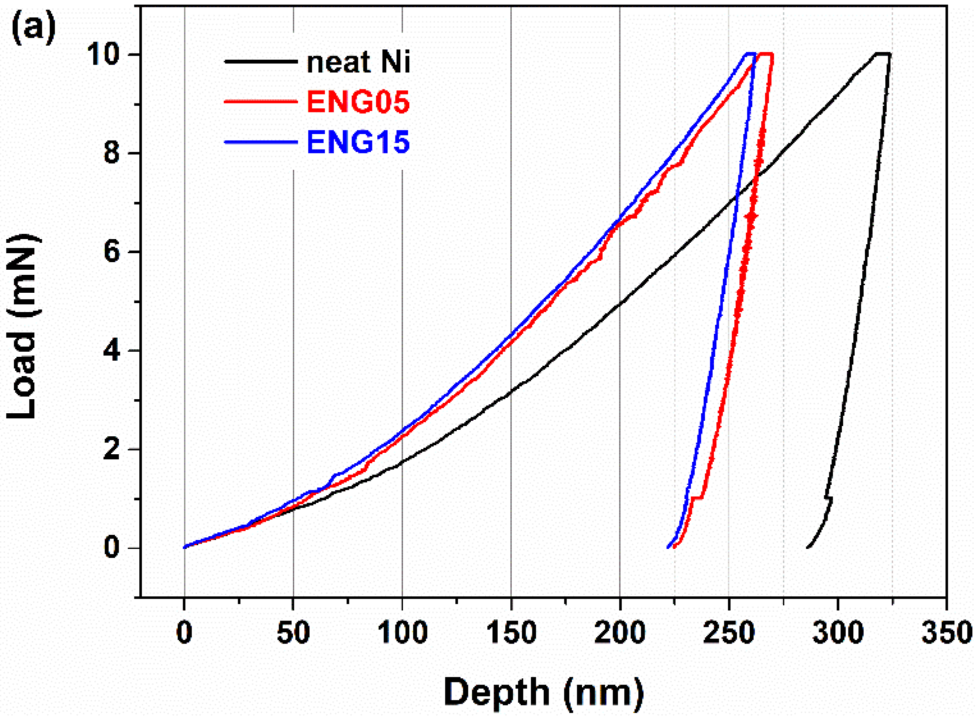

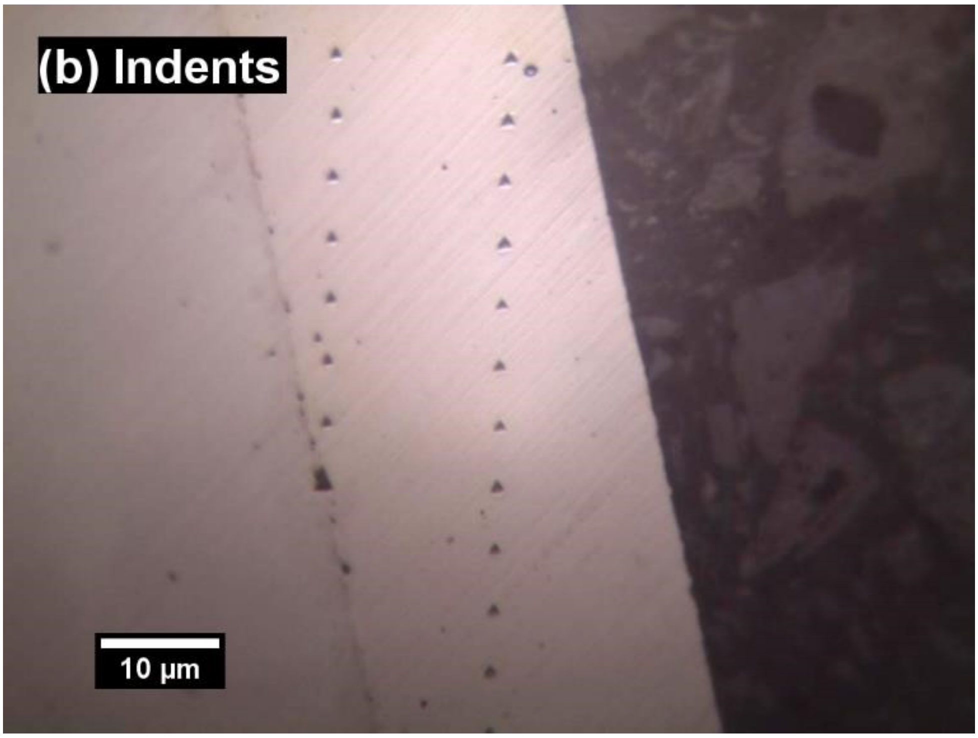

Figure 4.4-7 (a) Typical nanoindentation load-displacement curves of electroplated neat Ni, ENG05 and ENG15 coatings. (b) Snapshot of the indents across the coating thickness.

The nanoindentation hardness (*H*) and reduced modulus ($E_r$) were calculated using the Oliver-Pharr method [247] and the results are summarised in Table 4.4-3. The hardness of the neat Ni coating was measured as 3.58±0.24 GPa. This was improved by 36% for ENG05 (4.88±0.26 GPa) and 42% for ENG15 (5.07±0.47 GPa). The reduced moduli for both GO-containing coatings were also promoted to 214.62±13.49 GPa and 216.98±15.77 GPa, which are 6.4% and 7.5% higher than that (201.78±26.50 GPa) of the neat Ni. The results above indicate clear improvements in mechanical properties for Ni-GO composite coatings.

Table 4.4-3 Nanoindentation results of electroplated neat Ni, ENG05 and ENG15 coatings.

| Sample | Hardness (GPa) | Reduced modulus (GPa) |
|---|---|---|
| Ni | 3.58±0.24 | 201.78±26.50 |
| ENG05 | 4.88±0.26 | 214.62±13.49 |
| ENG15 | 5.07±0.47 | 216.98±15.77 |

### 4.4.3 Tribological behaviour

The frictional behaviour of neat Ni, ENG05 and ENG15 was investigated on a reciprocating ball-on-plate tribometer. An alumina ball with a diameter of 8 mm (ϕ8) was used as the counterpart, sliding against the sample surface with a speed of 5 mm/s and frequency of 1 Hz, under a normal load of 1 N. Before testing, the coatings were ground with 2500 grit grinding paper to smooth the surface irregularities and reach comparable roughness for the sliding contact. Figure 4.4-8 plots the COF of each sample over sliding cycles. The COF of the neat Ni climbed slowly during its first 600 cycles and reached a plateau at ~0.45. The COF for ENG05 was reduced slightly to ~0.40 owing to the GO addition. Likewise, a further reduction of the steady-state COF to ~0.3 was found on ENG15. It is worth noting, however, the COF curve of ENG15 fluctuated to a large extent during the initial 400 cycles before reaching its stable stage.

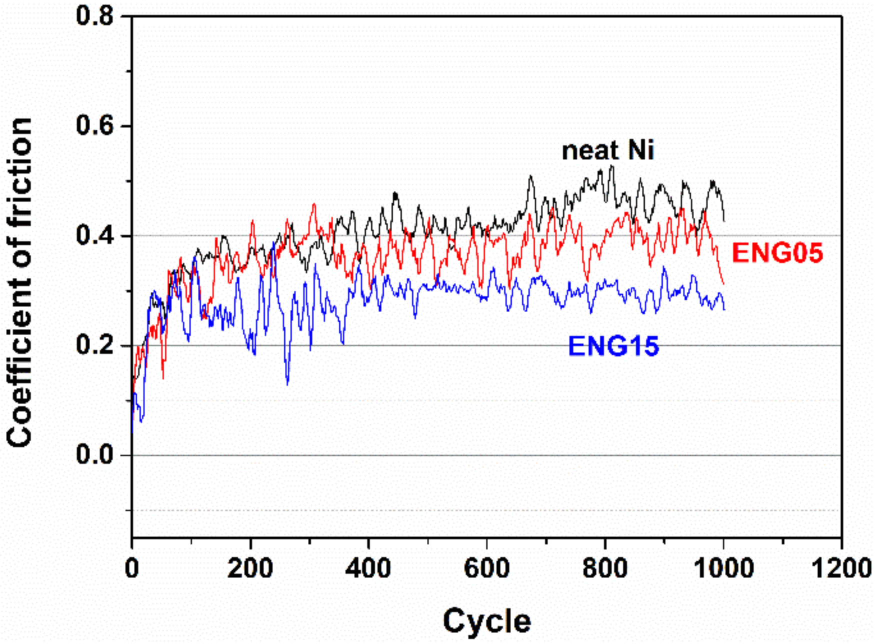

Figure 4.4-8 Coefficient of friction curves for electroplated neat Ni, ENG05 and ENG15 coatings sliding against an alumina ball in air under a load of 1 N.

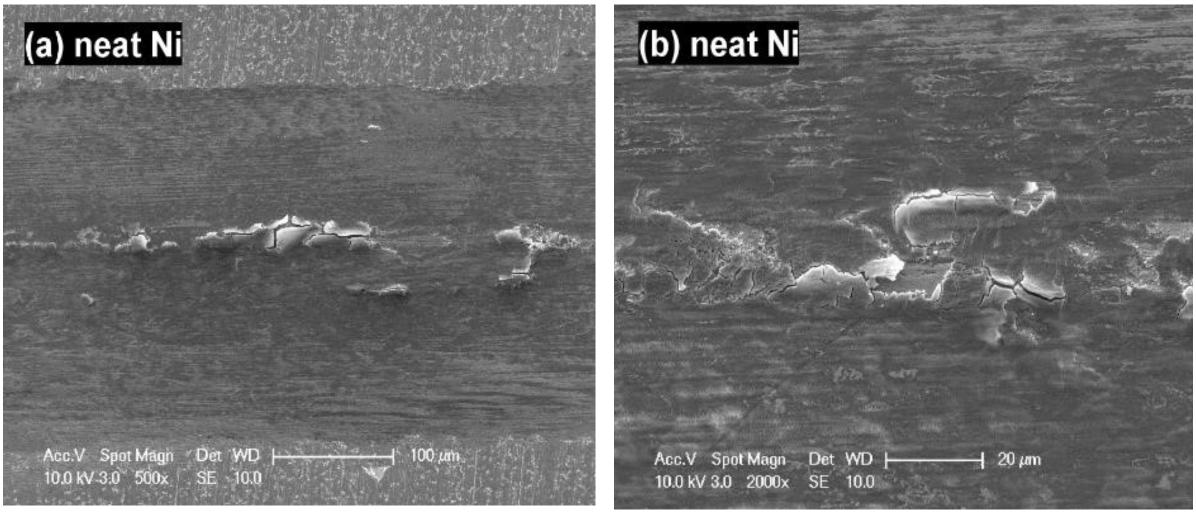

Figure 4.4-9 SEM images of the wear track on the neat Ni coating under (a) low and (b) high magnifications.

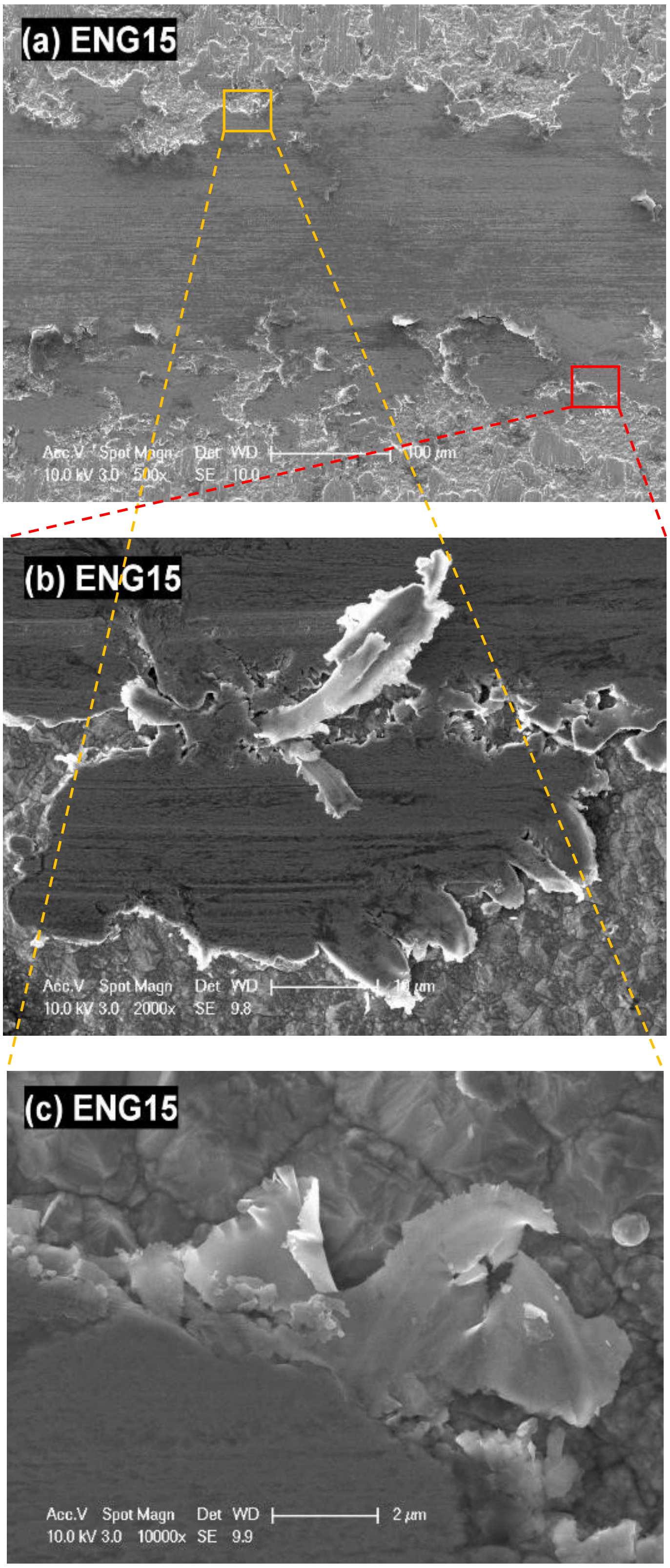

Figure 4.4-10 SEM images of the wear track on ENG15 surface under different magnifications.

Figure 4.4-9 shows SEM images of the worn neat Ni coating surface. Cracks and spallation were formed mostly around the centre of the wear scar, likely due to fatigue after repeatedly contact pressure (~530 MPa according to the Hertz contact theory). Adhesive wear was not found as an alumina ball which exhibits less affinity to metals was used. Nevertheless, grooves along the sliding direction were also present within the track due to abrasion. Unlike the neat Ni, fewer cracks were generated on ENG15 (Figure 4.4-10a). This could be attributed to the lubricating effect by the exposed GO sheets, as evidenced in Figures 4.4-10(b-c). The GO sheets incorporated in the nickel matrix were unearthed as the slider pushed the adjacent materials away, thus coming into contact with the slider directly and reducing the shear resistance.

### 4.4.4 Corrosion behaviour

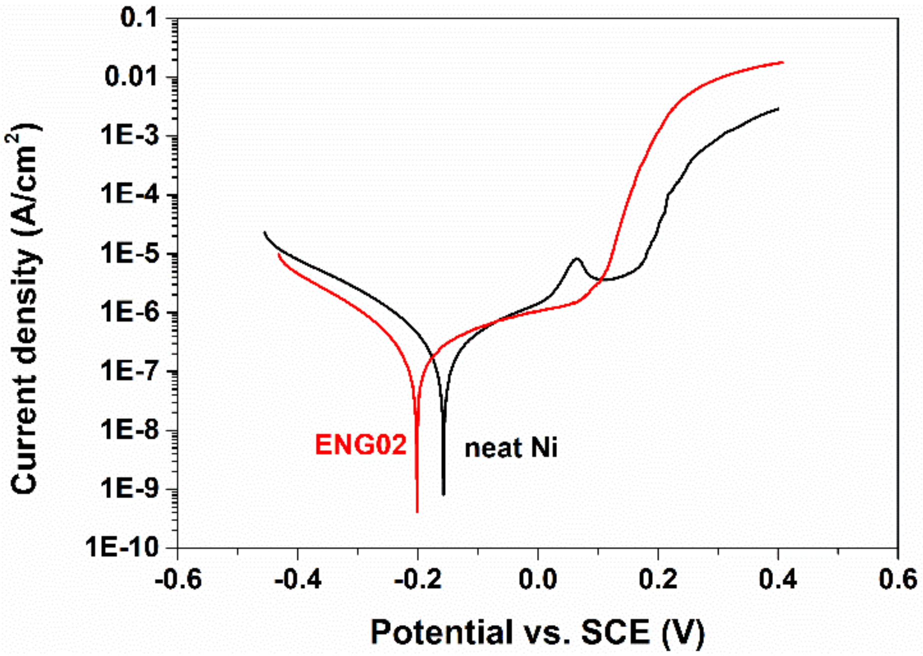

Figure 4.4-11 Polarisation curves of neat Ni and ENG02 in 3.5wt% NaCl solution.

The corrosion behaviour of neat Ni and GO containing ENG02 coatings were studied by potentiodynamic polarisation. The samples were tested in a 3.5wt% NaCl aqueous solution and the electrochemical signals monitored as described previously. Figure 4.4-11 demonstrates the polarisation curves of the neat Ni and ENG02 samples. The neat Ni coating exhibited a corrosion potential $E_{corr}$ of -157 mV (vs. SCE) and a corrosion current $I_{corr}$ of $459\times10^{-9}$ A/cm$^2$. It was unexpected that the GO-containing coating ENG02 showed a more negative $E_{corr}$ (-202 mV vs. SCE), which is indicative of lower corrosion resistance. In the meantime, the corrosion current of ENG02 was essentially the same as the neat Ni, suggesting little suppression to the corrosion rate.

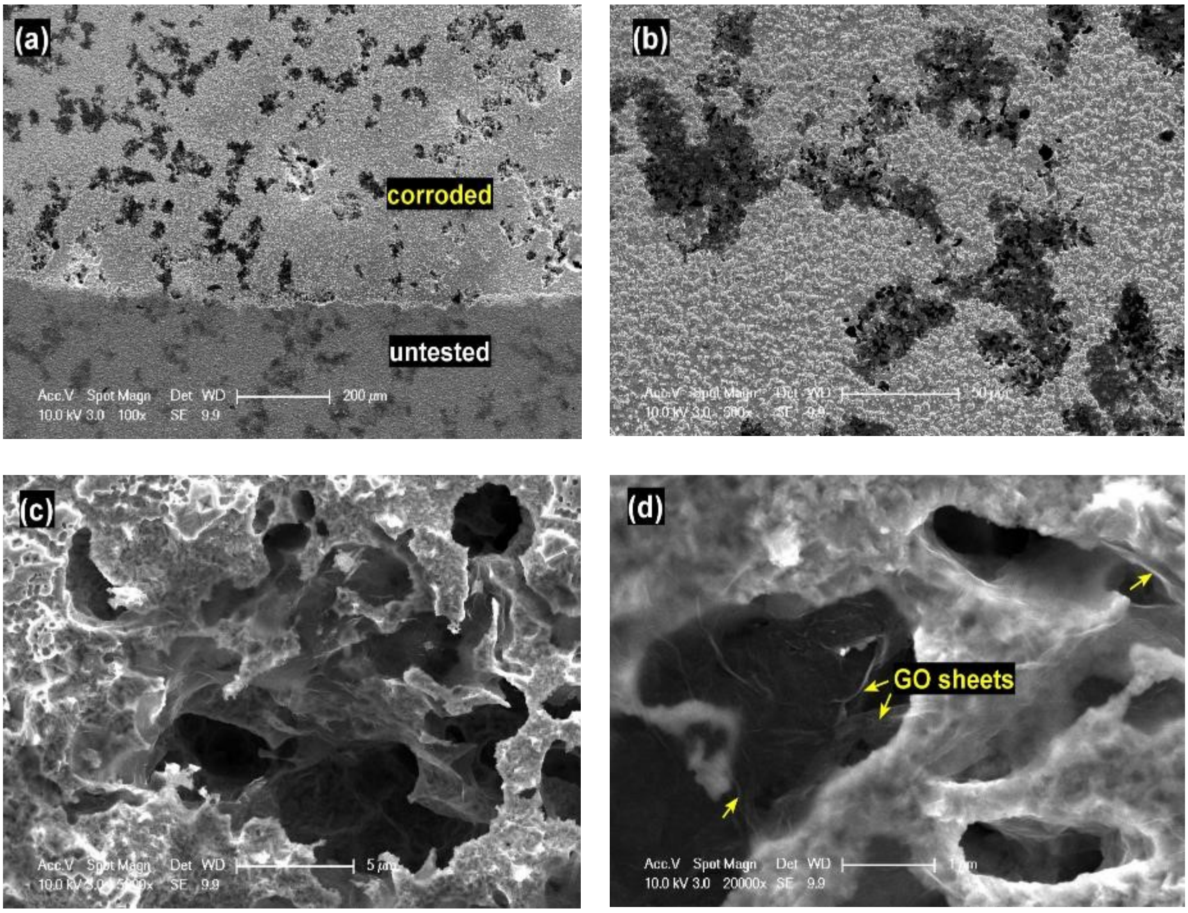

Figure 4.4-12 Morphology of ENG02 after the polarisation corrosion test. (c-d) show the details of severely corroded cavities.

The corroded surface of ENG02 was inspected under SEM and shown in Figure 4.4-12. As seen in Figure 4.4-12a a large number of corroded cavities were formed within the tested area. By comparing with the untested ENG02 it is clear that the corroded zones were mostly those rich in GO agglomerations, as already demonstrated in Figure 4.4-2. SEM images with a high magnification (Figures 4.4-12c-d) confirmed that the corroded cavities were explicitly associated with GO sheets. In these places, translucent GO sheets were clearly visible as the surrounding nickel has been removed by corrosion. It seems that the incorporated GO sheets promoted the localised corrosion of the nickel matrix. As the GO sheets formed agglomerations in the nickel matrix, the corrosion was non-homogeneous, as seen in Figures 4.4-12a-b. For this reason, ENG05 and ENG15 were not tested as GO agglomerated even worse in these two coatings (refer to Figures 4.4-3 and 4.4-4).

## 4.5 Discussion

### 4.5.1 Coating deposition

4.5.1.1 EPD

As mentioned in the Literature review as well as Section 4.1, GO sheets get deprotonated in many polar solvents (including water) and thus exhibit a negative zeta potential. The 1 mg/ml GO suspension used for EPD in this project showed a zeta potential of -61.7 mV (Figure 4.1-9), which provides enough particle stability and electrophoretic mobility for an EPD process. Driven by the electric field, the negatively charged GO sheets swim to the anode. The mechanism for deposit formation at the electrode during EPD is usually associated with particle charge neutralisation and flocculation near the electrode. Specifically for the EPD of GO, it has been suggested that the water electrolysis near the anode is essential for the whole process, as described below by Equations 4.5-1 to 4.5-3 [137, 145]:

$$\text{Anode} \quad 2H_2O \rightarrow 4H^+ + 4e^- + O_2 \uparrow \tag{4.5-1}$$

$$RCOO^- + H^+ \rightarrow RCOOH \tag{4.5-2}$$

$$\text{Cathode} \quad 2H_2O + 2e^- \rightarrow 2OH^- + H_2 \uparrow \tag{4.5-3}$$

Upon arriving at the anode, the negatively charged GO sheets ($RCOO^-$) were re-protonated, leading to the reduction of electrostatic repulsion between GO sheets, thus enabling the aggregation and deposition of GO sheets at the anode.

With regards to the electric current over the EPD process as shown in Figure 4.2-1, it is found that the current densities corresponding to all the voltages decreased quickly at the beginning of the EPD process. This is due to the formation of an insulating [252] GO layer on the anode which reduced its conductivity. Despite the fact that the deposited GO sheets had been simultaneously reduced to rGO (as will be discussed below), the conductivity of the deposit was still much less than the substrate (stainless steel), thus leading to the current drops. Also noticeable in Figure 4.2-1 is the current fluctuation during the EPD at 10 V. The unstable current density is very likely caused by water electrolysis as described above by Equations 4.5-1 and 4.5-3. The gas bubbles affected the normal deposition by agitating the electrolyte near the electrodes, thus causing turbulences to the electric field and the particle flow. It is also worth noting that the working voltage of 10 V is well beyond the normal electric potential of the stainless steel electrode, therefore facilitating dissolution of the anode and migration of metallic ions towards the suspension. These adverse factors led to the unstable electric current and relatively loose deposit, as shown in Figure 4.2-2b.

The voltage was then fixed at 3 V in the rest experiments in view of the inhibited gas evolution, smooth deposition process (Figure 4.2-1) as well as the uniform and compact deposit (Figure 4.2-2a). The deposition rate of the EPD process is then complied with the Hamaker's law (Equation 4.2-1), as proved by the data fitting in Figure 4.2-3. The coating thickness increased almost linearly with deposition time, and the fitting curve could be helpful in determining such a proper deposition time for a GO coating with a desirable thickness. As demonstrated in Figure 4.2-3, this EPD configuration produced a GO coating of half a micron for a deposition time of 10 min, and has the potential for thicker (a few microns) GO coatings. However, it is also clear in Figure 4.2-4 that after a prolonged deposition time (more than 4 min) the surface roughness of the resultant coating increased considerably, as wrinkles were formed on the coatings (Figure 4.2-4 d-f). This can be attributed to the accumulated coagulation of the GO suspension in the vicinity of the substrate during EPD. But more likely, it is due to the evaporation of trapped water in between the lamellar structure of the GO coating during the drying process after deposition [253]. This wrinkle formation is unfortunately inevitable for GO coatings from colloids as long as the solvent evaporation is part of the coating drying/curing process. Nevertheless, the GO wrinkles could be beneficial for some specific applications, such as electrochemical sensors and catalysts [152].

Another interesting phenomenon is the in-situ reduction of GO during the EPD process as shown by Raman and XPS (Figure 4.2-5). The slightly increased $I_D/I_G$ ratio for EPD-GO is in agreement with the literature on rGO and likely due to the changes in the sp$^2$-conjugated graphene-like domains which are higher in number but smaller in average size [73]. Quantitatively, XPS analysis revealed a significantly increased

C/O ratio (12:1 vs. 5:3), indicating a strong reduction of the oxygen content. The reduction effect (in terms of the C/O ratio) was comparable to, if no better than, the rGO chemically reduced by hydrazine [74] or HI [112]. The C1s spectra also confirmed that most of the oxygen functional groups on EPD-GO have been removed. The simultaneous reduction of GO during EPD was also reported by An et, al. [143] and Diba et, al. [138]. However, in the former case the EPD voltage was as high as 10 V, and in the latter case the reduction effect was barely found at lower voltages until 20 V. In sharp contrast, the transformation from GO to rGO in this study was fulfilled at a much lower voltage of 3 V. The experimental results of this work show that EPD is an effective, environment-friendly and simple method for the simultaneous deposition and reduction of GO.

### 4.5.1.2 Self-assembly

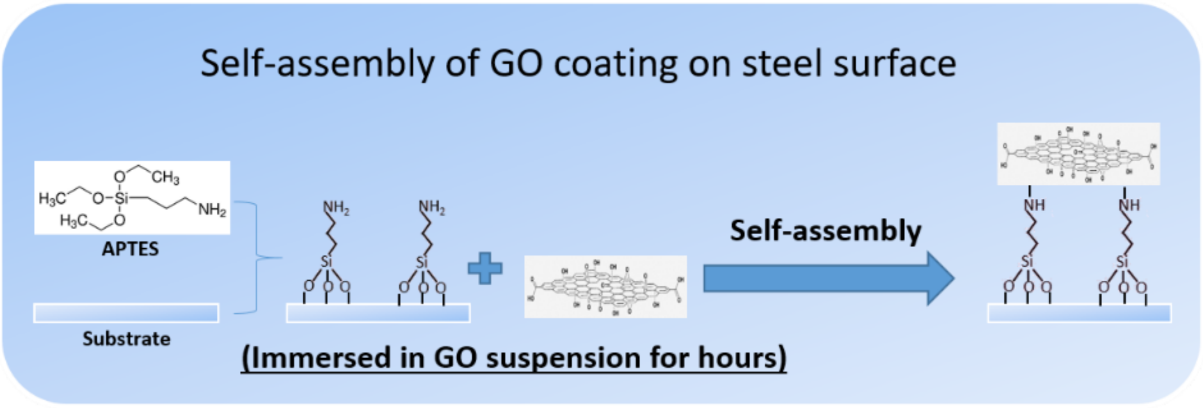

Figure 4.5-1 Schematic of the self-assembly of single-layer GO coating on 316L stainless steel.

Figure 4.5-1 is the schematic for the self-assembly process. It is believed that after the hydroxylation treatment the steel surface is functionalised with hydroxyl groups (-OH). During the self-assembly process APTES molecules and GO sheets assemble themselves in succession via condensation reactions between the hydroxyl groups (-

OH) on steel surface and the alkoxy groups (-O-R) on APTES, and between the amino head groups ($-NH_2$) of APTES and the oxygen groups (mainly -COOH) of GO. The assembly process stops when the amino sites are fully occupied, much like paving a floor with mosaic tiles. The redundant GO sheets are hence just floating on the top and can be easily removed by running water, leaving a GO coating of mainly one single layer, as observed by AFM in Figure 4.3-1. On the other hand, obviously, the GO sheets on the 316L-GO sample were just lying randomly on the surface, with no effective chemical bond or only weak van der Waals forces to the substrate.

The establishment of covalent bonds in between the GO-APTES-steel sandwich structure was proved by the improved tribological performance and durability of the resultant coating (Section 4.3.2). It has been reported that APTES can improve the bonding between graphene and silicon wafer [126]. It was also reported to modify a titanium alloy surface before a graphene coating for nano/micro tribological application [131]. However, to our knowledge there is no report yet about such use on such common metallic materials as steel. The results have shown by example that chemical surface modification could improve the service life of graphene-based coatings on metallic substrates. The macro-scale application, ultra-thin nano structure and very simple preparation procedures of this self-assembled GO coating could be of interest for many fields.

The main limitation of this self-assembly method is its low fabrication efficiency. For instance, usually an immersion time of more than 10 hours is necessary for well-established bonds between APTES molecules and the functional groups of GO (see Figure 4.5-1). According to the results reported in Section 4.3.2, a 15-hour immersion of the APTES-treated substrate in GO suspension improved the coating durability from

100 cycles to about 2500 cycles. While tribological tests showed that a one-hour self-assembly ended up with a quick failure (<100 sliding cycles) of the GO lubricating coating.

### 4.5.1.2 Composite electroplating

Figures 4.4-1 to 4.4-4 show the morphology of the nickel coatings without and with increasing content (0.2, 0.5 and 1.5 mg/ml) of GO reinforcement. The successful incorporation of GO has been visually proven by the embedment of semi-transparent GO layers within the nickel matrix (Figure 4.4-2b). It is the thin nature and high flexibility of GO that enabled the co-existence of GO sheets between the compact nickel crystals, and ensured that the incoming GO sheets can follow the contour of the nickel deposit and fit themselves into places as small as the grain boundaries.

The reasons for the formation of the surface bulges at higher GO loads (0.5 and 1.5 mg/ml) are two-fold. On one hand, it could be attributed to the agglomeration of GO sheets. As mentioned before, GO sheets naturally deprotonate and thus carry negative charges in water. It has been demonstrated that as nickel cations ($Ni^{2+}$) were dropwise added into a GO suspension, the Zeta potential of the GO sheets decreased quickly from -61.70 mV to -4.79 mV, which means a much lower electrophoretic mobility (Table 4.5-1). In a plating solution rich in $Ni^{2+}$, the negative charges of GO can be readily neutralised, thus resulting in flocculation of metallic Ni-GO or $Ni(OH)_2$-GO [141]. These agglomerations are then driven into the deposit by the electric field. On the other hand, as shown in Figures 4.4-3 and 4.4-4, the newly formed nickel clusters preferably settled on GO sheets. In Figure 4.4-4 the tendency is clear that the deposited GO sheets promoted the nickel nucleation on them. In other words, the GO sheets served as scaffolds for the nickel ions to attach, nucleate and grow on. The GO agglomerations in the plating solution, however, led to inhomogeneous GO reinforcement in the final deposit, as evidenced by EDS (Figure 4.4-3 and Section 4.4.1).

Table 4.5-1 Zeta potential of GO suspension and GO/Ni plating solutions

| $Ni^{2+}$ addition in GO suspension | Zeta potential (mV) | Particle mobility (μm·cm/Vs) | Conductivity (mS/cm) |
|---|---|---|---|
| 0 | -61.70 | -4.71 | 0.53 |
| 20 mg/ml | -12.95 | -1.02 | 31.43 |
| 40 mg/ml | -8.72 | -0.66 | 34.86 |
| 50 mg/ml | -4.79 | -0.38 | 42.1 |

Nonetheless, the incorporation of GO sheets influenced the normal crystallisation of the nickel matrix substantially, as the fractography showed in Figure 4.4-5. Meanwhile, the average crystallite size was found reduced effectively from 28 nm for the neat Ni coating to 20 nm for ENG15 (Figure 4.4-6). The disturbance to the normal crystal growth and grain refinement effect was also reported and the mechanisms proposed for Ni-$Al_2O_3$, Ni-SiC [158] and Ni-CNT [254] composites. It is likely that the GO sheets catalysed more nickel crystallite sites, while wrapping and intersecting the growing nickel grains, thus leading to a smaller crystallite size and a disordered microstructure. As a consequence, the hardness and elastic modulus of the Ni-GO composite coatings were improved (Figure 4.4-7 and Table 4.4-3).

### 4.5.2 Tribological performance

#### 4.5.2.1 Effect of substrate topography

The frictional tests on the GO coated 316L stainless steel by EPD (Figure 4.2-6) revealed a COF of 0.08-0.10, which is even lower than the values (COF 0.15-0.20) reported by Berman et, al. on the steel spin-coated with graphene sheets [13]. However, the frictional behaviour was unstable due to the early failure of the GO coating. As an inert carbonaceous material, graphene and its derivatives normally shows inadequate chemical compatibility with most engineering materials surfaces, making the coating fragile and vulnerable once in contact with moving parts [18]. Exceptionally, graphene grown by chemical vapour deposition can adhere to the nickel substrate strongly and exhibit a super low coefficient of friction (COF) of 0.03. However, the friction increased considerably after the graphene was transferred onto a silica substrate, as defects were formed and thus the coating integrity suffered [11].

The results in this work demonstrated that acid pickling, as an approach to modify the surface topography of the substrate, improved the durability of the EPD-GO coating on its surface (Figures 4.2-6 c-d). It is well known that a substrate with properly configured surface texture can not only retain solid lubricants [255, 256] but also trap wear debris and thus reduce the abrasion induced by the particles [257]. The trials on laser patterned steel demonstrated the potential of such artificial surface textures in improving the service life of GO surface coatings as solid lubricant (Figure 4.2-8). Unfortunately, the performance was obviously not the optimal and there are many influential factors to be studied in details, such as the pattern depth, pattern density (the ratio of patterned area to the whole area) and the groove or dimple width (in relationship to the diameter of Hertz contact area).

To verify this effect, similar experiments were performed on grey cast iron, which is known for the imbedded graphite of various shapes in its matrix. The cast iron samples (G3500) were etched in dilute acid as for the 316L stainless steel. The etched cast iron (G3500-E) was then coated with GO by EPD at 3 V for 2 min., Figure 4.5-2 displays the COF curves for G3500-GO, G3500-E-GO and the uncoated substrates against a 316 stainless steel ball (ϕ8 mm) under a normal load of 2 N. Without GO coating, the samples (G3500 and G3500-E) experienced high friction. Although for the etched substrate there were a large number of graphite strips exposed on surface, as shown in Figures 4.5-3(a-b), the sliding was barely lubricated by the exposed graphite. The wear scars on the as-ground and etched substrates were also very similar.

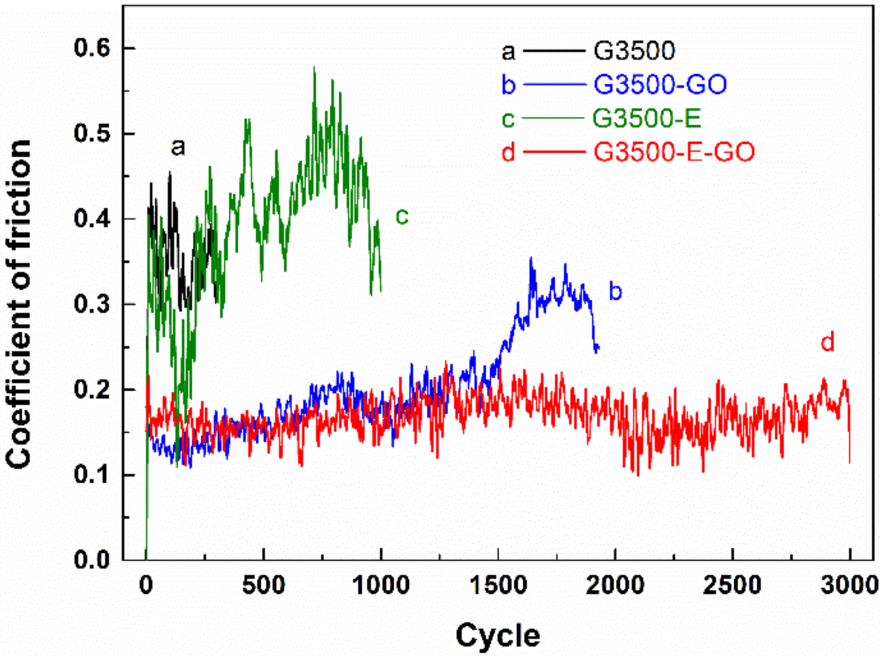

Figure 4.5-2 Coefficient of friction for (a) as-ground, (c) etched G3500 cast iron and (b, d) the corresponding GO-coated samples during reciprocating tribological tests under a normal load of 2 N. E: etched.

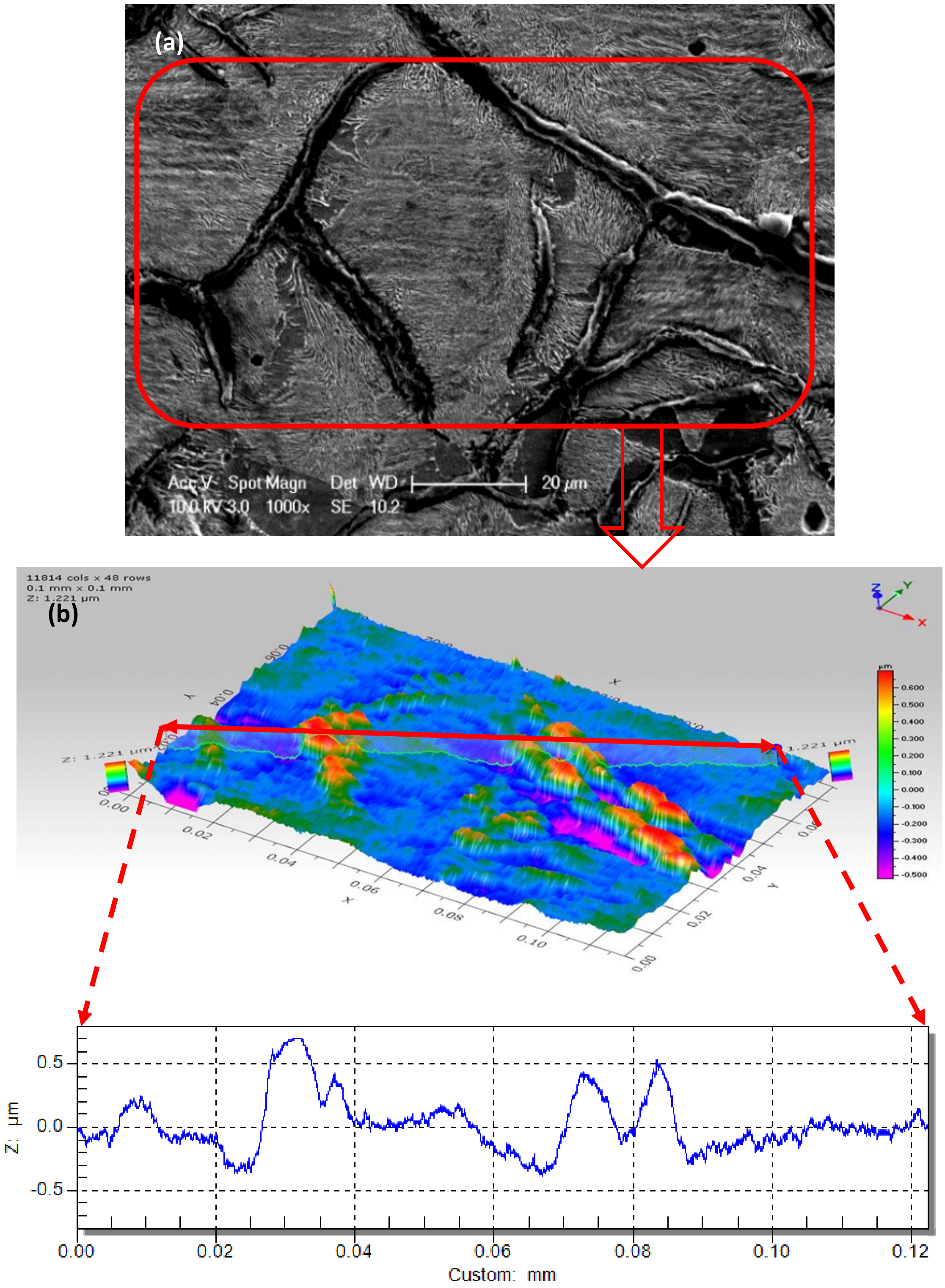

Figure 4.5-3 SEM image (a) and corresponding 3D height profile (b) of the etched grey iron (G3500-E).

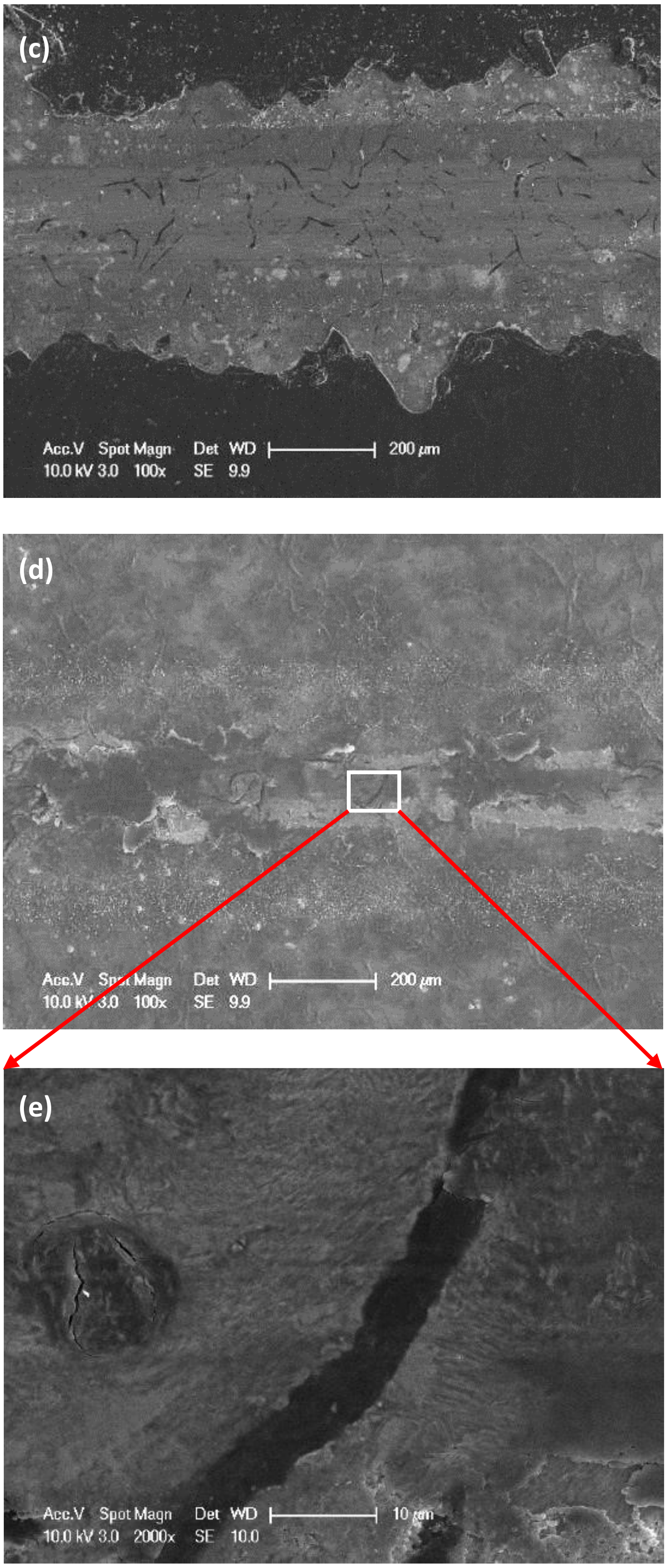

Figure 4.5-3(continued) worn surfaces of (c) G3500-GO and (d-e) G3500-E-GO.

The COF for both G3500-GO and G3500-E-GO were much lower than that of the uncoated samples and kept essentially the same values (~ 0.15) for the first 1500 cycles, as shown in Figure 4.5-2. After that, however, the COF of the G3500-GO increased rapidly to about 0.35; in contrast, the G3500-E-GO stayed in the low-friction regime throughout the 3000-cycle test, suggesting that the wear life of the same GO coating was prolonged when coated on the etched substrate.

From the SEM images of the worn coatings, it is clear that the GO coating on the untreated substrate was removed completely from the whole contact area (Figure 4.5-3c); while in contrast, the GO coating on the etched cast iron still covered the entire sliding path, despite of the cracks induced by the reciprocating contact (Figure 4.5-3d).

This enhanced retention of the GO coating can be attributed to the exposed graphite strips after etching which prevented the GO solid lubricant from being removed by sliding, as evidenced in Figure 4.5-3e. This proposed mechanism is also in line with the geometric mapping of the etched surface by a 3D profilometer, as shown in Figure 4.5-3b (to correlate the SEM image and the 3D topography, the mapping was carried out exactly at the same place as marked in Figure 4.5-3a). According to the 3D image as well as the cross-section height profile, it is clear that the graphite strips were sticking out due to the etching of the matrix. By virtue of the inert chemistry of graphite, the iron surrounding the graphite strips in the cast iron was preferably etched away, thus creating trenches for GO solid lubricant to stay in (Figures 4.5-3 a-b). During sliding, such trenches not only protected the GO coating from being sheared away, but also settled GO and metal debris from the wear, thus resulting in an improved anti-wear life of the GO coating. The investigations on etched 316L stainless steel and etched cast iron here are two examples showing that a proper surface roughness and topography can work well together with graphene coatings and exhibit long-lasting tribological properties.

#### 4.5.2.2 Effect of chemical bonding

With an APTES intermediate layer, the tribological performance of the top GO coating was improved effectively in terms of very low friction (COF ~0.1, Figure 4.3-2), 10-fold reduction in wear (Figure 4.3-3) and increased coating durability by some 20 times. The improvements can be mainly attributed to the enhanced coating bonding via the silane layer. During the self-assembly process, covalent bonds were established between the top GO coating and the steel substrate. The APTES interlayer therefore acts as a chain that locks the steel surface and the GO sheets together. The large reduction in $I_D/I_G$ ratio of the Raman spectrum for 316L-A-GO compared to the as-synthesised GO could be attributed to the condensation reactions between APTES molecules and GO sheets, which led to a reduction of the oxygen group concentration in GO and thus a recovery of its $sp^2$ conjugated structure [253, 258]. As a consequence of the enhanced connection, the GO Raman features were still retained after 2700 cycles tribological test (Figure 4.3-4), indicating a longer service life of the GO solid lubricant coating in the presence of APTES.

The dramatic drop in oxygen on the worn 316L-A-GO compared with 316L-A (Figure 4.3-6) is very likely due to the lubricating effect of the GO coating that reduces the friction and hence energy dissipation. As it is known, the flash temperature resulted from frictional heat at real contacted asperities can be up to hundreds of degrees high [259]. In ambient environment, these hot-spots can readily result in oxidation. In this study, the GO coating reduced the friction force so greatly that the transient heat generation was effectively inhibited; furthermore, the excellent thermal conductivity along the lamellar graphene structure [260] could minimise the heat accumulation. It is also possible that graphene oxide, a derivative of graphene which has been reported to be impermeable to even the smallest molecules [19], blocked external oxygen from contacting the underlying steel, thus hindering the oxidation process. However, this feature was degraded for 316L-GO due to lack of bonding.

### 4.5.3 Corrosion performance

#### 4.5.3.1 Physical barrier effect of GO

As presented in Section 4.2.3, the EPD-GO coatings showed excellent corrosion resistance in terms of much more positive corrosion potentials and significantly depressed corrosion current densities (Figure 4.2-9). In particular, the corrosion current of the EPD-GO coatings developed smoothly throughout the anodic polarisation period, denoting a complete inhibition of pitting on the stainless steel substrate (Figure 4.2-11). These changes are most likely due to the corrosion barrier effect of GO.

As already introduced in the literature review (Section 2.5.2.1), the carbon lattice of graphene (oxide) is so dense that the permeation of even the smallest molecules is not allowed [19]. The chloride irons ($Cl^-$) in the corrosive electrolyte, which is the main reason for the pitting of stainless steel, were blocked by the GO coating from going inside, thus largely reducing the chances for corrosion. Although GO contains a high level of structural defects and oxygen functional groups which can make the surface of GO hydrophilic, a thickness of ~100 nm (EPD-GO2) was able to separate the substrate from the electrolyte effectively. The barrier effect built up as the coating thickness increased (~200 nm, EPD-GO4). The value of $R_c+R_{ct}$, which can be regarded as the ability of electrolyte repelling, was doubled for EPD-GO4, as shown by the EIS measurements (Figure 4.2-10 and Table 4.2-2).

Moreover, according to the XPS analysis (Figure 4.2-5), the GO sheets in the EPD coating have been simultaneously reduced to rGO. The hydrophilicity of the deposited coatings was not quantitatively measured, but it is known that rGO behaves on the hydrophobic side due to its lowered oxidation degree, and hence less permeation of water and ions can be expected [58].

### 4.5.3.2 Importance of coating integrity and homogeneity

The results in Section 4.2.3 have demonstrated that a GO coating with a sub-micron thickness fabricated via EPD can inhibit the pitting corrosion of 316L stainless steel effectively. However, it must be emphasised that the excellent corrosion performance requires the GO coating to be intact and compact. In the case of a damaged GO coating, the electrolyte can reach the substrate easily and thus cause corrosion as if there was no any GO coating.

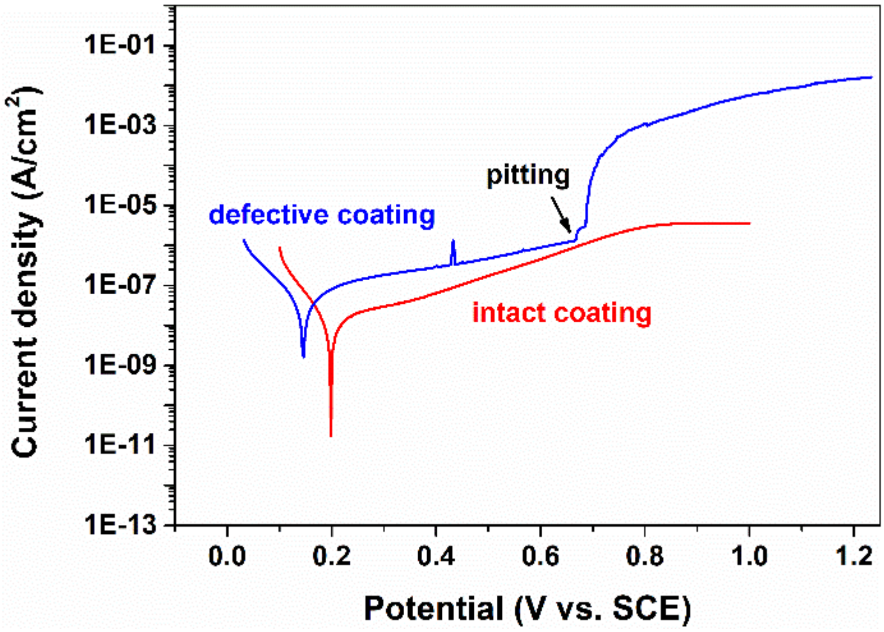

Figure 4.5-4 Polarisation curves of a 316L steel with an intact GO coating and the same material with a damaged GO coating.

For instance, Figure 4.5-4 displays the polarisation curve of a defective GO coating by the same EPD process. It is clear that not only the corrosion potential ($E_{corr}$) negatively shifted by 50 mV and the corrosion current density ($I_{corr}$) raised up by nearly one order of magnitude, but pitting also occurred as with the bare stainless steel (Figure 4.2-9b).

The failure of the protective GO coating in Figure 4.5-4 was mainly due to the destruction of the GO coating at the sealing contact, as demonstrated in Figure 4.5-5. The corrosion samples in this project were mounted at the bottom of the electrolyte container, pressing against the round testing window. The flexible GO coating can get torn, scratched and detached at these contact positions (Figures 4.5-5 a-e) during sample loading, or due to the penetration of water and corrosive ions through the overlapping edges and defects of GO sheets. Once reaching the substrate, the electrolyte undermined the GO coating and pushed the corrosion frontier inwards the tested area over time (Figure 4.5-5f). Gradually, the metallic substrate surface was corroded away and the GO coating collapsed due to no support. Figure 4.5-5g shows a fragment of the GO coating hanging at the edge of a corrosion pit. Figure 4.5-5h clearly shows the situation where the GO coating was damaged and corrosion has been initiated under the GO coating. Based on the discussion above, it is important to keep the integrity of the GO coating and ideally avoid physical impact on the coating for reliable anti-corrosion performance.

The electroplated Ni-GO composite coatings in Section 4.4 were developed in the hope of addressing the bonding and durability issues of the EPD and self-assembled GO coatings. However, the polarisation results suggested an even worse corrosion performance for the composite coatings compared with the neat Ni coating

(Figure 4.4-11). The morphology of corroded Ni-GO composite coating (ENG02) showed in Figure 4.4-12 might be a result of promoted galvanic corrosion of the nickel matrix. GO, as a carbon-based material, is chemically nobler than nickel. Therefore, in a corrosive environment galvanic corrosion cells can be formed between the GO sheets and the surrounding nickel matrix. As a consequence, the nickel would be preferably corroded. This corrosion promotion effect of GO has also been reported by others [22]. In this work the corrosion was even more pronounced due to the inhomogeneity of the Ni-GO composite coatings. The GO sheets agglomerated in the metal matrix. Where a coating defect was present and electrolyte diffuses through the defect, the corrosion current was concentrated around the GO agglomerations, thus facilitating more localised galvanic corrosion.

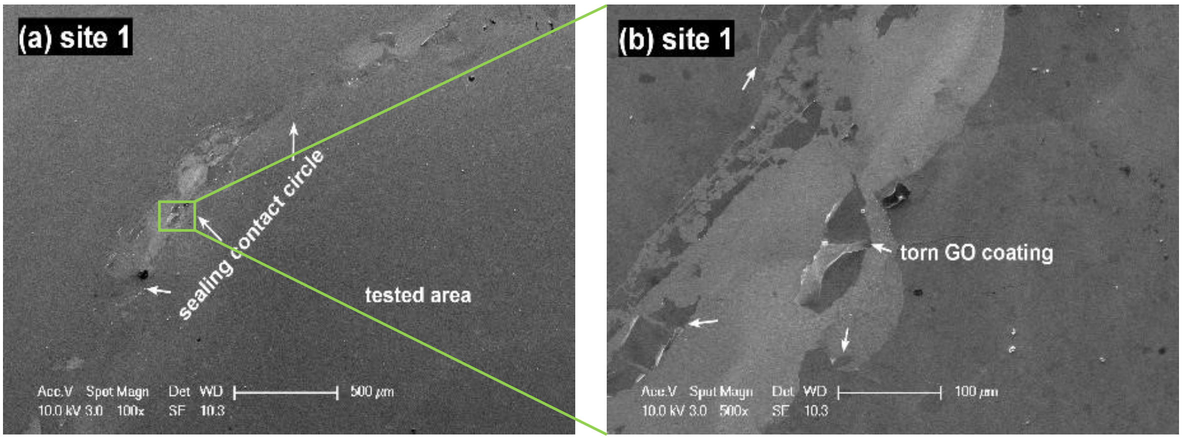

Figure 4.5-5 (a-b) GO coating damaged at the sealing contact.

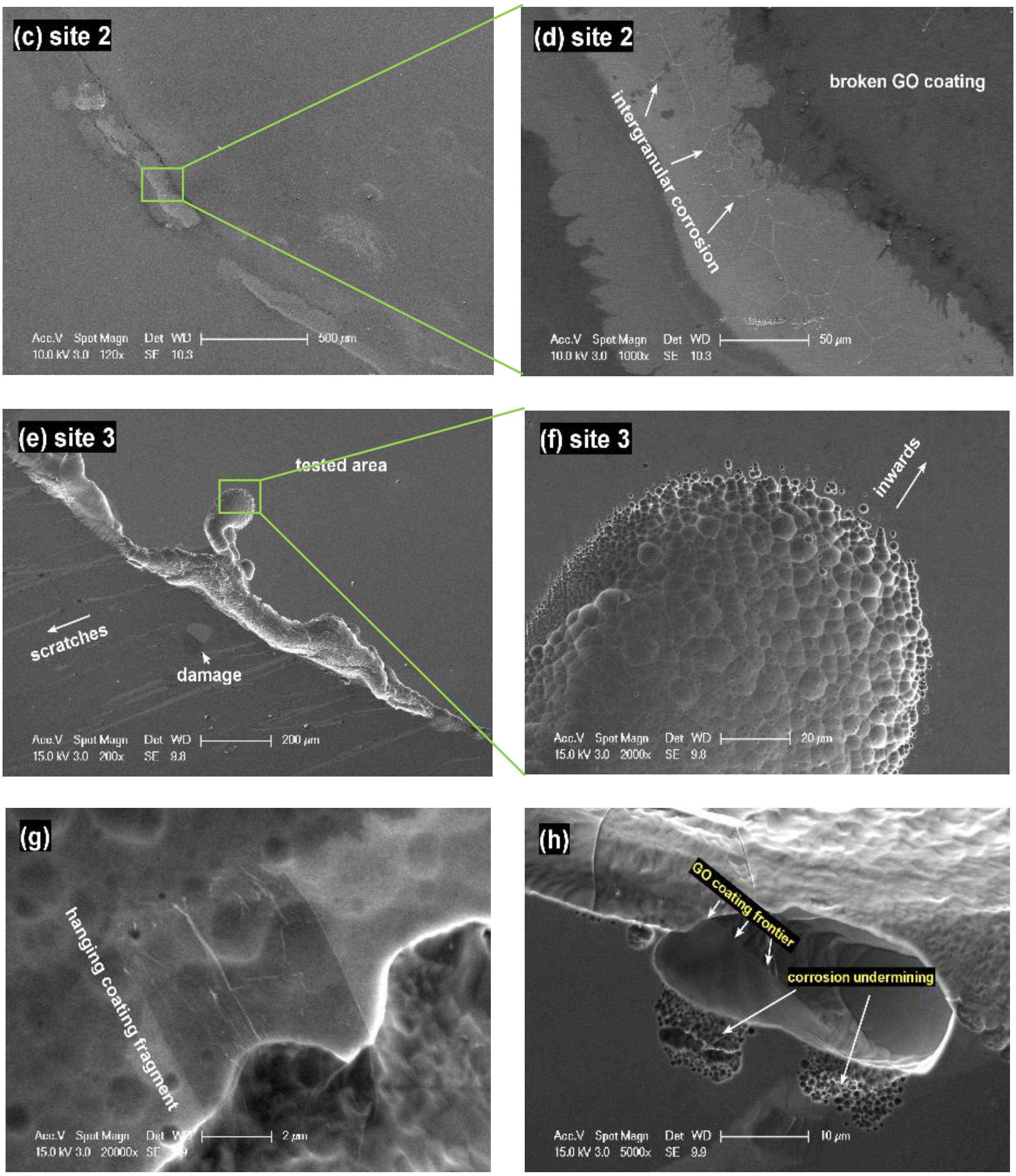

Figure 4.5-5(continued) Intergranular corrosion (c-d) and severe corrosion pits (e-f) after removal of GO coating at the sealing contact. (g-h) show corrosion propagating underneath damaged GO coatings.

# CHAPTER 5 RESULTS AND DISCUSSION: PART II

## - Electro-brush plated nickel-GO composite coatings

This chapter presents the results and discussion for the development of Ni-GO nano-composite coatings by electro-brush plating. The morphology and microstructures of the brush-plated nano-composite coatings are reported first in Section 5.1, which is followed by their mechanical properties (Section 5.2), corrosion behaviour (Section 5.3), tribological properties (Section 5.4) and thermal stability (Section 5.5). Finally, the experimental results are analysed and discussed for the advancement of scientific understanding (Section 5.6).

### 5.1 Coating morphology and structure

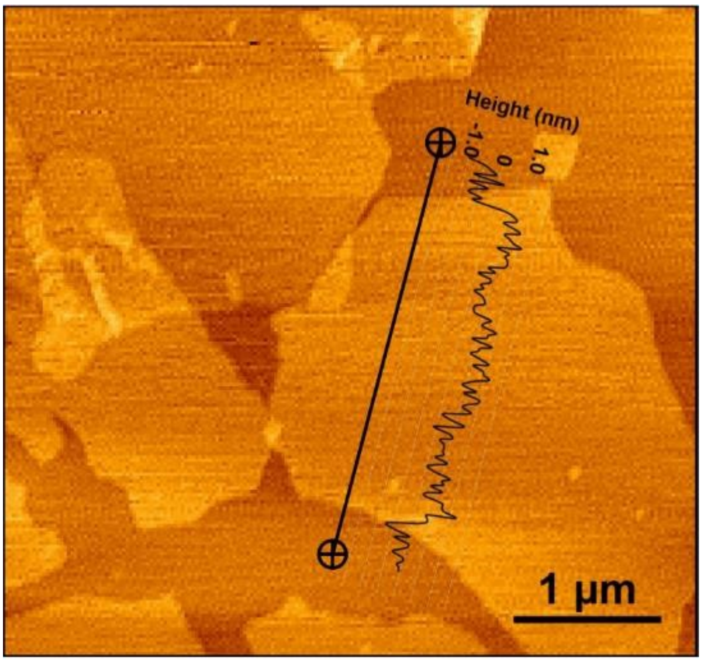

Figure 5.1-1 AFM image of the obtained graphene oxide (GO) and the height profile (black curve) of a GO sheet.

Figure 5.1-1 shows the morphology of the obtained GO sheets under AFM. The similar contrast between the planar sheets and the background (a silicon wafer) indicates a uniform thickness of the exfoliated GO sheets. The height profile across an individual GO sheet revealed a thickness of approximately 1 nm, suggesting that the GO sheets are single-layer.

Table 5.1-1 The four plating solutions and the corresponding coatings by electro brush plating

| GO content in solution (mg/ml) | 0 | 0.5 | 2.0 | 4.0 |
|---|---|---|---|---|
| Sample code | Ni | NG05 | NG20 | NG40 |

Four coatings, i.e. Ni, NG05, NG20 and NG40 were prepared by brush plating under the same plating conditions named according to the GO content in the solution for the electro-brush plating (Table 5.1-1). The coating morphologies are compared in Figures 5.1-2 a-d. There is a clear trend that the surface roughness of the resulting coatings increased with the increasing GO load. The GO-free Ni coating (Figure 5.1-2a) appeared to be compact and smooth, with few bumps and pin holes. The addition of 0.5 mg/ml GO into the plating solution resulted in the formation of nodules on the NG05 coating surface, together with some areas of clusters as circled in Figure 5.1-2b. As the GO concentration increased to 2.0 mg/ml, the nodules observed on coating NG20 (Figure 5.1-2c) became finer in size but higher in density. A further increase of the GO concentration to 4.0 mg/ml led to large surface fluctuation with a dense yet uniform distribution of agglomerations in the NG40 coating, as demonstrated in Figure 5.1-2d. The change in topography is believed to be caused by the introduction of GO. Figure 5.1-2e is a typical enlarged view of the Ni-GO composite coatings that was observed at some defect sites as pointed out in Figure 5.1-2c. The nickel clusters were all netted by ubiquitous translucent thin membranes, which is characteristic of graphene and graphene oxide sheets under SEM [238, 261].

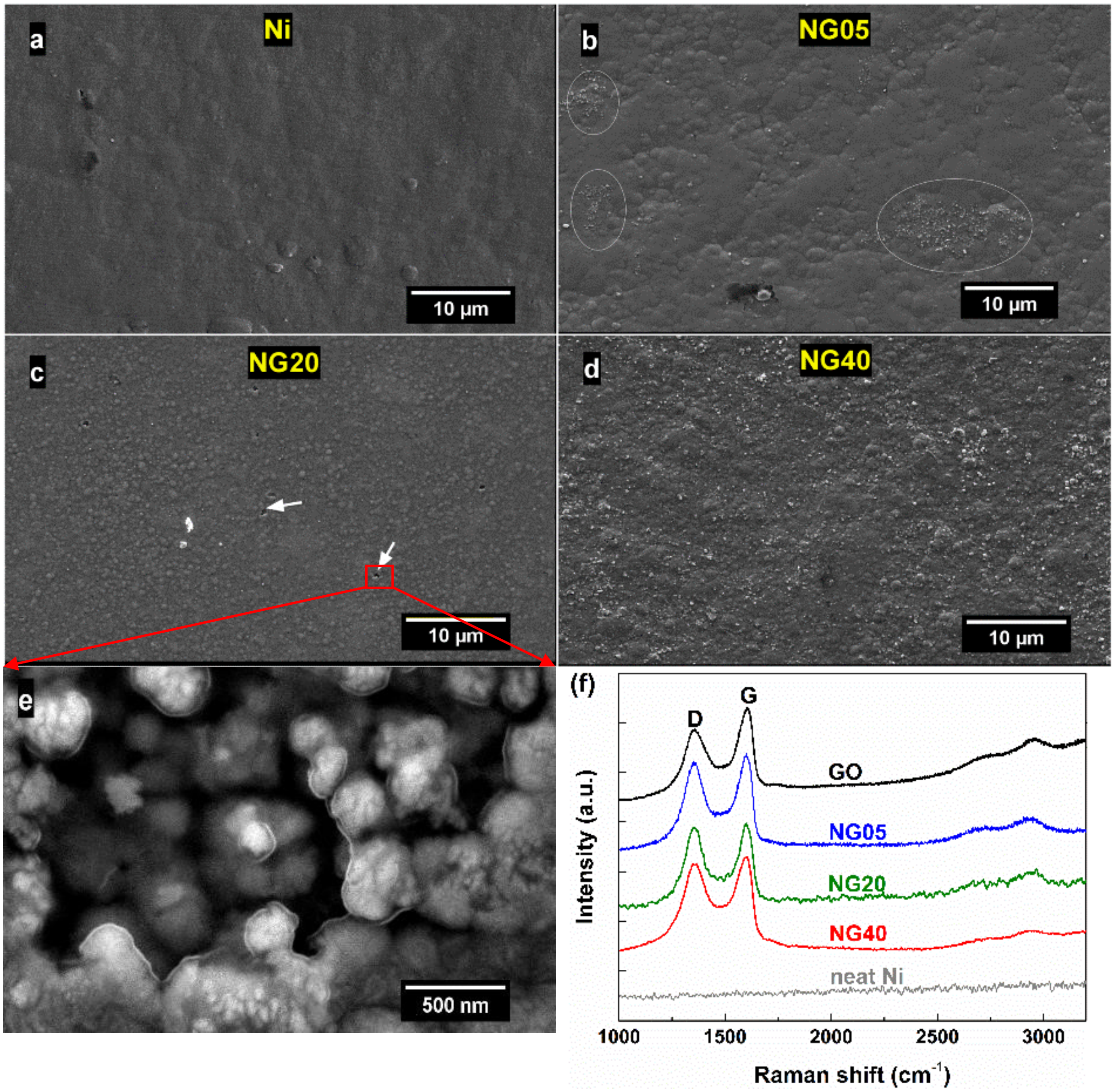

Figure 5.1-2 Morphologies of (a) neat Ni and (b-e) Ni-GO composite coatings. (f) compares the Raman spectra of GO sheets and two Ni-GO composite coatings.

Raman spectra of the original GO sheets and three Ni-GO composite coatings NG05, NG20 and NG40, were recorded and shown in Figure 5.1-2f. All the spectra display two bands around 1355 and 1580 cm$^{-1}$, which are characteristic of many carbonaceous materials. The G band at 1600 cm$^{-1}$ represents the intrinsic sp$^2$-conjugated structure of graphene, while the D band around 1350 cm$^{-1}$ rose in the presence of structural defects and disorders in the carbon skeleton. The peak shifts of the G and D bands relative to the standard values as mentioned above could be ascribed as the results of the residual stress within the composite matrixes, which will be discussed in more details in Section 5.6. The intensity ratio of D band to G band ($I_D/I_G$) is therefore usually used as an indicator of the disorder degree in graphene. The calculated $I_D/I_G$ ratios for NG05, NG20 and NG40 are 0.86, 0.88 and 0.84, respectively, which are both higher than that (0.71) of the original GO. This increase in the $I_D/I_G$ ratio for the Ni-GO composite coatings is a reflection of the increased disorder degree as mentioned above. This could be attributed to the distortion of the GO sheets among the nickel grains, and more likely the absorption or chemical bonding of nickel ions during the coating formation that could have introduced more defects and reduced the average size of the sp$^2$ domains in the graphene structure [141].

To evidence the incorporation of GO into the Ni-GO composite coatings developed, cross-sectional fractures of both neat nickel coating and a Ni-GO composite coating were prepared and compared in Figure 5.1-3. Without any GO addition to the brush plating solution, the cross-section of the resulted coating appeared to be layer-structured (Figure 5.1-3a), which is consistent with the observations on such brush-plated coatings in the literature [155, 262]. This Ni coating showed a thickness of approximately 6 μm after plating for 30 min. In comparison, the Ni-GO composite coating (Figure 5.1-3b) exhibited prominent turbulence in the layered structure. This is likely due to the GO sheets that wrapped and intersected the nickel clusters and thus disturbed the normal crystallisation process. It should also be noted that with the same working voltage and operation time the thickness of the Ni-GO composite coating measured to be about 4 μm, around 1/3 thinner than that of the neat Ni coating. Figures 5.1-3 c-d provide details of the fractography of the composite coating. Note that the cross-section was subject to mild argon plasma milling before SEM in order to enhance the presentation. It can be seen clearly that the thin semi-transparent sheets (GO) were embedded between nickel crystals (or vice versa) and conformed the contours of the nickel clusters well.

EDS analysis was performed on the cross-section of each coating with the representative result being demonstrated in Figure 5.1-3e-f. Compared with the neat Ni coating, a relatively higher content of carbon (5.37 vs 2.15, wt.%) was detected from the Ni-GO coating. The microscopical observation and elemental analysis confirm that GO sheets not only exist near the surface, but have also been incorporated into the bulk matrix of the coating successfully.

The XRD patterns of neat Ni and Ni-GO composite coatings (NG05, NG20 and NG40) are presented in Figure 5.1-4. All three patterns exhibit a prominent peak around 44° and another peak at ~51.5° which correspond to the (111) and (200) crystallographic planes of nickel, respectively. As shown in the plot, the (111) peak was broadened and the (200) peak attenuated as GO was introduced into the matrixes, implying a possible grain size reduction promoted by the incorporated GO. To this end, the average crystallite sizes of the coatings were estimated using Scherrer equation as below:

$$\beta = \frac{K\lambda}{L\cos\theta} \cdot \frac{180^\circ}{\pi} \tag{5.1-1}$$

where $\beta$ is the full width half maxima (FWHM) of the (111) diffraction in 2θ degree, $K$ is Scherrer constant (0.94 used here), $\lambda$ is the wavelength of Cu-$K_\alpha$ radiation (0.154 nm),

$\theta$ is the diffraction angle, and $L$ is the crystallite size in nm. In light of possible instrumental broadening and microstrain in the matrixes, the calculated values were normalised and compared in Table 5.1-2. In particular, the average grain size for NG40 was about 40% smaller than the neat Ni coating, suggesting a significant refinement.

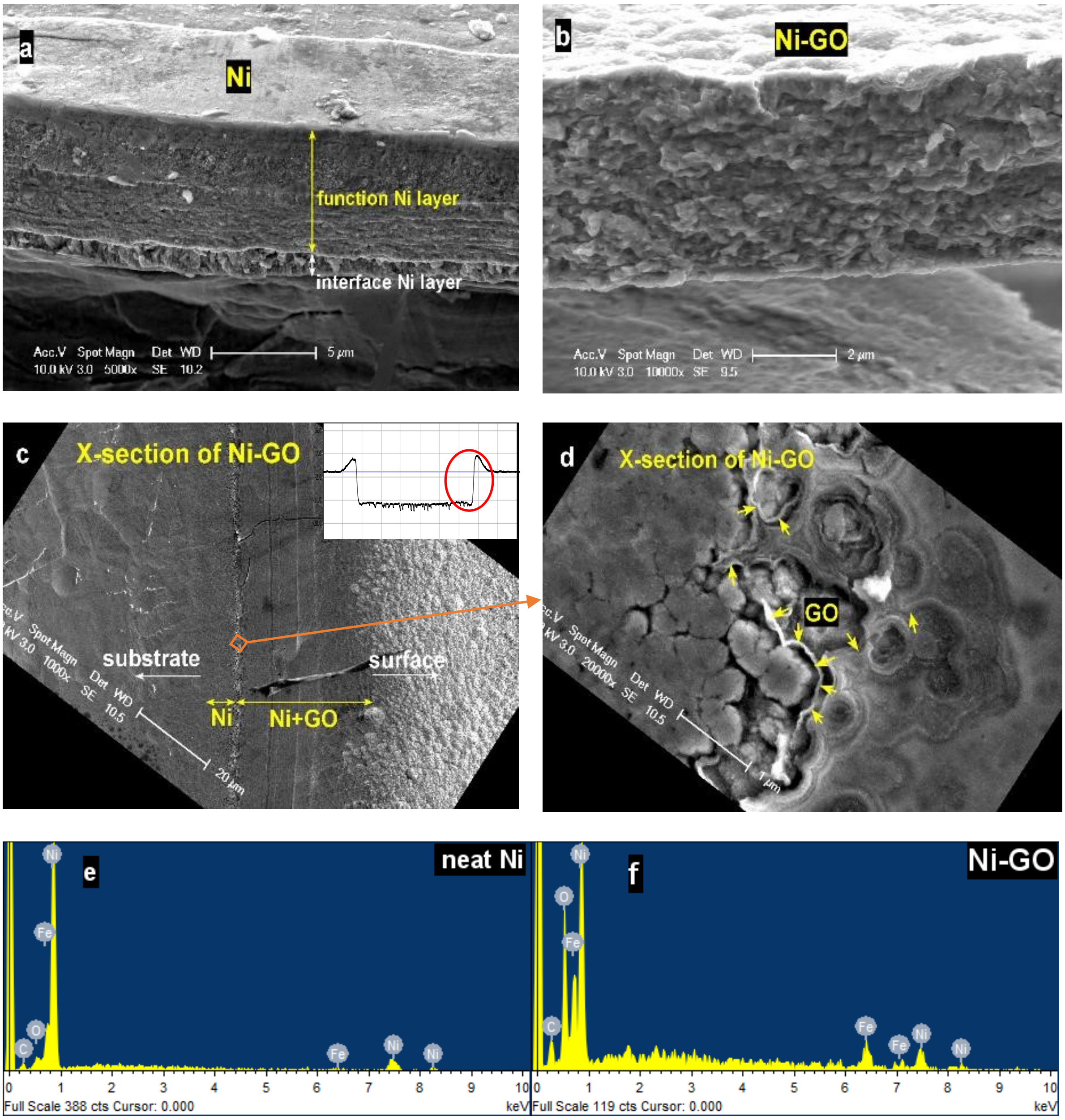

Figure 5.1-3 Cross-sectional SEM images of (a) neat Ni coating and (b-d) Ni-GO composite coatings and EDS spectra from (e) the neat Ni and (f) Ni-GO coating, respectively.

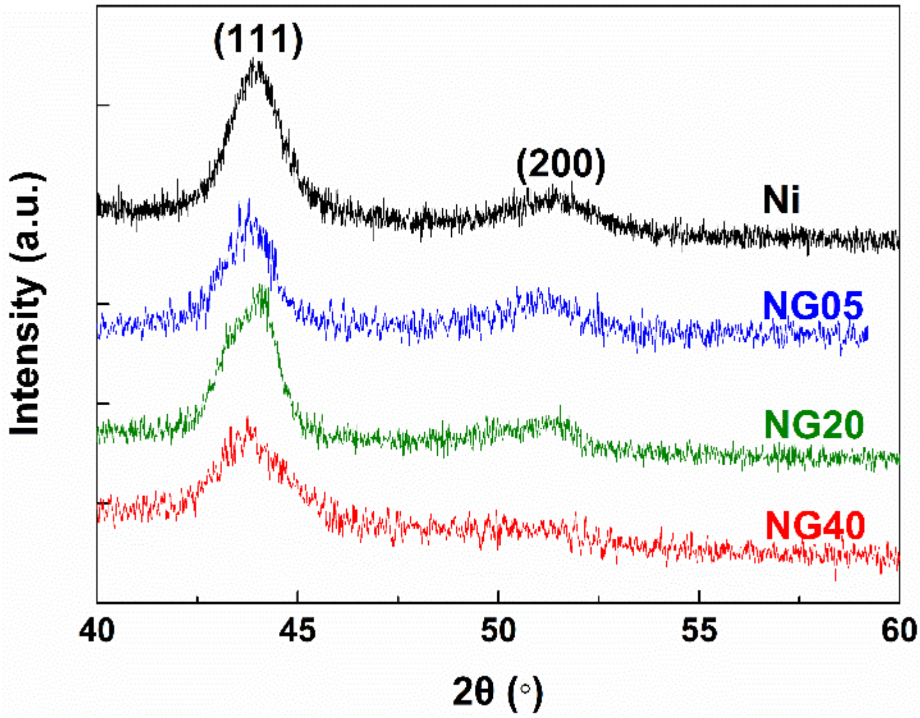

Figure 5.1-4 XRD patterns of neat Ni, NG05, NG20 and NG40 coatings.

Table 5.1-2 Calculated crystallite size for electro-brush plated neat Ni, NG05, NG20 and NG40 coatings

| | (111) FWHM (degree) | grain size approx. (normalised) |
|---|---|---|
| Ni | 1.1917 | 1 |
| NG05 | 1.2327 | 0.97 |
| NG20 | 1.3273 | 0.90 |
| NG40 | 1.9879 | 0.60 |

## 5.2 Mechanical properties

Nanoindentation tests were carried out on both neat Ni and Ni-GO composite coatings (NG05, NG20 and NG40) at a fixed peak load of 10 mN. To minimise the influence of the coating thickness and surface roughness, the measurements were performed on the polished cross-sections. Typical loading-unloading curves for each sample are presented in Figure 5.2-1. The Ni-GO composite coatings showed shallower indentation depths than that of the neat Ni at both the maximum and final stages, indicating their improved indentation resistance. As the GO content (concentration in the plating solution) increased from 0 to 2.0 mg/ml, the maximum indentation depth was reduced by ~25 nm, due to the improved hardness. This enhancement is likely related to the grain size reduction after the addition of GO nano sheets, as well as the inherent high mechanical properties of GO. However, NG40 exhibited a ‘softening’ effect compared with the other two composite coatings. This phenomenon may be the result of fine yet defective microstructure of NG40. Nonetheless, it is worth noting that the hardness of NG40 was still higher than that of the neat Ni coating.

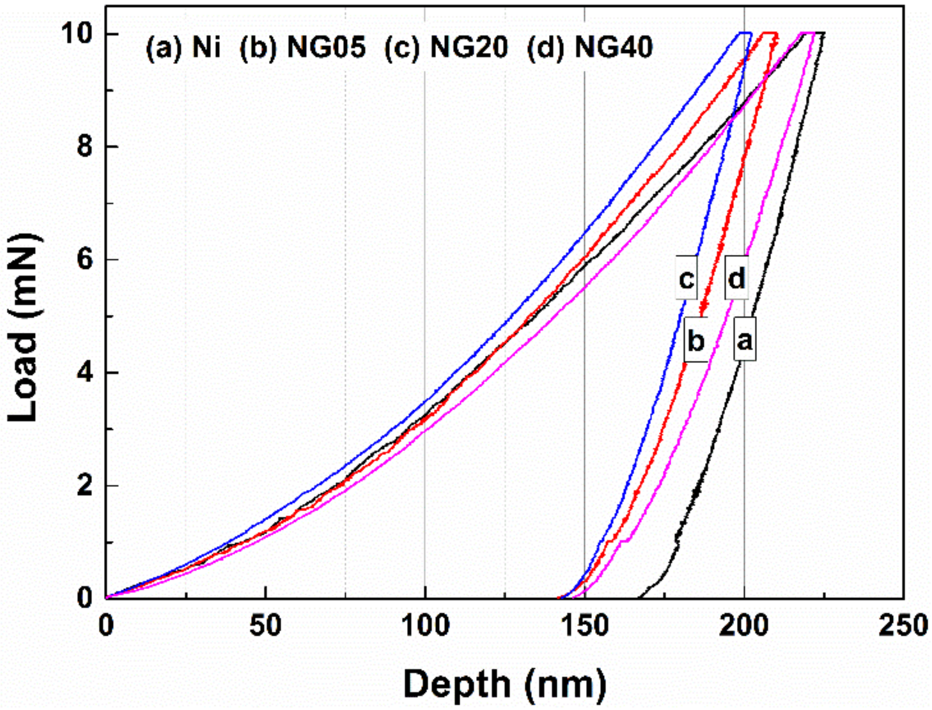

Figure 5.2-1 Typical load-displacement curves of the nanoindentation tests at a fixed peak load of 10 mN on (a) neat Ni, (b) NG05, (c) NG20 and (d) NG40 coatings.

The nanoindentation hardness and reduced modulus ($E_r$) were calculated from the loading-displacement curves based on the Oliver-Pharr fit [247]. The results are summarised in Table 5.2-1. The hardness and reduced modulus of the nano-composite coatings were improved by up to 0.9 GPa and 20 GPa respectively with GO addition until NG40 where a drop in both hardness and elastic modulus was observed. The unexpected drop in the NG40 case indicates that a too high GO concentration in the plating solution might have led to degraded mechanical properties of the resulting composite coating.

Table 5.2-1 Nanoindentation results for electro-brush plated neat Ni, NG05, NG20 and NG40 coatings

| Sample | Nano-hardness (GPa) | Reduced modulus (GPa) | Plasticity index |
|---|---|---|---|
| Ni | 7.75±0.84 | 184.52±8.08 | 0.716±0.036 |
| NG05 | 8.57±0.63 | 178.63±7.52 | 0.687±0.018 |
| NG20 | 8.65±0.41 | 206.38±14.82 | 0.704±0.015 |
| NG40 | 7.90±0.34 | 146.90±5.30 | 0.659±0.012 |

Plasticity index (PI) is a parameter usually used to evaluate the elastic-plastic response of a material to external applied forces. In nanoindentation, the PI of the tested material can be characterised by the area included in the load-displacement curve (non-reversible plastic work) using the following equation:

$$\psi = \frac{A_1 - A_2}{A_1} \quad (5.2\text{-}1)$$

where $\psi$ is the plasticity index, $A_1$ and $A_2$ are the areas under the loading curve (total work) and unloading curve (elastic work), respectively. The calculated PI values for each sample are listed in Table 5.2-1. Interestingly, all the three GO-containing coatings exhibited lower plasticity than the GO-free nickel coating, including NG40 which showed the highest reduction of ~8% towards the plasticity index. This is in line with the observation in Figure 5.2-1 that all the Ni-GO composite coatings left a smaller final indentation depth, regardless of the increased peak depth in the NG40 case.

More interestingly, nanoindentation study has revealed that GO improved the thermal stability of the Ni-GO composite coatings effectively. The GO-containing nickel coating exhibited less degradation in mechanical strength when annealed at elevated temperatures. The detailed investigation and results are documented in Section 5.5.

## 5.3 Corrosion behaviour

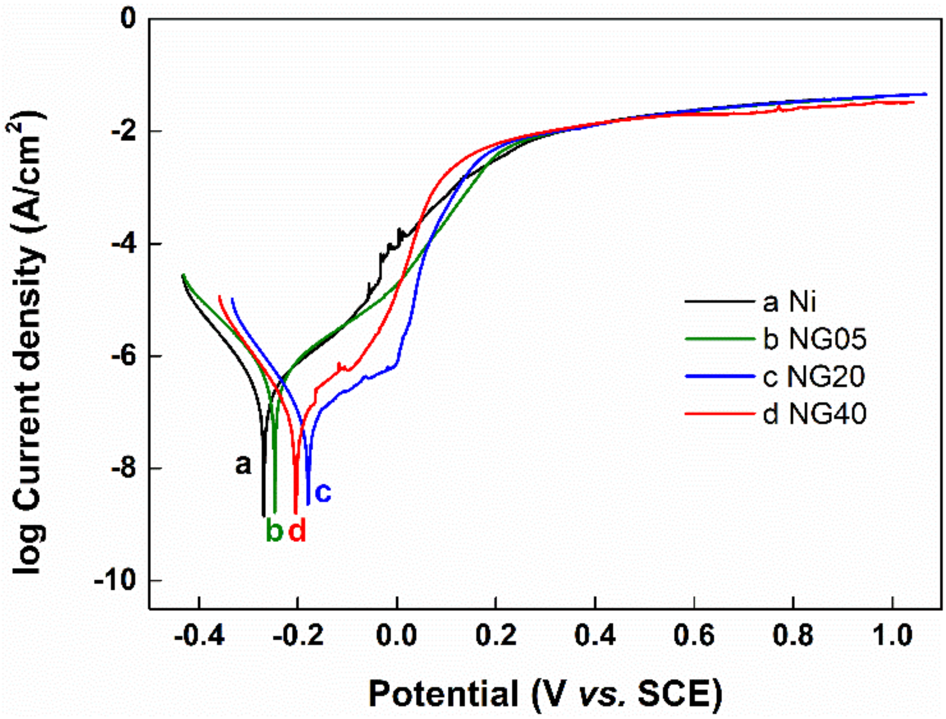

Figure 5.3-1 Polarisation curves of (a) neat Ni, (b) NG05, (c) NG20 and (d) NG40 coatings in a 3.5wt.% NaCl solution.

The corrosion behaviour of the brush-plated Ni-GO nano-composite coatings (NG05, NG20 and NG40) as well as the neat Ni coating was investigated by means of polarisation and EIS measurements in a 3.5 wt.% NaCl solution. Figure 5.3-1 shows the polarisation curves after an OCP measurement for 1 h. In comparison to the neat Ni coating, both NG20 and NG40 demonstrated a clear positive shift of the corrosion potential ($E_{corr}$), revealing a less corrosion tendency. NG05 showed marginal shift in $E_{corr}$, likely due to the small amount of GO incorporation.

Table 5.3-1 Tafel fit parameters for the polarisation curves of electro-brush plated neat Ni, NG05, NG20 and NG40 coatings

| Sample | OCP (mV) | $E_{corr}$ (mV) | $I_{corr}$ ($\times10^{-9}$ A/cm$^2$) | Corrosion rate ($\times10^{-3}$ mpy) |
|---|---|---|---|---|
| neat Ni | -232 | -269 | 309 | 131.4 |
| NG05 | -230 | -247 | 357 | 163.3 |
| NG20 | -133 | -179 | 131 | 55.8 |
| NG40 | -158 | -204 | 92.4 | 39.3 |

The results of Tafel fit to the polarisation curves (Table 5.3-1) also suggest that in the presence of GO fillers the corrosion current densities ($I_{corr}$) of NG20 and NG40 decreased remarkably by approximately 60% and 70%, respectively. Accordingly, the corrosion rate was suppressed down to 55.8 $\times10^{-3}$ mpy (NG20) and 39.3 $\times10^{-3}$ mpy (NG40) from the 131.4 $\times10^{-3}$ mpy for the GO-free coating. NG20 demonstrated a passive characteristic within a wide range of the anodic polarisation period (from $E_{corr}$ to ~0 V vs. SCE), indicating an enhanced impermeability owing to the GO sheets. A breakdown point at ~0 V was met, after which the polarisation current built up quickly to a high level equal to the neat Ni, suggesting that the GO components lost their power in preventing the corrosive electrolyte from penetrating through the coating. NG40 resembled NG20 roughly in terms of the polarisation curve shape, whilst exhibiting a slightly more negative corrosion potential and higher current densities in the anodic polarisation section, indicating a smaller polarisation resistance. The turbulences of the anodic polarisation currents occurred on some of the tested samples and could be related to solvent penetration through the localised defects within the nickel matrixes. The Tafel fitting suggests no reduction of the corrosion rate for NG05 ($163.3 \times 10^{-3}$ mpy).

To elucidate the corrosion protection mechanism for each type of coating, electrochemical impedance spectroscopy (EIS) measurements were carried out on neat Ni, NG05, NG20 and NG40. In EIS, a small sinusoidal electrical signal (±10 mV, 10m – 100k Hz in this work) about the open circuit potential is applied to the sample surface and the electrochemical response to the excitation at different frequencies is recorded and analysed [263]. Figure 5.3-2a is the Bode plot in which the absolute values of the impedance (|Z|) and the phase angle are plotted as the function of excitation frequency. At the highest frequencies the |Z| magnitude plots are flat, revealing primarily the resistance of the electrolyte solution ($R_s$). At intermediate frequencies, the capacitive response from the coating system ($C_c$) predominates, which is characterised by diagonal lines in the |Z| magnitude plots and the largest phase angles. As the frequency is further lowered, the coating resistance $R_c$ (or interfacial charge transfer resistance $R_{ct}$) tends to dominate the total impedance, depicted by flattened |Z| curves as resistors are independent of frequency. It is revealed in Figure 5.3-2a that the impedance moduli |Z| of NG20 and NG40 at the lowest frequency were both significantly higher than that of the neat Ni, which is a sign of higher corrosion resistance. The |Z| plots of NG05 and NG40 largely resembled that of

NG20, until around the lowest frequency end when the impedance moduli headed down to some extent.

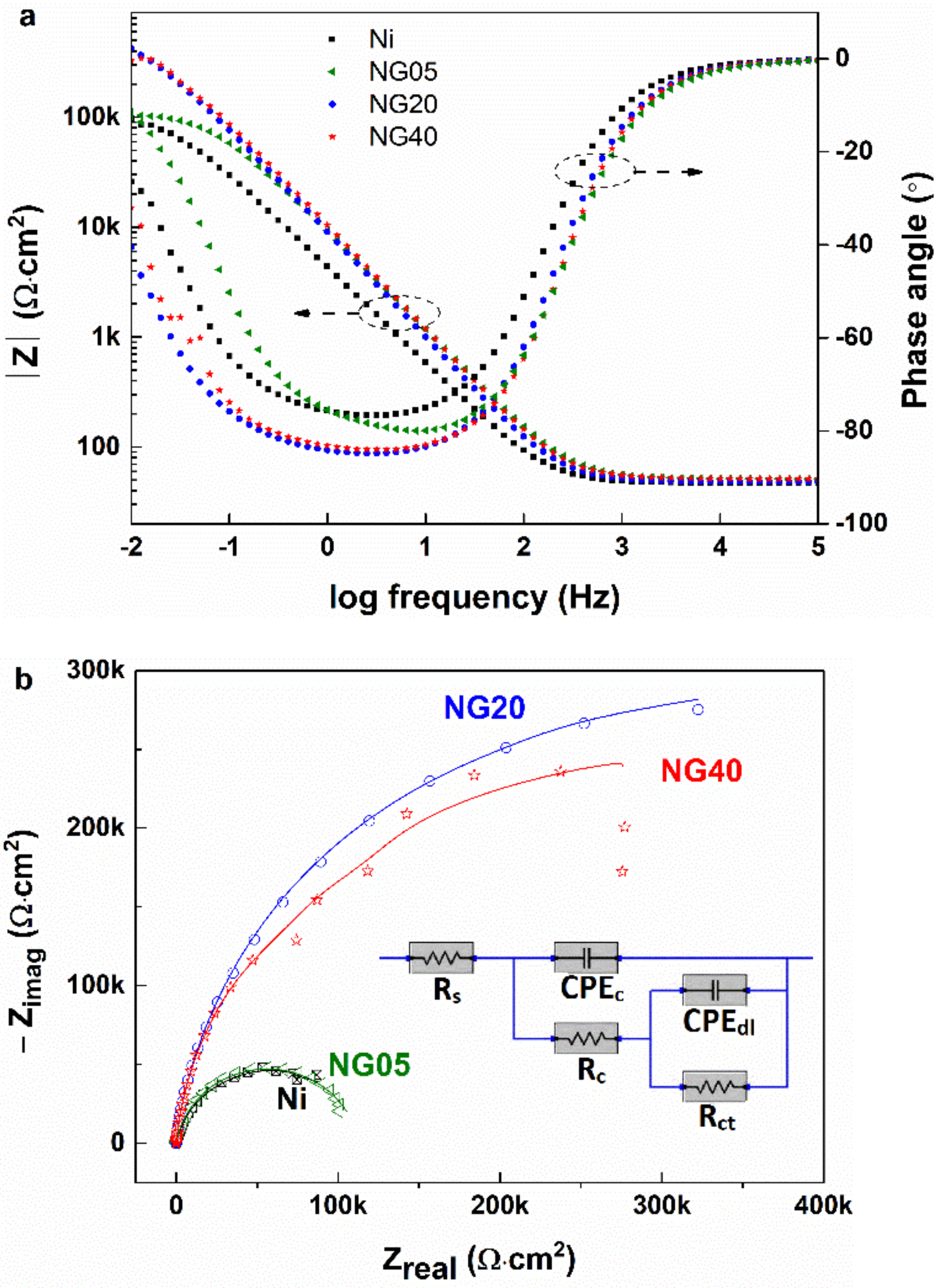

Figure 5.3-2 (a) Bode and (b) Nyquist plots for different samples in a 3.5wt.% NaCl solution and the equivalent circuit model proposed for the coating system (inset of b). The dots and the solid lines in (b) illustrate the original impedance data and the fitted curves, respectively.

Figure 5.3-2b displays the corresponding Nyquist plots for the tested samples, in which the impedance at each frequency is located according to its real (resistive) and imaginary (capacitive) components. NG05 showed a dataset similar to that of neat Ni. NG20 and NG40 coatings showed remarkably larger semi-circular arc compared with the neat Ni coating. In general, a larger impedance arc is the result of a higher polarisation (or electron charge transfer) resistance, and much likely a reflection of a greater corrosion resistance. It is also worth noting that the NG40 exhibited an unusual impedance loop at low frequencies (the far end of the impedance arc). This loop is related to an inductive behaviour rather than capacitive, which could be ascribed to the corrosion and dissolution of the metallic surface and the adsorption of the intermediate species [264].

In order to quantify the interpretation of the EIS spectra, electrical equivalent circuit models of the three corrosion systems were attempted. The adapted model and corresponding fitting curves (solid lines) are illustrated in Figure 5.3-2b and the refined fit parameters for each coating sample summarised in Table 5.3-2. A constant phase element (CPE) is a circuit element with a constant phase shift over the frequency, and was employed in this work to model an imperfect capacitor, whose impedance is expressed as:

$$Z_{CPE}(\omega) = \frac{1}{CPE\cdot(j\omega)^n} \tag{5.3-1}$$

where $n$ is the phase shift index ($n$=1 for an ideal capacitor). $R_s$, $R_c$ and $CPE_C$ ($C_C$) were employed as previously described. An additional pair of double layer capacitance ($CPE_{dl}$) and charge transfer resistance ($R_{ct}$) were introduced in order to simulate the situation where the electrolyte penetrates into the coating and forms a new electric double layer at the liquid/metal interface. It is revealed in Table 5.3-2 that the $R_c$ for the neat Ni coating was just 6.8 kΩ·cm$^2$, while NG20 and NG40 exhibited a dramatically increased $R_c$ of 519 kΩ·cm$^2$ and 371 kΩ·cm$^2$, respectively, indicative of a much greater resistance to the corrosion environment. Furthermore, their higher $R_{ct}$ and $CPE_{dl}$ values suggest that the two coatings were less permeable owing to the presence of GO sheets, thus exposing less active area to the corrosive electrolyte, and thus corrosion was less likely. Similar increase in $R_{ct}$ was also reported by Park et al. [150] and Zhou et al. [166]. The overall polarisation resistance ($R_c$ + $R_{ct}$) increases in the order of Ni (118 kΩ·cm$^2$) < NG05 (133 kΩ·cm$^2$) < NG40 (548 kΩ·cm$^2$) < NG20 (678 kΩ·cm$^2$).

Table 5.3-2 Equivalent circuit fit parameters for the EIS samples

| Sample | $R_s$ (Ω·cm$^2$) | $R_c$ (kΩ·cm$^2$) | $CPE_c$ (μS·s$^n$·cm$^{-2}$) | $n_1$ | $R_{ct}$ (kΩ·cm$^2$) | $CPE_{dl}$ (μS·s$^n$·cm$^{-2}$) | $n_2$ |
|---|---|---|---|---|---|---|---|
| Ni | 47.0 | 6.8 | 38.9 | 0.908 | 112 | 9.6 | 0.658 |
| NG05 | 51.0 | 19.2 | 7.3 | 1 | 114 | 13.3 | 0.829 |
| NG20 | 48.1 | 519 | 19.7 | 0.948 | 159 | 106 | 1 |
| NG40 | 51.4 | 371 | 16.8 | 0.949 | 177 | 37.2 | 0.998 |

## 5.4 Tribological behaviour

### 5.4.1 Surface roughness and hardness

The samples involved in this chapter and their corresponding surface roughness are listed in Table 5.4-1. It is clear that the surface roughness of the obtained composite coatings increased with the increasing GO load in the plating solution. The nickel-graphite composite coating (NGr40) showed a much higher surface roughness (~234 nm) than the nickel-GO composite coatings (132 nm for NG40). Figure 5.4-1 compares the microhardness of the samples. The original nickel deposit exhibited a hardness of

$H_v$ 500, which is comparable to the values reported for electro-brush plated nickel coatings [153, 160]. The hardness was improved gradually as GO was introduced into the plating solution, with a peak value of $H_v$ 680±57 for NG20, which is 31% higher than that ($H_v$ 524±38) of the neat (GO-free) nickel coating. NG40 exhibited a less improved hardness ($H_v$ 609±37), likely due to more structural defects. In comparison, the Ni-graphite composite coating NGr40 showed a hardness of $H_v$ 574±20.

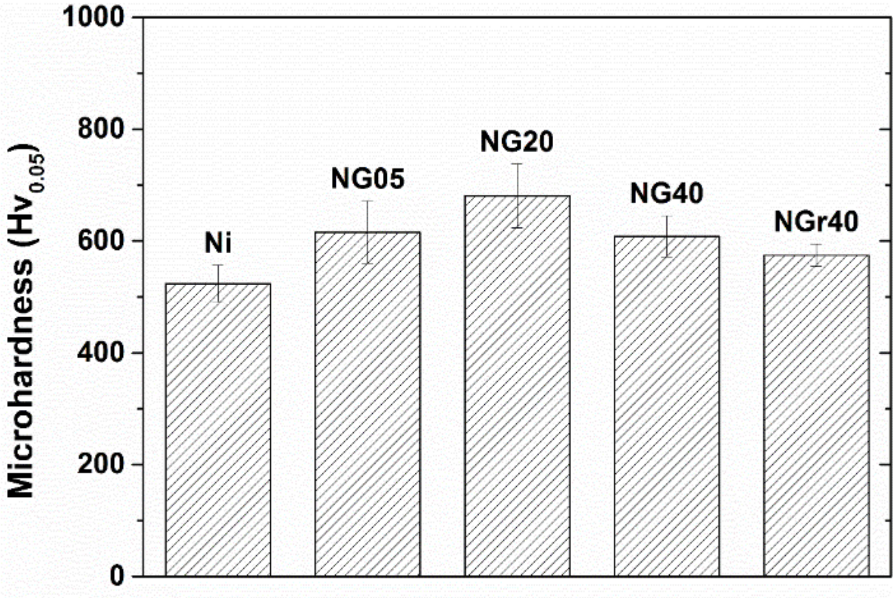

Figure 5.4-1 Microhardness of the brush-plated coatings.

Table 5.4-1 Specification and surface roughness of samples

| Material | GO/graphite load (mg/ml) | Surface roughness ($R_a$, nm) |
|---|---|---|
| Ni | 0 | 42.2±10.3 |
| NG05 | 0.5 | 54.8±17.7 |
| NG20 | 2.0 | 86.8±16.1 |
| NG40 | 4.0 | 131.7±17.0 |
| NGr40 | 4.0 | 234.8±22.9 (as-made) |
|  |  | 71.3±5.9 (polished) |

### 5.4.2 Sliding against a chromium steel ball in air

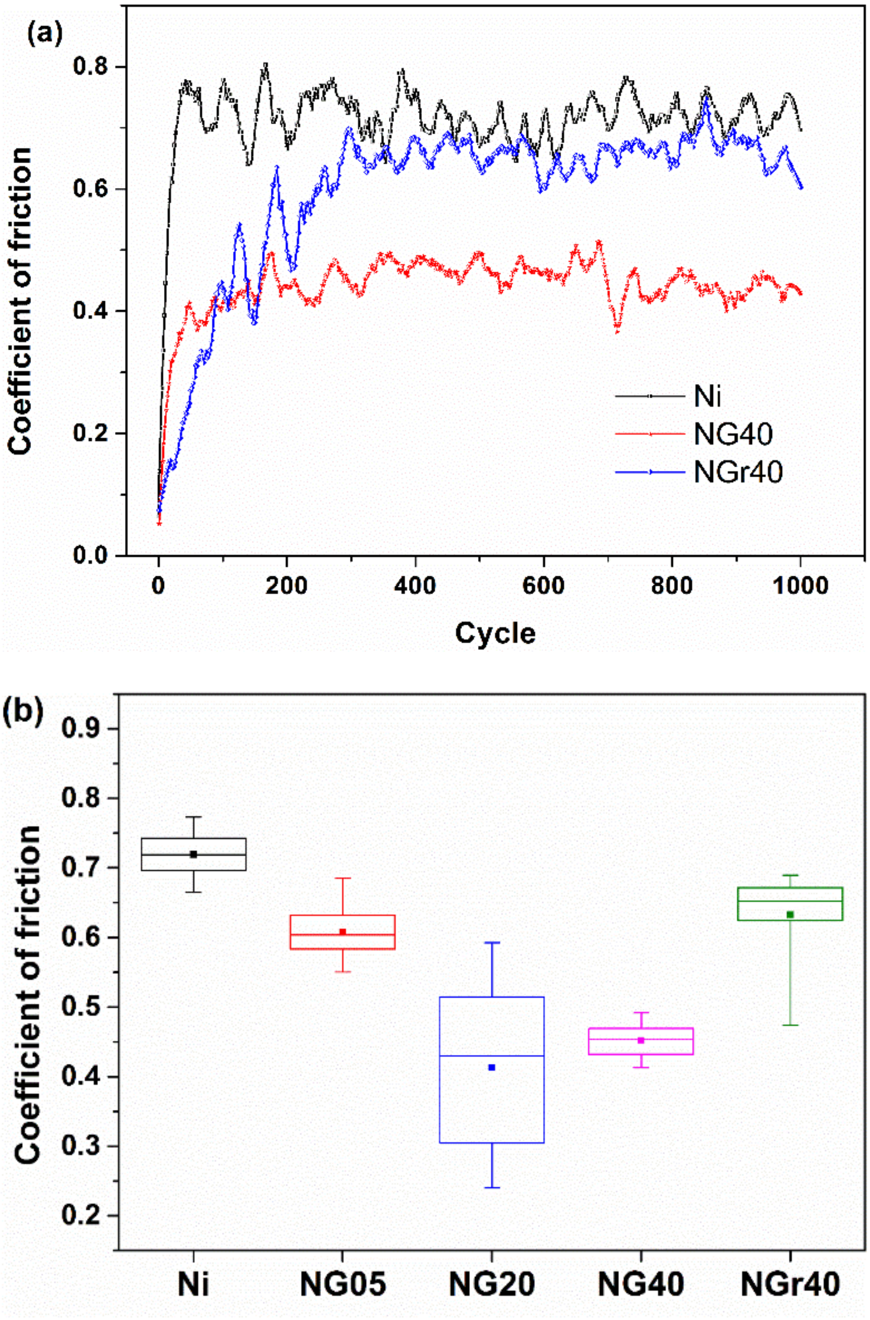

Figure 5.4-2 (a) Coefficient of friction (COF) for neat Ni, NG40 and NGr40 coatings over 1000 cycle reciprocating sliding in air against a chromium bearing steel ball under a load of 1 N (G: graphene oxide; Gr: graphite). (b) COF distribution of Ni, NG05, NG20, NG40 and NGr40.

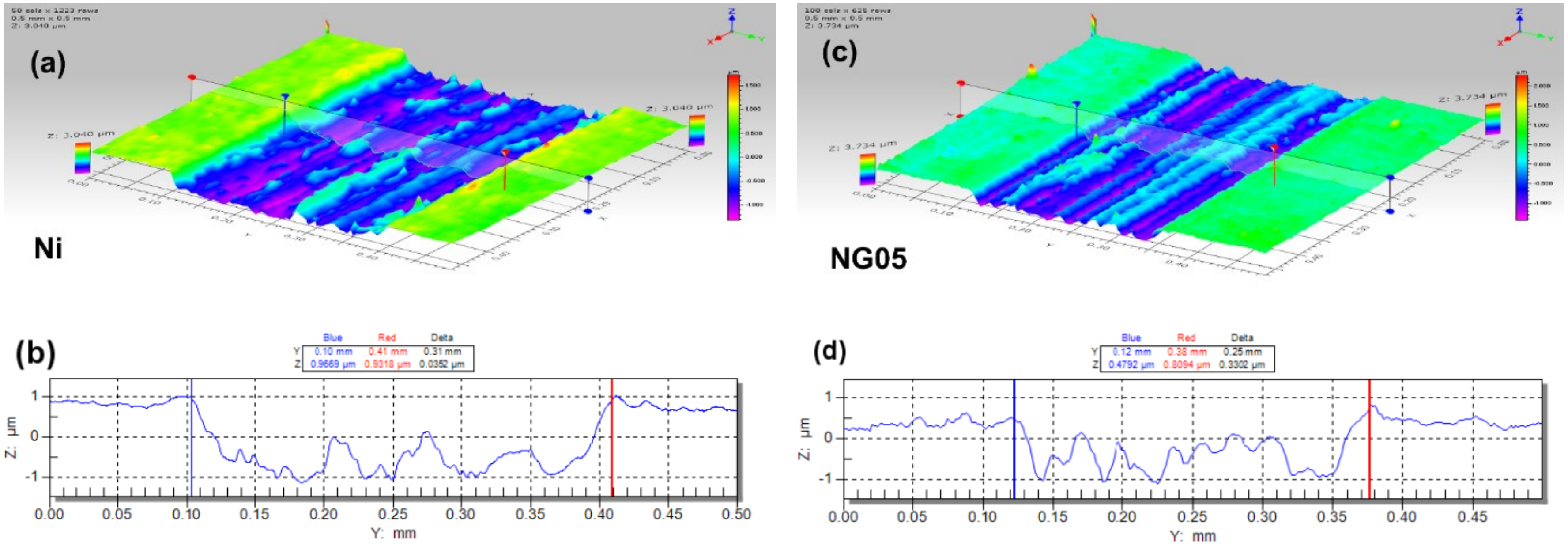

Figure 5.4-3 3D and the corresponding cross-sectional height profiles of the worn (a-b) neat Ni and (c-d) NG05. The blue and red cursors in the plots indicate the edges of the wear track.

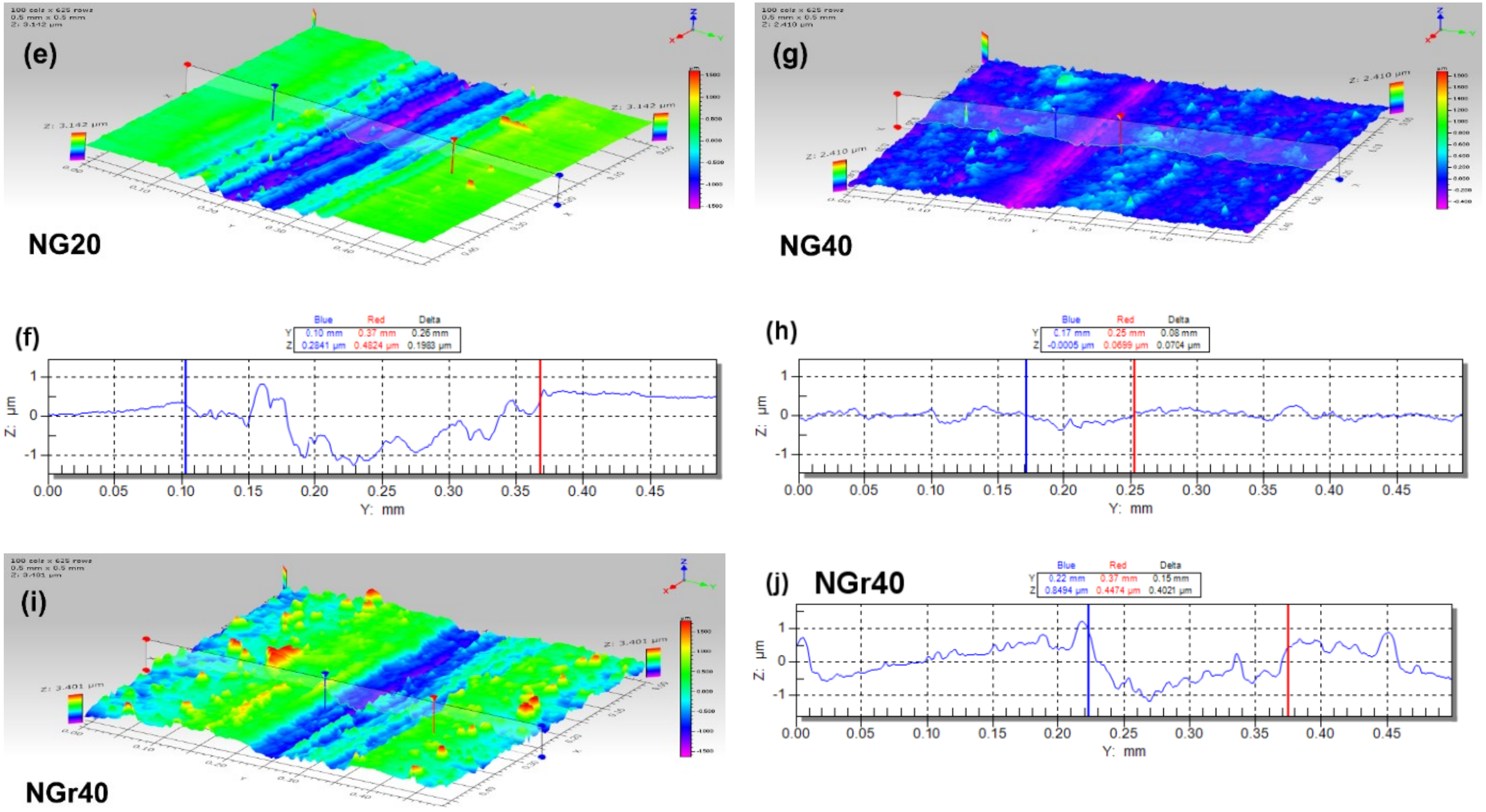

Figure 5.4-3(continued) 3D and the corresponding cross-sectional height profiles of the worn (e-f) NG20, (g-h) NG40 and (i-j) NGr40. The blue and red cursors in the plots indicate the edges of the wear track.

Reciprocating tribological tests were performed on a ball-on-plate tribometer with a chromium bearing steel counter ball under a normal load of 1 N. The coefficient of friction (COF, $\mu$) curves for neat Ni, NG40 and NGr40 over sliding cycles were demonstrated in Figure 5.4-2a. The COF of the GO-free coating reached a plateau around 0.7 after a short running-in period. NG40 exhibited a substantially lower steady-state $\mu$ of ~0.45, indicating effectively suppressed friction benefited from GO. With a comparable particle load as NG40, NGr40 showed a marginally reduced $\mu$, levelling at ~0.65. Its prolonged running-in period can be attributed to its high surface roughness which increased the time required for stabilising the contact.

Table 5.4-2 Static Hertz stress and contact width for the ball-on-plate frictional tests using different ball materials

| Ball | Load (N) | Maximum Hertz stress (MPa) | Contact width (μm) |
|---|---|---|---|
| Chrome bearing steel | 1 | 540 | 59 |
| | 3 | 779 | 86 |
| | 5 | 924 | 102 |
| α-Alumina | 1 | 631 | 55 |
| | 3 | 910 | 79 |
| | 5 | 1079 | 94 |

Figure 5.4-2b is the box plots of the steady-state COF for each sample. The upper and lower borders of a box indicate the 75% and the 25% limits of the data set, while the two ends of the whiskers represent the 95% and the 5% limits, respectively. As shown in the chart, all the four composite coatings showed reduced friction compared to the neat nickel coating ($\mu$ ~0.72). With the smallest amount of GO incorporation, NG05 showed slightly reduced COF (~0.6). NG20 exhibited the lowest friction against

the chromium steel ball ($\mu$ down to ~0.25). However, note that its coefficient of friction fluctuated in a wide range, due to its unstable friction conditions. NG40, as already demonstrated in Figure 5.4-2a, was able to show a stable low $\mu$ of around 0.45. It is also worth noting that the three nickel-GO coatings outperformed the nickel-graphite coating.

Figure 5.4-3 demonstrates the 3D and the corresponding cross-sectional height profiles of the wear tracks. The neat Ni coating (Figure 5.4-3a&b) showed the widest (310 μm) and deepest (2 μm) wear scar, with heavy furrows and push-ups on the bottom, denoting severe sliding adhesive wear. NG05 (Figure 5.4-3c&d) ended up with a wear scar of slightly reduced width (250 μm) and depth (~1.2 μm). There was no appreciable difference in the worn depth for NG20, but the edges of the wear track were less rigid (Figure 5.4-3e&f), indicating a reduced wear loss. As the GO content further increased, a smooth and shallow (0.3 μm in depth and 60 μm in width) wear scar was found on NG40 (Figure 5.4-3g&h), indicative of a significant reduction in wear. This is in sharp contrast to the brush-plated nickel-graphite composite coating NGr40 (Figure 5.4-3i&j), whose wear loss was much larger than that of NG40. The dimensionless wear coefficient was calculated using the following equation:

$$k = \frac{V}{F \cdot s} \tag{5.4-1}$$

where $V$ is the volume of material loss, $F$ is the applied normal load, $s$ is the total sliding distance, $k$ is the dimensionless wear coefficient in $mm^3N^{-1}m^{-1}$. The wear volume was obtained by multiplying the cross-section area and the length of the wear track. The cross-section area was determined by averaging three measurements at different positions of a wear track. The values of the wear coefficient for each sample are summarised in Figure 5.4-4. Compared with the neat Ni coating, the wear coefficients for NG05 and NG20 were reduced by 51.5 % and 58.0 %, respectively. NG40 showed a wear coefficient of 52.7×$10^{-6}$ mm$^3$N$^{-1}$m$^{-1}$, nearly 9 times less than that (448.4×$10^{-6}$ mm$^3$N$^{-1}$m$^{-1}$) of neat Ni. NGr40 was also able to achieve reduced wear (121.2×$10^{-6}$ mm$^3$N$^{-1}$m$^{-1}$) but still twice higher compared to NG40.

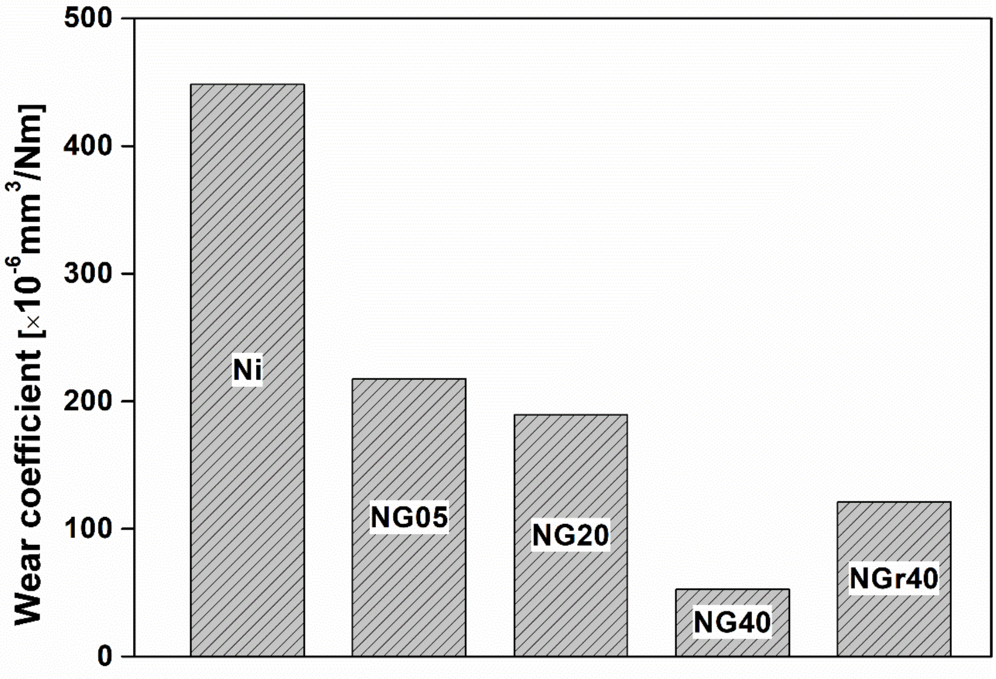

Figure 5.4-4 Wear coefficient for neat Ni, NG05, NG20, NG40 and NGr40 measured after 1000-cycle sliding in air against a bearing steel ball under a normal load of 1 N.

The worn surfaces were examined under SEM. Figures 5.4-5a-b present the worn neat nickel coating. The high roughness and discrete 'islands' of material indicate that major material deformation has happened during wear. A large density of fine wear debris was present both alongside and inside the wear scar, implying that three-body abrasive wear could also have taken place. Cutting due to abrasion and fatigue cracks due to high friction stress were observed (Figure 5.4-5b). EDS analysis showed that the islands were high in oxygen while the bottom of the wear track showed little oxygen (Figures 5.4-5c&e). The chemical analysis of the wear debris (Figures 5.4-5d and 5.4-5f) showed that the larger debris was mainly delamination of the un-oxidised metallic coating, whilst the fine particles were mostly oxide. The quantitative results of the EDS analysis above are summarised in Table 5.4-3. The information above suggests that the oxidised surface of the neat nickel coating was destructed into debris during the unlubricated wear. As a result, severe metal-to-metal rubbing occurred.

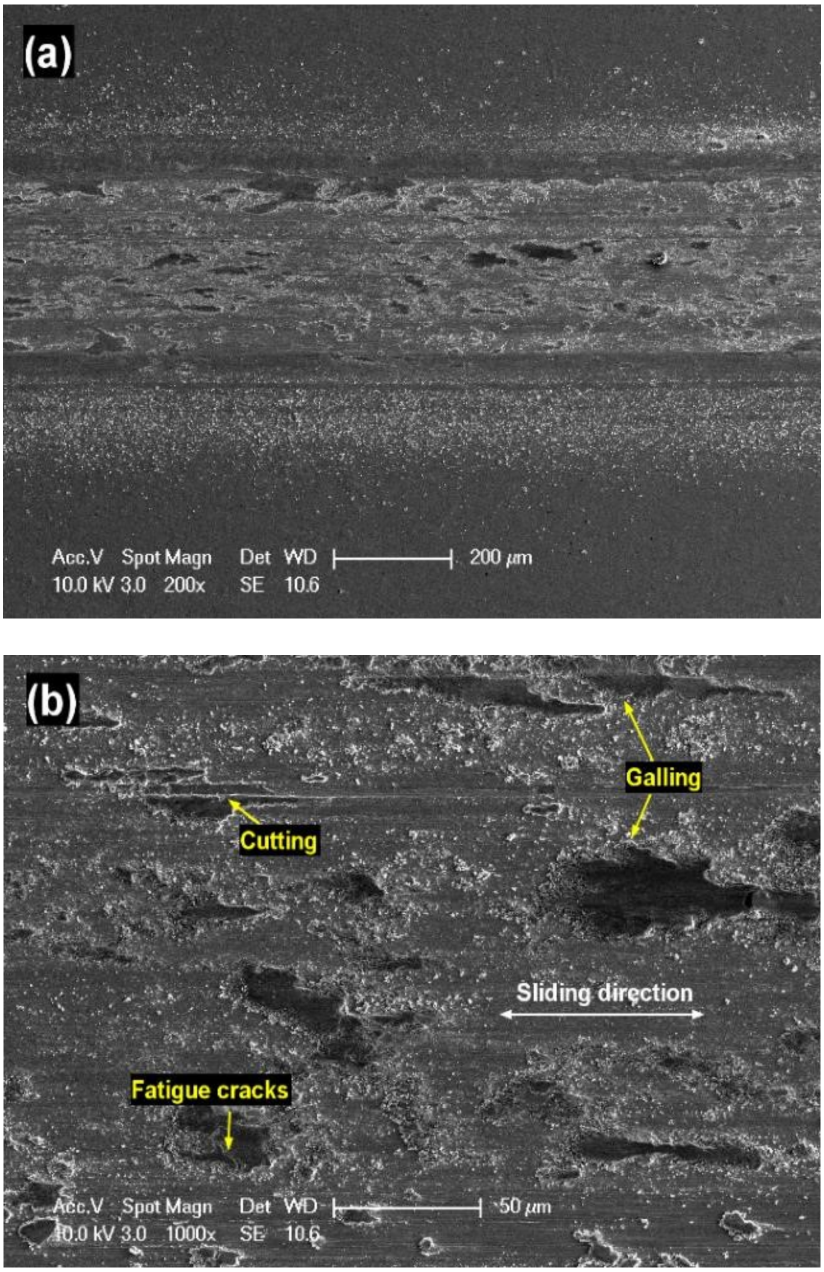

Figure 5.4-5 (a-b) SEM images of the worn surface of the brush-plated neat Ni coating sliding against a Cr ball in air under a load of 1 N.

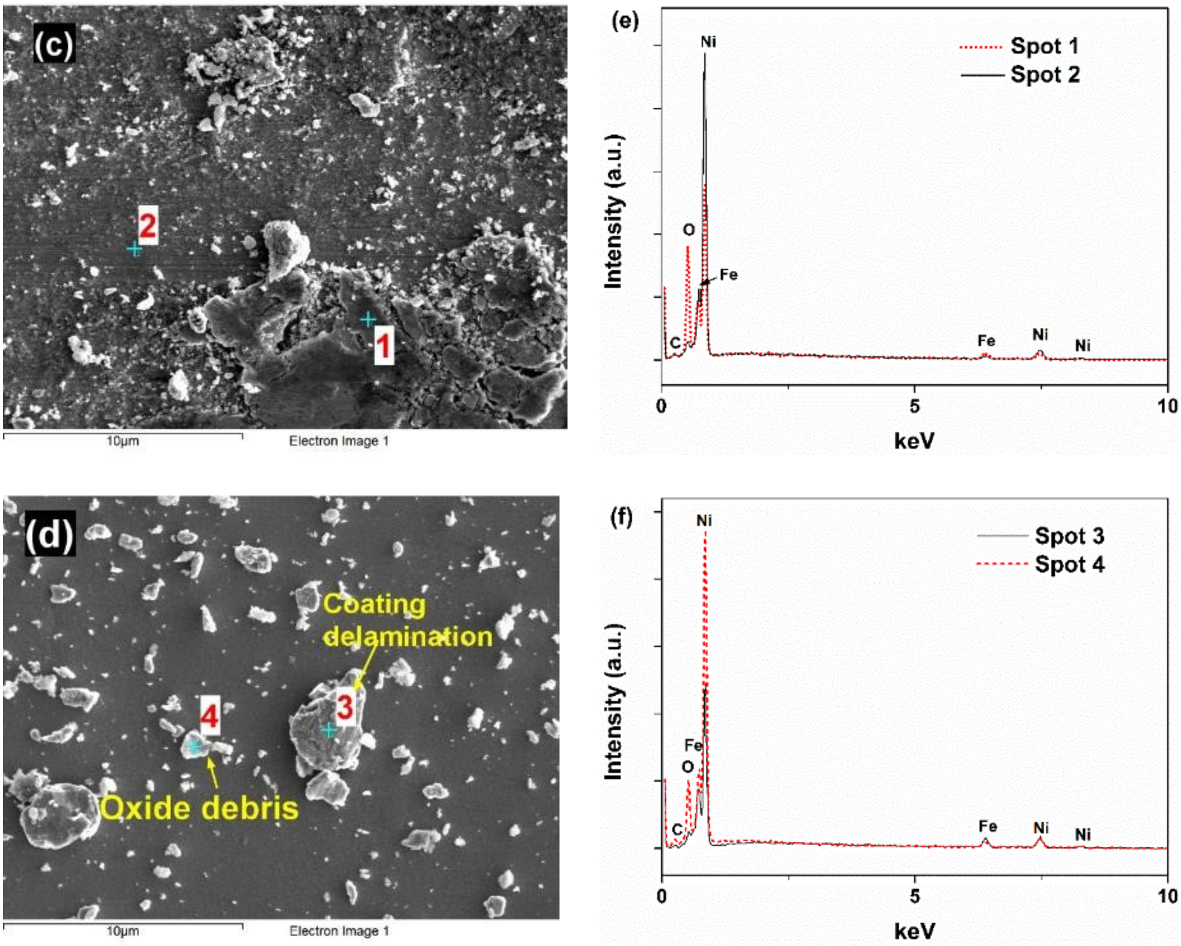

Figure 5.4-5(continued) (c-d) SEM images and (e-f) the corresponding EDS analysis of the wear debris on the brush-plated neat Ni coating.

Table 5.4-3 EDS results from the wear track and debris on the neat Ni surface. Analysis positions as indicated in Figure 5.4-5.

| Spot | Composition (in at.%) | | | |
|---|---|---|---|---|
| | Ni | Fe | O | C |
| 1 | 45.27 | 13.24 | 38.68 | 2.80 |
| 2 | 81.89 | 6.81 | 5.18 | 6.11 |
| 3 | 67.64 | 18.79 | 6.64 | 6.93 |
| 4 | 64.59 | 9.47 | 20.03 | 5.91 |

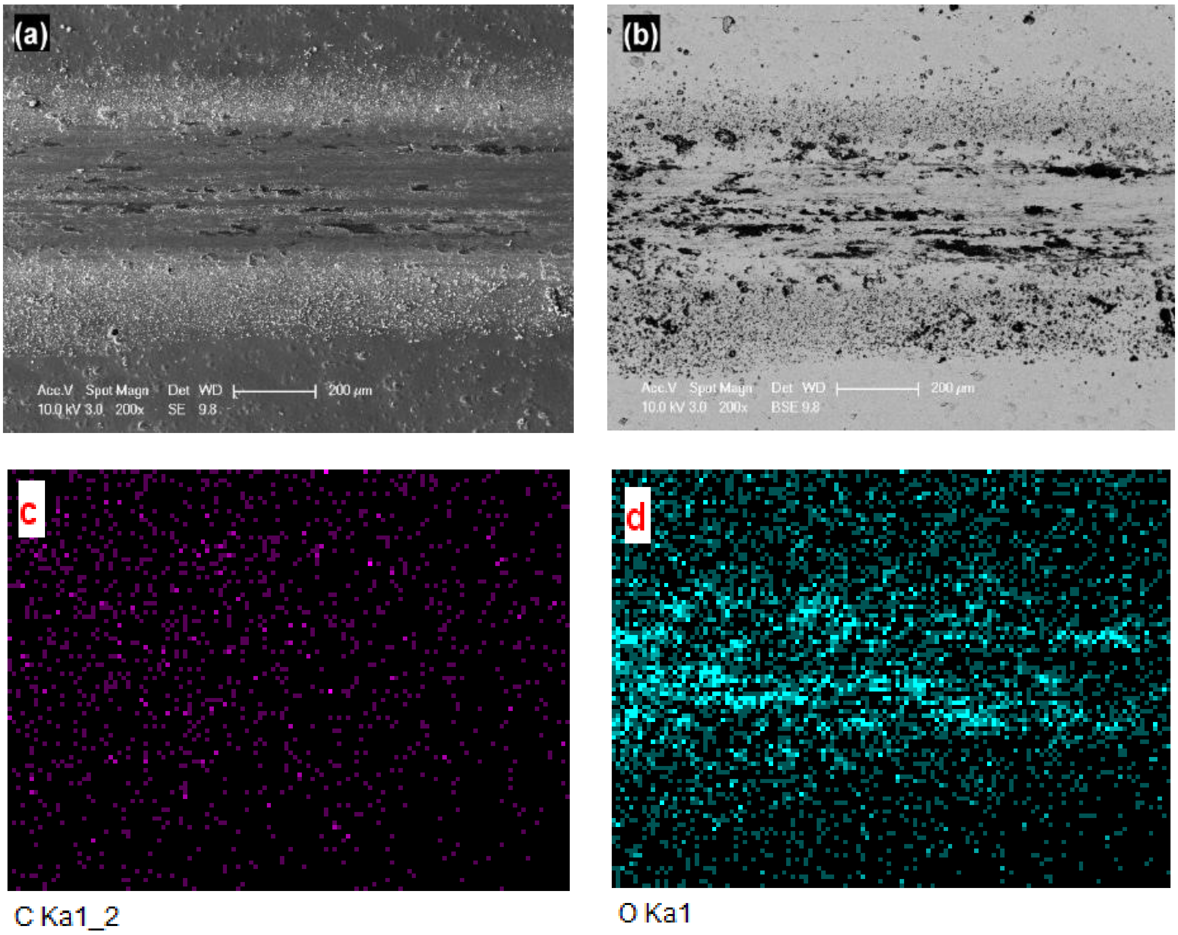

Figure 5.4-6 (a-b) SEM images and (c-d) EDS mapping analysis of the worn surface of NGr40 coating after sliding against a Cr ball in air under a load of 1 N.

The worn NGr40 (Figure 5.4-6) resembled the worn neat nickel coating, while showing more wear debris alongside the wear track likely due to the breakdown of the bulges on its surface during sliding. Back-scattered electron microscopy (Figure 5.4-6b) suggested that the discrete lumps and debris present on the worn site were rich in light elements, which was predominately oxygen, confirmed by EDS mapping (Figures 5.4-6c&d). The results indicate a discontinuous oxide film remaining on the worn NGr40, likely due to the insufficient lubricating effect by the graphite fillers, which led to severe plastic flow at the sliding contact as previously seen on neat nickel coating.

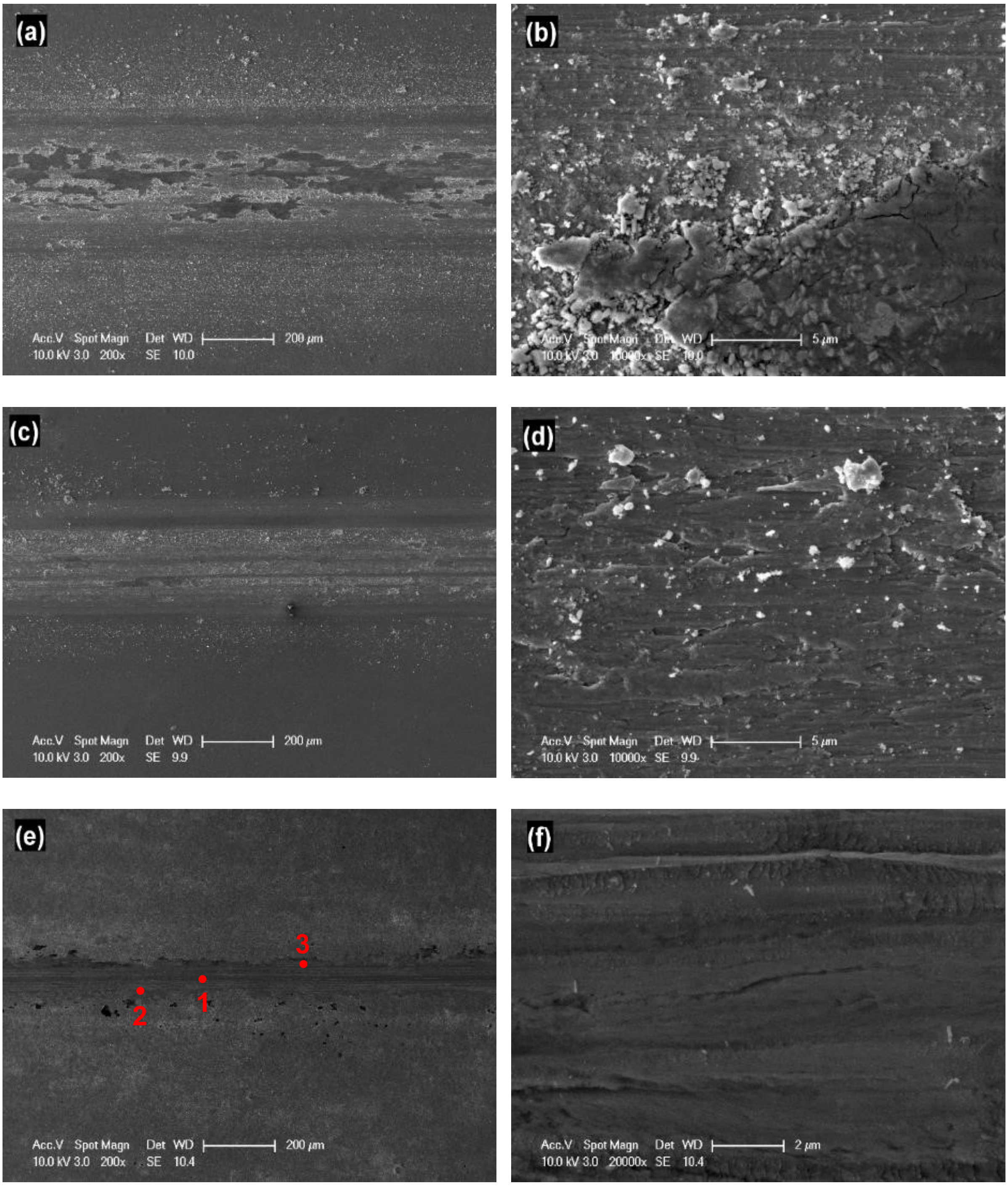

Figure 5.4-7 Worn surfaces of (a, b) NG05, (c, d) NG20 and (e, f) NG40 after sliding against a Cr ball in air under a load of 1 N.

Figure 5.4-7 demonstrates the morphology of the worn NG05 (a, b), NG20 (c, d) and NG40 (e, f). The surface of NG05 was rubbed severely, presenting similar features due to galling and adhesive wear as with the neat Ni. Nonetheless, a larger fraction of the surface oxide film was retained. The surface of NG20 was less damaged with fewer coating deformation and wear debris. The higher magnification micrograph (Figure 5.4-7d) revealed no cracking and minor scuffing. NG40 exhibited substantially reduced wear, with a much smaller wear track and no appreciable amount of wear debris (Figure 5.4-7e). The Enlarged view of the worn site showed a lower roughness compared with the other samples, and a minor degree of materials flow was observed. The progressively enhanced wear resistance shown by NG05, NG20 and NG40 is very likely due to the incorporation of GO.

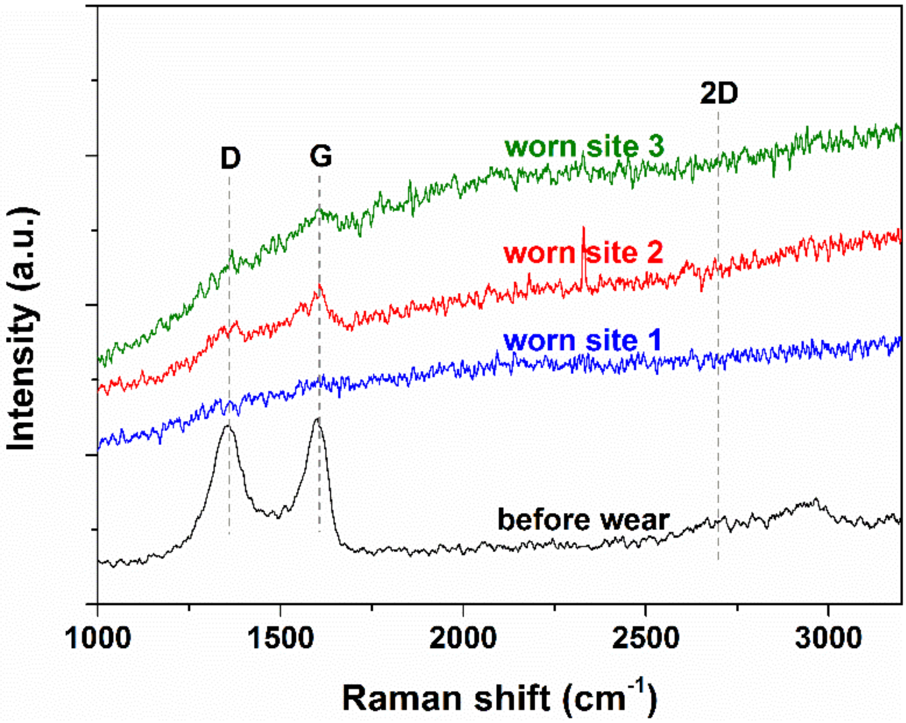

Figure 5.4-8 Raman spectra obtained from unworn and worn NG40 surface.

In order to track the structural changes of GO during wear, the worn surface of NG40 was inspected using Raman spectroscopy. As shown in Figure 5.4-8, a typical GO spectrum containing a D band around 1350 cm$^{-1}$ and a G band around 1600 cm$^{-1}$ can be obtained from the unworn surface. After wear, the D and G bands of GO were still detectable within the wear scar (worn site 2 and 3 in Figure 5.4-7e), but these

Raman features diminished to minimum around the centre of the wear scar (worn site 1 in Figure 5.4-7e) where the contact pressure was at its maximum.

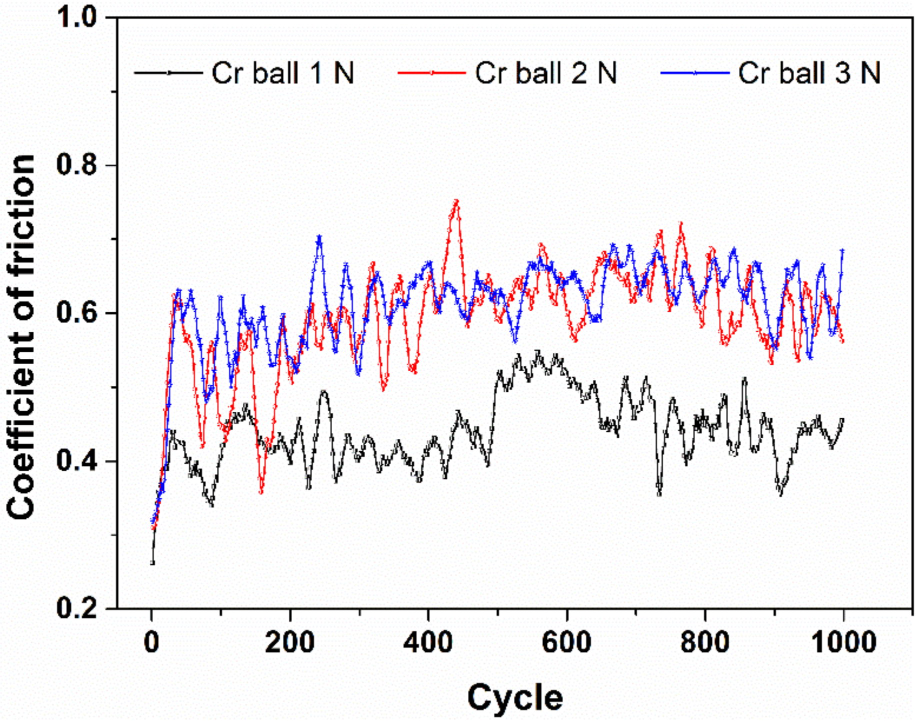

Figure 5.4-9 Coefficient of friction of NG40 composite coating sliding against a Cr bearing steel ball under varying loads of 1-3 N.

NG40 was further tested under higher loads of 2 and 3 N with otherwise the same conditions. Figure 5.4-9 plots the corresponding friction curves. Although NG40 exhibited low *μ* averaged at ~0.45 under the load of 1 N, under 2 and 3 N it showed higher friction (*μ* ~0.65). SEM revealed deep and regularly arrayed grooves accompanied by scuffing on the worn surface (Figure 5.4-10). The reason for the increased friction and wear lies in that under a light load of 1 N, the oxide film formed on the nickel coating surface was able to withstand the normal force and mitigate friction effectively. In case of heavier loads, however, the normal force was high enough to penetrate through and plough away the oxide film, thus causing an increase of friction due to more metallic contact.

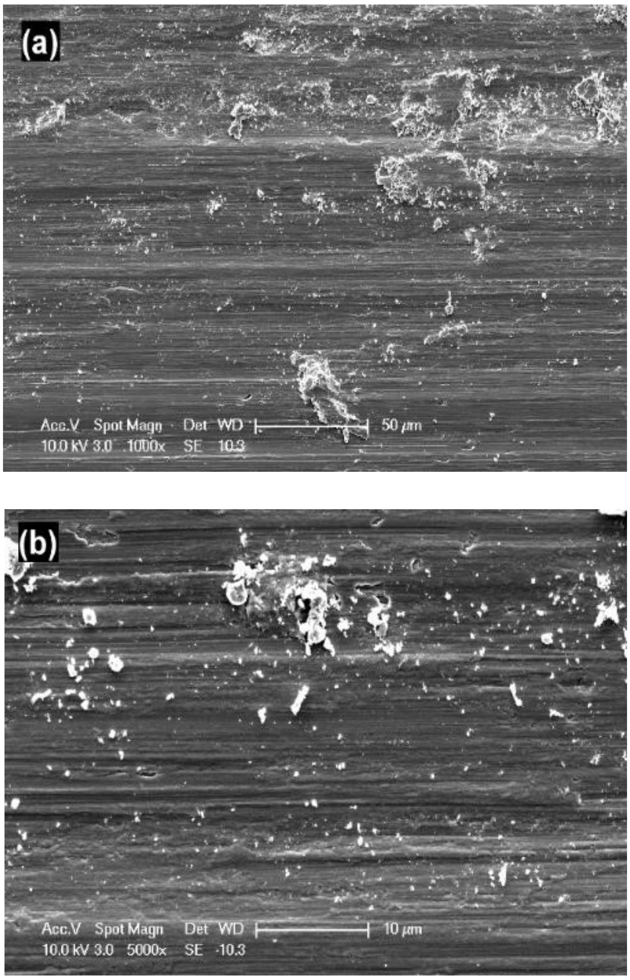

Figure 5.4-10 Worn surface of NG40 after sliding against a Cr ball in air under a load of 3 N under (a) low and (b) high magnifications.

### 5.4.3 Sliding against an alumina ball in air

Following the sliding tests against chromium bearing steel, the tribological behaviour of samples against an alumina ($Al_2O_3$) ball (ϕ8 mm) was also investigated. Figure 5.4-11a demonstrates the COF curves for Ni, NG40 and NGr40 against the alumina ball under a load of 3 N. All the samples exhibited lower friction against alumina than against steel as previously seen, due to less affinity between ceramic and metallic coating. The COF of neat Ni was the highest among the tested samples and kept increasing from 0.4 upwards over cycles, denoting a changing sliding condition. NG40 showed a steady-state COF of 0.35 after a quick running-in process. The COF of the as-prepared NGr40 was lower than that of NG40 throughout the test, reaching a steady-state value of 0.3. Note that NGr40 has much higher surface roughness than NG40 due to the incorporation of bulky graphite flakes, which could be responsible for the lower friction. For a fair comparison, NGr40 was polished slightly to remove most of the lumps away and the tested again. As can be seen in Figure 5.4-11a, the polished NGr40 exhibited COF comparable to NG40.

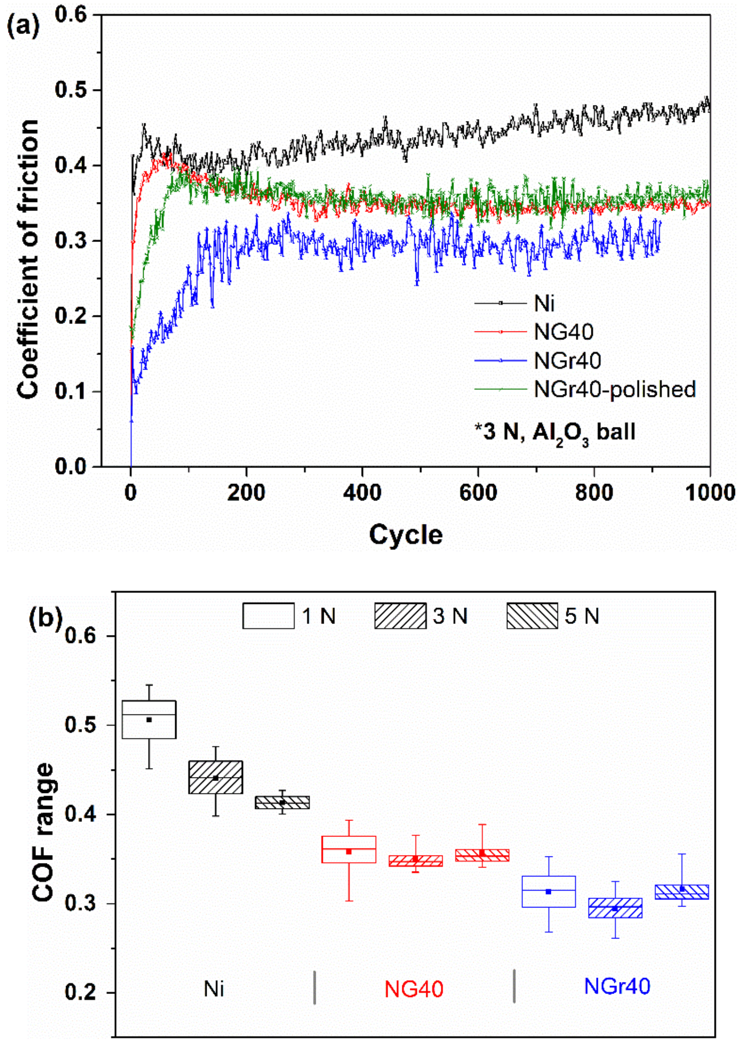

Figure 5.4-11 Coefficient of friction of neat Ni, NG40 and NGr40 sliding against an alumina ball in air under (a) 3 N and (b) 1-3-5 N loads.

The steady-state COFs for neat Ni, NG40 and NGr40 under varied loads of 1, 3 and 5 N were statistically summarised in Figure 5.4-11b. Unlike the wear against chromium steel where the COF of NG40 increased with the normal load due to the penetration and removal of the surface oxide film, when sliding against alumina counterface the COF of NG40 was barely affected by the increasing load, likely due to reduced adhesion between metallic nickel and alumina.

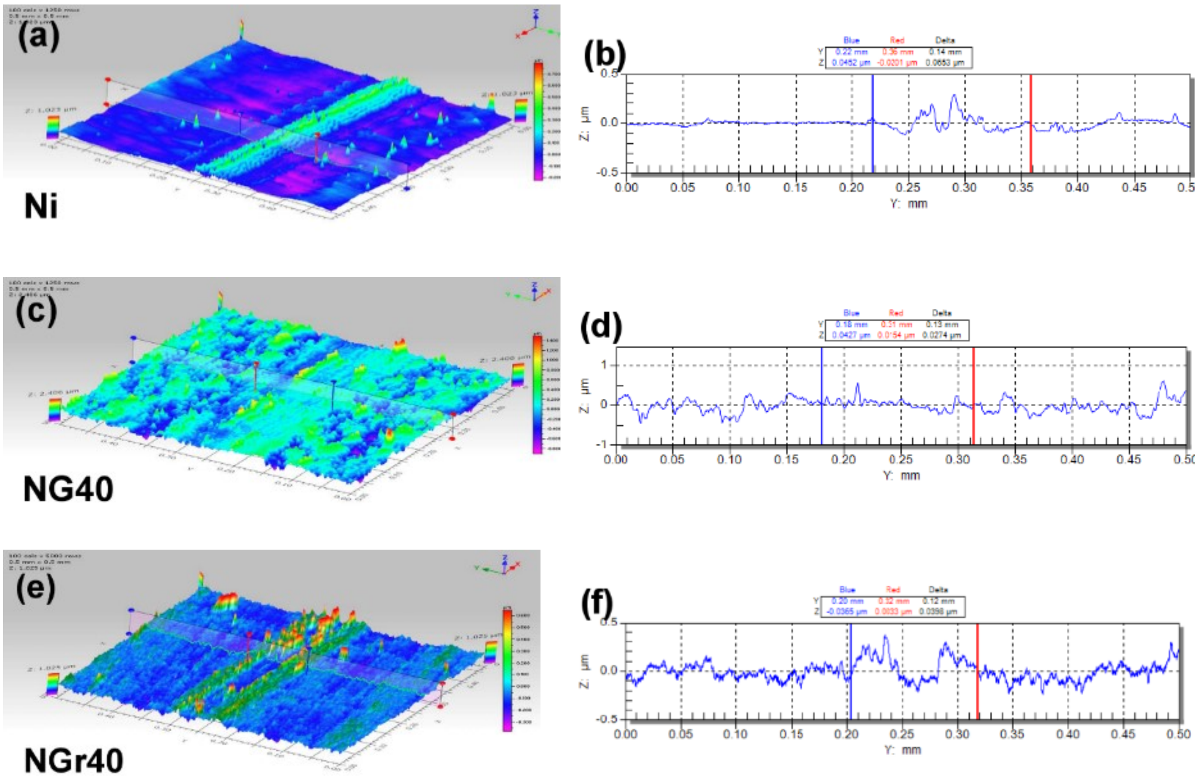

Figure 5.4-12 3D and cross sectional profiles of the worn surfaces of (a, b) neat Ni, (c, d) NG40 and (e, f) NGr40 after reciprocating against an alumina ball in ambient air under a load of 3 N.

Figure 5.4-12 demonstrates the topography of the wear tracks on Ni, NG40 and NGr40 after sliding against the alumina ball under a load of 3 N. The roughness of the worn site increased clearly for the neat Ni coating. The alumina counter ball pressed into the coating and caused scratches and build-ups at the centre of the wear scar. For

NG40, no appreciable material loss but a reduced roughness was found within the wear track. For NGr40, the wear track was slightly smaller yet irregular, featuring randomly distributed build-ups. The wear coefficients against the alumina counterface were compared in Figure 5.4-13. As expected, the wear coefficient for neat Ni coating was the largest ($9\times10^{-6}$ $mm^3N^{-1}m^{-1}$). It decreased by about 60% for NG40, indicating the enhanced wear resistance. Although NGr40 exhibited lower $\mu$ than NG40 (Figure 5.4-11), its wear coefficient was found to be nearly doubled when compared with NG40.

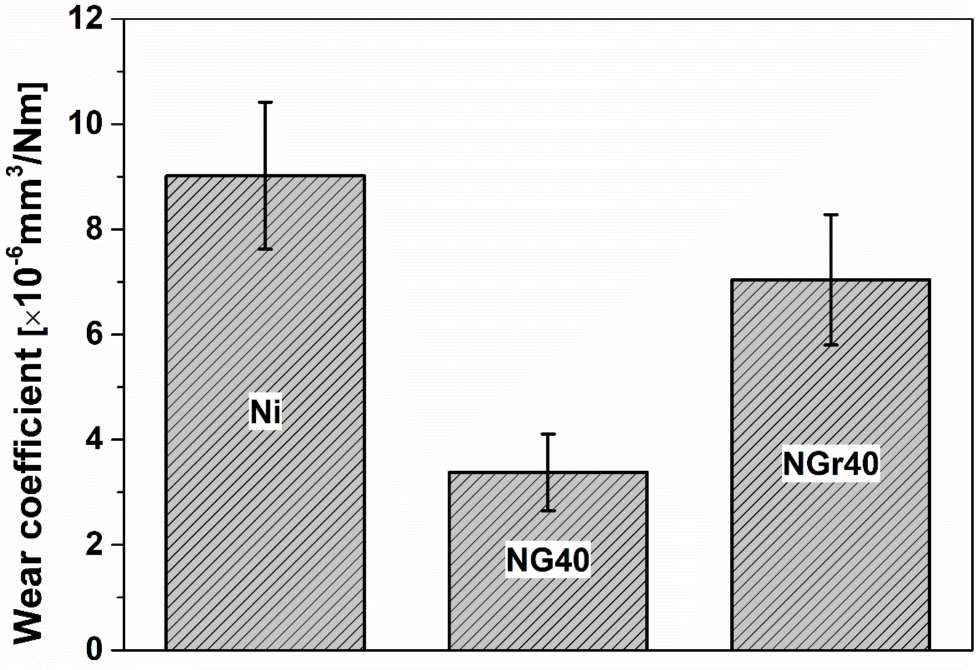

Figure 5.4-13 Wear coefficient for neat Ni, NG40 and NGr40 sliding in air against an alumina ball under a normal load of 3 N.

Figures 5.4-14(a-b) present the morphology of the worn neat Ni against the alumina counterface. It showed a wavy topography after wear due to lack of lubrication. The enlarged view of the worn site (Figure 5.4-14b) revealed stripe-like plastic deformations that are perpendicular to the sliding direction. Cracks were found propagating towards the edges of the deformed material layer, as indicated in Figure 5.4-14b, probably due to the accumulation and release of the shear stress during wear.

EDS analysis was performed in both the deformed zone (Spot 1 in Figure 5.4-14b) and un-deformed zone (Spot 2). As demonstrated in Figure 5.4-14d, Spot 1 showed a high peak for oxygen, while Spot 2 showed mostly nickel and iron (coating composition) with little oxygen. Fine-sized wear debris was visible alongside and at the ends of the wear scar (Figure 5.4-14c). EDS spectrum of the wear debris (Figure 5.4-14d, Spot 3) was very similar to Spot 1, showing a high oxygen content.

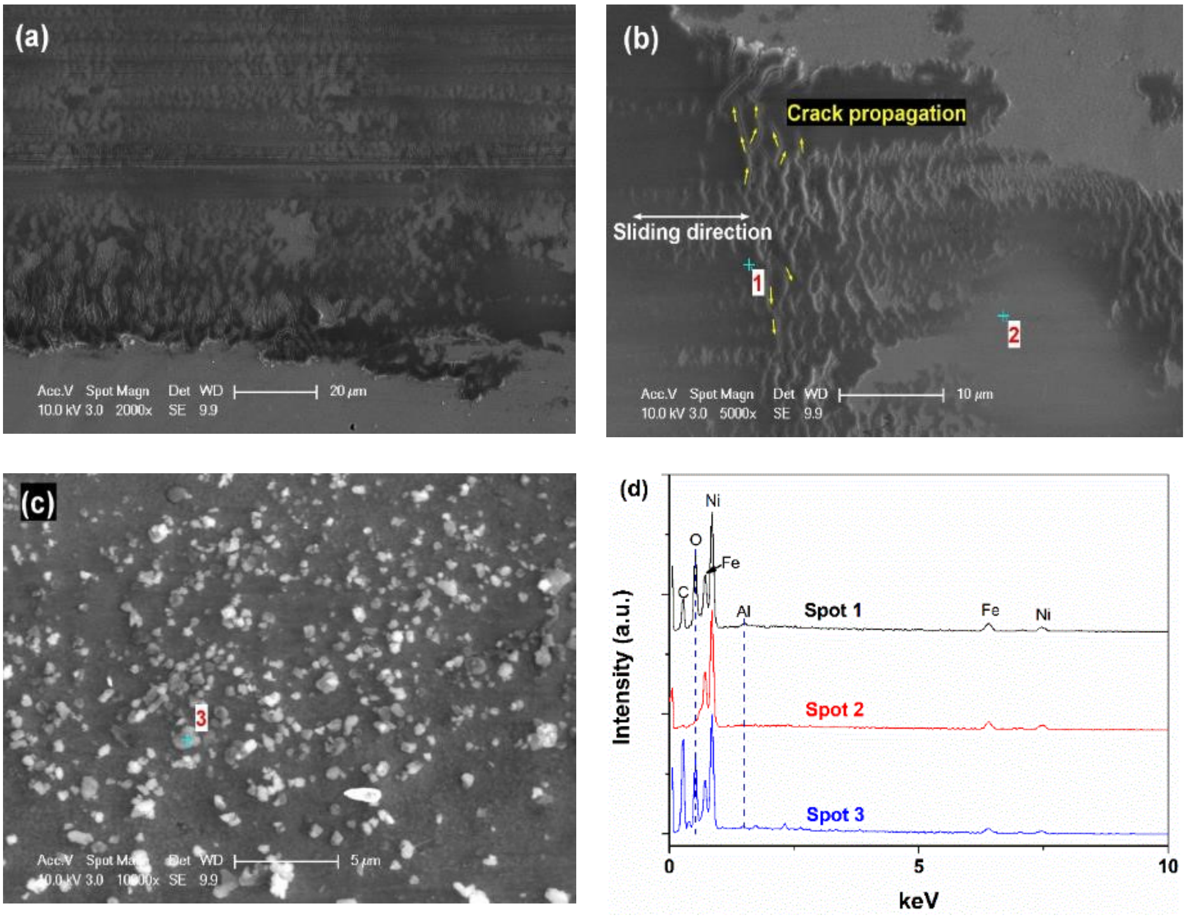

Figure 5.4-14 Worn surface (a, b) and debris (c) of neat Ni after sliding against an alumina ball in air under a load of 3 N. (d) EDS spectra of the three spots labelled in the images.

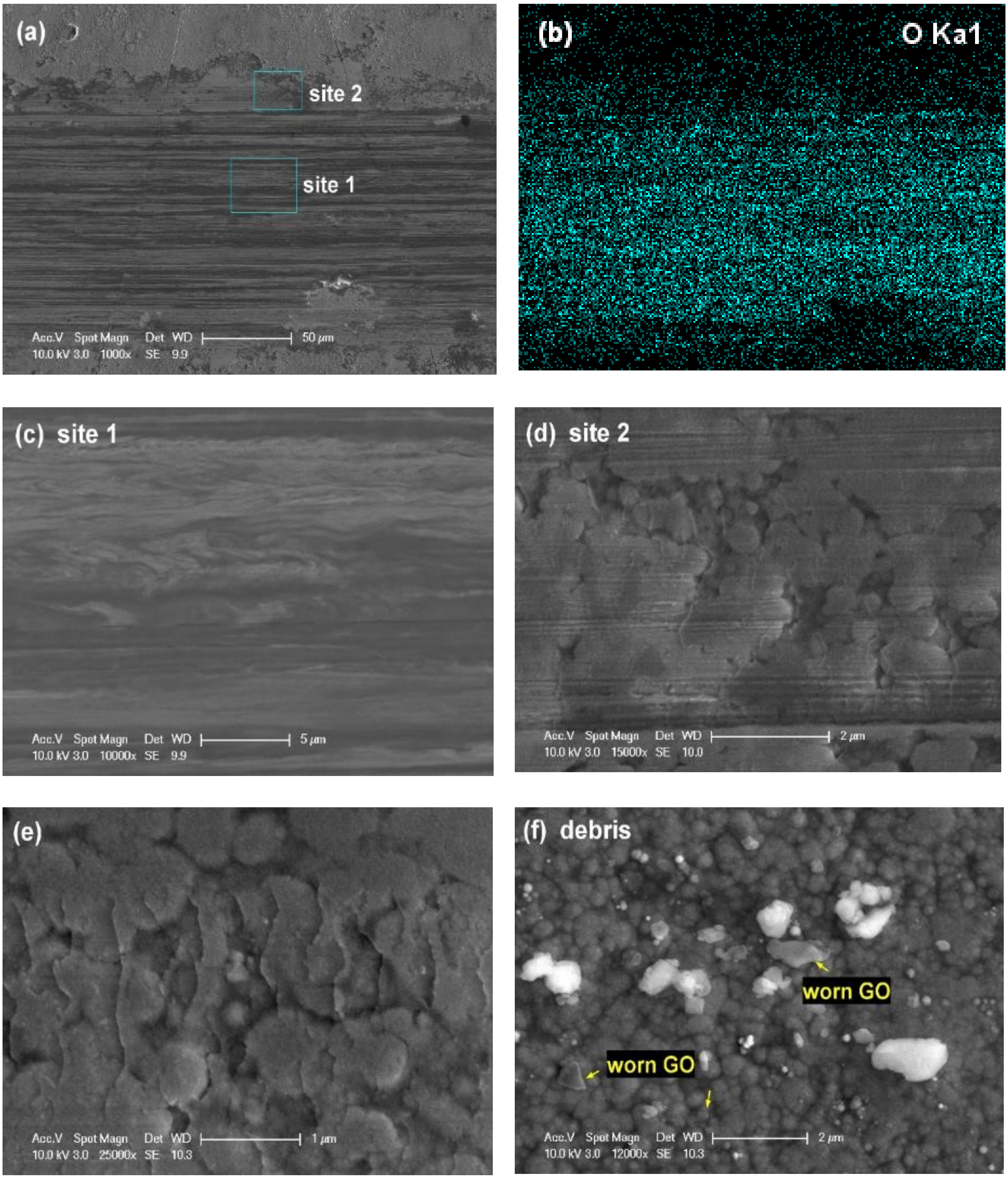

Figure 5.4-15 Worn surface (a, c-e) and debris (f) of NG40 after sliding against an alumina ball in air under a load of 3 N. (b) EDS mapping of oxygen in (a).

Figure 5.4-15 demonstrates the worn surface of NG40. The wear scar appeared smooth and clear with little cracking found. EDS elemental mapping showed that oxygen was homogeneously present over the worn area (Figure 5.4-15b). This is in contrast with the neat Ni wear test, indicating that a continuous oxide film covering the entire sliding path was able to establish and retain on NG40. Around the centre of the wear track, signs of minor material flow along the sliding direction were observed as shown in Figure 5.4-15c. At places close to the edge of the wear track, translucent carbon-rich scales were widely seen, as shown in Figure 5.4-15(d, e). They were therefore very likely lubricant films formed of worn GO sheets, which were also observed among the wear debris of NG40 (Figure 5.4-15f).

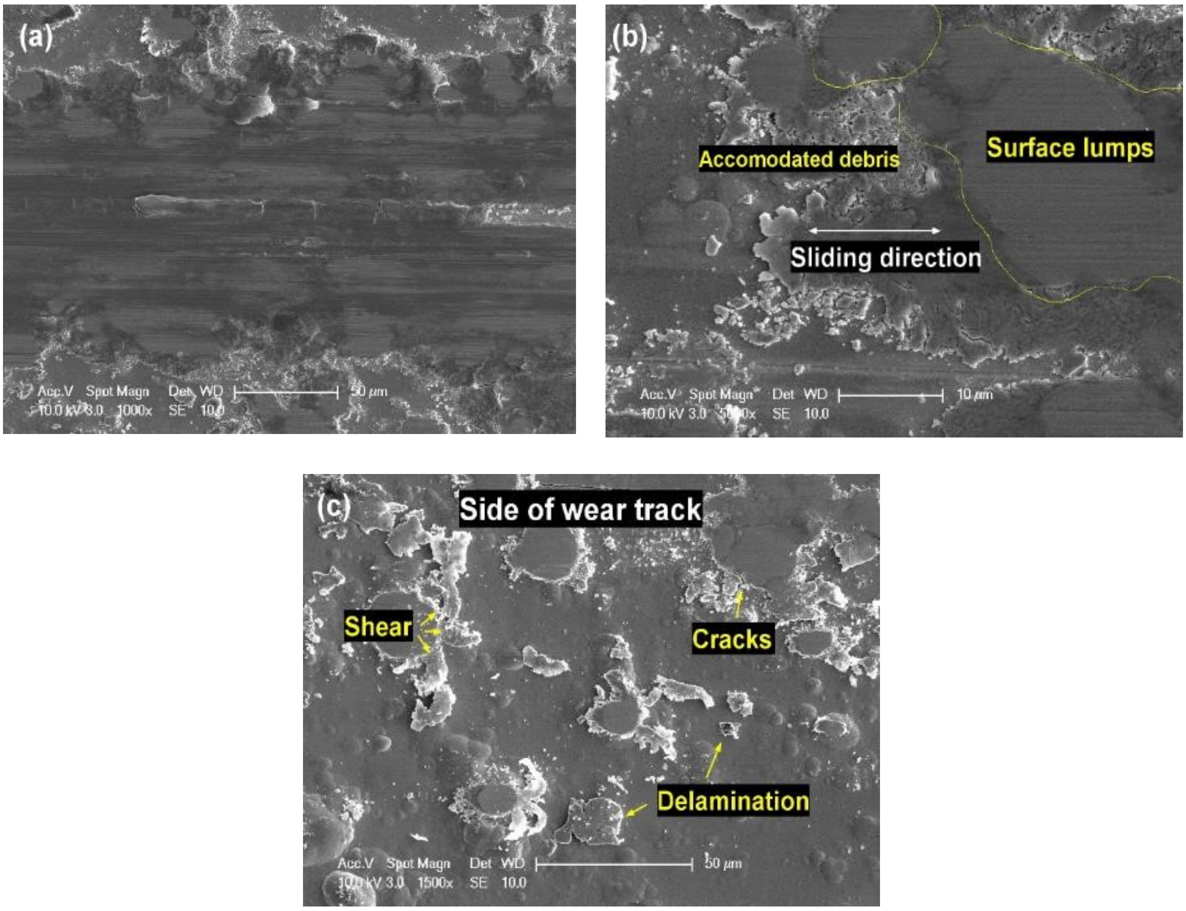

Figure 5.4-16 Worn surface of NGr40 after sliding against an alumina ball in air under a load of 3 N.

Figure 5.4-16 displays the morphology of the worn NGr40. It also showed smoothed wear track compared with neat Ni coating. However, cracks and spallation were clearly seen on the worn site. The original surface lumps were flattened by the slider and the wear debris was accommodated between these surface irregularities (Figure 5.4-16b), which could have contributed to the lower friction coefficient of NGr40 shown in Figure 5.4-11. Heavy plastic shearing deformations were found close the side of the wear track, along with cracks and coating fragments (Figure 5.4-16c).

### 5.4.4 Sliding against an alumina ball in nitrogen-rich atmosphere

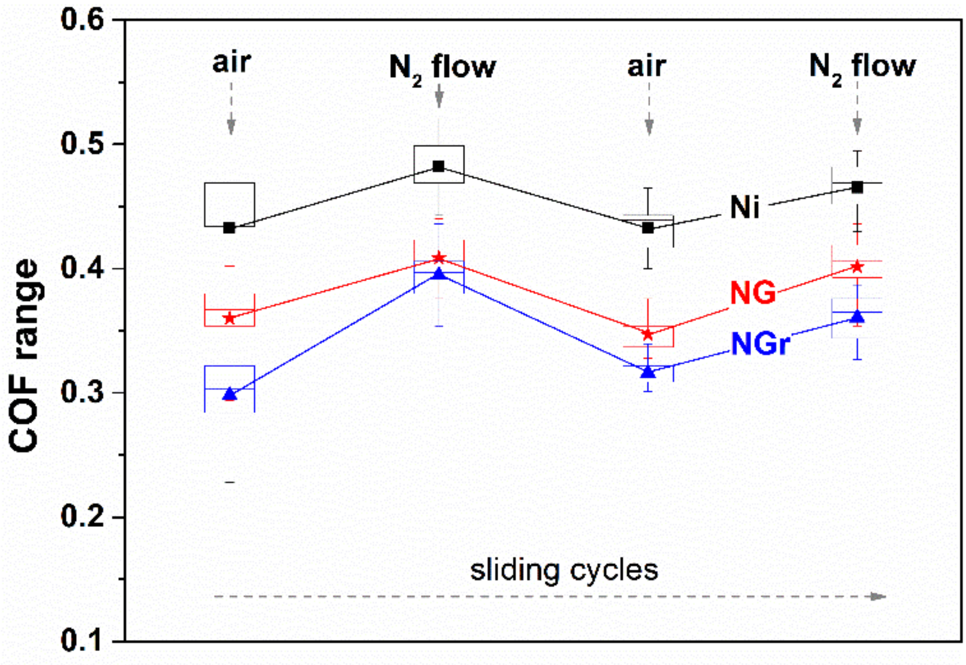

Figure 5.4-17 Coefficient of friction (COF) evolution of neat Ni, NG and NGr coatings sliding against an alumina ball under a normal load of 3 N. Nitrogen flow was applied intermittently during a frictional test. The air-nitrogen-air-nitrogen intervals were set to be 300-300-200-200 in cycle.

In order to study the influence of oxygen and humidity on the tribological behaviour of the Ni-GO composite coating, tribo-tests were run on NG40, as well as neat Ni and NGr40 in a nitrogen-rich atmosphere. The same alumina counterpart and a normal load of 3 N were used as described above. Nitrogen gas purging was applied intermittently during the 1000-cycle frictional tests. The frictional responses of the samples to the environment changes during sliding are plotted in Figure 5.4-17. In general, all the samples exhibited increased COFs in presence of nitrogen flow, and the COFs dropped back when the nitrogen purging was off. For NG40 and NGr40, it was found that the friction under nitrogen flow increased as observed on neat Ni. For NG40 in particular, the COF showed less fluctuation upon nitrogen purging than with NGr40.

SEM observations (Figure 5.4-18) revealed the morphology of NG40 and NGr40 after wear in ambient air and in nitrogen flow. The worn NG40 surface showed barely perceptible difference except for slightly deeper scratches when the environment changed from open air to nitrogen-rich atmosphere. In contrast, the wear track of NGr40 exhibited heavier cracking and spallation when the sliding environment changed. This indicates that the graphite in the composite coating was less effective in the nitrogen-rich environment, resulting in heavier surface damage and material loss.

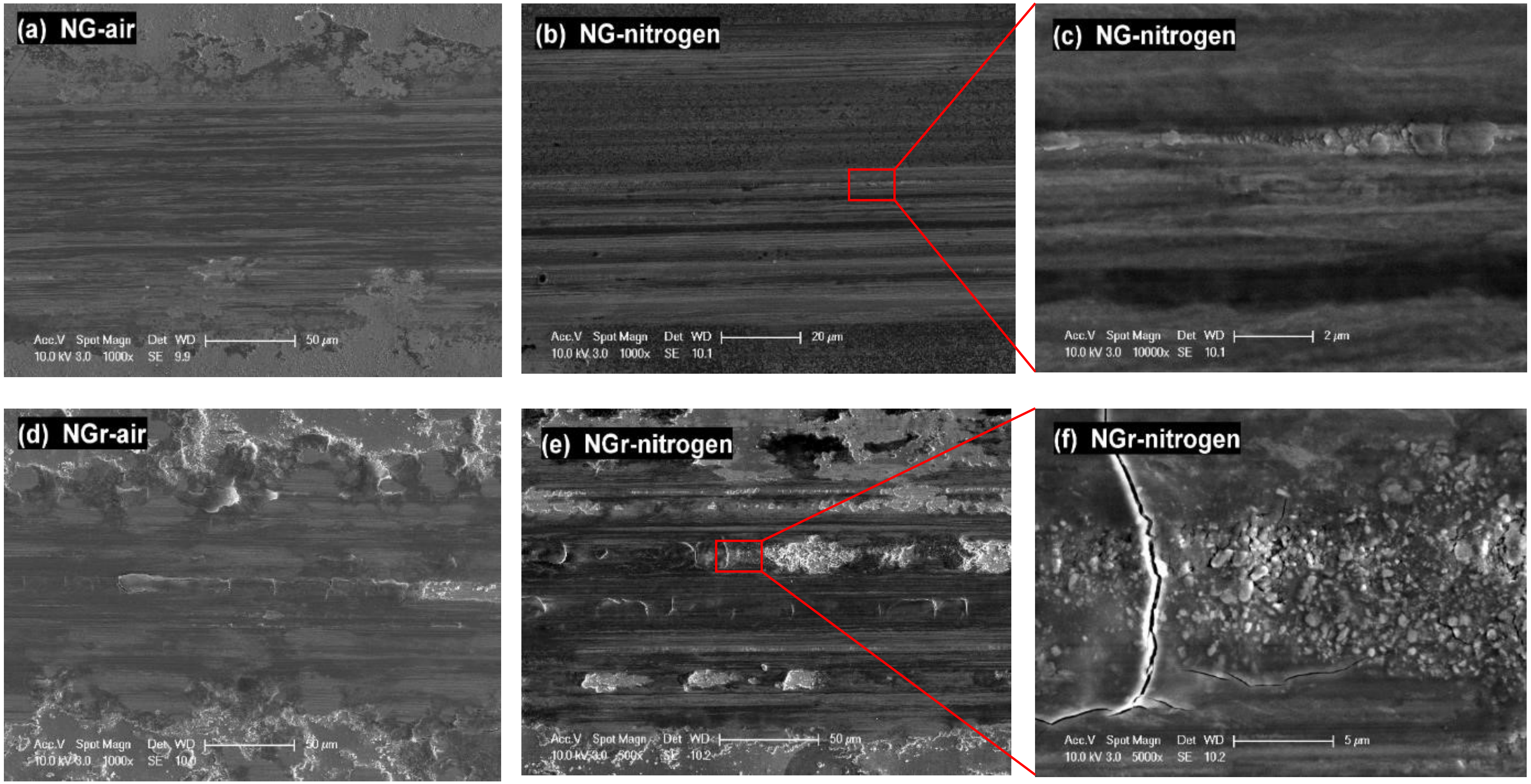

Figure 5.4-18 Worn surfaces of (a, b) NG40 and (c, d) NGr40 after sliding against an alumina ball in air and nitrogen.

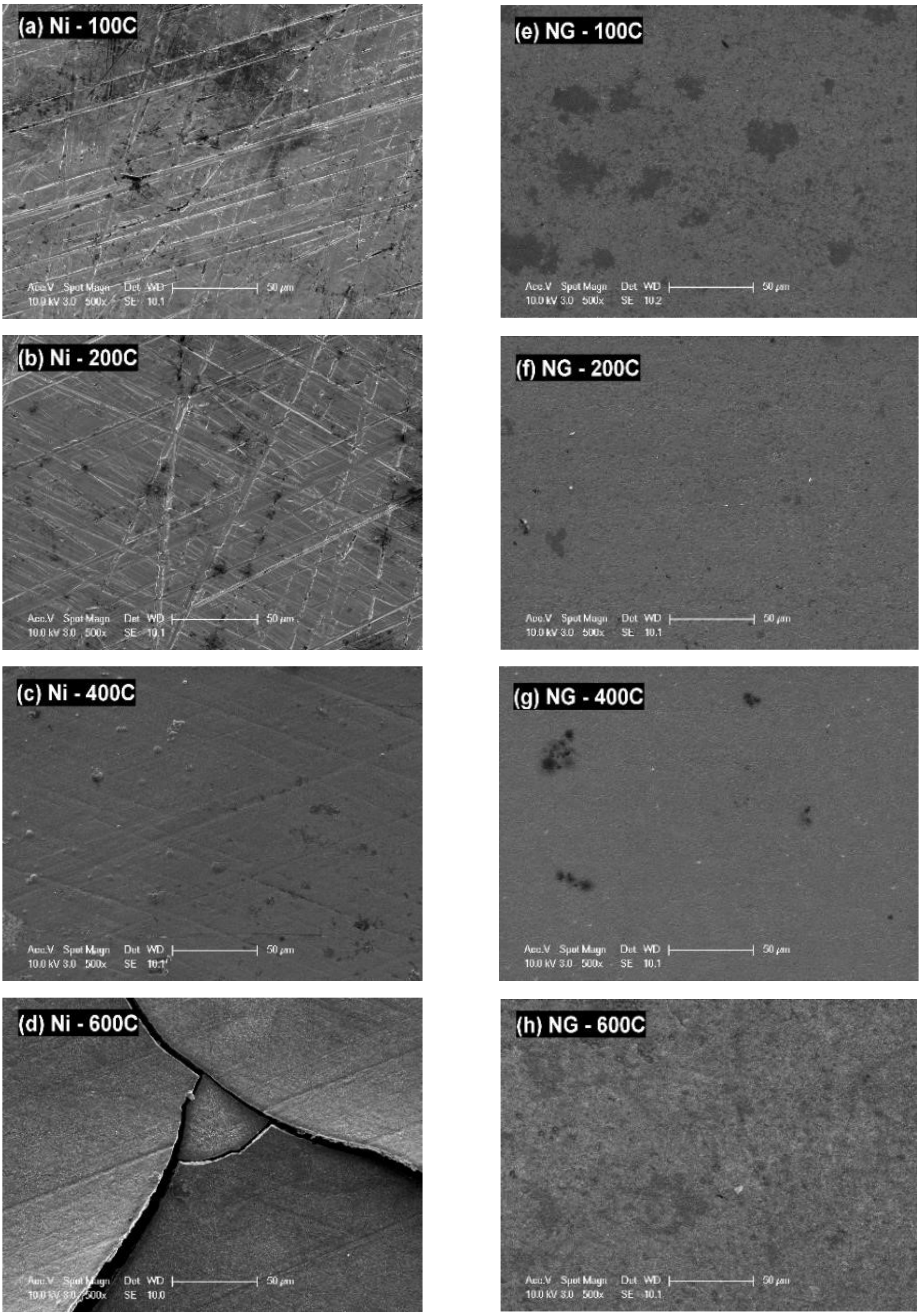

Figure 5.5-1. Morphology of (a-d) neat Ni and (e-h) Ni-GO nano-composite coatings after annealing in air at the indicated temperatures for 30 min.

## 5.5 Thermal stability

### 5.5.1 Morphology and microstructure after annealing

Neat Ni and Ni-GO (NG20) coatings produced by electro-brush plating as described before were subject to annealing in air at temperatures varying from 100 to 600 ℃ to study their thermal stability, which is very important for application. The heating rate was fixed at 8℃ up to the target temperatures, where a dwell time of 30 min was applied. The samples were then cooled down in furnace.

Figures 5.5-1 a-d show the micrographs of the neat Ni coating surfaces after heat treatments. Note that the scratches on the surface were unintentionally from sample handling, not from the heat treatments. Although the neat Ni coating showed little change in morphology up to 400℃, major cracking happened during the 600℃ annealing. In contrast, throughout the annealing temperature range the Ni-GO composite coating (NG, Figure 5.5-1 e-h) exhibited a crack-free topography. The annealed coatings were smooth and flat, with a small number of localised dark zones, likely caused by oxidation.

EDS analysis was performed on the surfaces of the annealed coatings and the results are summarised in Figures 5.5-2 a-b. The four main elements, Ni, Fe, O and C were plotted as a function of annealing temperature. Note that the nickel plating solution shipped from the market contains a small fractions of iron (~10 wt%) and a trace of carbon (likely from additives). As shown in Figure 5.5-2a, after annealing at 400℃ increased oxygen and iron contents were detected from the surface due to oxidation. After annealing at 600℃, the Ni content dropped to minimal within the penetration depth of EDS (around 2 μm), and the surface was mainly formed of Fe (~ 38 at%) and O (~ 58 at%). The surface composition of NG (Figure 5.5-2b) changed in a similar way; after annealing at 600℃, the coating surface was also dominated by Fe (~ 37 at%) and O (~ 60 at%). The ratio of Fe to O for both were around 2:3, corresponding to the stoichiometry of $Fe_2O_3$. Indeed, high resolution micrographs of the two coating surfaces after 600℃ annealing revealed similar flake- and needle-like $Fe_2O_3$ crystals (Figures 5.5-2 c-d).

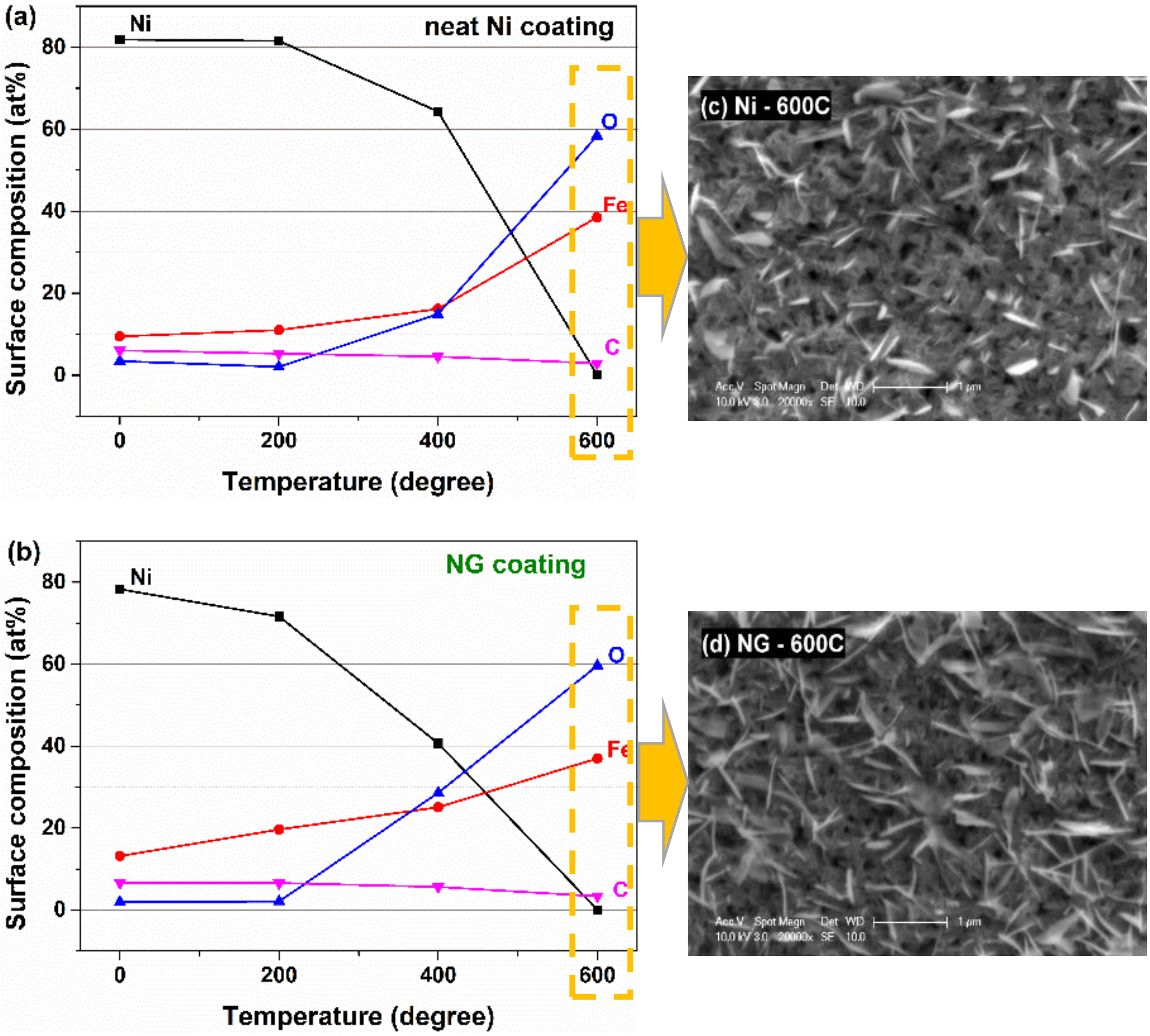

Figure 5.5-2. EDS analysis results of the surface compositions after annealing in air at varying temperatures. Note that the ‘0’ means room temperature, not zero degree (Hereafter).

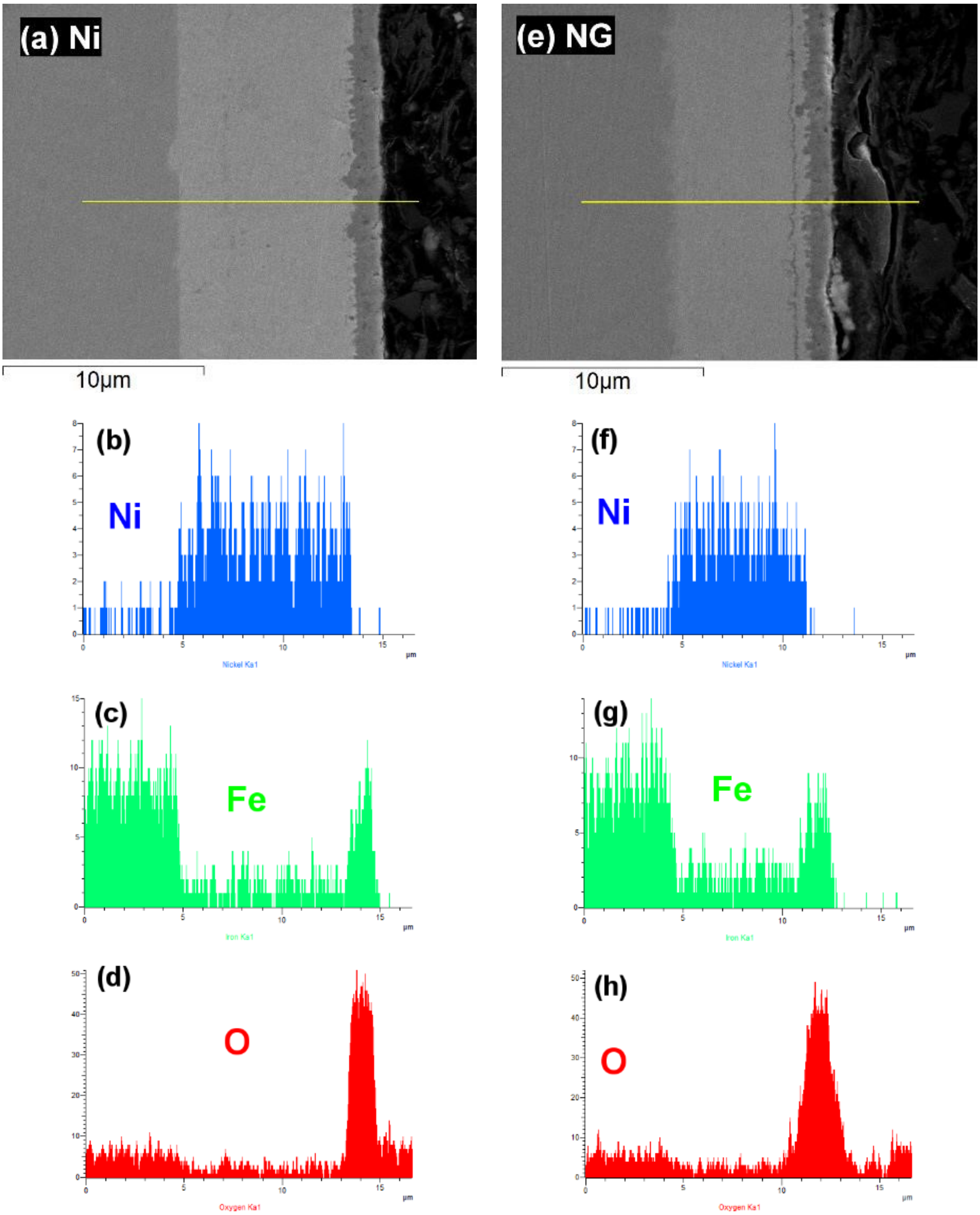

Figure 5.5-3. Cross-sectional views and EDS line scans of (a-d) neat Ni and (e-h) NG coatings after annealing in air at 600℃.

Figure 5.5-3 demonstrates the cross-sectional views of the 600℃ annealed neat Ni and NG coatings and the corresponding EDS line scans. It is clear that a scale layer of about 2 μm was formed on the outer surface of each coating. EDS analysis revealed that the scale layers were mostly iron and oxygen, which is consistent with the surface EDS analysis (Figure 5.5-2), indicating that the annealed surfaces were dominated by iron oxide.

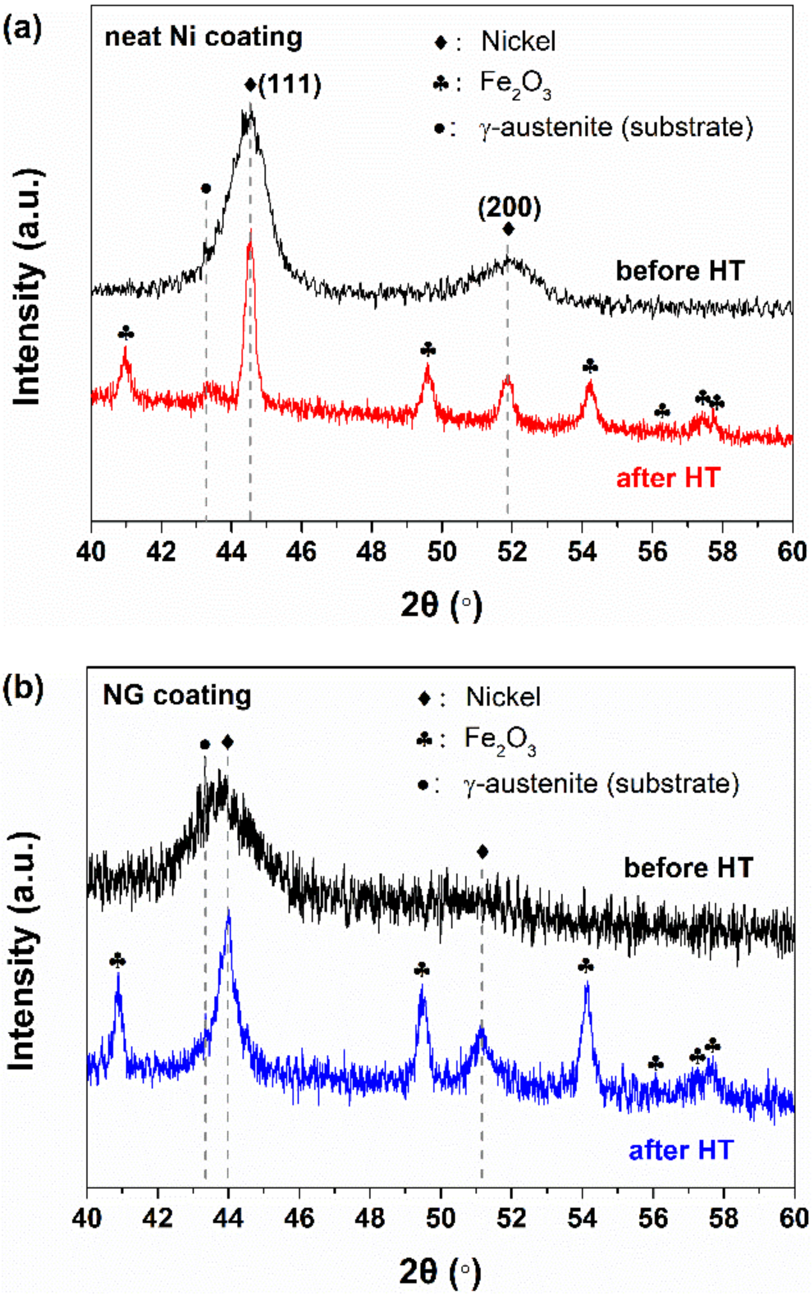

Figure 5.5-4. XRD patterns of (a) neat Ni and (b) NG coatings as-produced and after heat treatment at 600℃, respectively.

The XRD patterns of neat Ni and NG coatings, both before and after annealing (at 600℃), are shown in Figure 5.5-4. Before the heat treatment, both coatings exhibited a strong yet broad peak around 44° which corresponds to the (111) crystallographic planes of nickel. Another low-rise peak around 52° was present due to the (200) plane diffractions of nickel. After annealing, the neat Ni coating (Figure 5.5-4a) exhibited strongly narrowed (111) and (200) diffraction peaks, implying potential changes in the crystallisation status of the nickel matrix. In the meantime, peaks for α-$Fe_2O_3$ phase arose due to the formation of oxide scale on the coating surface. A trace of diffraction signal for γ-phase in the stainless steel substrate was detected due to the penetration of X-ray. The Ni-GO composite coating (Figure 5.5-4b) showed a similar XRD pattern in terms of the phase composition. However, the pattern exhibited relatively less reduction in the width of the nickel diffraction peaks after annealing.

Table 5.5-1. Calculated crystallite size for the neat Ni, and NG coatings before and after heat treatment at 600℃.

|  | (111) FWHM (degree) | grain size approx. (nm) |
|---|---|---|
| Ni | 1.2292 | 7.3 |
| Ni-annealed | 0.2949 | 30.4 |
| NG | 1.9879 | 4.5 |
| NG-annealed | 0.6532 | 13.7 |

To obtain a quantitative comparison of the crystallisation between the two samples, the average crystallite sizes for each coating were estimated using Scherrer equation as described before, and summarised in Table 5.5-1. The grain sizes of the as-prepared neat Ni and NG coatings were approximately 7.3 nm and 4.5 nm, respectively. It is clear that the GO incorporation has induced a grain refinement effect to the nickel matrix. More interestingly, while after annealing the grain size of the neat Ni coating increased largely by four times (7.3 nm to 30.4 nm), the annealed NG coating showed a grain size of only 13.7 nm. It is also worth noting that in the XRD pattern of the NG composite coating the nickel (111) and (200) diffraction peaks shifted to the left by approximately 0.6° and 0.7°, respectively, probably due to macroscopic tensile strain within the composite coating.

### 5.5.2 Nanoindentation results

Nanoindentation tests were carried out on both the neat Ni and the NG composite coatings after annealing with a peak load of 10 mN. To minimise the influence of the coating thickness and the oxide scale on the surface, the measurements were performed on cross-sections. Figures 5.5-5a and 5.5-5b show typical load-displacement curves for all the as-deposited and the heat-treated samples. For the as-deposited neat Ni coating, the penetration depth at the peak load was about 225.2 nm. It was found that the indentation curves of the annealed neat Ni coating deviated clearly from that of the as-deposited sample; as the annealing temperature increased, the maximum indentation depth of the neat Ni coating drifted by -5.8 nm (100 ℃), -18.4 nm (200 ℃), +15.5 nm (400 ℃) and +9.1 nm (600 ℃).

For the NG coatings (Figure 5.5-5b), in comparison, the maximum indentation depth on the as-deposited sample was 202.1 nm, which is 10% percent less than that for the as-deposited neat Ni. More importantly, after heat treatments at varying temperatures the NG coating exhibited similar indentation response, in terms of essentially the same indentation maxima and marginally differentiated unloading curves. It was only after annealing at 600 ℃ that the NG coating showed a slightly increased indentation depth (209.1 nm) at the peak stage.

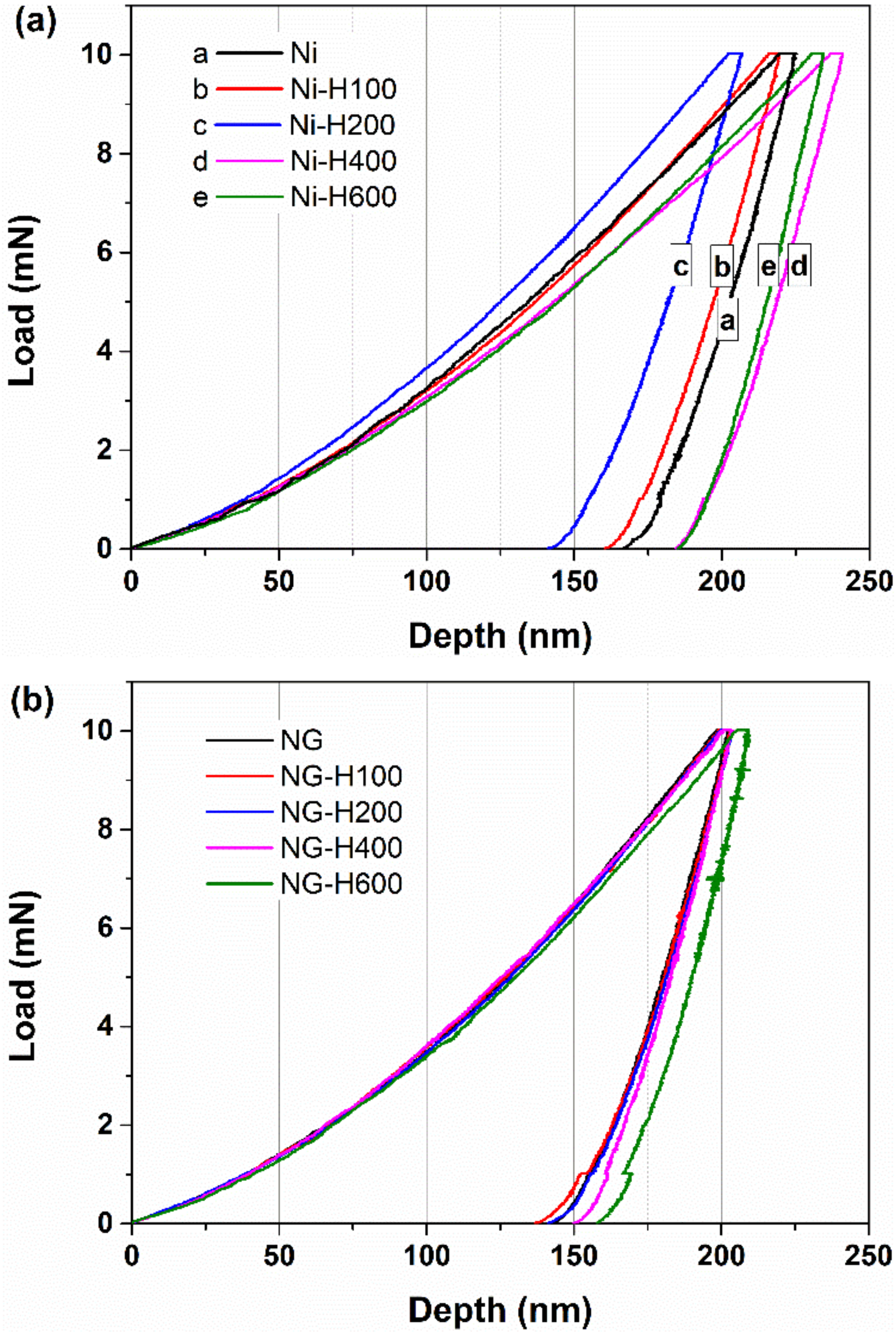

Figure 5.5-5. Typical load-displacement curves of the nanoindentation tests on (a) neat Ni and (b) NG composite coatings without annealing and annealed at varying temperatures (up to 600 degree).

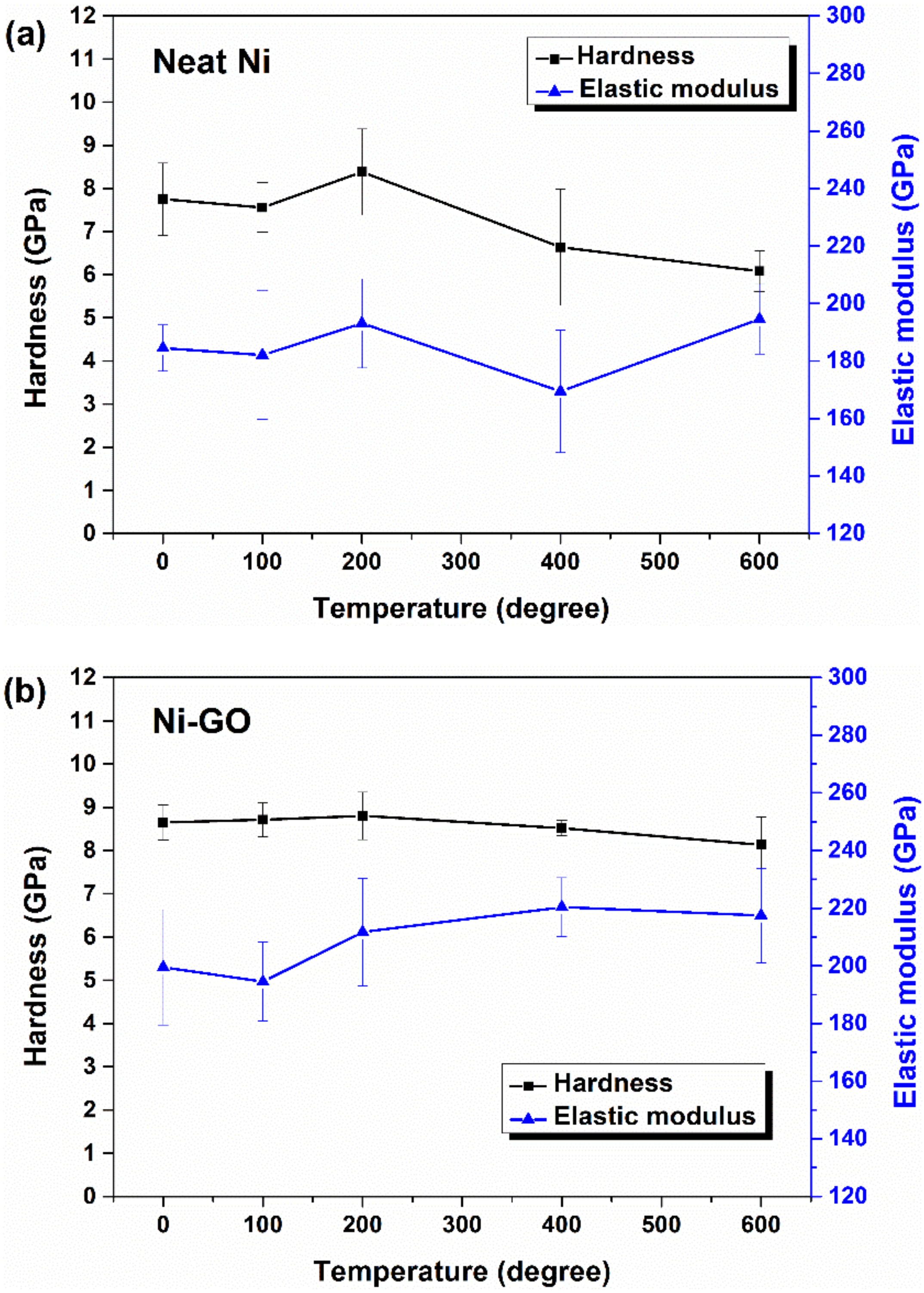

Figure 5.5-6. Nanoindentation hardness and elastic modulus for (a) neat Ni and (b) NG coatings after annealing at varying temperatures.

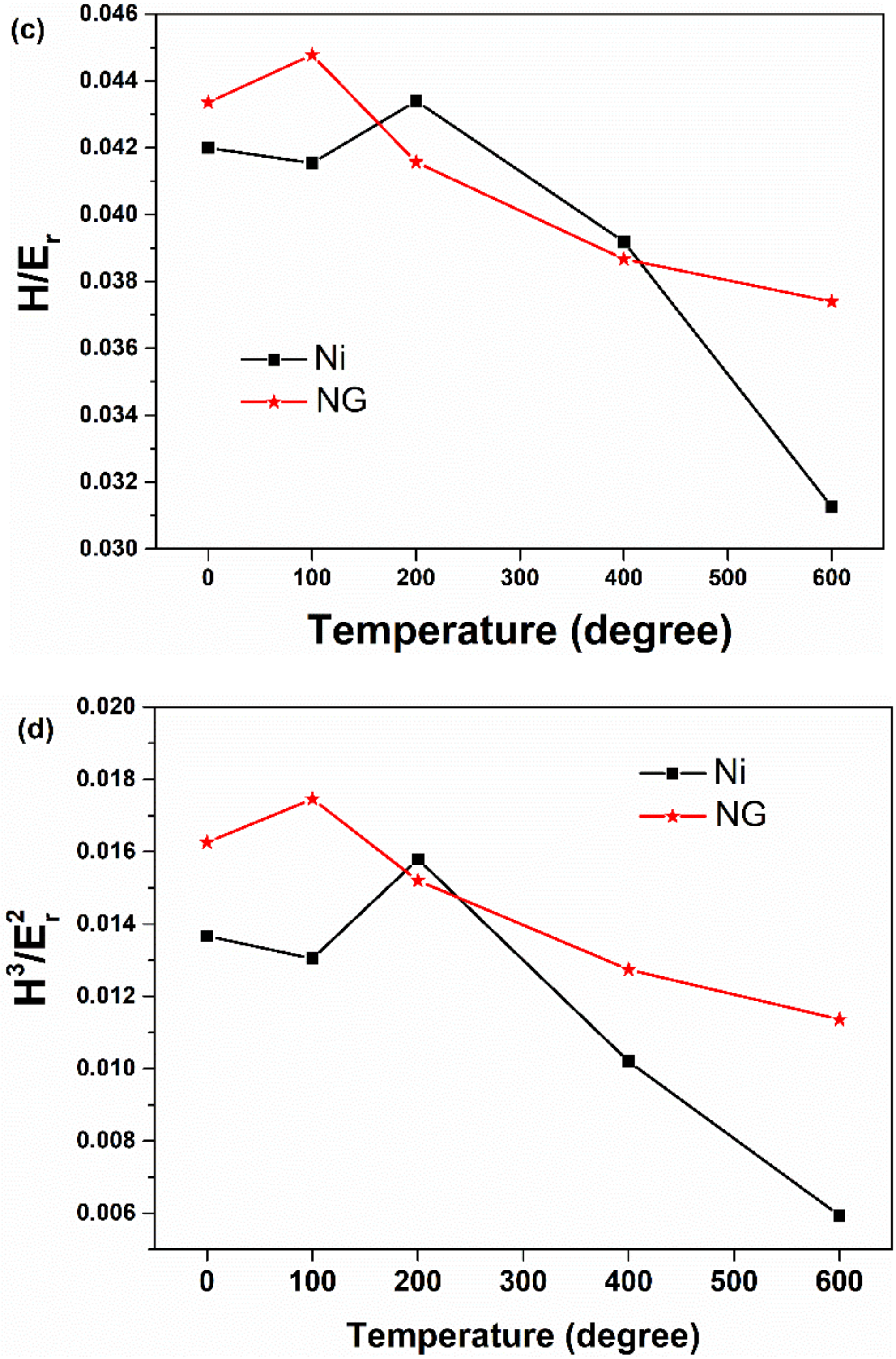

Figure 5.5-6(continued) (c) $H/E_r$ and (d) $H^3/E_r^2$ evolutions of the two coatings.

The nanoindentation hardness ($H$) and reduced elastic moduli ($E_r$) of the samples were calculated from the loading-displacement curves based on Oliver-Pharr fit [247] . The obtained statistics as functions of the annealing temperature are plotted in Figure 5.5-6. The as-deposited neat Ni coating (Figure 5.5-6a) exhibited a hardness of 7.8 GPa and a reduced modulus of 184.5 GPa. The coating experienced considerable changes in both hardness and elastic modulus with the increasing heat treatment temperature. After the mild rise in both $H$ and $E_r$ at 200 ℃, the hardness value decreased down to 6.1 GPa for the 600 ℃ annealed samples. The reduced elastic modulus exhibited a similar trend of change, except at 600 ℃ where the modulus increased to 194.5 GPa.

In comparison, the NG coatings (Figure 5.5-6b) exhibited improved mechanical properties as its hardness and elastic moduli were clearly higher than those of the neat Ni all round regardless of the heat treatment temperature. The hardness and elastic modulus of the as-deposited NG coating were measured to be 8.7 GPa and 199.5 GPa, respectively. The hardness was maintained nearly constant after annealing at 100, 200 and 400 ℃, and showed just a mild reduction to 8.2 GPa after annealing at 600 ℃. The $H/E_r$ and $H^3/E_r^2$ ratios for each annealing group are shown in Figures 5.5-6c&d. Compared to the neat Ni coating, the NG composite coating exhibited less reduction rate in both parameters. For instance, after annealing at 600 ℃ the $H/E_r$ and $H^3/E_r^2$ values of the NG coating decreased by 13.7% and 30.1% respectively from the original, while for the neat Ni the corresponding percentages were 25.6% and 56.5%.

## 5.6 Discussion

### 5.6.1 The successful incorporation of GO in the nickel matrix

The current study explored the use of electro-brush plating for the fabrication of a nickel-graphene oxide nano-composite coating. Several characterisation methods, such as top-view and cross-sectional SEM observation, EDS, Raman as well as XRD were employed to confirm the successful incorporation of GO sheets which was not only at the surface but also deep into the nickel matrixes. Due to their flexibility and high aspect ratio, GO sheets were able to fit in small corners and caves and wrap nickel clusters of whatever sizes during the coating fabrication, as evidenced in Figure 5.1-2e and Figures 5.1-3 c-d. It is likely that in the final composite matrix the ultrathin GO sheets were entangled and cross linked with each other and appear as a high-density 3D network architecture in which nickel grains nucleate, grow and connect.

In addition, due to the hydrolysis of the oxygen functional groups (in particular the –COOH carboxyl groups) on the GO structure, a GO sheet can readily show negative charges in water. Thus, it is plausible that nickel cations show a high affinity to GO sheets and tend to settle down on them. Meanwhile, it has been reported that GO can be electrochemically reduced (and thus form rGO) at a very small negative potential [118], via cyclic voltammetry sweeping [117, 265, 266] or during electroplating [165]. In this study, the voltage applied between the brush (anode) and the substrate (cathode) during coating fabrication was 14 V. Although the exact value of the potential applied on the cathode is difficult to monitor due to technical reasons, as a potential of -1 V to -2 V is enough to initiate the electrochemical reduction of GO [118], it is believed that the GO sheets in the nickel matrixes might have been reduced.

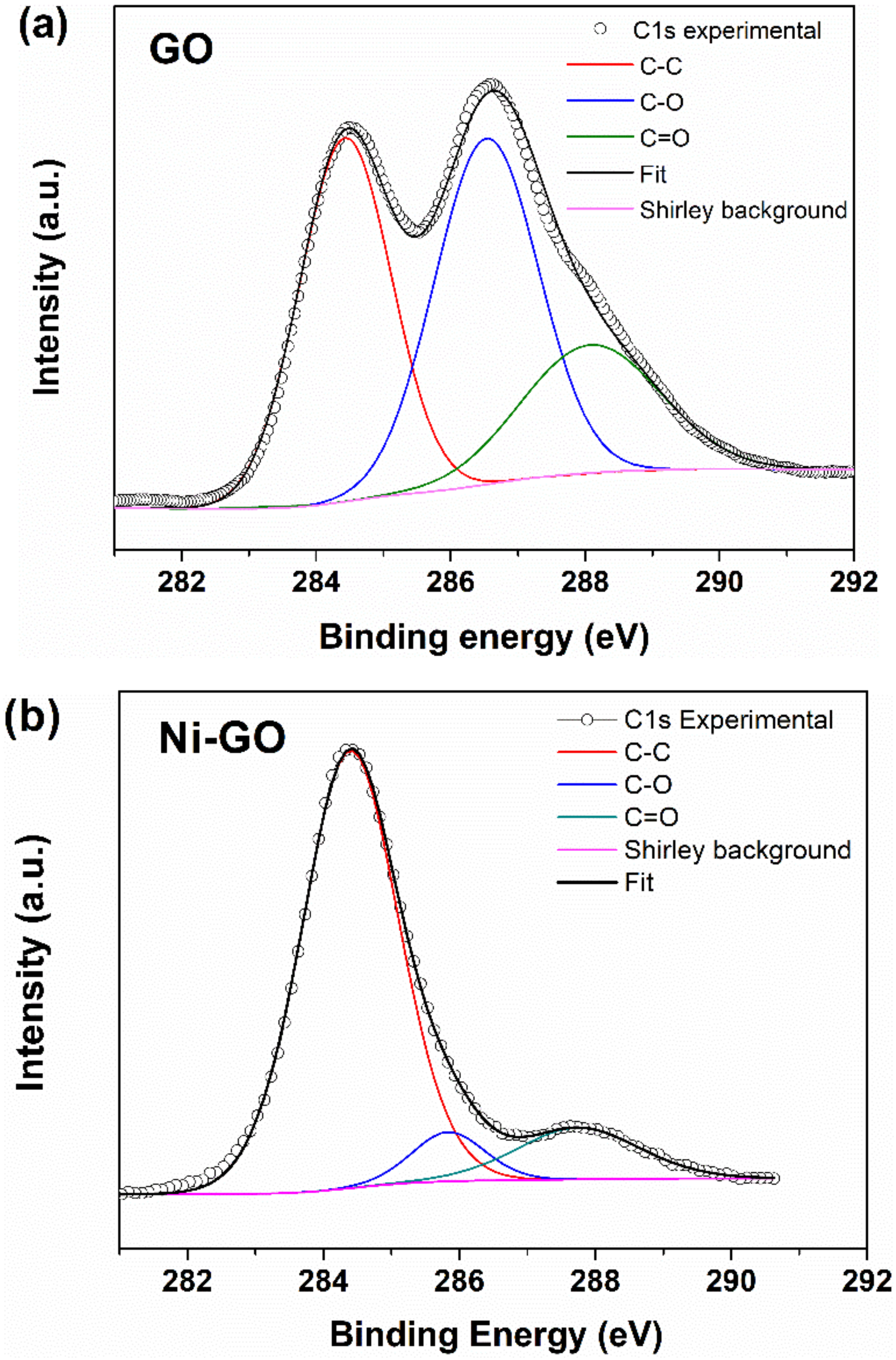

Figure 5.6-1 XPS C1s spectra of (a) as-prepared GO and (b) Ni-GO composite coating.

To this end, XPS analysis of the as-prepared GO and the resultant Ni-GO composite were performed. Figure 5.6-1 compares the C1s spectra of the two samples. The Ni-GO composite showed significant attenuated C-O and C=O peaks compared to as-prepared GO, indicating a remarkable reduction effect during the coating deposition. Once nickel ions attach to the surface of rGO sheets they can be instantly reduced to metallic nickel owing to the electrical conductivity of rGO, which enables quick electron transfer from the substrate (cathode). In other words, GO incorporation promoted the nucleation process of nickel ions. This is evidenced in this work by the observation that fine nickel spheres formed on GO sheets (Figure 5.6-2). It is also echoed by Zhang et al. [141] who demonstrated the fabrication of Ni ion decorated GO making use of the chemical activity of GO.

The reduced coating thickness after introducing GO as compared in Figure 5.1-3 could be two-fold. On one hand, it could be a result of the lower deposition efficiency from the GO-containing plating solution. As discussed in the preceding paragraph, the GO sheets were reduced electrochemically at the cathode during deposition, thus consuming a fraction of the current efficiency and leading to a lower deposition rate for nickel. On the other hand, it could also be ascribed to the increased viscosity of the plating solution with increasing GO load due to the very high aspect ratio of GO sheets. As basically it is a liquid-based deposition technique, the deposition rate would decrease if the plating solution became thicker. Actually, at a GO concentration of 6 mg/ml, all the attempts to obtain a coating from the plating slurry failed.

There have been a number of reports on the electrodeposition of Ni-graphene composites and the majority of them are about conventional electroplating [165-170]. In the available reports, a small GO load of 0.05-2 mg/ml was commonly used, while the obtained coatings usually showed rough morphology due to the agglomerations of GO sheets [168-170]. To the best of our awareness, there is no any report yet on the brush-plating of such nano-composite coatings. One of the largest advantages of brush plating over conventional electrodeposition techniques is that the former enables higher nano filler load (up to 4 mg/ml in this work) into the matrix while smoothing the coating surface owing to the use of an additional mechanical force during the plating process. As shown in Figure 5.1-2, the electro-brush plated Ni-GO coatings possess low surface roughness. For comparison, Figure 5.6-3 displays the morphology of a Ni-GO composite coating by conventional electroplating with a GO load of 0.5 mg/ml. Around the bulges it showed well-defined crystals, which was pure nickel (GO-free) by EDS analysis. A large number of carbon-rich bulges formed on the coating surface, which is consistent with the literature on similar composites [170].

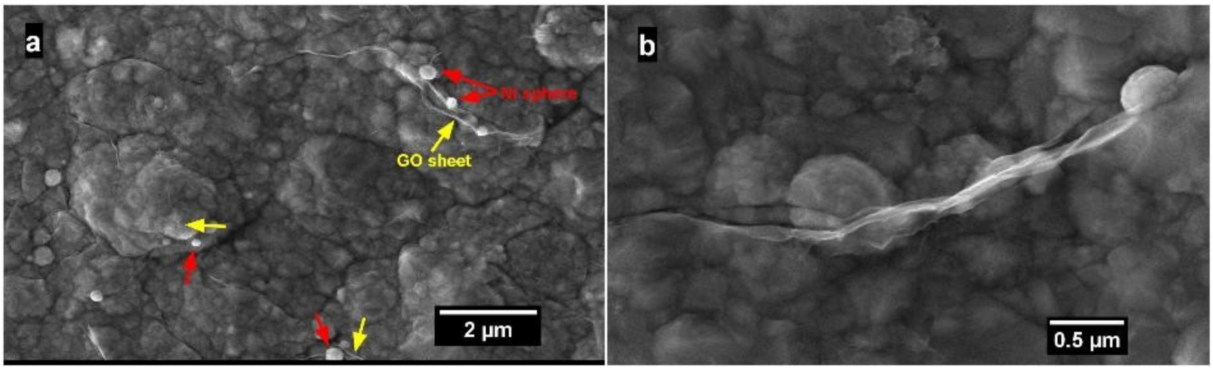

Figure 5.6-2 (a) Surface of a Ni-GO composite coating showing nickel crystalline spheres grown on GO sheets. (b) Nickel grains intersected by a GO sheet.

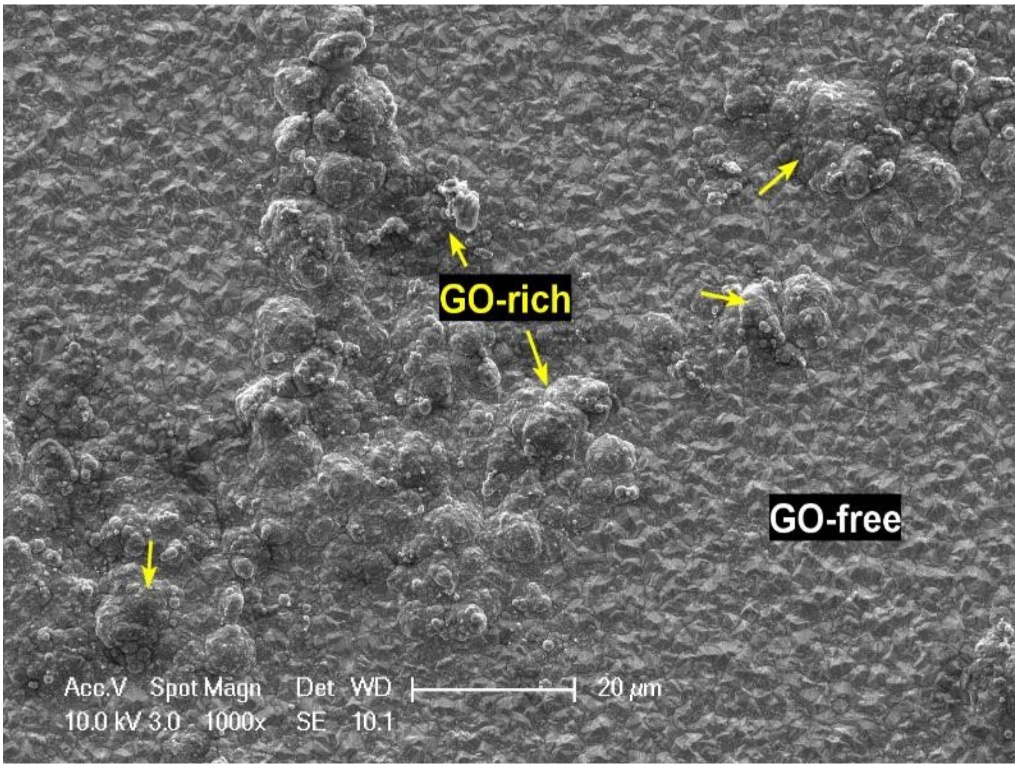

Figure 5.6-3 SEM image showing the high degree of GO agglomeration of the composite coating by conventional electroplating.

### 5.6.2 Microstructure – mechanical property relationship

It has been demonstrated by means of XRD that the average crystallite sizes of the GO-containing composite coatings were smaller, which could be associated with the nucleation promotion effect of GO as discussed above. In an electrochemical deposition process the nucleation and crystal growth compete against each other [168], i.e. the higher the nucleation rate, the smaller the grown crystals could be. Moreover, it was evidenced by SEM (see Figure 5.6-2b) that GO sheets intersected the nickel clusters randomly, thus obstructing the normal growth of the nickel crystals and providing nucleation sites for new grains [254]. Based on the discussion above, the grain size refinement could be explained.

With regards to mechanical properties, it is well known that grain size refining is among the main ways for the strengthening of a material. Thus, the improved hardness and Young's modulus of the Ni-GO composite coating could be associated with the reduced grain size of the matrix (Table 5.1-2). Moreover, the incorporated graphene oxide sheets could demonstrate an anchor effect which prevented nickel grains from sliding, thus enhancing the mechanical properties [254, 267]. Additionally, the intrinsic mechanical strength of graphene oxide might have a contribution to the enhancement of the Ni-GO composite coatings. While pristine graphene possesses a Young's modulus of 1 TPa and an intrinsic strength of 130 GPa [3], it is reported that the mechanical properties of a graphene sheet are inversely affected by the degree of structural defects, such as holes, vacancies and oxygen functional groups [268]. AFM tip indentation experiments showed effective Young's moduli of 207.6±23.4 GPa, 223.9±17.7 GPa and 229.5±27.0 GPa for monolayer, bilayer and three-layer GO, respectively [269]. After reduction, rGO monolayers showed a Young's modulus of 250 GPa [270]. Given that the GO sheets in the nickel matrixes in this work have been reduced as discussed in Section 5.6.1, the elastic modulus of the incorporated GO sheets should fall between the reported values for GO (~200 GPa) and rGO (~250 GPa), either of which is higher than that of the neat Ni (~185 GPa, see Table 5.2-1) in this work. Improvements of the mechanical properties of the resultant composites can thus be expected.

However, when the GO content is beyond a specific level (for instance, NG40 in this work) agglomeration is likely to occur, which may lead to more defects and ultimately result in a reduced hardness [271]. Nevertheless, the NG40 composite coating was still able to show an improved resistance to plastic deformation, much likely due to the inherent strength of the cross-linked GO sheets.

### 5.6.3 Effect of GO on the corrosion resistance of the composite coating

The impermeability of the GO structure is believed to be the origin for the improvement in corrosion resistance of the Ni-GO composite coatings. Although only one-atom-thick, graphene can block all molecules including helium the smallest from passing through [57]. The chloride ions ($Cl^-$) whose van der Waals diameter is 0.35 nm are much larger than the pore size (0.064 nm) on the carbon network of graphene oxide, which means GO can act as an extraordinary physical barrier against corrosive species [19]. Given the limited dimensions of a GO sheet, it seems that the edges of the GO sheets as well as the micro voids/defects generated within the nickel matrixes were the possible passages for the electrolyte. Therefore, the interaction between the GO sheets and the nickel matrix is of much importance for the anti-corrosion performance.

Brush-plated Ni coatings naturally contain a more or less number of voids and pin holes [155, 262], leading to an unstable electrolyte/coating interface due to transient penetration of water and corrosive species (mainly $Cl^-$) via these defects. As a result, the electrochemical interface area would increase and so the total corrosion current flow. This is consistent with the observation of sparkles in the anodic polarisation curves of the neat Ni and NG40 (Figure 5.3-1).

However, unlike the common pitting featuring catastrophic increase of the corrosion current, the pitting in Figure 5.3-1 was metastable and stopped by re-passivation of the interior of the voids and pinholes. In such a circumstance, a low coating resistance $R_c$ but a relatively high capacitance $CPE_c$ for the neat Ni coating were measured as the pinholes were filled with electrolyte which largely increased the ion conductivity and dielectric constant. As the internal area exposed to the electrolyte accumulated, it could also be expected that an electric double layer formed at the electrolyte/metal interface, modelled by a double layer capacitance ($CPE_{dl}$) and charge transfer resistance ($R_{ct}$) as seen in Figure 5.3-2b. It is worth noting that unlike organic coating systems where the $CPE_{dl}$ and $R_{ct}$ are usually allocated at the coating/metal substrate interface, in this case the electric double layer could be formed at the GO/Ni interface within the coating, too. Given these information, the remarkable increase in $R_c$ and the depressed $CPE_c$ for both GO-containing coatings could be attributed to the excellent barrier effect of GO which inhibited the water uptake effectively. In the meantime, GO could have reduced the chemical activities for electrolyte/Ni and electrolyte/substrate interfaces, suggested by the higher $R_{ct}$ and $CPE_{dl}$. The corrosion behaviour of the electro-brush plated composite coatings outperformed those by conventional electroplating. For example, the EIS results showed an improvement of 2 times [170] and 1.5 times [166] in cases of electroplated Ni-graphene (oxide) composite coatings, while in this study the corrosion impedance of NG20 was remarkably 6 times larger than neat Ni.

With reference to NG40, the negative shift in corrosion potential, higher current density and the degraded EIS data set in comparison with NG20 might be related to a loose and defective microstructure which let more electrolyte in than NG20. This is in line with the findings from the XRD and mechanical measurements that NG40 was weaker in terms of its mechanical strength in spite of its reduced grain size. It has been reported that the graphene or carbon nanotube (CNT) fillers inside a metallic matrix even promoted the corrosion at the carbon/metal interface in the presence of electrolyte, as graphene and CNT are chemically nobler than the coating metals [22, 272]. Therefore, it is essential to enhance the interaction between the nano fillers and the matrix for a good mechanical and anti-corrosion performance.

### 5.6.4 Tribological performance

This study aimed at evaluating the tribological performance of a nickel-GO composite coating produced by electro-brush plating. To this end, coatings with varied GO content were fabricated and tribological tests under different conditions were performed. Meanwhile, a nickel-graphite composite coating was purposely designed and tested for comparison. In general, GO was found to improve the anti-friction and anti-wear properties of the nickel matrixes effectively. In this section, the influence of GO content, counterpart material and nitrogen gas on the tribological behaviour of the nickel-GO composite coating is discussed. Finally, different wear mechanisms for Ni-GO and Ni-graphite composites are suggested.

#### 5.6.4.1 Influence of GO content

The results of the tribo-tests against the chromium steel ball (Figure 5.4-2b and Figure 5.4-3) suggested a clear tendency that as the GO content increased, the tribological performance of the resultant composite coating was improved progressively, in terms of lower friction coefficient (Figure 5.4-2b) and reduced wear (Figures 5.4-3 and 5.4-4). The most pronounced improvement, for instance, was observed on NG40 (GO load 4 mg/ml in the plating solution), whose COF and wear coefficient were about 37% and 88% lower than those of the neat Ni, respectively.

The reasons for the reduction in friction coefficient and wear could be three-fold. Firstly, it can be ascribed to the improved mechanical properties of the composite coatings, including the indentation hardness ($H$) and the plasticity. According to the adhesive theory of wear [273], the coefficient of friction $\mu$ between a tribo-pair, formed of a rigid counterpart and an engineering surface in multi-asperity contact, can be expressed by the following equation:

$$\mu_{adh} = \frac{F}{W} = \frac{\tau}{\sqrt{\sigma^2 - a\tau^2}} \approx \frac{\tau_i}{\sigma} \qquad (5.6\text{-}1)$$

where $F$ is the tangential frictional force, $W$ is the normal load, $\tau$ is the shear strength of the bulk material, $\sigma$ is the corresponding compression yield strength, and $a$ is a numerical factor, determined empirically. The equation receives a simplified form as shown at its right end when the surface is covered by a weak interfacial film of low shear strength $\tau_i$, such as oxide scale grown in-situ. It is therefore clear that a lower $\mu_{adh}$ could be obtained if the yield strength $\sigma$, which is proportional to the indentation hardness of the bulk, is improved. Hardness is also known to affect the resistance to abrasive wear inversely. Indeed, the COF evolution (Figure 5.4-2b) of the composite coatings NG05, NG20 and NG40 exhibited good compliance to their hardness values; the COFs were reduced to an extent comparable to the degree of their hardness improvement (Figure 5.4-1).

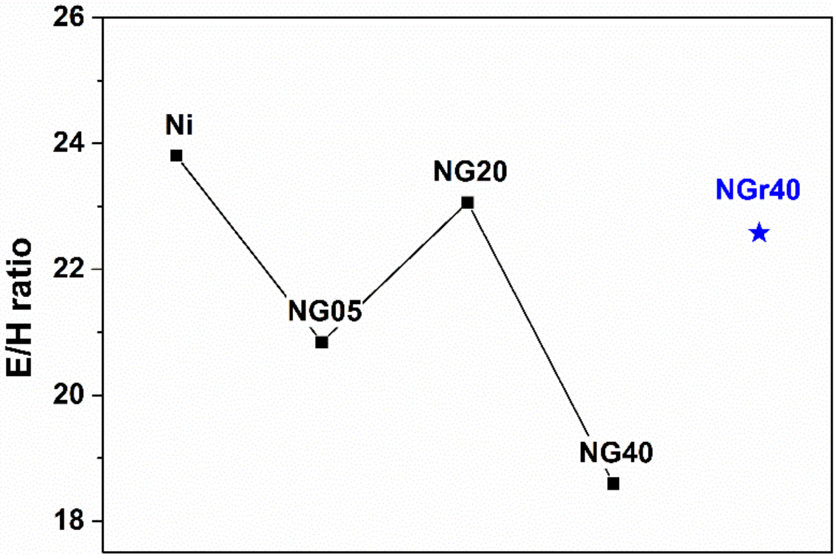

Figure 5.6-4 E/H ratio of neat Ni and Ni-GO composite coatings.

More importantly, the ratio between Young’s (elastic) modulus and hardness *E/H*, which is indicative of the plasticity of a material, can play a significant role in the tribological performance [274, 275]. A lower *E/H* ratio means that the material is less prone to plastic deformation, i.e., the contact between sliding asperities is more elastic. As a result, the plastic flow over the sliding interface, which is commonly seen in severe adhesive wear, is mitigated. The *E/H* ratio values for neat Ni and the Ni-GO composite coatings in this work were calculated from nanoindentation measurement results and plotted in Figure 5.6-4. It shows that the *E/H* ratio values were reduced effectively by introducing GO into the matrixes. Particularly, NG40 showed an *E/H* ratio of 18.6, which is remarkably lower than that (23.8) of the neat Ni coating. This is in agreement with its wear coefficient which was the smallest among all the samples (Figure 5.4-4).

The improved tribological performance of Ni-GO composite coatings is also owing to the formation of a continuous easy-shear oxide film on the coating surface. As can be seen in Figure 5.4-5, the worn neat Ni coating showed material 'islands' across the wear track, which were the oxides of the metallic coating. It is known that oxide films, formed naturally on metals in air, are of much significance in determining the tribological behaviour, as the oxides can serve as a low shear strength film which reduces the $\mu$ of the tribo-pair (refer to Equation 5.6-1). However, if the oxide film is incomplete or when it is penetrated by the slider, a high value of $\mu$ is very likely, due to direct metallic contact, and so the wear coefficient, as in the case of the neat Ni. The damaged oxide film was detached and then transformed into oxide particles (Figures 5.4-5c&d) due to work-hardening and cutting by the slider, thus leading to considerably three-body abrasion. The formation of such an incomplete oxide film was also observed on the worn coating incorporating graphite flakes (Figure 5.4-6), which could be the reason for the marginally lowered $\mu$ and wear of NGr40.

In contrast, the worn Ni-GO composite coatings showed decreasing amount of surface irregularities as the GO content increased (Figure 5.4-7), which may imply a better retention of the surface oxides. The enhanced retention of the oxide films is likely due to the reduced plasticity of the bulk coatings as discussed above, and can also be related to the lubricating GO sheets which mitigated the tangential frictional force applied to the surface metallic oxide. As a result, the adhesion and plastic flow during sliding were suppressed, and the wear behaviour of the coatings changed gradually from plasticity-dominated for neat Ni (severe wear) to oxidation-dominated for NG40 (mild wear).

Last but not least, the lubricating effect originated from GO itself, as mentioned a few lines above, should be appreciated, too. Graphene and its derivatives (including GO) have been reported to be promising novel solid lubricants [192]. With regards to graphene-containing composites, it has been reported that a carbon-rich transfer layer can be formed on top of the sliding composite surface [201]. This carbon-rich transfer layer can further contribute to a lower $\tau_i$ in Equation 5.6-1, thus lubricating the sliding. Such a carbon-rich surface film was not verified by means of EDS analysis in this work as it was difficult to distinguish the low intensity carbon from adsorbed surface contaminations. However, Raman spectra obtained within the wear track did show residues of the features of GO (Figure 5.4-8, worn sites 2 and 3), indicating that GO of high degree of defects was still present on at least part of the surface. The Raman features were gone at the centre of the wear scar (Figure 5.4-8, worn site 1), suggesting that the GO sheets at that place may have been transformed into amorphous carbon, if not a complete removal.

More interestingly, apart from the Raman analysis results, nano-sized GO rolls were also observed existing within the worn scar as already seen in Figure 5.4-7f and magnified in Figure 5. 6-5. Figure 5. 6-6 demonstrates the sectioning process of the GO rolls using focused ion beam (FIB). The hollow structure of the GO rolls is clearly observed as the cutting continued. These are direct evidence for the participation of GO in the tribological activities of the composite coatings.

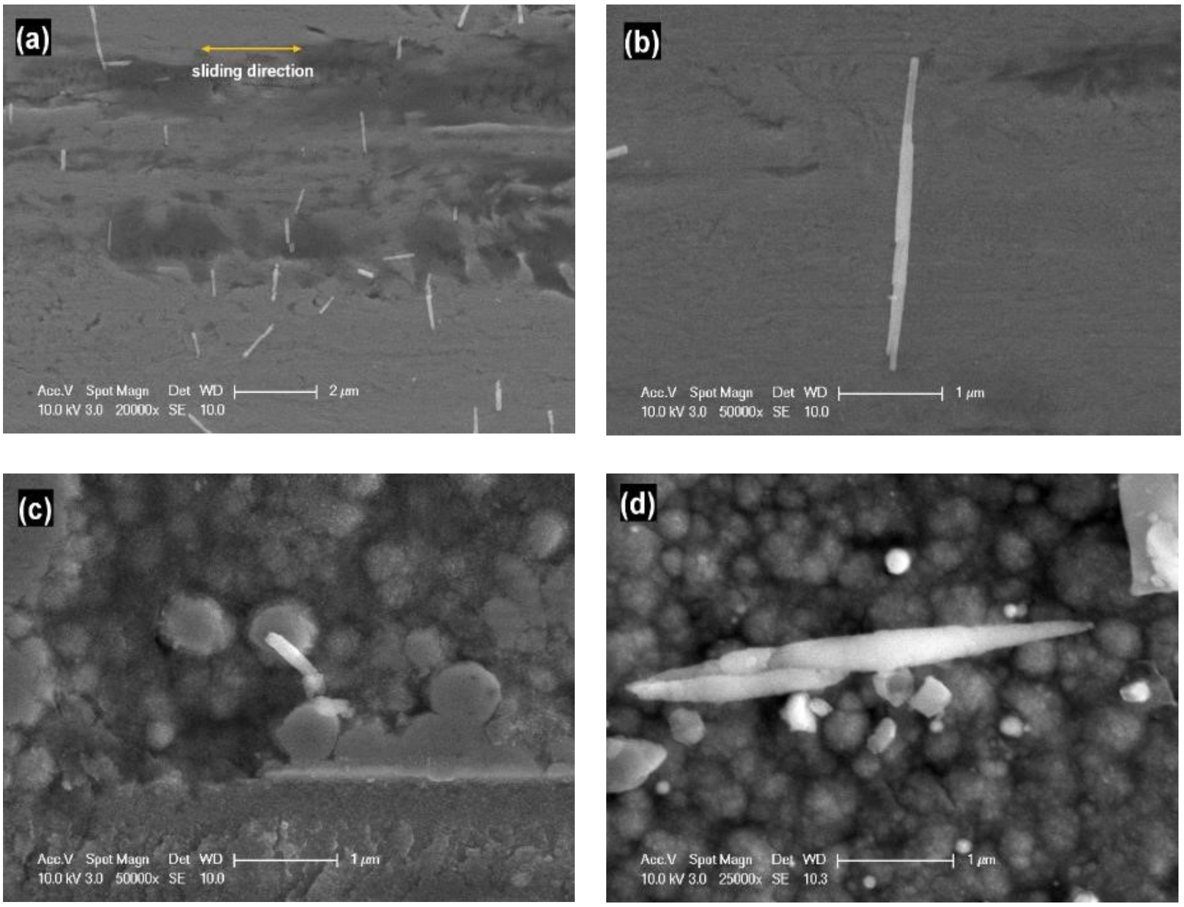

Figure 5.6-5 GO rolls formed within the wear track during sliding.

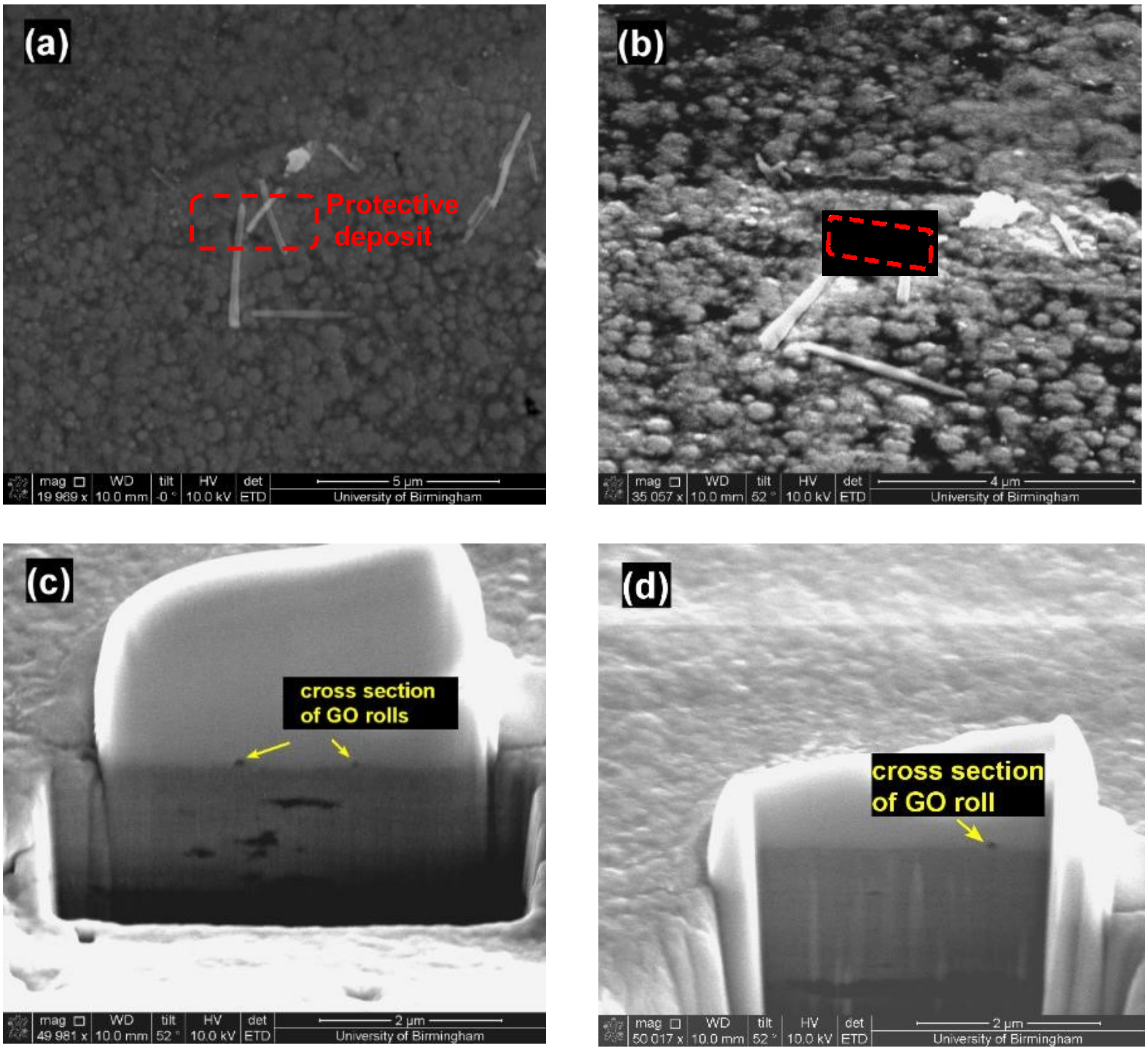

Figure 5.6-6 Snapshots during FIB sectioning of GO rolls on the NG coating after sliding wear.

Berman et al. [276] report the formation and macroscale superlubricity of graphene nanoscrolls in the presence of nano-diamond particles which could be the first of this kind. Recently, graphene nanoscrolls were found to form on the surface of an amorphous carbon film during sliding which is responsible for the friction drop [277]. A few other rolling-up carbon structures, such as crumpled graphene balls [278], carbon nano-horns [279], have also been reported to improve the tribology of the sliding surface underneath. However, to our awareness, this is the first report on the observed formation of such graphene nanorolls not out of a single graphene coating or as lubricant additives but from a graphene-based composite during sliding contact.

As can be seen in Figure 5. 6-5, the GO nanorolls were uniform in diameter and distributed mostly perpendicular to the sliding direction. The formation could therefore be attributed to the generation of structural defects on the upside of the GO sheets during sliding in conjunction with the dragging force of the slider [276]. The friction-reduction mechanisms that have previously been suggested for these rolling graphene structures include nano ball bearing, sliding and exfoliation [277, 279]. In view of the high contact pressure (500-1000 MPa) applied in this work which may squeeze and permanently deform the hollow GO rolls once upon formation, the nano bearing effect is unlikely to take place (Indeed, the GO rolls were mainly found close the edges of the wear scar, while few GO rolls were observed at the centre where the contact pressure was maximum). Rather, the sliding mechanism, in which the GO nanorolls acted as separators of low surface energy between the tribo-pair, is more plausible. Moreover, GO sheets are so thin and flexible that a fraction of the sliding motion energy can be easily dissipated by means of nanoroll formation, hence leaving less energy that is converted into friction.

### 5.6.4.2 Influence of counterface

When sliding against chromium steel, although the Ni-GO composite coatings exhibited favourable tribological behaviour under a light load of 1 N, the $\mu$ increased largely and so did the wear when heavier normal loads of 2 N and 3 N were applied (Figures 5.4-9 and 5.4-10). This is likely due to the penetration of the lubricating oxide film under higher loads, which led to metal-to-metal contact. The rise of metallic contact was then followed by strong adhesion and cold-welding between the steel counterface and the nickel coating, finally leading to fracture of the cold-welded asperities by sliding and complete failure of the oxide film.

When sliding against an alumina ball, however, the COFs for both GO-free and GO-containing coatings were about 0.1-0.2 lower than those against the chromium steel ball (Figure 5.4-11). It is also worth noting that the COFs did not show appreciable increase with the increasing load (Figure 5.4-11b) as seen with the coating-steel tribo-pair. The differences can be attributed to the alumina counterpart, which enabled constant ceramic-metal oxides or ceramic-metal contact, hence reducing adhesion and securing lower $\mu$ values.

The cracks observed on worn neat Ni (Figure 5.4-14) were likely caused by fatigue under the reciprocating normal load. They propagated in such a way that the metallic oxides formed on the surface were pulled and detached into lamellar pieces (Figure 5.4-14b) or debris particles (Figure 5.4-14c), leaving a wavy topography. Such severe plastic deformation was mostly inhibited for NG40 (Figure 5.4-12). The smooth and shallow wear scar of the GO-containing composite coating (Figure 5.4-15) can be mostly attributed to the formation of a continuous oxide film, as evidenced by EDS mapping (Figure 5.4-15b). Meanwhile, despite the difficulties in resolving potential GO lubricating film at the centre of the smooth track, flake-like translucent films were found widely distributed around edges of the wear scar (Figures 5.4-15d&e). These carbon-rich thin films, according to EDS analysis, were much likely formed of segregated and squeezed GO sheets. It is then expected that similar GO-based transfer films, although highly deformed, could be also covering the central part of the wear scar and contribute to the reduced friction and wear.

The lower COF for NGr40 could be attributed to the shearing and exfoliation of graphite flakes within the composite (mainly capsuled in the surface bulges), and the effectively reduced abrasion by storing the wear debris between surface irregularities (Figure 5.4-16b). Nonetheless, this configuration can lead to inhomogeneous stress distribution and therefore cracking and spallation, as shown in Figure 5.4-16c.

#### 5.6.4.3 Influence of nitrogen gas

Graphite is a well-known solid lubricant that demonstrates high efficiency especially in humid environments, due to the easy shear enabled by water vapour or other condensable gaseous molecules intercalated between or adsorbed on the edges of the graphitic layers. However, graphite usually shows inferior lubricating effect in dry environments. It has been reported that graphene differs from graphite for its ability to lubricate regardless of the humidity of the environment [192]. It is therefore interesting to verify this idea with composite coatings containing either GO or graphite.

The COF increase for neat Ni under nitrogen flow revealed in Figure 5.4-17 is mainly because oxides were difficult to form due to the lack of oxygen in the atmosphere, thus limiting the lubricating effect of the metallic oxides [280]. The Ni-GO and Ni-graphite composite coatings also showed increased friction when subject to nitrogen purging. The distinct advantage of graphene lubricant in nitrogen as reported [12] was not observed, partially due to the influence of the less metallic oxide formation as discussed above, and could be also due to the reduced lubricating efficiency of GO which contains more structural defects and promotes formation of interlayer hydrogen bonds [188]. Nevertheless, the GO-containing composite coating showed less COF fluctuations (Figure 5.4-17) and surface destructions (Figure 5.4-18) upon environment switches than the graphite-containing coating, denoting a much more reliable wear resistance.

### 5.6.4.4 Wear mechanisms for GO- and graphite-containing composites

Based on the results and discussion above, different wear mechanisms for graphene-metal composite coatings and graphite-metal composite coatings are proposed, as illustrated in Figure 5.6-7. Owing to the extremely thin nature of graphene, the composite incorporating graphene oxide (or other graphene derivatives), given that the GO fillers are homogeneously distributed (Figure 5.6-7a), is a real nano-structured material, which is free of surface lumps like what with its graphite counterpart (Figure 5.6-7d). The ultra-high aspect ratio of graphene also enables effective strengthening to the matrix while using the same or less mass of fillers, as shown in Figure 5.4-1.

During sliding wear, a continuous metallic oxide film, which is favourable for lower friction and wear, can be developed on the surface of the GO-reinforced composite coating, due to the pinning and strengthening effects of GO (Figure 5.6-7b). As the sliding continues, not only the metallic oxide layer gets thicker and work-hardened, an extra thin lubricating film comprising of squeezed GO sheets is formed on top (Figure 5.6-7c). There are also chances that GO sheets are peeled off by the slider and form nanorolls (see Figure 5.6-5) which reduce the surface energy and thus the friction.

The graphite-reinforced composite coating, by contrast, achieves its low friction mainly on the smearing of graphite flakes (Figure 5.6-7e). Given the limited availability of graphite sites on the surface, discrete metallic oxide islands instead of a continuous oxide film are formed, and a large amount of wear debris occurs. Meanwhile, the uneven distribution of stress between the graphite-containing lumps and the squeezed wear debris can lead to cracks and spallation (Figure 5.6-7f).

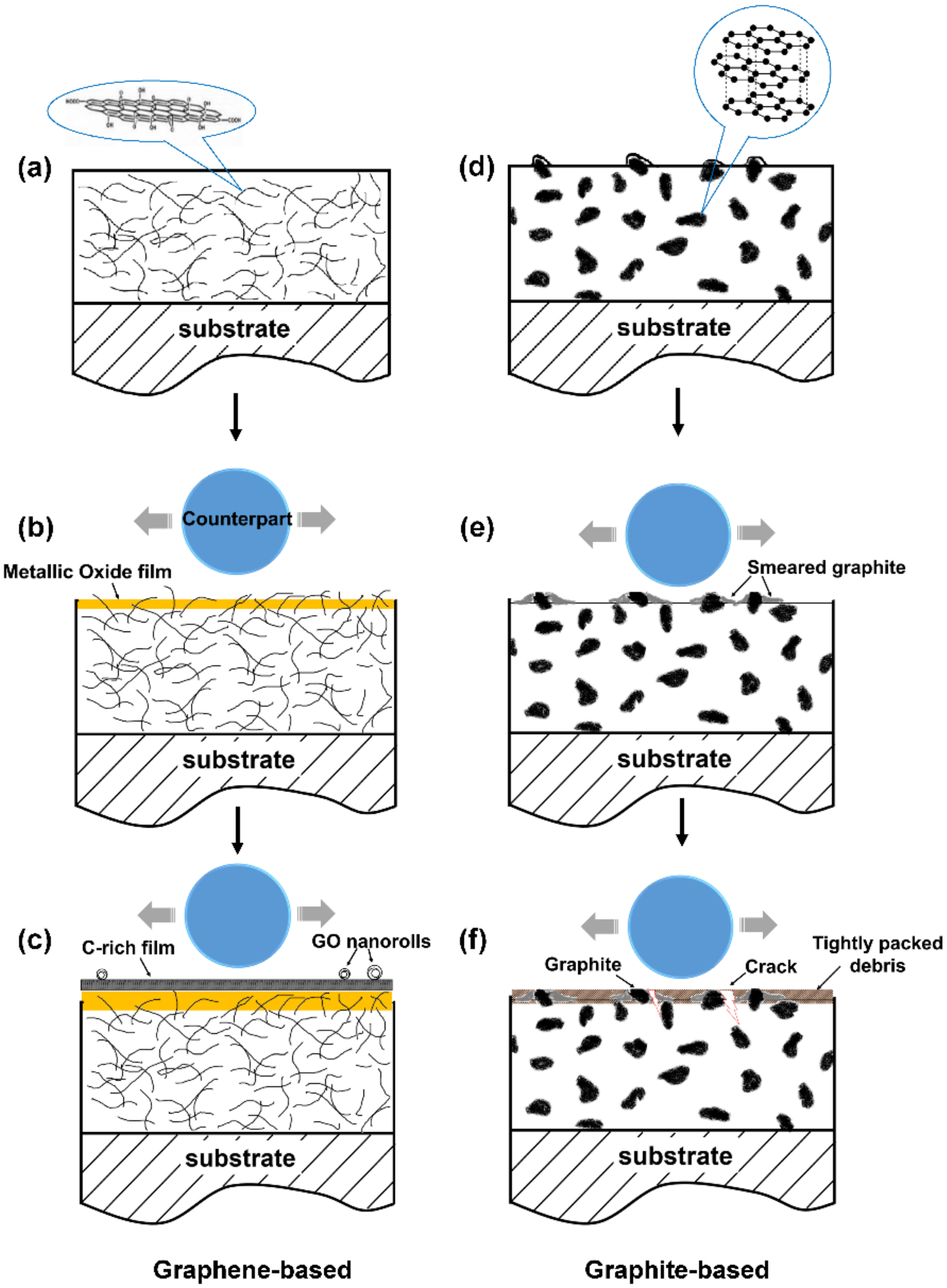

Figure 5.6-7 Illustrations of the different wear mechanisms for (a-c) graphene-metal composite and (d-f) graphite-metal composite.

### 5.6.5 Thermal stability

5.6.5.1 Microstructure and mechanical properties relationship

The nickel coatings by electro-brush plating (EBP) in this study possess a hardness of more than 500 Hv. This is mainly due to the dense and nanocrystalline structure, as discussed in Section 5.6.2. However, during a heat treatment the growth of crystallites can lead to degradation of the material's mechanical properties [281-283].

In this study, the X-ray diffraction peaks of the neat Ni coating were sharpened largely upon annealing at 600 ℃ (Figure 5.5-4), most likely due to significantly increased grain size as per the Scherrer assumptions (Equation 5.1-1 and Table 5.5-1). As a consequence, a 22% decrease in hardness for the 600 ℃ annealed Ni coating was measured (Figure 5.5-6a). The slight hardness increase at 200 ℃ could be attributed to the short-range re-arrangement of the microstructure [282].

It is worth pointing out that residual stress may be introduced into the deposit during the coating fabrication process. The microscopic residual strain within the crystallites can also affect the shape of the diffraction profile shape as described by the following equation:

$$\beta = 4\varepsilon \cdot tan\,\theta_{hkl} \tag{5.6-2}$$

where $\beta$ is the full width at half maximum (FWHM) of the diffraction peak in radian, $\varepsilon$ is the average microstrain, $\theta_{hkl}$ is the Bragg diffraction angle. Combing the effects of grain refinement as estimated by the Scherrer equation and microstrain as shown above, and given that the peak profile is of Lorentzian type (shape factor 0.9 according to X'Pert HighScore software), the peak width can be expressed as:

$$\beta_{tot} = \frac{K\lambda}{L\cos\theta_{hkl}} + 4\varepsilon \cdot \tan\theta_{hkl} \tag{5.6-3}$$

or in an alternative form:

$$\beta_{tot} \cdot \frac{\cos\theta}{\lambda} = 4\varepsilon \cdot \frac{\sin\theta}{\lambda} + \frac{K}{L} \qquad (5.6\text{-}4)$$

where $K$ is Scherrer constant, $\lambda$ is the wavelength of the radiation, and $L$ is the average crystallite size. Therefore, the relaxation of the microstrain inside the coating matrix during annealing could also be responsible for the sharpening of the nickel diffraction peaks and the decrease of the hardness.

The quantification of the microstrain before and after the heat treatments, however, was not conducted based on Equation 5.6-4 for several reasons. Technically, according to Equation 5.6-4 a reliable estimation of the microstrain ε requires data from an enough number of diffraction peaks, especially those at higher diffraction angles, which were low in both quantity and intensity for the brush plated coatings in this study. More importantly, the manual brushing operation during coating application has determined that the stress distribution across the coating is inhomogeneous by nature. Some other factors, such as any minor discrepancies in the heating/cooling conditions and the element segregation (to be discussed below) can also make the stress status very complicated. In that case, the microstrain cannot be reasonably quantified based on one simple equation. Nevertheless, from a qualitative point of view, the impact of residual stress was visually pronounced, as the neat Ni coating bended and cracked after annealing at 600 ℃ (Figure 5.5-1d), likely due to non-uniform relief of the internal stress during the annealing.

It is also possible that the segregation of iron near the coating surface during annealing induced changes in the microstructure and stress status of the coatings, and in turn resulted in changes in the mechanical properties. As mentioned before, the plating solution formula used in this study contains a fraction of iron (Figure 5.5-2a). In the as-deposited coating, the minor content of Fe existed as substitutional atoms within the face centred cubic (fcc) lattice of nickel, which can lead to some extent of microstrain due to lattice parameter mismatch. As shown in Figure 5.5-2 and Figure 5.5-3, it seems that upon annealing the iron element diffused from the bulk Ni and NG coatings to the surface and formed oxide. Although there is uncertainty in the oxygen quantification by means of EDS (Figure 5.5-2 a-b), the XRD analysis confirmed that the oxide scale was α-$Fe_2O_3$ (Figure 5.5-4). According to the theory of metal oxidation by Wagner [284], when the coating was exposed to hot oxidising atmosphere, iron migrated outwards and formed a continuous oxide scale on the coating surface due to the lower free energy of formation for iron oxide compared with it is for NiO. The original iron sites were substituted by nickel atoms, thus resulting in relaxation of the strain induced by lattice mismatch. It is hence likely that the localised stress concentration changed due to the depletion of Fe.

Based on the discussion above, the effects of GO should be two-fold. On one hand, the grain growth of the NG composite during a thermal exposure was strongly suppressed due to GO sheets' confining and pinning effect towards the developing nickel grain boundaries and dislocations as reported for other reinforcements such as $Al_2O_3$ [158], SiC [285], Carbon nanotubes [254] and recently graphene [168, 286]. On the other hand, due to the high aspect ratio and flexibility of its 2D structure, graphene (and GO) can be more advantageous than other reinforcing particulates in conditioning the distribution of residual stress and facilitating smooth relief of the internal stress during annealing. As estimated via the Scherrer approach, the NG (Ni-GO) composite coating underwent much less grain growth (Table 5.5-1). In the meantime, the crack-free morphology of the annealed NG coating (Figure 5.5-1h) suggests that the residual stress from coating deposition and thermal annealing (where iron migration also took place) was evenly accommodated in presence of GO. Consequently, the NG composite coating exhibited highly similar indentation response after annealing at varying temperatures, and a hardness reduction of merely 6% (22% for the neat Ni) after annealing at 600 ℃, indicating a significantly improved thermal stability.

The benefit of incorporating GO in the metallic matrix is also shown by the retarded decline in the $H/E_r$ and $H^3/E_r^2$ ratios after thermal treatments (Figure 5.5-6 c-d). $H/E$ and $H^3/E^2$ are two tribologically important parameters, indicating the elastic strain to failure and the resistance to plastic deformation, respectively [275, 287]. As suggested by Layland and Matthews [288], $H/E$ is one of the key criteria in designing wear-resistant coatings as it is responsible for the durability and resilience of the coating material. It is also closely related to the fracture toughness of the material [275, 289]. Besides, it has been reported that the resistance of the film to cracking (toughness) increases with the $H^3/E^2$ value [290]. In this report, $E_r$ instead of $E$ is used, assuming that the Poisson's ratio $v$ is a constant. The $H/E_r$ and $H^3/E_r^2$ of the NG composite coating were less affected by the heat treatments than they were with the neat Ni, indicating a better retention of the elastic properties.

#### 5.6.5.2 Graphene *vs.* graphite

Along with any improvement made by graphene or its derivatives such as GO, there always comes a question about the effectiveness of graphite for the same task. It is therefore beneficial to study the mechanical properties of Ni-graphite composite coatings, in particular those after thermal treatments. To this end, a Ni-graphite composite coating (namely NGr) was produced with the same particle load and operation conditions as for the NG composite coating.

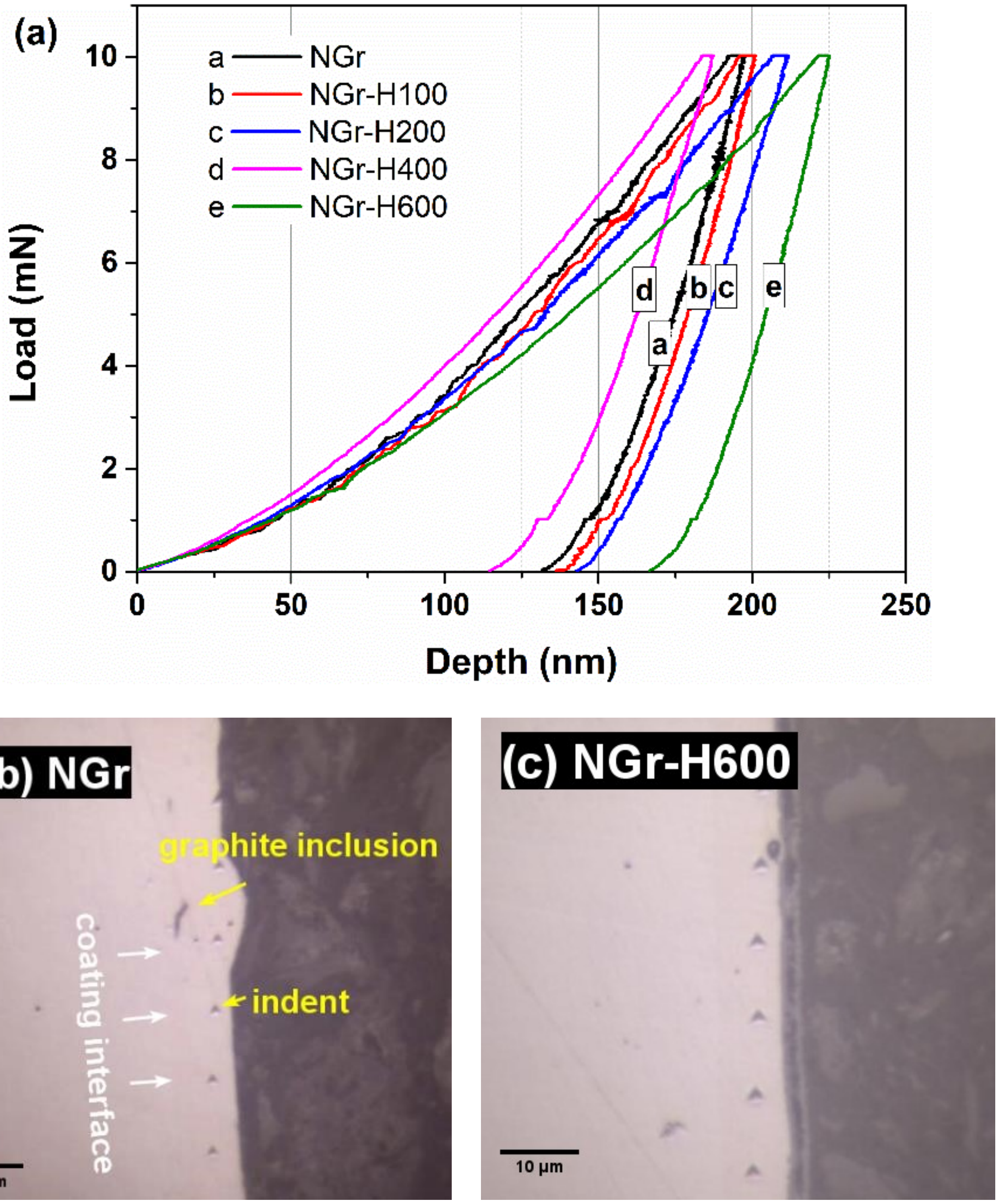

Figure 5.6-8. (a) Typical load-displacement curves of the nanoindentation tests on Ni-graphite (NGr) coatings as-deposited and annealed at varying temperatures and indents on (b) the original NGr and (c) the 600-degree-annealed NGr.

Figure 5.6-8a shows the indentation curves for the as-deposited and annealed NGr samples. Like the neat Ni samples, the indentation response of the NGr coating varied with the annealing temperature, which is indicative of an unstable microstructure and so the mechanics. The as-deposited NGr coating showed an improved hardness of 9.1 GPa. However, after annealing at 600 ℃, the hardness of the composite decreased by approximately 27%, even slightly higher than that (22%) for the neat Ni coating. The indents after the heat treatment were also clearly larger (Figure 5.6-8b&c). This suggests that although graphite reinforced the coating matrix successfully in the first place, it was unable to stabilise the microstructure of the coating upon heating.

The differences in the thermal stability of NG and NGr composite coatings can be attributed to the different incorporation status for GO sheets and graphite flakes. Owing to its extremely thin nature and flexibility, the GO sheets were uniformly incorporated in the composite matrix, wrapping and interacting with the nickel grains effectively and continuously across the whole coating. The incorporation of graphite flakes, in contrast, was discrete as many other conventional particulate reinforcements. The bulky graphite inclusions can lead to localised irregularity and surface fluctuation, as demonstrated in Figure 5.6-8b, and more importantly the ineffectiveness of the reinforcement phase at elevated temperatures.

Figure 5.6-9 show the fractography of the NGr coating, which is nearly the same lamellar structure as neat Ni (Figure 5.1-3). Individual graphite flakes can be clearly seen from the cross section, as indicated in Figure 5.6-9b. For comparison, the fracture of the NG coating is shown in Figure 5.6-10. Obviously, the microstructures of NG and NGr are substantially different, which is the reason for their different mechanical properties, in particular the thermal stability.

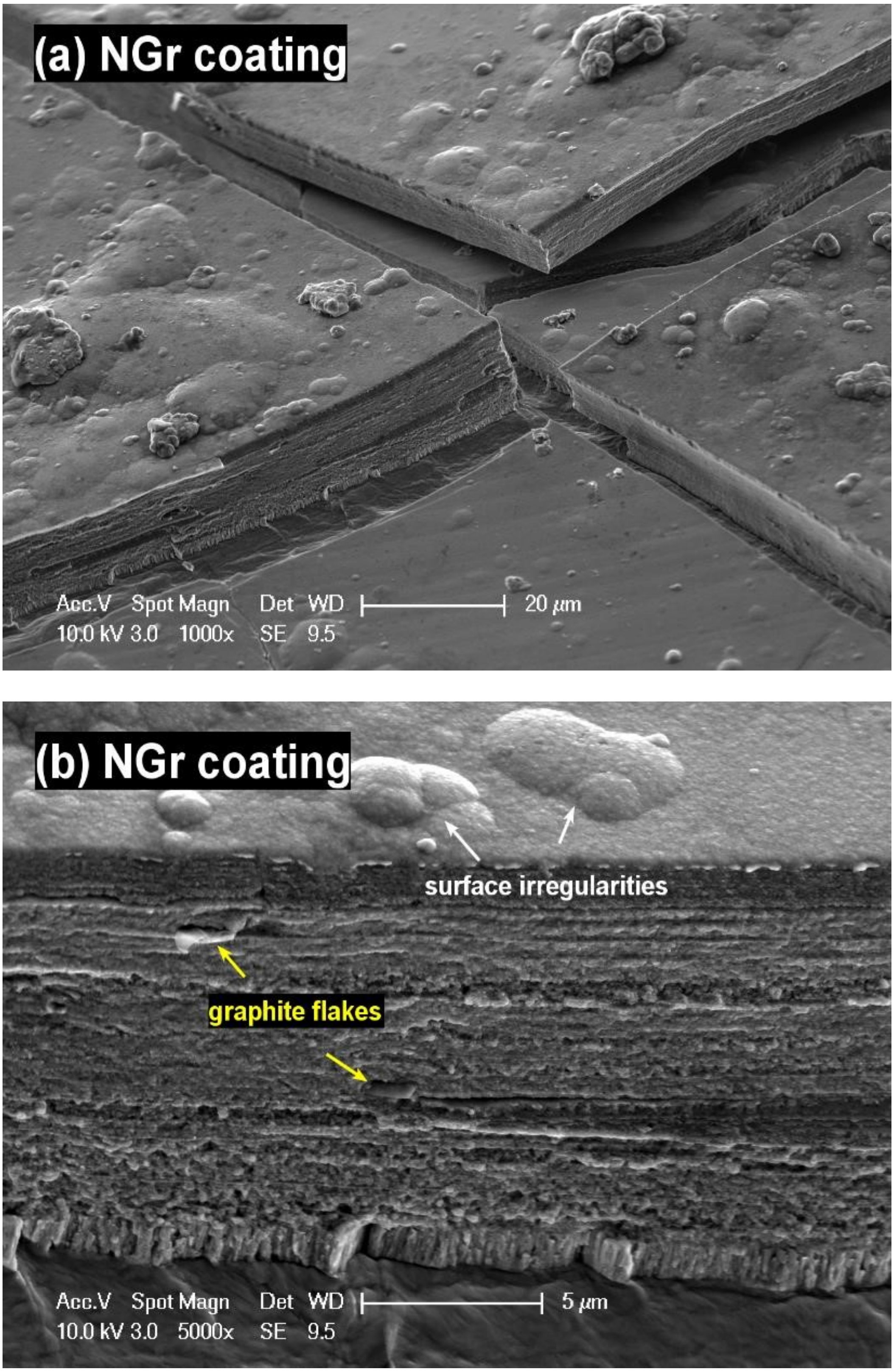

Figure 5.6-9. Morphology and fractography of NGr (Ni-graphite) composite coating.

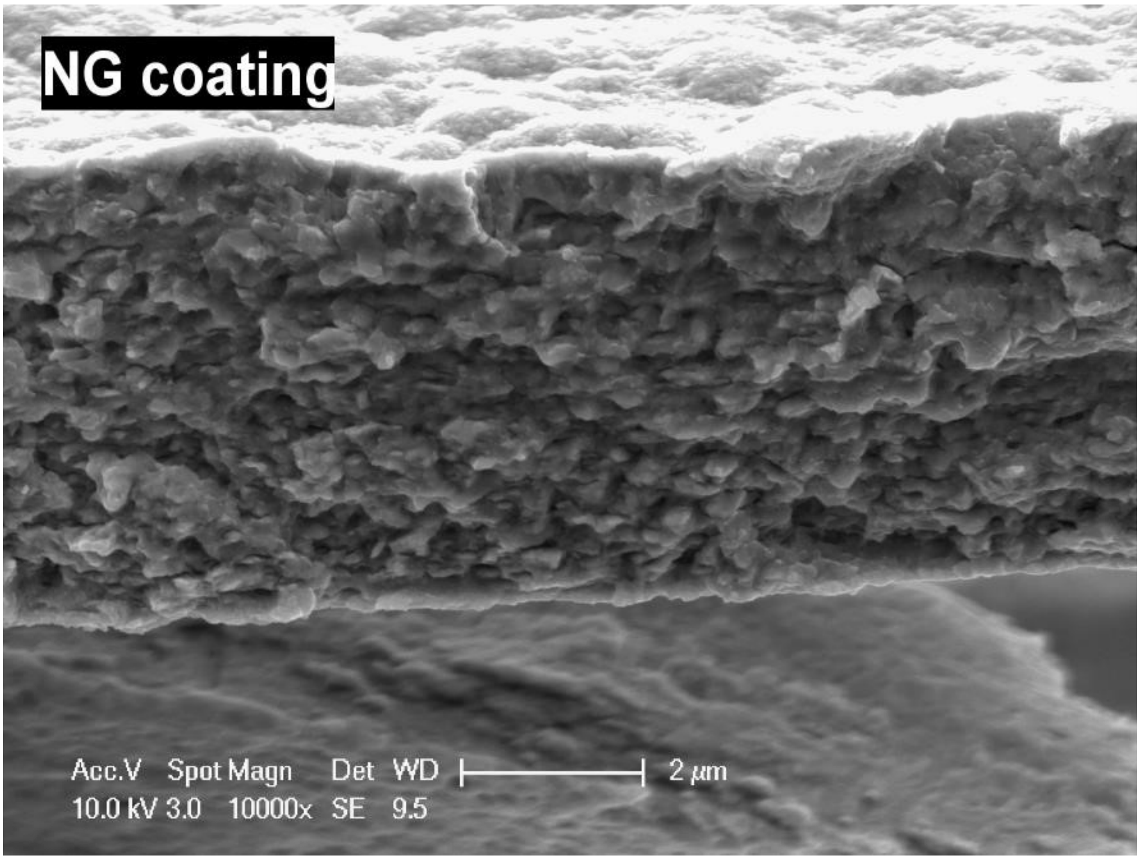

Figure 5.6-10. Fractography of NG (Ni-GO) composite coating.

# CHAPTER 6 CONCLUSIONS

In the present project, various routes have been explored towards cost-effective and scalable fabrication of graphene-based coatings on engineering metallic surfaces. The microstructures of the resultant coatings have been characterised and the mechanical, tribological and corrosion properties fully investigated. The key findings and implications produced throughout the results and discussion are summarised as follows:

## Part I - Electrophoretic deposition of GO coatings

1. Graphene oxide (GO) coatings can be deposited efficiently on 316L stainless steel substrate with tunable thickness of a few nm to hundreds of nm via electrophoretic deposition (EPD) from a simple aqueous GO suspension. GO can be reduced *in-situ* during the EPD process.
2. The GO-coated 316L steel shows low (COF ~0.1) yet unstable friction, due to insufficient bonding between the GO coating and the steel substrate. A specific topography of the metallic substrate, such as those modified by acid pickling and laser patterning, could contribute to a long-lasting performance of the coating.
3. The GO-coated 316L stainless steel can exhibit substantially improved anti-corrosion properties. This is attributed to the excellent physical barrier effect of GO. However, the protection is lost immediately when damages are generated in the thin GO coating.

## Part II - Self-assembled GO coatings

4. A graphene oxide coating can be fabricated on the surface of 316L stainless steel by self-assembly. The obtained GO coating is uniformly around 1 nm thin, corresponding to one single layer GO.
5. Pre-modification of the steel surface with an APTES intermediate layer can effectively enhance the tribological performance and durability of the GO coating.
6. The improvement could be mainly attributed to the enhanced bonding of the GO coating to the steel surface via the APTES intermediate layer. The results have shown, for example, that chemical surface modification can improve the service life of graphene-based coatings on metallic substrates.

## Part III - Electroplated Ni-GO composite coatings

7. Ni-GO composite coatings can be produced by electroplating from a GO-containing Watts plating bath. The composite coatings show surface irregularities and reduced average crystallite sizes (28 nm down to 20 nm) because of the incorporation of GO sheets.
8. The hardness and elastic modulus of the nickel matrix can be improved significantly with GO reinforcements.
9. GO incorporation can reduce the friction of the nickel matrix effectively due to the lubricating effect of the exposed GO sheets during wear.
10. GO agglomerations in the nickel matrix can promote localised galvanic corrosion, leading to even worse corrosion performance for Ni-GO composite coatings compared to neat nickel coating.

## Part IV - Electro-brush plated Ni-GO composite coatings

11. An electro-brush plating (EBP) technique has been developed for the novel fabrication of a nickel-GO nano-composite coating. It has been confirmed that GO sheets can be incorporated into the nickel matrix homogeneously. The brush plating method is beneficial as it allows a high GO load yet a compact and smooth coating morphology.
12. The average crystallite size of the nickel matrix can be reduced by 40% by the GO sheets. Nanoindentation and electrochemical studies have revealed that GO nano fillers can effectively improve the hardness and Young's modulus due to the grain refining and pinning effect of the GO nano sheets.
13. Electro-brush plated Ni-GO composite coatings have exhibited clearly enhanced thermal stability in terms of a better retention of the hardness and elastic properties after annealing at elevated temperatures up to 600 °C.
14. Ni-GO composite coatings by EBP can show significantly suppressed friction and wear (37% and 88% lower respectively in this study) compared to neat nickel coating. The wear mechanism changes from plasticity-dominated severe adhesive wear and galling to oxidation-dominated mild wear in the presence of GO reinforcements.
15. GO incorporation can improve the anti-corrosion performance of the nickel matrix significantly (a 70% reduction in corrosion current and 5-times increase in total corrosion impedance in this study).

# CHAPTER 7 FUTURE WORK

The present project has shown that graphene-based coatings can be fabricated effectively on metallic surfaces for various engineering applications. This work may also contribute to the understanding of the strengthening, anti-friction as well as the anti-corrosion mechanisms of graphene-based materials. Based on the results and implications out of the performed experiments, the following topics are suggested for future studies:

**EPD on complex shapes**

The results have shown that the EPD technique is effective in fabricating GO coatings uniformly on flat surfaces. It is worth attempting to deposit GO or GO-based composite coatings onto metallic substrates in complex shapes using EPD for potential applications, such as anti-corrosion paintings for offshore pipelines.

**Optimisation of electro-brush plating**

The electro-brush plating process, including the instrumental design and operation parameters, should be optimised in order to further improve the uniformity and minimise the residual stress within the deposit.

# REFERENCES

1. K.S. Novoselov, et al., *A roadmap for graphene.* Nature, 2012. **490**(7419): p. 192-200.

2. A.C. Ferrari, et al., *Science and technology roadmap for graphene, related two-dimensional crystals, and hybrid systems.* Nanoscale, 2015. **7**(11): p. 4598-4810.

3. C. Lee, et al., *Measurement of the elastic properties and intrinsic strength of monolayer graphene.* Science, 2008. **321**(5887): p. 385-388.

4. Z.-S. Wu, et al., *Field emission of single-layer graphene films prepared by electrophoretic deposition.* Adv. Mater., 2009. **21**(17): p. 1756-1760.

5. G. Eda, G. Fanchini, and M. Chhowalla, *Large-area ultrathin films of reduced graphene oxide as a transparent and flexible electronic material.* Nat. Nanotechnol., 2008. **3**(5): p. 270-274.

6. X. Li, et al., *Highly conducting graphene sheets and Langmuir-Blodgett films.* Nat. Nanotechnol., 2008. **3**(9): p. 538-542.

7. X. Wang, L. Zhi, and K. Mullen, *Transparent, conductive graphene electrodes for dye-sensitized solar cells.* Nano Lett., 2008. **8**(1): p. 323-327.

8. J.D. Fowler, et al., *Practical chemical sensors from chemically derived graphene.* ACS Nano, 2009. **3**(2): p. 301-306.

9. O. Penkov, et al., *Tribology of graphene: A review.* Int. J. Precis. Eng. Man., 2014. **15**(3): p. 577-585.

10. H. Dong and S. Qi, *Realising the potential of graphene-based materials for biosurfaces – A future perspective.* Biosurf. Biotribol., 2015. **1**(4): p. 229-248.

11. K.S. Kim, et al., *Chemical vapor deposition-grown graphene: the thinnest solid lubricant.* ACS Nano, 2011. **5**(6): p. 5107-5114.

12. D. Berman, A. Erdemir, and A.V. Sumant, *Reduced wear and friction enabled by graphene layers on sliding steel surfaces in dry nitrogen.* Carbon, 2013. **59**: p. 167-175.

13. D. Berman, A. Erdemir, and A.V. Sumant, *Few layer graphene to reduce wear and friction on sliding steel surfaces.* Carbon, 2013. **54**: p. 454-459.

14. T. Kobayashi, et al., *Production of a 100-m-long high-quality graphene transparent conductive film by roll-to-roll chemical vapor deposition and transfer process.* Appl. Phys. Lett., 2013. **102**(2): p. 023112.

15. C. Mattevi, H. Kim, and M. Chhowalla, *A review of chemical vapour deposition of graphene on copper.* J. Mater. Chem., 2011. **21**(10): p. 3324-3334.

16. H.A. Becerril, et al., *Evaluation of solution-processed reduced graphene oxide films as transparent conductors.* ACS Nano, 2008. **2**: p. 463-470.

17. S. Gijie, et al., *A chemical route to graphene for device applications.* Nano Lett, 2007. **7**: p. 3394-3398.

18. S. Das, et al., *Measurements of the adhesion energy of graphene to metallic substrates.* Carbon, 2013. **59**: p. 121-129.

19. V. Berry, *Impermeability of graphene and its applications.* Carbon, 2013. **62**: p. 1-10.

20. S. Chen, et al., *Oxidation resistance of graphene-coated Cu and Cu/Ni alloy.* ACS Nano, 2011. **5**(2): p. 1321-1327.

21. D. Prasai, et al., *Graphene- Corrosion-inhibiting coating.* ACS Nano, 2012. **6**(2): p. 1102-1108.

22. W. Sun, et al., *Inhibiting the corrosion-promotion activity of graphene.* Chem. Mater., 2015. **27**(7): p. 2367-2373.

23. B. Ramezanzadeh, et al., *Covalently-grafted graphene oxide nanosheets to improve barrier and corrosion protection properties of polyurethane coatings.* Carbon, 2015. **93**: p. 555-573.

24. Z. Yu, et al., *Fabrication of graphene oxide–alumina hybrids to reinforce the anti-corrosion performance of composite epoxy coatings.* Appl. Surf. Sci., 2015. **351**: p. 986-996.

25. K. Krishnamoorthy, et al., *Graphene oxide nanopaint.* Carbon, 2014. **72**: p. 328-337.

26. K.-C. Chang, et al., *Room-temperature cured hydrophobic epoxy/graphene composites as corrosion inhibitor for cold-rolled steel.* Carbon, 2014. **66**: p. 144-153.

27. K.S. Novoselov, et al., *Electric field effect in atomically thin carbon films.* Science, 2004. **306**(5696): p. 666-669.

28. A.K. Geim and K.S. Novoselov, *The rise of graphene.* Nat. Mater., 2007. **6**: p. 183-191.

29. *The Nobel Prize in Physics 2010*. [Internet] 2010 [cited 2016 August 03]; Available from: http://www.nobelprize.org/nobel_prizes/physics/laureates/2010/.

30. P. Wallace, *The band theory of graphite.* Phys. Rev., 1947. **71**(9): p. 622-634.

31. J.W. McClure, *Diamagnetism of graphite.* Phys. Rev., 1956. **104**(3): p. 666-671.

32. G. Semenoff, *Condensed-matter simulation of a three-dimensional anomaly.* Phys. Rev. Lett., 1984. **53**(26): p. 2449-2452.

33. E. Fradkin, *Critical behavior of disordered degenerate semiconductors. I. Models, symmetries, and formalism.* Phys. Rev. B, 1986. **33**(5): p. 3257-3262.

34. R. Peierls. *Quelques propriétés typiques des corps solides*. in *Annales de l'institut Henri Poincaré*. 1935. Presses universitaires de France.

35. L. Landau, *Zur Theorie der phasenumwandlungen II.* Phys. Z. Sowjetunion, 1937. **11**: p. 26-35.

36. N.D. Mermin, *Crystalline order in two dimensions.* Phys. Rev., 1968. **176**(1): p. 250-4.

37. H.P. Boehm, *Graphene--how a laboratory curiosity suddenly became extremely interesting.* Angew. Chem. Int. Ed. Engl., 2010. **49**(49): p. 9332-9335.

38. A.J. Van Bommel, J.E. Crombeen, and A. Van Tooren, *LEED and Auger electron observations of the SiC (0001) surface.* Surf. Sci., 1975. **48**(2): p. 463-472.

39. T.A. Land, et al., *STM investigation of single layer graphite structures produced on Pt(111) by hydrocarbon decomposition.* Surf. Sci., 1992. **264**: p. 261-270.

40. C. Oshima and A. Nagashima, *Ultra-thin epitaxial films of graphite and hexagonal boron nitride on solid surfaces.* J. Phys. Condens. Matter., 1997. **9**: p. 1-20.

41. I. Forbeaux, J.-M. Themlin, and J.-M. Debever, *Heteroepitaxial graphite on 6 H-SiC (0001): Interface formation through conduction-band electronic structure.* Phys. Rev. B, 1998. **58**(24): p. 16396-16406.

42. X. Lu, et al., *Tailoring graphite with the goal of achieving single sheets.* Nanotechnology, 1999. **10**(3): p. 269-272.

43. C. Berger, et al., *Ultrathin Epitaxial Graphite: 2D Electron Gas Properties and a Route toward Graphene-based Nanoelectronics.* J. Phys. Chem. B, 2004. **108**(52): p. 19912-19916.

44. H.P. Boehm, R. Setton, and E. Stumpp, *Nomenclature and terminology of graphite intercalation compounds.* Carbon, 1986. **24**(2): p. 241-245.

45. J.H. Warner, et al., *Graphene: Fundamentals and emergent applications*. 1 ed. 2013, Waltham, USA: Elsevier.

46. J.C. Meyer, et al., *The structure of suspended graphene sheets.* Nature, 2007. **446**: p. 60-63.

47. A. Fasolino, J.H. Los, and M.I. Katsnelson, *Intrinsic ripples in graphene.* Nat. Mater., 2007. **6**: p. 858-861.

48. A.C. Neto, et al., *The electronic properties of graphene.* Rev. Mod. Phys., 2009. **81**(1): p. 109.

49. K. Novoselov, et al., *Two-dimensional gas of massless Dirac fermions in graphene.* Nature, 2005. **438**(7065): p. 197-200.

50. Y. Zhang, et al., *Experimental observation of the quantum Hall effect and Berry's phase in graphene.* Nature, 2005. **438**(7065): p. 201-204.

51. *Researchers successfully grow defect-free graphene, commercial uses now in sight*. 2013 [cited 2016 August 03]; Available from: http://www.extremetech.com/extreme/147456-researchers-successfully-grow-defect-free-graphene-commercial-uses-now-in-sight.

52. *Columbia Engineers Prove Graphene is the Strongest Material*. [Internet] 2008 [cited 2016 August 03]; Available from: http://www.columbia.edu/cu/news/08/07/graphene.html.

53. A. Zandiatashbar, et al., *Effect of defects on the intrinsic strength and stiffness of graphene.* Nat. Commun., 2014. **5**.

54. Editorial, *Not so transparent.* Nat. Mater., 2013. **12**(10): p. 865-865.

55. Z. Li, et al., *Effect of airborne contaminants on the wettability of supported graphene and graphite.* Nat. Mater., 2013. **12**(10): p. 925-931.

56. C.-J. Shih, M.S. Strano, and D. Blankschtein, *Wetting translucency of graphene.* Nat. Mater., 2013. **12**(10): p. 866-869.

57. J.S. Bunch, et al., *Impermeable atomic membranes from graphene sheets.* Nano Lett., 2008. **8**(8): p. 2458-2462.

58. Y. Su, et al., *Impermeable barrier films and protective coatings based on reduced graphene oxide.* Nat. Commun., 2014. **5**.

59. J.S. Oh, K.N. Kim, and G.Y. Yeom, *Graphene doping methods and device applications.* J. Nanosci. Nanotechno., 2014. **14**(2): p. 1120-1133.

60. H. Wang, T. Maiyalagan, and X. Wang, *Review on recent progress in nitrogen-doped graphene: Synthesis, characterization, and its potential applications.* ACS Catalysis, 2012. **2**(5): p. 781-794.

61. K.P. Loh, et al., *The chemistry of graphene.* J. Mater. Chem., 2010. **20**(12): p. 2277-89.

62. R. Imran Jafri, N. Rajalakshmi, and S. Ramaprabhu, *Nitrogen doped graphene nanoplatelets as catalyst support for oxygen reduction reaction in proton*

*exchange membrane fuel cell.* J. Mater. Chem., 2010. **20**(34): p. 7114-7.

63. Y. Shao, et al., *Nitrogen-doped graphene and its electrochemical applications.* J. Mater. Chem., 2010. **20**(35): p. 7491-6.

64. H.M. Jeong, et al., *Nitrogen-doped graphene for high-performance ultracapacitors and the importance of nitrogen-doped sites at basal planes.* Nano Lett., 2011. **11**(6): p. 2472-7.

65. Y. Shao, et al., *Graphene based electrochemical sensors and biosensors: A review.* Electroanalysis, 2010. **22**(10): p. 1027-1036.

66. L. Feng and Z. Liu, *Graphene in biomedicine: opportunities and challenges.* Nanomedicine, 2011. **6**(2): p. 317-324.

67. H. Zhang, G. Grüner, and Y. Zhao, *Recent advancements of graphene in biomedicine.* J. Mater. Chem. B, 2013. **1**(20): p. 2542-67.

68. M. Song and D. Cai, *Graphene functionalization: A review*, in *Polymer-Graphene Nanocomposites*. 2012, RSC.

69. O.C. Compton and S.T. Nguyen, *Graphene oxide, highly reduced graphene oxide, and graphene: versatile building blocks for carbon-based materials.* Small, 2010. **6**(6): p. 711-23.

70. D.R. Dreyer, et al., *The chemistry of graphene oxide.* Chem. Soc. Rev., 2010. **39**(1): p. 228-40.

71. A. Lerf, et al., *Structure of graphite oxide revisited.* J. Phys. Chem. B, 1998. **102**(23): p. 4477-4482.

72. S. Stankovich, et al., *Stable aqueous dispersions of graphitic nanoplatelets via the reduction of exfoliated graphite oxide in the presence of poly(sodium 4-styrenesulfonate).* J. Mater. Chem., 2006. **16**(2): p. 155-158.

73. S. Pei and H.-M. Cheng, *The reduction of graphene oxide.* Carbon, 2012. **50**(9): p. 3210-3228.

74. S. Stankovich, et al., *Synthesis of graphene-based nanosheets via chemical reduction of exfoliated graphite oxide.* Carbon, 2007. **45**(7): p. 1558-1565.

75. G. Eda and M. Chhowalla, *Chemically derived graphene oxide: towards large-area thin-film electronics and optoelectronics.* Adv Mater, 2010. **22**(22): p. 2392-415.

76. T. Kuila, et al., *Chemical functionalization of graphene and its applications.* Prog. Mater. Sci., 2012. **57**(7): p. 1061-1105.

77. N.A. Kumar, et al., *Plasma-assisted simultaneous reduction and nitrogen doping of graphene oxide nanosheets.* J. Mater. Chem. A, 2013. **1**(14): p. 4431-5.

78. A. Bianco, et al., *All in the graphene family – A recommended nomenclature for two-dimensional carbon materials.* Carbon, 2013. **65**: p. 1-6.

79. A.A. Balandin, et al., *Superior thermal conductivity of single-layer graphene.* Nano Lett., 2008. **8**(3): p. 902-907.

80. R. Moriya, et al., *Large current modulation in exfoliated-graphene/MoS2/metal vertical heterostructures.* Appl. Phys. Lett., 2014. **105**(8): p. 083119.

81. P.S. Toth, et al., *Electrochemistry in a drop: a study of the electrochemical behaviour of mechanically exfoliated graphene on photoresist coated silicon substrate.* Chem. Sci., 2014. **5**(2): p. 582-589.

82. S. Niyogi, et al., *Solution properties of graphite and graphene.* JACS, 2006. **128**(24): p. 7720-7721.

83. J.N. Coleman, *Liquid exfoliation of defect-free graphene.* Acc. Chem. Res., 2013. **46**(1): p. 14-22.

84. V. Nicolosi, et al., *Liquid exfoliation of layered materials.* Science, 2013. **340**(6139): p. 1226419.

85. Y. Hernandez, et al., *High-yield production of graphene by liquid-phase exfoliation of graphite.* Nat. Nanotechnol., 2008. **3**(9): p. 563-568.

86. M. Lotya, et al., *Liquid Phase Production of Graphene by Exfoliation of Graphite in Surfactant-Water Solutions.* JACS, 2009. **131**(10): p. 3611–3620.

87. U. Khan, et al., *High-concentration solvent exfoliation of graphene.* Small, 2010. **6**(7): p. 864-871.

88. R.J. Smith, M. Lotya, and J.N. Coleman, *The importance of repulsive potential barriers for the dispersion of graphene using surfactants.* New J. Phys., 2010. **12**(12): p. 125008.

89. K.R. Paton, et al., *Scalable production of large quantities of defect-free few-layer graphene by shear exfoliation in liquids.* Nat. Mater., 2014. **13**: p. 624-630.

90. X. Li, L. Colombo, and R.S. Ruoff, *Synthesis of Graphene Films on Copper Foils by Chemical Vapor Deposition.* Adv. Mater., 2016. **28**(29): p. 6247-52.

91. M.S. Choi, S.H. Lee, and W.J. Yoo, *Plasma treatments to improve metal contacts in graphene field effect transistor.* J. Appl. Phys., 2011. **110**(7): p. 073305.

92. X. Li, et al., *Large-area synthesis of high-quality and uniform graphene films on copper foils.* Science, 2009. **324**(5932): p. 1312-1314.

93. S. Bae, et al., *Roll-to-roll production of 30-inch graphene films for transparent electrodes.* Nat. Nanotechnol., 2010. **5**(8): p. 574-8.

94. G. Deokar, et al., *Towards high quality CVD graphene growth and transfer.* Carbon, 2015. **89**: p. 82-92.

95. D. Wei, et al., *Low temperature critical growth of high quality nitrogen doped graphene on dielectrics by plasma-enhanced chemical vapor deposition.* ACS Nano, 2015. **9**(1): p. 164-171.

96. W. Norimatsu and M. Kusunoki, *Epitaxial graphene on SiC {0001}: advances and perspectives.* Phys. Chem. Chem. Phys., 2014. **16**(8): p. 3501-3511.

97. K.V. Emtsev, et al., *Towards wafer-size graphene layers by atmospheric pressure graphitization of silicon carbide.* Nat. Mater., 2009. **8**(3): p. 203-207.

98. X. Yang, et al., *Two-dimensional graphene nanoribbons.* JACS, 2008. **130**(13): p. 4216-4217.

99. D.R. Dreyer, R.S. Ruoff, and C.W. Bielawski, *From conception to realization: an historial account of graphene and some perspectives for its future.* Angew. Chem. Int. Ed. Engl., 2010. **49**(49): p. 9336-44.

100. B.C. Brodie, *On the atomic weight of graphite.* Philos. Trans. R. Soc. London, 1859. **149**: p. 249-259.

101. L. Staudenmaier, *Method for representing the graphite acid.* Ber. Dtsch. Chem. Ges., 1898. **31**: p. 1481-1487.

102. W.S. Hummers and R.E. Offeman, *Preparation of graphitic oxide.* JACS, 1958.

103. D.C. Marcano, D.V. Kosynkin, and J.M. Berlin, *Improved synthesis of graphene oxide.* ACS Nano, 2010. **4**: p. 4806-4814.

104. S. Park, et al., *Aqueous suspension and characterization of chemically modified graphene sheets.* Chem. Mater., 2008. **20**: p. 6592-6594.

105. J. Zhao, et al., *Efficient preparation of large-area graphene oxide sheets for transparent conductive films.* ACS Nano, 2010. **4**: p. 5245-5252.

106. N.I. Kovtyukhnova and e. al., *Layer-by-layer assembly of ultrathin composite films from micron-sized graphite oxide sheets and polycations.* Chem. Mater., 1999. **11**: p. 771-778.

107. A.M. Dimiev and J.M. Tour, *Mechanism of graphene oxide formation.* ACS Nano, 2014. **8**(3): p. 3060-3068.

108. J.I. Paredes, et al., *Graphene oxide dispersions in organic solvents.* Langmuir, 2008. **24**: p. 10560-10564.

109. D. Li, et al., *Processable aqueous dispersions of graphene nanosheets.* Nat. Nanotechnol., 2008. **3**(2): p. 101-105.

110. V.C. Tung, et al., *High-throughput solution processing of large-scale graphene.* Nat. Nanotechnol., 2009. **4**(1): p. 25-9.

111. Y. Si and E.T. Samulski, *Synthesis of water soluble graphene.* Nano Lett., 2008. **8**(6): p. 1679-1682.

112. S. Pei, et al., *Direct reduction of graphene oxide films into highly conductive and flexible graphene films by hydrohalic acids.* Carbon, 2010. **48**(15): p. 4466-4474.

113. M.J. Fernandez-Merino, et al., *Vitamin C is an ideal substitute for hydrazine in the reduction of graphene oxide suspensions.* J. Phys. Chem. C, 2010. **114**: p. 6426-6432.

114. *Our Nobel Prize winners-Sir Norman Haworth*. [cited 2016 August 07]; Available from: http://www.birmingham.ac.uk/alumni/ouralumni/nobelprizewinners/haworth.aspx.

115. C.K. Chua and M. Pumera, *Chemical reduction of graphene oxide: a synthetic chemistry viewpoint.* Chem. Soc. Rev., 2013. **43**: p. 291-312.

116. H.C. Schniepp, et al., *Functionalized single graphene sheets derived from splitting graphite oxide.* J. Phys. Chem. B, 2006. **110**(17): p. 8535-8539.

117. M. Zhou, et al., *Controlled synthesis of large-area and patterned electrochemically reduced graphene oxide films.* Chemistry, 2009. **15**(25): p. 6116-20.

118. X.-Y. Peng, et al., *Synthesis of electrochemically-reduced graphene oxide film with controllable size and thickness and its use in supercapacitor.* Carbon, 2011. **49**(11): p. 3488-3496.

119. Z. Wang, et al., *Comparative studies on single-layer reduced graphene oxide films obtained by electrochemical reduction and hydrazine vapor reduction.* Nano. Res. Lett., 2012. **7**(1): p. 1-7.

120. X. Wang and Y. Shi, *CHAPTER 1 Fabrication techniques of graphene nanostructures*, in *Nanofabrication and its Application in Renewable Energy*. 2014, The Royal Society of Chemistry. p. 1-30.

121. W. Regan, et al., *A direct transfer of layer-area graphene.* Appl. Phy. Lett., 2010. **96**(11): p. 113102.

122. Y. Wang, et al., *Electrochemical delamination of CVD-grown graphene film: Toward the recyclable use of copper catalyst.* ACS Nano, 2011. **5**(12): p. 9927-9933.

123. V. Mišković-Stanković, et al., *Electrochemical study of corrosion behavior of graphene coatings on copper and aluminum in a chloride solution.* Carbon, 2014. **75**: p. 335-344.

124. L.J. Cote, F. Kim, and J. Huang, *Langmuir−Blodgett assembly of graphite oxide single layers.* JACS, 2009. **131**: p. 1043-1049.

125. J.C. Love, et al., *Self-assembled monolayers of thiolates on metals as a form of nanotechnology.* Chem. Rev., 2005. **105**(4): p. 1103-1170.

126. J. Ou, et al., *Tribology study of reduced graphene oxide sheets on silicon substrate synthesized via covalent assembly.* Langmuir, 2010. **26**(20): p. 15830-15836.

127. J. Ou, et al., *Self-assembly of octadecyltrichlorosilane on graphene oxide and the tribological performances of the resultant film.* J. Phys. Chem. C, 2011. **115**(20): p. 10080-10086.

128. Z. Liu, et al., *Tribology study of lanthanum-treated graphene oxide thin film on silicon substrate.* RSC Adv., 2014. **4**(31): p. 15937-44.

129. G. Bai, et al., *Self-assembly of ceria/graphene oxide composite films with ultra-long antiwear lifetime under a high applied load.* Carbon, 2015. **84**: p. 197-206.

130. P.F. Li, Y. Xu, and X.-H. Cheng, *Chemisorption of thermal reduced graphene oxide nano-layer film on TNTZ surface and its tribological behavior.* Surf. Coat. Tech., 2013. **232**: p. 331-339.

131. P.F. Li, H. Zhou, and X.-H. Cheng, *Nano/micro tribological behaviors of a self-assembled graphene oxide nanolayer on Ti/titanium alloy substrates.* Appl. Surf. Sci., 2013. **285**: p. 937-944.

132. J. Ou, et al., *Fabrication and tribological investigation of a novel hydrophobic polydopamine/graphene oxide multilayer film.* Tribol. Lett., 2012. **48**(3): p. 407-415.

133. S. Liu, et al., *Layer-by-layer assembly and tribological property of multilayer ultrathin films constructed by modified graphene sheets and polyethyleneimine.* Appl. Surf. Sci., 2012. **258**(7): p. 2231-2236.

134. L. Besra and M. Liu, *A review on fundamentals and applications of electrophoretic deposition (EPD).* Prog. Mater. Sci., 2007. **52**(1): p. 1-61.

135. O.O. Van der Biest and L.J. Vandeperre, *Electrophoretic deposition of materials.* Annu. Rev. Mater. Sci., 1999. **29**(1): p. 327-352.

136. A.R. Boccaccini, et al., *Electrophoretic deposition of carbon nanotubes.* Carbon, 2006. **44**(15): p. 3149-3160.

137. S.A. Hasan, et al., *Transferable Graphene oxide films with tunable microstructures.* ACS Nano, 2010. **4**(12): p. 7367-7372.

138. M. Diba, et al., *Quantitative evaluation of electrophoretic deposition kinetics of graphene oxide.* Carbon, 2014. **67**: p. 656-661.

139. Y. Chen, et al., *Electrophoretic deposition of graphene nanosheets on nickel foams for electrochemical capacitors.* J. Power Sources, 2010. **195**(9): p. 3031-3035.

140. M. Li, et al., *Graphene oxide/hydroxyapatite composite coatings fabricated by electrophoretic nanotechnology for biological applications.* Carbon, 2014. **67**: p. 185-197.

141. H. Zhang, et al., *One-step electrophoretic deposition of reduced graphene oxide and Ni(OH)2 composite films for controlled syntheses supercapacitor electrodes.* J. Phys. Chem. B, 2013. **117**(6): p. 1616-27.

142. R. Ishikawa, et al., *Electrophoretic deposition of high quality transparent conductive graphene films on insulating glass substrates.* J. Phys. Conf. Ser., 2012. **352**: p. 012003-9.

143. S.J. An, et al., *Thin film fabrication and simultaneous anodic reduction of deposited graphene oxide platelets by electrophoretic deposition.* J. Phys. Chem. Lett., 2010. **1**(1259-1263).

144. Y. Su and I. Zhitomirsky, *Electrophoretic deposition of graphene, carbon nanotubes and composite films using methyl violet dye as a dispersing agent.* Colloids Surf. A, 2013. **436**: p. 97-103.

145. W. He, et al., *Electrophoretic deposition of graphene oxide as a corrosion inhibitor for sintered NdFeB.* Appl. Surf. Sci., 2013. **279**: p. 416-423.

146. S. Liu, et al., *A simple two-step electrochemical synthesis of graphene sheets film on the ITO electrode as supercapacitors.* J. Appl. Electrochem., 2011. **41**(7): p. 881-884.

147. A. Chavez-Valdez, M.S. Shaffer, and A.R. Boccaccini, *Applications of graphene electrophoretic deposition. A review.* J. Phys. Chem. B, 2013. **117**(6): p. 1502-15.

148. H. Liang, et al., *Graphene oxide film as solid lubricant.* ACS Appl. Mater. Interfaces, 2013. **5**(13): p. 6369-75.

149. M. Wang, et al., *Large-area, conductive and flexible reduced graphene oxide (RGO) membrane fabricated by electrophoretic deposition (EPD).* ACS Appl. Mater. Interfaces, 2014. **6**(3): p. 1747-53.

150. J.H. Park and J.M. Park, *Electrophoretic deposition of graphene oxide on mild carbon steel for anti-corrosion application.* Surf. Coat. Tech., 2014. **254**: p. 167-174.

151. G. Zhu, et al., *Electrophoretic deposition of reduced graphene-carbon nanotubes composite films as counter electrodes of dye-sensitized solar cells.* J. Mater. Chem., 2011. **21**(38): p. 14869-14875.

152. L. Tang, et al., *Uniform and rich-wrinkled electrophoretic deposited graphene film: a robust electrochemical platform for TNT sensing.* Chem. Comm., 2010. **46**(32): p. 5882-5884.

153. Z. Li, et al., *High-temperature tribological properties of Ni-P alloy coatings deposited by electro-brush plating.* Rare Met., 2011. **30**(6): p. 669-675.

154. B. Wu, et al., *Automatic brush plating: An update on brush plating.* Mater. Lett., 2006. **60**(13-14): p. 1673-1677.

155. B. Xu, et al., *Fretting wear-resistance of Ni-base electro-brush plating coating reinforced by nano-alumina grains.* Mater. Lett., 2006. **60**(5): p. 710-713.

156. C. Guo, et al., *Effects of surfactants on electrodeposition of nickel-carbon nanotubes composite coatings.* Surf. Coat. Tech., 2008. **202**(14): p. 3385-3390.

157. E. Rudnik, et al., *Electrodeposition of nickel/SiC composites in the presence of cetyltrimethylammonium bromide.* Appl. Surf. Sci., 2010. **256**(24): p. 7414-7420.

158. T. Borkar and S.P. Harimkar, *Effect of electrodeposition conditions and reinforcement content on microstructure and tribological properties of nickel composite coatings.* Surf. Coat. Tech., 2011. **205**(17-18): p. 4124-4134.

159. X. Li, et al., *Study of deposition patterns of plating layers in SiC/Cu composites by electro-brush plating.* Appl. Surf. Sci., 2011. **257**(23): p. 10294-10299.

160. B. Jiang, et al., *Contact fatigue behavior of nano-ZrO2/Ni coating prepared by electro-brush plating.* Surf. Coat. Tech., 2007. **202**(3): p. 447-452.

161. G. Ma, et al., *Research on the microstructure and space tribology properties of electric-brush plated Ni/MoS2–C composite coating.* Surf. Coat. Tech., 2013. **221**: p. 142-149.

162. H. Liu, X. Wang, and H. Ji, *Fabrication of lotus-leaf-like superhydrophobic surfaces via Ni-based nano-composite electro-brush plating.* Appl. Surf. Sci., 2014. **288**: p. 341-348.

163. J. Tan, et al., *Microstructure and wear resistance of nickel–carbon nanotube composite coating from brush plating technique.* Tribol. Lett., 2006. **21**(2): p. 107-111.

164. X. Jiang, X. Xie, and Z. Xu, *Double glow surface alloying of low carbon steel with electric brush plating Ni interlayer for improvement in corrosion resistance.* Surf. Coat. Tech., 2003. **168**(2): p. 156-160.

165. Z. Ren, et al., *Mechanical properties of nickel-graphene composites synthesized by electrochemical deposition.* Nanotechnology, 2015. **26**(6): p. 065706-065711.

166. P. Zhou, et al., *Fabrication and Corrosion Performances of Pure Ni and Ni-*

*Based Coatings Containing Rare Earth Element Ce and Graphene by Reverse Pulse Electrodeposition.* J. Electrochem. Soc., 2017. **164**(2): p. D75-D81.

167. C.M.P. Kumar, T.V. Venkatesha, and R. Shabadi, *Preparation and corrosion behavior of Ni and Ni–graphene composite coatings.* Mater. Res. Bull., 2013. **48**(4): p. 1477-1483.

168. H. Algul, et al., *The effect of graphene content and sliding speed on the wear mechanism of nickel–graphene nanocomposites.* Appl. Surf. Sci., 2015. **359**: p. 340-348.

169. D. Kuang, et al., *Graphene–nickel composites.* Appl. Surf. Sci., 2013. **273**: p. 484-490.

170. K. Jiang, J. Li, and J. Liu, *Electrochemical codeposition of graphene platelets and nickel for improved corrosion resistant properties.* RSC Adv., 2014. **4**(68): p. 36245-52.

171. C. Lee, et al., *Elastic and frictional properties of graphene.* Phys. Status Solidi B, 2009. **246**(11‐12): p. 2562-2567.

172. T. Filleter, et al., *Friction and dissipation in epitaxial graphene films.* Phys. Rev. Lett., 2009. **102**(8): p. 086102-5.

173. C. Lee, et al., *Frictional characteristics of atomically thin sheets.* Science, 2010. **328**(5974): p. 76-80.

174. Q. Li, et al., *Substrate effect on thickness‐dependent friction on graphene.* Phys. Status Solidi B, 2010. **247**(11‐12): p. 2909-2914.

175. Z. Ye, et al., *Role of wrinkle height in friction variation with number of graphene layers.* J. Appl. Phys., 2012. **112**(11): p. 116102-4.

176. P. Liu and Y.W. Zhang, *A theoretical analysis of frictional and defect characteristics of graphene probed by a capped single-walled carbon nanotube.* Carbon, 2011. **49**(11): p. 3687-3697.

177. T. Filleter and R. Bennewitz, *Structural and frictional properties of graphene films on SiC(0001) studied by atomic force microscopy.* Phys. Rev. B, 2010. **81**(15): p. 155412-8.

178. C.H. Lui, et al., *Ultraflat graphene.* Nature, 2009. **462**(7271): p. 339-341.

179. D.H. Cho, et al., *Effect of surface morphology on friction of graphene on various substrates.* Nanoscale, 2013. **5**(7): p. 3063-9.

180. D. Marchetto, et al., *Friction and wear on single-layer epitaxial graphene in multi-asperity contacts.* Tribol. Lett., 2012. **48**(1): p. 77-82.

181. Y.J. Shin, et al., *Frictional characteristics of exfoliated and epitaxial graphene.*

Carbon, 2011. **49**(12): p. 4070-4073.

182. F. Bonelli, et al., *Atomistic simulations of the sliding friction of graphene flakes.* Eur. Phys. J. B, 2009. **70**(4): p. 449-459.

183. M.-S. Won, O.V. Penkov, and D.-E. Kim, *Durability and degradation mechanism of graphene coatings deposited on Cu substrates under dry contact sliding.* Carbon, 2013. **54**: p. 472-481.

184. Q. Li, et al., *Fluorination of graphene enhances friction due to increased corrugation.* Nano Lett., 2014. **14**(9): p. 5212-5217.

185. J.-H. Ko, et al., *Nanotribological properties of fluorinated, hydrogenated, and oxidized graphenes.* Tribol. Lett., 2013. **50**(2): p. 137-144.

186. S. Kwon, et al., *Enhanced nanoscale friction on fluorinated graphene.* Nano Lett., 2012. **12**(12): p. 6043-8.

187. G. Fessler, et al., *Friction force microscopy studies on $SiO_2$ supported pristine and hydrogenated graphene.* Appl. Phy. Lett., 2014. **104**(4): p. 041910-3.

188. D. Berman, et al., *Nanoscale friction properties of graphene and graphene oxide.* Diam. Relat. Mater., 2014. **54**: p. 91-6.

189. Y. Peng, Z. Wang, and C. Li, *Study of nanotribological properties of multilayer graphene by calibrated atomic force microscopy.* Nanotechnology, 2014. **25**(30): p. 305701-9.

190. H. Chen and T. Filleter, *Effect of structure on the tribology of ultrathin graphene and graphene oxide films.* Nanotechnology, 2015. **26**(13): p. 135702-12.

191. H. Lee, et al., *Comparison of frictional forces on graphene and graphite.* Nanotechnology, 2009. **20**(32): p. 325701-6.

192. D. Berman, A. Erdemir, and A.V. Sumant, *Graphene: a new emerging lubricant.* Mater. Today, 2014. **17**(1): p. 31-42.

193. D. Berman, et al., *Extraordinary macroscale wear resistance of one atom thick graphene layer.* Adv. Funct. Mater., 2014. **24**(42): p. 6640-6646.

194. D. Berman, A. Erdemir, and A.V. Sumant, *Graphene as a protective coating and superior lubricant for electrical contacts.* Appl. Phys. Lett., 2014. **105**(23): p. 231907-10.

195. J. Pu, et al., *Preparation and tribological study of functionalized graphene–IL nanocomposite ultrathin lubrication films on Si substrates.* J. Phys. Chem. C, 2011. **115**(27): p. 13275-13284.

196. X. Liu, et al., *Novel DLC/ionic liquid/graphene nanocomposite coatings towards high-vacuum related space applications.* J. Mater. Chem. A, 2013. **1**(11): p.

3797-809.

197. W. Zhao, et al., *Fabrication and investigation the microtribological behaviors of ionic liquid–graphene composite films.* Tribol. Trans., 2013. **56**(3): p. 480-487.

198. E. Thangavel, et al., *Structural and tribological characteristics of poly(vinylidene fluoride)/functionalized graphene oxide nanocomposite thin films.* Compos. Sci. Tech., 2014. **90**: p. 187-192.

199. C. Min, et al., *Study of tribological properties of polyimide/graphene oxide nanocomposite films under seawater-lubricated condition.* Tribol. Int., 2014. **80**: p. 131-140.

200. H.-J. Song, et al., *Preparation and tribological behaviors of poly (ether ether ketone) nanocomposite films containing graphene oxide nanosheets.* J. Nanopart. Res., 2013. **15**(2): p. 1433-42.

201. H. Li, et al., *Microstructure and wear behavior of graphene nanosheets-reinforced zirconia coating.* Ceram. Int., 2014. **40**(8): p. 12821-12829.

202. S. Stankovich, et al., *Graphene-based composite materials.* Nature, 2006. **442**: p. 282-286.

203. M.A. Rafiee, et al., *Buckling resistant graphene nanocomposites.* Appl. Phys. Lett., 2009. **95**(22): p. 223103-5.

204. M.A. Rafiee, et al., *Fracture and fatigue in graphene nanocomposites.* Small, 2010. **6**(2): p. 179-83.

205. M.A. Rafiee, et al., *Enhanced mechanical properties of nanocomposites at low graphene content.* ACS Nano, 2009. **3**(12): p. 3884-3890.

206. S. Suñer and N. Emami, *Investigation of graphene oxide as reinforcement for orthopaedic applications.* Tribology, 2014. **8**(1): p. 1-6.

207. Y. Chen, et al., *Preparation, mechanical properties and biocompatibility of graphene oxide/ultrahigh molecular weight polyethylene composites.* Eur. Polym. J., 2012. **48**(6): p. 1026-1033.

208. S. Baradaran, et al., *Mechanical properties and biomedical applications of a nanotube hydroxyapatite-reduced graphene oxide composite.* Carbon, 2014. **69**: p. 32-45.

209. M.M. Shokrieh, et al., *Nanoindentation and nanoscratch investigations on graphene-based nanocomposites.* Polym. Test, 2013. **32**(1): p. 45-51.

210. Z. Tai, et al., *Tribological behavior of UHMWPE reinforced with graphene oxide nanosheets.* Tribol. Lett., 2012. **46**(1): p. 55-63.

211. Y. Li, et al., *Preparation and tribological properties of graphene oxide/nitrile*

*rubber nanocomposites.* J. Mater. Sci., 2011. **47**(2): p. 730-738.

212. Z. Xu, et al., *Preparation and tribological properties of TiAl matrix composites reinforced by multilayer graphene.* Carbon, 2014. **67**: p. 168-177.

213. Z. Xu, et al., *Formation of friction layers in graphene-reinforced TiAl matrix self-lubricating composites.* Tribol. Trans., 2015. **58**(4): p. 668-78.

214. X.-J. Shen, et al., *Tribological performance of carbon nanotube–graphene oxide hybrid/epoxy composites.* Compos. Part B Eng., 2014. **57**: p. 120-125.

215. X.-J. Shen, et al., *Significantly modified tribological performance of epoxy nanocomposites at very low graphene oxide content.* Polymer, 2013. **54**(3): p. 1234-1242.

216. S.S. Kandanur, et al., *Suppression of wear in graphene polymer composites.* Carbon, 2012. **50**(9): p. 3178-3183.

217. R.S. Raman and A. Tiwari, *Graphene: The thinnest known coating for corrosion protection.* JOM, 2014. **66**(4): p. 637-642.

218. S.P. Koenig, et al., *Selective molecular sieving through porous graphene.* Nat. Nanotechnol., 2012. **7**(11): p. 728-732.

219. N. Raghav, S. Chakraborty, and P.K. Maiti, *Molecular mechanism of water permeation in a helium impermeable graphene and graphene oxide membrane.* Phys. Chem. Chem. Phys., 2015. **17**(32): p. 20557-20562.

220. L. Tsetseris and S.T. Pantelides, *Graphene: An impermeable or selectively permeable membrane for atomic species?* Carbon, 2014. **67**: p. 58-63.

221. O. Leenaerts, B. Partoens, and F.M. Peeters, *Graphene: A perfect nanoballoon.* Appl. Phys. Lett., 2008. **93**(19): p. 193107.

222. R.R. Nair, et al., *Unimpeded permeation of water through helium-leak–tight graphene-based membranes.* Science, 2012. **335**(6067): p. 442-444.

223. L. Nilsson, et al., *Graphene coatings: probing the limits of the one atom thick protection layer.* ACS Nano, 2012. **6**(11): p. 10258-10266.

224. N.T. Kirkland, et al., *Exploring graphene as a corrosion protection barrier.* Corros. Sci., 2012. **56**: p. 1-4.

225. R. Singh Raman, et al., *Protecting copper from electrochemical degradation by graphene coating.* Carbon, 2012. **50**(11): p. 4040-4045.

226. Y.-P. Hsieh, et al., *Complete corrosion inhibition through graphene defect passivation.* ACS Nano, 2014. **8**(1): p. 443-448.

227. J.-H. Huh, et al., *Enhancement of seawater corrosion resistance in copper using*

*acetone-derived graphene coating.* Nanoscale, 2014. **6**(8): p. 4379-4386.

228. N.-W. Pu, et al., *Graphene grown on stainless steel as a high-performance and ecofriendly anti-corrosion coating for polymer electrolyte membrane fuel cell bipolar plates.* J. Power Sources, 2015. **282**: p. 248-256.

229. A. Krishnamurthy, et al., *Passivation of microbial corrosion using a graphene coating.* Carbon, 2013. **56**: p. 45-49.

230. W. Zhang, et al., *Use of graphene as protection film in biological environments.* Sci. Rep., 2014. **4**: p. 4097-104.

231. I. Wlasny, et al., *Role of graphene defects in corrosion of graphene-coated Cu (111) surface.* Appl. Phy. Lett., 2013. **102**(11): p. 111601.

232. M. Schriver, et al., *Graphene as a Long-Term Metal Oxidation Barrier- Worse Than Nothing.* ACS Nano, 2013. **7**(7): p. 5763–5768.

233. F. Zhou, et al., *Enhanced room-temperature corrosion of copper in the presence of graphene.* ACS Nano, 2013. **7**(8): p. 6939-6947.

234. S.J. Richard Prabakar, et al., *Graphene oxide as a corrosion inhibitor for the aluminum current collector in lithium ion batteries.* Carbon, 2013. **52**: p. 128-136.

235. K.S. Aneja, et al., *Graphene based anticorrosive coatings for Cr(VI) replacement.* Nanoscale, 2015. **7**(42): p. 17879-88.

236. M. Merisalu, et al., *Graphene–polypyrrole thin hybrid corrosion resistant coatings for copper.* Synth. Met., 2015. **200**: p. 16-23.

237. C.-H. Chang, et al., *Novel anticorrosion coatings prepared from polyaniline/graphene composites.* Carbon, 2012. **50**(14): p. 5044-5051.

238. S. Mayavan, T. Siva, and S. Sathiyanarayanan, *Graphene ink as a corrosion inhibiting blanket for iron in an aggressive chloride environment.* RSC Adv., 2013. **3**(47): p. 24868-24871.

239. S.C. Sahu, et al., *A facile electrochemical approach for development of highly corrosion protective coatings using graphene nanosheets.* Electrochem. Commun., 2013. **32**: p. 22-26.

240. B.P. Singh, et al., *Development of oxidation and corrosion resistance hydrophobic graphene oxide-polymer composite coating on copper.* Surf. Coat. Tech., 2013. **232**: p. 475-481.

241. B.P. Singh, et al., *The production of a corrosion resistant graphene reinforced composite coating on copper by electrophoretic deposition.* Carbon, 2013. **61**: p. 47-56.

242. Y.-H. Yu, et al., *High-performance polystyrene/graphene-based*

*nanocomposites with excellent anti-corrosion properties.* Polym. Chem., 2014. **5**(2): p. 535-550.

243. W. Sun, et al., *Synthesis of low-electrical-conductivity graphene/pernigraniline composites and their application in corrosion protection.* Carbon, 2014. **79**: p. 605-614.

244. B. Ramezanzadeh, et al., *Enhancement of barrier and corrosion protection performance of an epoxy coating through wet transfer of amino functionalized graphene oxide.* Corros. Sci., 2016. **103**: p. 283-304.

245. A. Janković, et al., *Bioactive hydroxyapatite/graphene composite coating and its corrosion stability in simulated body fluid.* J. Alloy. Compd., 2015. **624**: p. 148-157.

246. M. Li, et al., *Electrophoretic deposition and electrochemical behavior of novel graphene oxide-hyaluronic acid-hydroxyapatite nanocomposite coatings.* Appl. Surf. Sci., 2013. **284**: p. 804-810.

247. W.C. Oliver and G.M. Pharr, *An improved technique for determining hardness and elastic modulus using load and displacement sensing indentation experiments.* J. Mat. Res., 1992. **7**(06): p. 1564-1583.

248. C. Bao, et al., *Preparation of graphene by pressurized oxidation and multiplex reduction and its polymer nanocomposites by masterbatch-based melt blending.* J. Mater. Chem., 2012. **22**(13): p. 6088-6096.

249. M.H. Lee, et al., *The effect of non-specific interactions on cellular adhesion using model surfaces.* Biomater., 2005. **26**(14): p. 1721-30.

250. Q. Gu and X. Cheng, *Tribological behaviors of self-assembled 3-aminopropyltriethoxysilane films on silicon.* Curr. Appl. Phys., 2008. **8**(5): p. 583-588.

251. A.C. Ferrari, *Raman spectroscopy of graphene and graphite: Disorder, electron–phonon coupling, doping and nonadiabatic effects.* Solid State Commun., 2007. **143**(1-2): p. 47-57.

252. S. Park and R.S. Ruoff, *Chemical methods for the production of graphenes.* Nat. Nanotechnol., 2009. **4**(4): p. 217-224.

253. Q. Zheng, et al., *Transparent conductive films consisting of ultralarge graphene sheets produced by Langmuir-Blodgett assembly.* ACS Nano, 2011. **5**: p. 6039-6051.

254. T. Borkar and S. Harimkar, *Microstructure and wear behaviour of pulse electrodeposited Ni–CNT composite coatings.* Surf. Eng., 2011. **27**(7): p. 524-530.

255. J. Li, et al., *Effect of surface laser texture on friction properties of nickel-based*

*composite.* Tribol. Int., 2010. **43**(5-6): p. 1193-1199.

256. R.L. Fusaro, *Effect of substrate surface finish on the lubrication and failure mechanisms of molybdenum disulfide films.* ASLE Trans., 1982. **25**(2): p. 141-156.

257. P. Basnyat, et al., *Surface texturing for adaptive solid lubrication.* Surf. Coat. Tech., 2008. **203**(1-2): p. 73-79.

258. V. Lee, et al., *Large-area chemically modified graphene films: Electrophoretic deposition and characterization by soft X-ray absorption spectroscopy.* Chem. Mater., 2009. **21**(16): p. 3905-3916.

259. S.C. Lim and M.F. Ashby, *Wear-Mechanism maps.* Acta Metall., 1987. **35**(1): p. 1-24.

260. A.A. Balandin, *Thermal properties of graphene and nanostructured carbon materials.* Nat. Mater., 2011. **10**(8): p. 569-81.

261. M.-S. Wu, et al., *Formation of nano-scaled crevices and spacers in NiO-attached graphene oxide nanosheets for supercapacitors.* J. Mater. Chem., 2012. **22**(6): p. 2442-8.

262. W.-h. Li, et al., *Microstructure of Ni–polytetrafluoroethylene composite coating prepared by brush electroplating.* Surf. Coat. Tech., 2006. **201**(3-4): p. 1276-1281.

263. R.G. Kelly, et al., *Electrochemical techniques in corrosion science and engineering*. 2003, USA: Marcel Dekker, Inc.

264. F.H. Cao, et al., *Electrochemical impedance spectroscopy analysis on aluminum alloys in EXCO solution.* Mater. Corros., 2005. **56**(5): p. 318-324.

265. J. Molina, et al., *Synthesis of Pt nanoparticles on electrochemically reduced graphene oxide by potentiostatic and alternate current methods.* Mater. Charact., 2014. **89**(3): p. 56-68.

266. L. Chen, et al., *Direct electrodeposition of reduced graphene oxide on glassy carbon electrode and its electrochemical application.* Electrochem. Commun., 2011. **13**(2): p. 133-137.

267. A. Dorri Moghadam, et al., *Mechanical and tribological properties of self-lubricating metal matrix nanocomposites reinforced by carbon nanotubes (CNTs) and graphene – A review.* Compos. Part B Eng., 2015. **77**: p. 402-420.

268. Q. Zheng, et al., *Molecular dynamics study of the effect of chemical functionalization on the elastic properties of graphene sheets.* J. Nanosci. Nanotechnol., 2010. **10**(11): p. 7070-7074.

269. J.W. Suk, et al., *Mechanical properties of monolayer graphene oxide.* ACS Nano,

2010. **4**(11): p. 6557-6564.

270. C. Gómez-Navarro, M. Burghard, and K. Kern, *Elastic properties of chemically derived single graphene sheets.* Nano Letters, 2008. **8**(7): p. 2045-2049.

271. L.Y. Wang, et al., *Friction and wear behavior of electroless Ni-based CNT composite coatings.* Wear, 2003. **254**(12): p. 1289-1293.

272. S.-K. Kim and T.-S. Oh, *Electrodeposition behavior and characteristics of Ni-carbon nanotube composite coatings.* Trans. Nonferrous Met. Soc. China, 2011. **21**: p. s68-s72.

273. I.M. Hutchings, *Tribology: friction and wear of engineering materials*. 1992, London: Edward Arnold.

274. H. Dong and T. Bell, *Enhanced wear resistance of titanium surfaces by a new thermal oxidation treatment.* Wear, 2000. **238**: p. 131-137.

275. A. Leyland and A. Matthews, *On the significance of the H/E ratio in wear control: a nanocomposite coating approach to optimised tribological behaviour.* Wear, 2000. **246**(1): p. 1-11.

276. D. Berman, et al., *Macroscale superlubricity enabled by graphene nanoscroll formation.* Science, 2015. **348**(6239): p. 1118-1122.

277. Z. Gong, et al., *Graphene nano scrolls responding to superlow friction of amorphous carbon.* Carbon, 2017. **116**: p. 310-317.

278. X. Dou, et al., *Self-dispersed crumpled graphene balls in oil for friction and wear reduction.* PNAS, 2016. **113**(6): p. 1528-1533.

279. V. Zin, et al., *Improved tribological and thermal properties of lubricants by graphene based nano-additives.* RSC Adv., 2016. **6**(64): p. 59477-59486.

280. Z. Zhang, et al., *Sliding friction and wear behaviour of Titanium-Zirconium-Molybdenum (TZM) alloy against $Al_2O_3$ and $Si_3N_4$ balls under several environments and temperatures.* Tribol. Int., 2017. **110**: p. 348-357.

281. C.S. Lin, et al., *Annealing behavior of electrodeposited Ni-TiO2 composite coatings.* Surf. Coat. Tech., 2006. **200**(12-13): p. 3690-3697.

282. M. Spasojević, et al., *Effect of Deposition Current Density and Annealing Temperature on the Microstructure, Hardness and Magnetic Properties of Nanostructured Nickel-Iron-Tungsten Alloys.* J. Electrochem. Soc., 2014. **161**(10): p. D463-D469.

283. W.X. Chen, et al., *Tribological application of carbon nanotubes in a metal-based composite coating and composites.* Carbon, 2003. **41**(2): p. 215-222.

284. N. Birks, G.H. Meier, and F.S. Pettit, *Introduction to the high temperature*

*oxidation of metals*. 2006: Cambridge University Press.

285. G. Gyawali, et al., *Fabrication and Characterization of Electrodeposited Ni–SiC–h/BN Composite Coatings.* J. Mater. Sci. Technol., 2014. **30**(8): p. 796-802.

286. C. Liu, F. Su, and J. Liang, *Producing cobalt–graphene composite coating by pulse electrodeposition with excellent wear and corrosion resistance.* Appl. Surf. Sci., 2015. **351**: p. 889-896.

287. J. Chen, et al., *Low Temperature Nano-Tribological Study on a Functionally Graded Tribological Coating Using Nanoscratch Tests.* Tribol. Lett., 2011. **43**(3): p. 351-360.

288. A. Leyland and A. Matthews, *Design criteria for wear-resistant nanostructured and glassy-metal coatings.* Surf. Coat. Tech., 2004. **177**: p. 317-324.

289. K.I. Schiffmann, *Determination of fracture toughness of bulk materials and thin films by nanoindentation: comparison of different models.* Philos. Mag., 2011. **91**(7-9): p. 1163-1178.

290. J. Musil and M. Jirout, *Toughness of hard nanostructured ceramic thin films.* Surf. Coat. Tech., 2007. **201**(9-11): p. 5148-5152.